CHARACTERIZING THE ROLES OF EXIT TUNNEL RESIDUES IN LIGAND BINDING AND CATALYSIS OF HISTONE DEACETYLASE-8

A Thesis
Submitted to the Graduate Faculty
of the
North Dakota State University
of Agriculture and Applied Science

By

Ruchi Gupta

In Partial Fulfillment
for the Degree of
MASTER OF SCIENCE

Major Department:
Chemistry and Biochemistry

March 2014

Fargo, North Dakota

North Dakota State University
Graduate School

Title

Characterizing the Roles of Exit Tunnel Residues in Ligand Binding and Catalysis of Histone Deacetylase-8

By

Ruchi Gupta

The Supervisory Committee certifies that this ***disquisition*** complies with North Dakota State University's regulations and meets the accepted standards for the degree of

MASTER OF SCIENCE

SUPERVISORY COMMITTEE:

Dr. D.K. Srivastava
Chair

Dr. Gregory Cook

Dr. Stuart Haring

Dr. Jane Schuh

Approved:

03/26/2014	Gregory Cook
Date	Department Chair

ABSTRACT

Histone deacetylases are an important class of enzymes that catalyze the hydrolysis of acetyl-L-lysine side chains in histone and non-histone proteins to yield L-lysine and acetate, effecting the epigenetic regulation of gene expression. In addition to the active site pocket, the enzyme harbors an internal cavity for the release of acetate by-product. To probe the role of highly conserved amino acid residues lining this exit tunnel, site-directed alanine substitutions were made at tyrosine-18, tyrosine-20 and histidine-42 positions. These mutants were characterized by various biochemical and biophysical techniques to define the effect of mutations on ligand binding and catalysis of the enzyme.

The mutations altered the catalytic activity of HDAC8 significantly. Y18A mutation dramatically impaired the structural-functional aspects of the enzymatic reaction. Our data reveal that there is long range communication between the exit tunnel residues and the active site pocket of HDAC8, presumably regulating the overall catalysis of the enzyme.

TABLE OF CONTENTS

LIST OF TABLES

LIST OF FIGURES

LIST OF SCHEMES

LIST OF ABBREVIATIONS

AMC 7-amino-4-methylcoumarin

BSA.....Bovine serum albumin

CD.....Circular dichroism

CNS.....Central nervous system

c-SAHA ….....Coumarin-suberoylanilide hydroxamic acid

DAD ……..Deacetylase-activation domain

DMSO.....Dimethylsulfoxide

DTT .....Dithiothreitol

FPLC.....Fast protein liquid chromatography

GPCR .....G-protein coupled receptor

HDAC ……...Histone deacetylase

HDLP ……Histone deacetylase like protein

HEPES .....4-(2-Hydroxyethyl)piperazine-1-ethanesulfonic acid

IPTG.....Isopropyl thio-β-galactopyranoside

ITC .....Isothermal Titration Calorimetry

kcal .....Kilo calories

kD.....Kilo Dalton

mdeg .....milli-degrees

MES .....2-Morpholinoethanesulfonic acid

min .....Minute

NCBI.....National center for biotechnology information

NMR .....Nuclear magnetic resonance

ns .....Nanosecond

PAGE.....Polyacrylamide gel electrophoresis

PCR.....Polymerase chain reaction

PKA .....Protein kinase A

PMSF .....Phenylmethylsulfonyl fluoride

s.....Second

SAHA ……Suberoylanilide hydroxamic acid

SDS .....Sodium dodecyl sulfate

TM-2-51..... N(phenylcarbothiol)benzamide

TSA ……Trichostatin A

CHAPTER 1. INTRODUCTION

1.1. A Literature Review Detailing the Histone Deacetylase (HDACs) Family

1.1.1. Discovery of Histone Deacetylases (HDACs)

Histones and DNA constitute the nucleosomes which are very important in packaging of eukaryotic DNA into chromosomes. In the mid 1960's, experiments were performed to identify the role of histones in nuclear function with major focus on post-translational modifications of histones by adding and removing acetyl groups and thereby having an important role in gene transcription. Results from these experiments suggested that relatively minor modifications of histone structure, taking place on the intact protein molecule, acted as an on- or off-switch for RNA synthesis, and they occurred at different loci on the chromosome. Hence, the overall feature play an important role in the global gene transcription (1).

The acetylation and deacetylation of histones is catalyzed by two different classes of enzymes, namely histone acetyl transferases and histone deacetylases (HDACs) , respectively (2). Histone deacetylases (HDACs) catalyze the removal of the acetyl group from the ε-amino group of lysine side chains clustered near the hydrophilic N-terminal ends of the core histones. This stabilizes the interaction between histones and DNA by reconstituting the positive charges of the lysine residues. Deacetylation is often correlated with transcriptional silencing as it makes the promoter elements inaccessible to certain transcription factors. Leipe et al., (1997) showed that histone deacetylases share significant sequence similarity with two groups of prokaryotic enzymes, the *acu*C (acetoin utilization protein) gene product and the acetylpolyamine amidohydrolases (3).Acetylpolyamine amidohydrolases catalyze deacetylation of a polyamine by cleaving a non-peptide amide bond. The *acu*C protein from *Bacillus subtilis* and *Staphylococcus*

xylosus may share deacetylating chemistry with histone deacetylase and polyamine amidohydrolase. HD1 is the gene for histone deacetylase (4). Two potential histone deacetylases (human and mouse RPD3) have been shown to enhance transcriptional repression activity of the mammalian zinc finger transcription factor YY1 (5). Yeast proteins HDA1 and RPD3 have been identified as the catalytic subunits of two distinct histone deacetylase complexes, HAD and HDB, respectively (6,7) . Histone deacetylases comprise one of the groups of proteins that share a sequence similarity to HD1 along with prokaryotic acetylpolyamine amidohydrolases. The sequence alignment between HD1 and HDACs comprised of 163 residues distributed among nine sequence blocks. It included a region of ~ 70 amino acids with no length variation between residues 77 and 136, along with many highly conserved and 11 invariant residues.

The highest similarity to HD1 was found in a group of eukaryotic proteins that were originally identified because of their similarity to yeast RPD3 (8). It is also known that human and mouse RPD3 are similar enough to be considered as orthologs-they are much more similar to HD1 than to yeast RPD3. Existence of several HDACs in human and mouse suggests that there was at least one gene duplication event that predated the divergence of the rodents and primate lineages.

Acetylpolyamine amidohydrolases and histone deacetylases recognize the same target - (an acetylaminopropyl group) and they catalyze the removal of an acetyl group by cleaving a non-peptide amide bond. It is speculated that before the eukaryotes and histones evolved, there was a gene regulatory mechanism in place that relied on reversible acetylation and deacetylation of DNA- binding cations to influence DNA organization. It means that instead of histones there were other positively charged molecules that could bind DNA and as a result influence its

organizational state. Once histones evolved, duplication of the acetylpolyamine amidohydrolase genes provided proteins that needed to undergo only a slight shift in their substrate specificity to be able to act as HDACs.

1.1.2. Classification of Histone Deacetylases (HDACs)

Histone deacetylases (HDACs) are a large family of hydrolytic enzyme, and there are nearly 18 HDACs whose activities have been implicated in a number of physiological processes in eukaryotes (Table 1.1). They have been broadly classified into three classes based upon their sequence homology to yeast HDACs, phylogeny and cofactor requirement. The Class I HDACs are most closely related to yeast (S*accharomyces cerevisiae*) RPD3 which functions as a transcriptional regulator. Class II HDACs share a high degree of sequence homology with the HDA1 gene found in yeast and its protein exhibits the deacetylase activity. Class III HDACs are a family of enzymes with a close resemblance to SIR2 family of NAD^+-dependent HDACs. Recently discovered HDAC 11 shares the properties of both the Class I & II HDACs but due to overall low sequence similarity, it has been placed in Class IV of the HDAC family (9).

1.1.2.1. Class I HDACs

HDAC1, HDAC2, HDAC3 and HDAC8 belong to the class I of HDACs(10–13). They are ubiquitously present in most of the cell types including many human cell lines and tissues. These enzymes are 400-500 amino acids long and all of them contain a deacetylase catalytic domain. A C- terminal RB- binding motif is located adjacent to a basic region in HDAC1 and HDAC2. Their locations on the chromosome have been mapped using techniques like FISH(14) and radiation hybrid mapping(15) . They are mainly present in the nucleus, especially HDAC1 and HDAC2, due to the absence of the nuclear export peptide sequence (NES) (16). HDAC3 has

been mostly found to be localized in the nucleus but it does have a nuclear import signal in addition to the NES. It's preferable localization is important because of its recruitment by HDACs 4, 5 and 7 when they are bound to the DNA via co-repressors (17–19).

The Class I HDACs are components of large protein complexes *in vivo* that direct gene-specific regulation of transcription, hormone signaling, DNA repair and differentiation (20). It has been shown that Class I HDACs associate with the silencing mediator for the retinoid and thyroid hormone receptor complex (SMRT) (20), the CoREST complex as well as the Sin3 and Mi-2/NuRD corepressor complexes (21,22). Along with RbAp46/48, HDACs 1 and 2 are part of the core complex. This core complex forms a part of the Sin3 complex along with SAP18 and SAP 30, having an important role in stabilizing the protein interactions. Of these, mSin3A plays the role of a scaffold for the assembly of the complex (23).

The NuRD , along with the core complex contains MTA2, CHD3 and CHD4, all of which have the DNA- helicase domains (24). In the CoREST complex, RbAp46/48 proteins are absent but HDACs 1 and 2 are present along with proteins homologous to MTA 1 and 2 (known as CoREST and p110, respectively) (25). Other Class I HDACs have also been found in complex with DNA methyltransferase 1(26,27), Rb (28,29), glucocorticoid receptor(30) TGIF/Smads (31) and Sp1 (32). It has been further shown that HDAC 3 forms a complex with N-CoR (Nuclear receptor corepressor) (33,34) and this complex inhibits JNK activation(35). The post-translational modifications of HDACs have a role in regulating their own activity. The phosphorylated form of HDAC1 has lower activity than its non-phosphorylated form. The most pronounced effect of HDAC1 phosphorylation has been found to be the disruption of protein complex formation between HDACs 1 and 2 as well as between HDAC 1 and

mSin3(36).Casein- Kinase 2 (CK2) and cAMP-dependent protein kinase A (PKA) have both been shown to phosphorylate HDAC1, whereas HDAC2 is phosphorylated exclusively by CK2. The phosphorylation of HDAC2 promotes the enzyme activity and it regulates the complex formation with mSin3 and Mi2. However, the above feature does not have any effect on transcriptional repression of the cognate genes (37).

Table 1.1. Human Histone Deacetylases (modified from Thiagalingam *et al*) (38)

Histone Deacetylase		**Size (amino acids)**	**Chromosomal location**
CLASS I	HDAC1	482	1p34.1
	HDAC2	488	6q21
	HDAC3	428	5q31.1-5q31.3
	HDAC8	377	Xq21.2-Xq21.3 or Xq13
CLASS II	HDAC4	1084	2q37
	HDAC5	1122	17q21
	HDAC6	1215	Xp11.23
	HDAC7	952	12q13.1
	HDAC9	1011	7p15-p21
	HDAC10	669	22q13.31-13.33
	HDAC11	347	3p25.1
CLASS III (sirtuins)	SIRT1	747	10q22.2
	SIRT2	389	19q13
	SIRT3	399	11p15.5
	SIRT4	314	12q
	SIRT5	310	6p22.3
	SIRT6	355	19p13.3
	SIRT7	400	17q

1.1.2.2. Class II HDACs

HDAC isozymes 4, 5, 6 ,7, 10 and 11 are the members of the Class II HDACs, which are homologous to yeast HDA1(39–42). These enzymes are large (~ 1000 amino acids) as compared to the Class I HDACs, which are constituted of 400-500 amino acids (22). The catalytic domains of class II HDACs are present toward the C-terminal ends of the protein sequence. However, in the case of HDAC6, a second catalytic domain is also present at the N-terminal end. With exception of HDAC10, the Class II HDACs are localized in the cytoplasm, and they shuttle to the nucleus in response to a stimulus. HDAC10 has an N-terminal catalytic domain and a C-terminal pseudo-repeat that is homologous to the catalytic domain. Class II HDACs are differentially expressed in human tissues, with the highest concentrations being in the brain, skeletal muscle and heart (22,43). They have also been reported to be involved in larger multi-protein complexes. It has been shown that HDAC4 and HDAC5 associate with HDAC3(39) and then form a complex with N-CoR and SMRT(44).The interactions of HDACs 4 and 5 with the cytoplasmic protein 14-3-3 sequesters these proteins in the cytoplasm, thereby preventing their association with HDAC3 (present in the nucleus). Loss of interaction with 14-3-3 protein results in the translocation of HDACs 4 and 5 to the nucleus where these proteins associate with HDAC3,causing gene repression (45). A recent study suggests that Class II HDACs regulate transcription by bridging the N-CoR/SMRT-HDAC3 complex with selected transcription factors, irrespective of its HDAC activity (17).

Class II HDACs also play an important role in activating muscle-specific genes and hence have a role in the differentiation of both skeletal and smooth muscles. This regulation is mediated via the interaction of the N-terminal extensions of HDACs 4, 5 and 7 with MEF2

transcription factors in the nucleus (46,47). HDACs have also been shown to repress MEF2-mediated transcription by interacting with the carboxyl-terminal binding protein (CtBP) (48).

1.1.2.3. Class III HDACs

Class III HDACs are known as Sirtuins, and they are the homologs of the yeast Sir2 gene product, which has a function in cellular metabolism, chromatin silencing and aging (49).There are seven sirtuins (SIRT 1-7) in humans, ranging in size from 300-400 amino acids except for SIRT1 which is larger and contains nearly 750 amino acids. These sirtuins require NAD^+ for their activity (50). In addition to their nearly 300 amino acids long catalytic domain, these enzymes contain a leucine zipper and motifs that function as zinc fingers(51).A number of functionally important amino acids have been identified in sirtuins. For example, G270 and N345 are important as their absence results in, either diminished or complete disruption of the deacetylase activity (50). These proteins are localized in different cellular compartments.

Human Sir2 is not present in the nucleus. SIRT1 has been shown to deacetylate p53 leading to repression of p53-mediated transcriptional activation. This inhibits growth or an apoptotic response due to DNA-damage (52–56). The above mentioned association of the proteins has a tremendous potential for developing p53-based cancer therapy.

1.1.3. Functions and Localization of Class I HDACs/HDAC8

HDACs deacetylate acetylated forms of histones in the nucleus, which results in altering the gene expression. In addition, HDACs also have many non-histone substrates, e.g., p53 and α-tubulin .Class I HDACs (HDACs 1, 2, 3 and 8) are homologous to yeast RPD3. They have been known to have roles in various biological processes like cell proliferation and survival. Increased levels of HDACs have been associated with many cancers (57) and their inhibition leads to

decreased proliferation and apoptosis in case of neoplastic transformed cells(58). HDAC1 and HDAC2 are ubiquitously present in the nucleus and are over-expressed in many cancers, making these promising targets for cancer therapy (59). Deletion of HDAC1 causes a G1- arrest leading to the disruption of mitosis (60,61). HDAC1 plays a major role in the proliferation of human osteosarcoma and breast cancer (62). Its inhibition can lead to induction of autophagy which is an important mechanism in the treatment of certain cancers (63).HDAC2 has been found to have an anti-apoptotic function in cancerous cells (64).

Class I HDACs are expressed during most stages of development and in many different cell-types (65). With a few exceptions, HDACs are localized mostly in the nucleus. HDAC8, although present predominantly in the nucleus, is a prominent cytosolic marker of smooth muscle differentiation (66), and has a role in smooth muscle cytoskeleton regulation. HDAC8 is expressed in multiple human tissues, including liver, heart, brain, lung, pancreas, placenta, prostate and kidney and it preferentially deacetylates histones H3 and H4. HDAC8 has diverse functions (67) and has been shown to influence interferon-β gene expression (68). It also has a role in acute myeloid leukemia where it specifically associates with inv fusion protein (69). Vannini et al.(70) reported an important role of HDAC8 in tumor cell proliferation by demonstrating that HDAC8 knockdown led to the inhibition of human lung, colon and cervical cancer cell lines. HDAC8 has also been found to be involved in telomerase regulation where its phosphorylated form protects human ever-shorter telomerase 1B (hEST1B) from degradation by CHIP (C-terminal heat shock protein interacting protein), a E3 ubiquitin ligase, via the recruitment of HSP70 (67).

1.1.4. Structures of Class I HDACs and Histone Deacetylase-like Protein (HDLP)

1.1.4.1. Histone Deacetylase-like Protein (HDLP)

Histone Deacetylase-like protein (HDLP) is a bacterial homolog of Class I HDACs and was isolated for the first time from a hyperthermophilic bacterium *Aquifex aeolicus*. It shares 35.2 % sequence identity with HDAC1 over 375 residues and has been shown to deacetylate histones *in vitro*(71). Finnin et al.(71) solved the crystal structure of HDLP in complex with SAHA and TSA, two of the known inhibitors of HDAC Class I enzymes. These structures revealed a tube-shaped active site, a zinc-binding pocket and two Aspartate-Histidine charge-relay systems. The crystal structure reveals that HDLP consists of a single-domain structure belonging to the open α/β class of folds(71). The structure can be described as consisting of eight-stranded parallel β-sheets and 16 α-helices (Figure 1.1). The core α/β structure is formed by four helices packing on either face of the β-sheet while the remaining 8 helices appear to be mostly clustered near one side of the β-sheet (Figure 1.1). The presence of a deep, narrow pocket and an internal cavity adjacent to the pocket, as shown by Figure.1.3, are two prominent features of this protein. They are formed by the large, well-defined loops originating from the carboxy-terminal ends of the β-strands (loops L1-L7; Figure. 1.2) and the extra α-helices (apart from those forming the core α/β motif).

The architecture of the active-site pocket is very important in explaining the deacetylase mechanism of this protein. The tube-like pocket mentioned above is ~ 11 Å deep. This pocket constricts halfway down but eventually becomes wider at the bottom (Figure. 1.3). Seven loops (L1-L7), as mentioned above, make up the pocket and its immediate surroundings. Hydrophobic

and aromatic amino acid residues (P22, G140, F141, F198, L265 and Y297) dominate the walls of the pocket. These residues are identical in HDAC1.

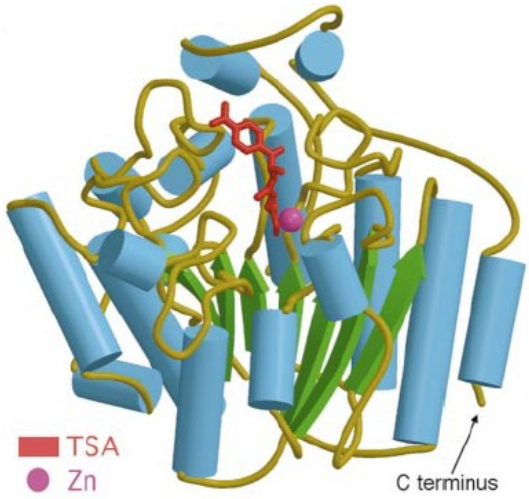

Figure 1.1. Structure of a HDLP-Zn^{2+}-TSA complex.
HDLP structure revealing the deacetylase catalytic core comprising of α/β folds, is shown. Trichostatin A (TSA) (red) is bound to the active site where it co-ordinates with the active site zinc (pink).Figure adapted from reference (71).

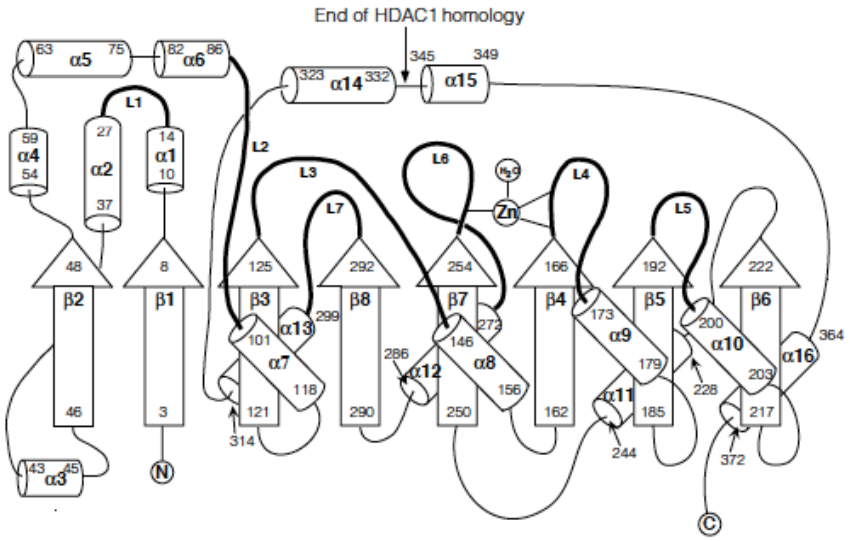

Figure 1.2. Schematic of the topology of HDLP.
Loops involved in the formation of the active site pocket are shown in bold. End of the deacetylase motif is indicated by an arrow. Figure adapted from reference (71).

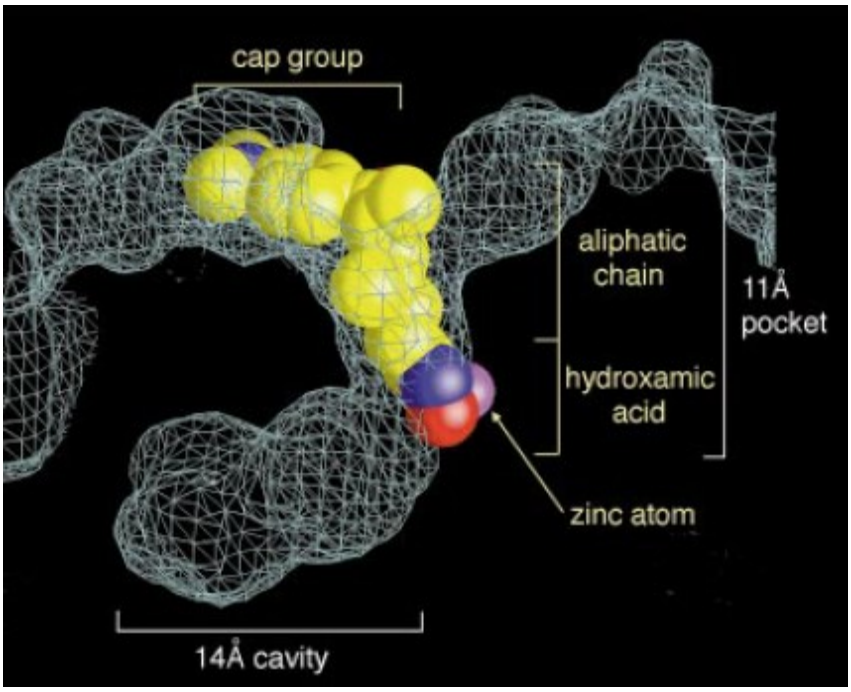

Figure 1.3. Space-filling representation of the active site pocket of HDLP.
Positioning of the different components of TSA (inhibitor) which includes a cap group, linker and hydroxamate moiety (as labeled in the Figure) is shown in the context of the active site pocket of HDLP. Demarcation of the active site pocket and the internal cavity has also been depicted. Adapted from reference (71).

In the crystal structure of HDLP, the zinc-ion is positioned towards the bottom of the pocket. It is co-ordinated mainly by D168, H170, D258 and a water molecule with a little deviation from the tetrahedral geometry. This water molecule also forms the hydrogen bond with His-131. Apart from the zinc co-ordinated ligands, the bottom of the pocket contains two histidines (H131 and H132), two aspartic acids (D166 and D173) and a tyrosine (Y297) residue. The D166-H131 and D173-H132 form charge relay pairs(72). The former pair is deeply positioned and more buried inside the pocket and makes a hydrogen bond to the zinc-bound water molecule, hence causing its deviation from the tetrahedral geometry. Y297 lies next to the zinc ion, adjacent to an opening in the pocket leading to the internal cavity. This hydrophobic

internal cavity is made up of parts of L3 and L7 loops and the α1-L1-α2 segment. This cavity is thought to function in the release of the acetate product away from the catalytic center.

Homology with HDAC1: The sequence identity (Figure. 1.4) and the homology mapping reveal that HDLP and HDAC1 have a homologous hydrophobic core and the loops (L1-L7). All the active-site residues (both polar and hydrophobic) are identical in both the proteins. This portion has also been found to be conserved in Class II HDACs as well. The amino acids making up the internal cavity and the ones that are close to the active site are conservatively substituted (71). The high sequence similarity indicates that this HDLP-protein corresponds to the conserved deacetylase catalytic core across the HDAC family except for the last 40 residues towards the C-terminal.

These conserved residues, herein suggest a mechanism for the deacetylation reaction and provide a framework for development of inhibitors of HDAC functioning as anti-tumor agents.

1.1.4.2. Histone Deacetylase 2 (HDAC2)

In 2010, Bressi et al. solved the crystal structure of HDAC2 in complex with one of its synthetic inhibitors, N-(4-aminobiphenyl-3-yl) benzamides (73). With the help of this association, they were able to demonstrate for the first time the function of the foot pocket or the internal cavity in HDAC2. Anilide inhibitors synthesized in their laboratory revealed that unlike the hydroxamate inhibitors, the anilides accessed the foot pocket adjacent to the zinc binding site. Their analysis of the HDAC2 structure suggests that substitutions at the 5-position of the N-(2-aminophenyl) benzamides provide the appropriate site for their interaction with the foot pocket.

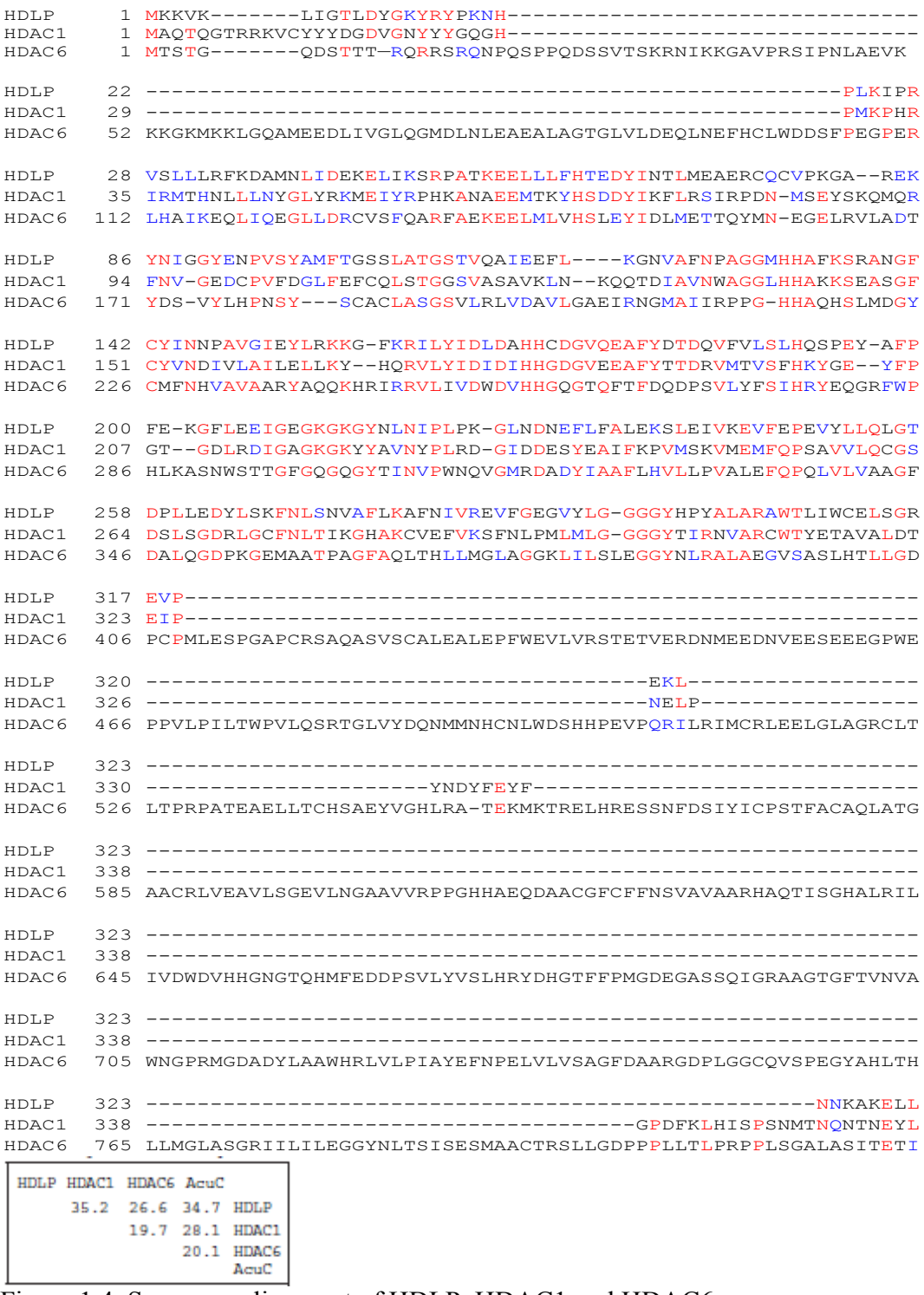

Figure 1.4. Sequence alignment of HDLP, HDAC1 and HDAC6.
Sequence alignment here shows a 35.2% identity between HDLP and HDAC1 (see box).
Identical residues between HDLP and HDAC1 or HDLP and HDAC6 have been colored in red.

The active site's catalytic machinery of HDAC2 consists of a lipophilic tube, lined mainly by the hydrophobic residues and extending from the surface into the 'foot pocket' immediately adjacent to the catalytic machinery. The crystal structure (Figure 1.5) reveals the co-ordination of the zinc atom to the D181, H183 and D269 residues. The residues lining the lipophilic tube consist of G154, F155, H183, F210 and L276. The foot pocket is lined by Y29, M35, F114 and L144.

Figure 1.6 highlights the hydrogen bonds formed in the ligand-bound versus unbound form of HDAC2. The comparative analysis of the two structures shows that in the ligand-bound HDAC2, the hydrogen atoms of the ortho-NH2 group of the ligand forms hydrogen bonds with the side chains of H145 and H146. The nitrogen of the ortho-NH_2 group chelates the zinc ion, and the carbonyl oxygen atom interacts with both the zinc and the side chain hydroxyl of the tyrosine residue. In the unbound form, the ortho-NH2 group of the anilide ligand forms an internal hydrogen bond with its own carbonyl oxygen atom. Upon binding of the anilide molecule to the active site, this internal hydrogen bond is not disrupted as the gross conformation of the anilides does not change much in the bound form. Although in this case the ligand will not be able to access the active site pocket as deeply. However, a proportion of these transiently bound molecules experience a disruption of this internal hydrogen bond upon incubation with HDAC2 and form a more stable complex with the active site.

1.1.4.3. Histone Deacetylase 3 (HDAC3)

HDAC3 has been crystallized (74) in complex with the deacetylase-activation domain (DAD) of its co-repressor, SMRT (Figure 1.7). SMRT is a multi-domain protein, and it functions as a transcriptional co-repressor that regulates neuroprotective and neurogenic

pathways by controlling the neuronal responsiveness of several transcription factors (75). Aside from forming complex with HDAC3(33–35,76–78), SMRT is capable of interacting with HDACs 1, 4, 5 and 7(74). HDAC3 interaction with the DAD domain of SMRT is important for its deacetylase function, and it mediates repression by certain nuclear receptors as well as it maintains normal circadian physiology (79–81).

It has been shown that HDAC3 also interacts with other nuclear receptor-co-repressor domains (N-CoR) causing the augmentation of its deacetylase activity (33). Assembly of the HDAC3-SMRT complex has been shown to be dependent on inositol tetraphosphate molecule, acting as a regulator (74).HDAC3 and SMRT-DAD do not form a complex when co-expressed in bacteria. Thus, it has been proposed that their association must require a chaperone complex in eukaryotes (82).

The structure of HDAC3 is similar to that of HDAC2 (73), and the former consists of an eight-stranded parallel beta-sheet surrounded by a number of alpha-helices. A tyrosine residue present at the surface of the active site tunnel is unique to HDAC3, and it might be involved in the substrate specificity of this enzyme (74).The SMRT-DAD interacts with the NH_2-terminal of HDAC3 (amino acid residues 9-49) forming H1 helix, L2 loop, H2 helix and S2 strand. The H1 helix is distorted in the absence of SMRT, confirming that both H1 and the DAD-domain undergo large structural rearrangements upon forming the complex. The structure reveals the importance of inositol tetraphosphate (Ins-1,4,5,6-P_4) which acts as an inter-molecular glue to cement the complex of HDAC3 and SMRT together. The presence of Ins-1,4,5,6-P_4 was important to circumvent the charge repulsion of many basic residues on the either side of the binding cleft of both the proteins (74). The structure of HDAC3: SMRT-DAD complex provides

insight into the mechanism of catalysis of this enzyme. The crystal structure of the complex shows the active site bound to the acetate molecule, where it forms hydrogen bonds with zinc and side chains of Y298 and H134. Also, a methionine side chain (from SMRT-DAD), mimicking a lysine residue is bound in the active site tunnel. Binding of the DAD and Ins-1,4,5,6-P_4 close to the active site of HDAC3 facilitates the substrate accessibility to the active site pocket resulting in the enhancement of the enzyme activity. Knowledge of the HDAC3 structure (Figure. 1.7 & 1.8), has made it clear that Ins-1,4,5,6-P_4 is an important molecule required for HDAC3 activity. It has been proposed that this phenomenon may present novel opportunities for the therapeutic interventions that can complement the existing inhibitors of Class I HDACs, by targeting the Ins-1,4,5,6-P_4 binding site on HDAC3 (74).

1.1.4.4. Histone Deacetylase 8 (HDAC8)

Like other HDACs, HDAC8 is a zinc-containing metallo-protein. It is a 377-residue class I enzyme and catalyzes the removal of acetyl moieties from the ε-amino groups of lysines near the amino terminal of the histones. Somoza et al.(83) for the first time crystallized HDAC8 in complex with its inhibitors- trichostatin A (TSA), suberoylanilide hydroxamic acid (SAHA) (Figure 1.9), 4-dimethylamino-N-(6-hydroxycarbamoyethyl)benzamides-N-hydroxy-7-(4-dimethylaminobenzoyl)aminoheptanamide (MS-344), and 5-(4-methyl-benzoylamino)-biphenyl-3,4'-dicarboxylic acid 3-dimethylamide 4'-hydroxyamide (CRA-A)(Figure 1.13).

These inhibitors were chosen as they have been shown to bind at the active site pockets of class I and class II HDACs .The structures of the above inhibitors have been shown in Figure 1.15.These inhibitors have also been shown to induce cell differentiation, cause tumor suppression and cell cycle arrest (84–88)**.**

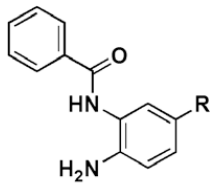

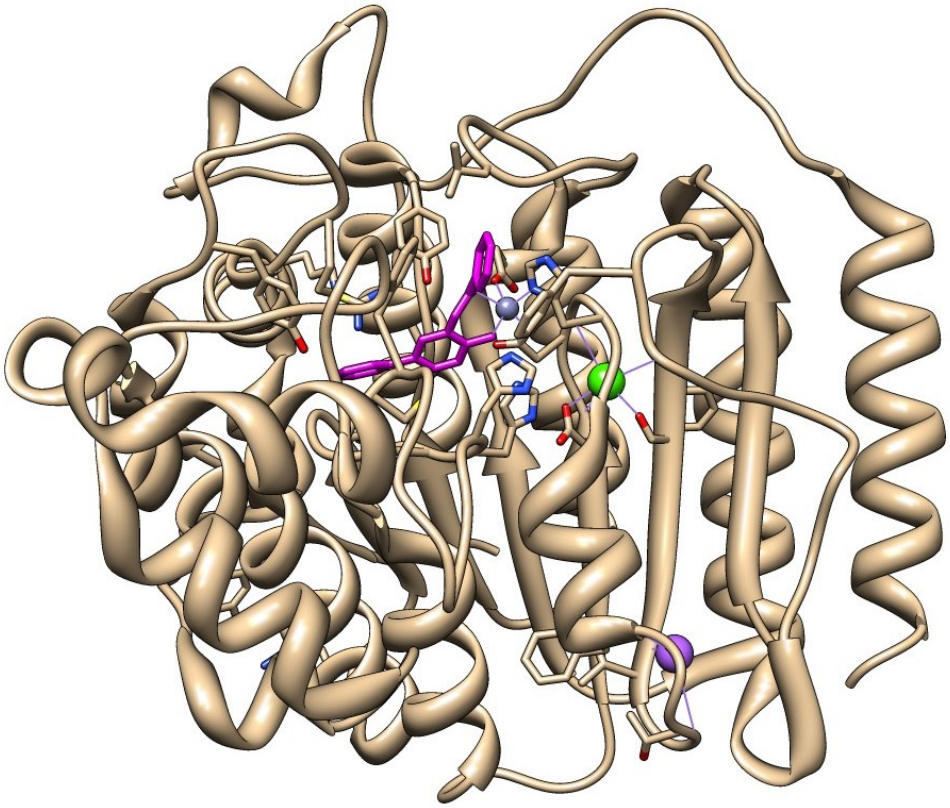

Figure 1.5. HDAC2 crystal structure co-complexed with N-(4-aminobiphenyl-3-yl) benzamides (magenta).
The structure of HDAC2 (PDB ID: 3MAX) modeled by UCSF Chimera ® software is shown. The catalytic zinc is shown in blue, calcium ion in green and sodium ion in purple. Chemical structure of the ligand that binds the catalytic core is shown on top left. Active site of HDAC2 consists of the catalytic machinery, a lipophilic tube connecting the surface to the catalytic core, and a foot pocket, immediately adjacent to the machinery (shown in figure 1.7.). Zinc atom is co-ordinated to D181, H183 and D269.The lipophilic tube islined by G154, F155, H183, F210 and L276. Foot pocket is occupied by the phenyl group of the ligand. (73)**.**

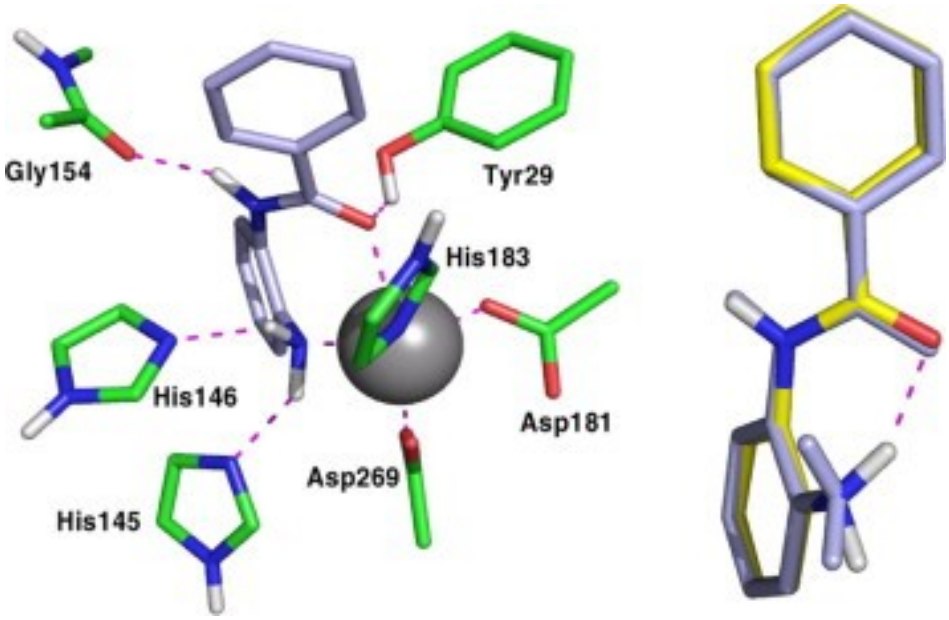

Figure 1.6. Simulated system figure of HDAC2 active site co-complexed with N-(2-aminophenyl) benzamides created using program VAMP.
The truncated anilide ligand is shown in light blue, the zinc as a silver sphere and the protein carbon atoms in green. Figure on the left shows the final geometry achieved and indicates the numerous polar interactions formed. Polar interactions are indicated by the dashed, magenta, lines. Anilide nitrogen acts as a surrogate for the water molecule needed for the hydrolysis of the acetylated lysine residues. Figure on the right shows a comparison of the bound ligand conformation (light blue), with hydrogen atoms optimized with Austin Model 1 (AM1), and the unbound ligand (carbon atoms in yellow), fully-optimized at the 6-31G* level. The internal hydrogen bond is indicated by the dashed, magenta, line. In the bound form, the H-atoms of the ortho-NH2 group form H-bond with the side chains of H145 & H146, the nitrogen of the ortho-NH2 group chelates zinc, and the carbonyl oxygen interacts with both the tyrosine side chain hydroxyl and the zinc. In the unbound conformation, the ortho-NH2 group forms an internal hydrogen bond with the carbonyl oxygen. Figure adapted from reference (73).

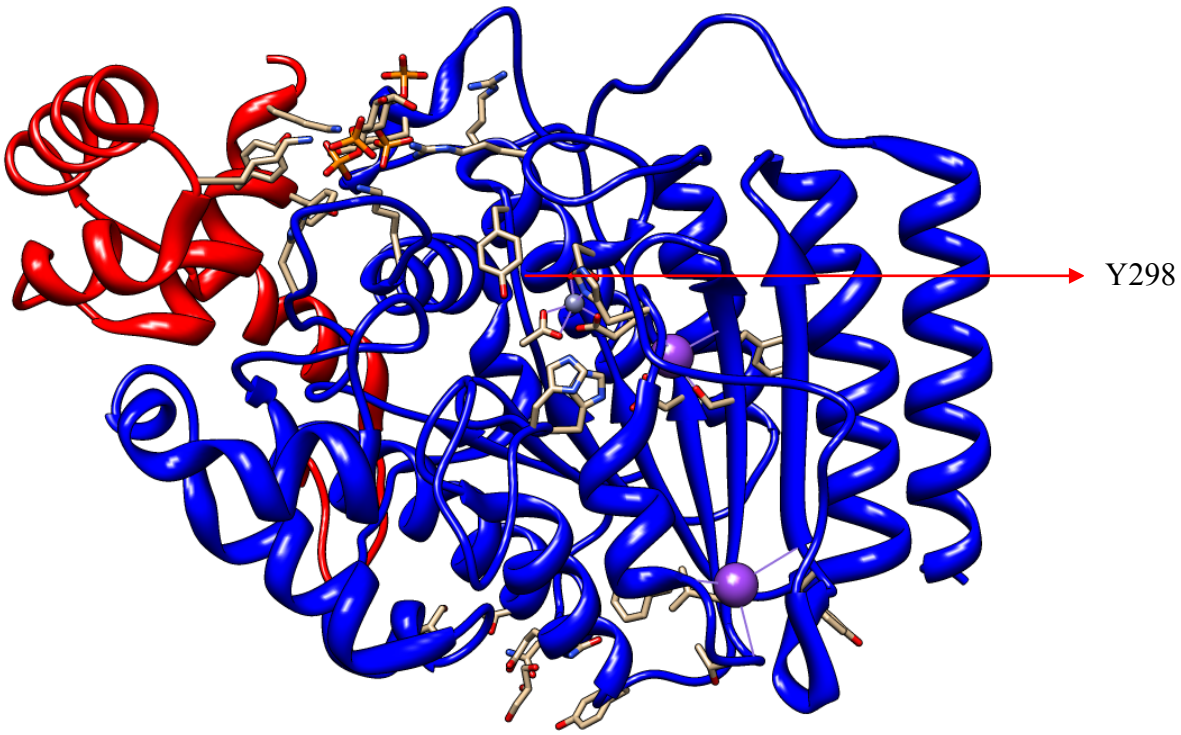

Figure 1.7. Ribbon structure of HDAC3 (blue) crystal co-complexed with SMRT-DAD (red). The structure of HDAC3 (PDB ID: 4A69) modeled by UCSF Chimera ® software. Structure here consists of an eight-stranded parallel beta-sheet surrounded by a number of alpha-helices. The active site lies at the base of the tunnel, with zinc at the center (blue sphere), leading from the surface of the protein. A solvent exposed tyrosine residue (Y298: unique to HDAC3) is present on the enzyme surface immediately adjacent to the active site tunnel. This residue is thought to interact with the substrate and may contribute to the substrate specificity. The DAD (red) lies along the surface of HDAC3 making extensive intermolecular interactions. The SMRT-DAD (red) interacts with the amino terminal region of HDAC3 (residues 9-49) that form helix H1, loop L2, helix H2 and strand S2. IP4 (yellow and red structure) is bound at the interface between HDAC3 and DAD(74).

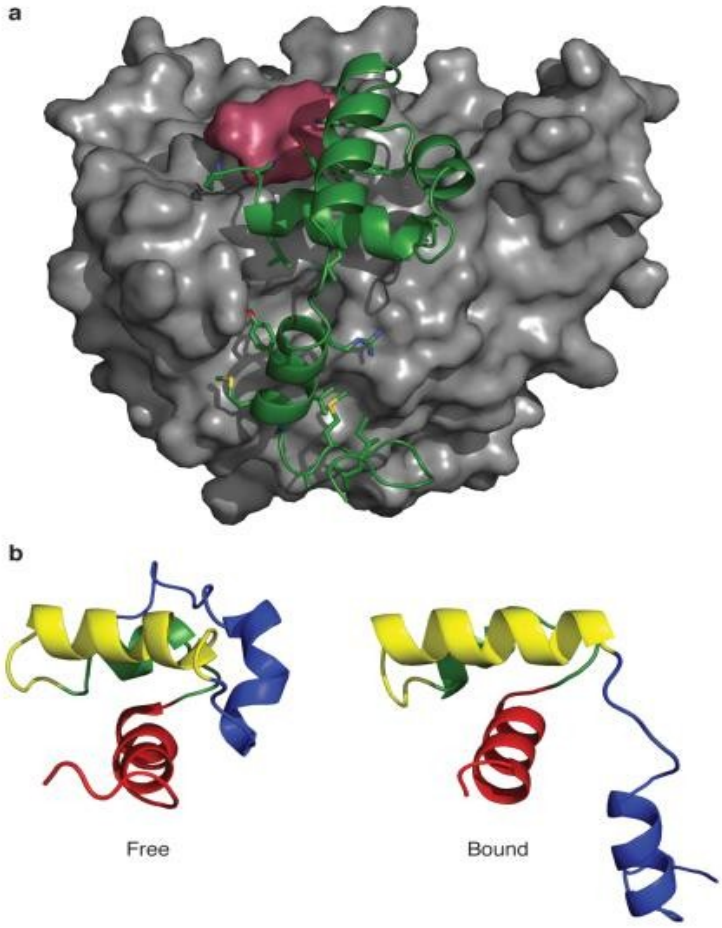

Figure 1.8. Crystal structure of the HDAC3-SMRT-DAD complex.
a) The interaction of the SMRT-DAD (green ribbon) with the HDAC3 protein (grey space filling model) is shown. The Ins(1,4,5,6)P4 (raspberry surface) is bound at the interface between HDAC3 and DAD. The side chains in the DAD moiety that are instrumental in mediating interaction with Ins(1,4,5,6)P4 are shown as stick models. b) Solution structure of the DAD domain (PDB ID: 1XC5) in free (left panel) and bound (right panel) forms is shown. Figure adapted from reference (74).

Similar to HDAC2 and HDAC3 structures, HDAC8 also belongs to the family of proteins with α/β folds. HDAC8 is a single domain metallo-enzyme that includes an 8-stranded parallel beta-sheet sandwiched between 13-alpha helices (Figure 1.12). The structure has a nearly 1:1 ratio of the amino acid residues in classical secondary structures with those in the form of loops connecting the regular secondary structures. The long loops shooting out from the C-terminal ends of the beta-strands of the central beta-sheet form a major portion of the enzyme and surround the residues that make up the enzyme's active site and the catalytic machinery. The core structure of the HDAC8 enzyme is similar to arginase (89), which catalyzes the conversion of arginine to ornithine, as well as to HDLP (71) that shares nearly 35 % sequence identity with HDAC8.

A comparison of the structures of HDAC8 and HDLP reveals that while they have similar folds, they differ strikingly in the outer part of their active sites as well as in architecture of their last 50 amino acid residues.

1.1.4.4.1. Active Site Pocket of HDAC8

HDAC8 is structurally and functionally unique as compared to other class I HDACs and HDLP. The key distinguishing features in its structure also have corresponding roles in its function. Absence of a 50-111 amino acid residue at the C-terminal end (90) indicates that HDAC8 does not require recruitment of other protein complexes and can function in isolation (13,91).In contrast, HDACs 1, 2 and 3 require association with large multi-subunit co-repressor complexes for maximal activity (23,34,35,92–94).

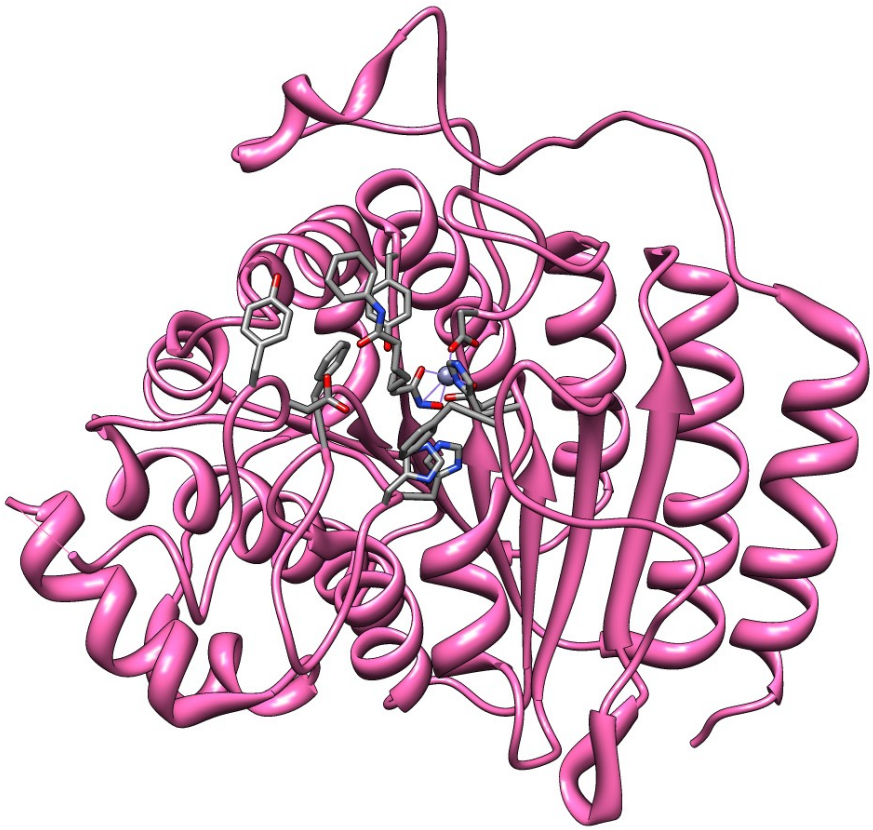

Figure 1.9. Ribbon structure of HDAC8 co-complexed with SAHA.
The structure of HDAC8 (PDB ID: 1T69) is modeled by UCSF Chimera ® software. The Figure shows the α/β fold of HDAC8 (pink ribbon), as well as SAHA (colored by heteroatom) and the zinc ion (blue). The HDAC8 structure comprises of eight-stranded parallel β-sheet sandwiched between 13 α-helices (83).

Also, HDAC8 has a wider active site pocket by virtue of two missing residues (His 21 and Pro 22 present in HDLP) in loop 1, which are otherwise present in the HDLP structure (Figure 1.10). This makes HDAC8, a structural outlier in the vicinity of the L1 loop in the active site pocket compared to HDLP and other class I HDACs .The active site consists of a long, narrow tunnel leading to the cavity that contains the catalytic machinery. The walls of the tunnel primarily contain hydrophobic amino acid residues and are lined by F152, F208, H180, G151, M274, and Y306 (Figure 1.11and 1.12). It has been proposed that during deacetylation reaction,

this tunnel likely accommodates the non-polar methylene groups of the acetylated lysine (70). These residues are conserved among class I HDACs except for M274, which is conservatively substituted in the other members of the enzyme family (Figure 1.10).

The catalytic site of the enzyme lies at the end of the hydrophobic/ active site tunnel. The zinc-ion is tetrahedrally co-ordinated to the carboxylate oxygens of D178 and D267, and to the Nδ1 atom of H180 (Figure 1.11 and 1.13). In case of bound hydroxamate inhibitors, the other two coordination sites are occupied by the carbonyl and hydroxyl oxygens of the hydroxamate moiety. Thus, it is likely that in the presence of the substrate, these sites might be coordinated by the carbonyl oxygen of the acetyl group and by a water molecule, respectively. The carboxylate moieties of D176 and D183 are important for catalysis as they form hydrogen bonds with the Nδ1 atom of each of histidine (H142 and H143).

This assembly constitutes a similar charge relay system as observed in serine proteases that is known to enhance the basicity of the NЄ2 moiety of the imidazole group(83). It has been suggested that H143 protonates the epsilon amino group of lysine after the deacetylation reaction is complete (71).

An important finding of the HDAC8 structure is the elucidation of a second metal ($Na^{+)}$ binding site that is buried in the interior of the protein structure. Such metal ion (Na^{+}) is located in the vicinity of the active site pocket, and is nearly 7 Å away from the catalytic zinc ion. The sodium ion is octahedrally coordinated with a distance between 2.5 Å- 3 Å to six oxygen ligands: carboxylate oxygen of D176, the side chain hydroxyl oxygen of S199, and the backbone carbonyl oxygens of residues 176, 178, 180 and 200 (81).

Figure 1.10. Sequence alignment of class I HDACs with HDLP.
Identical residues across the Class I enzymes and HDLP are colored in red. The key catalytic residues in HDAC are also conserved in other Class I HDACs. The sequences corresponding to the C-terminal domains of HDACs 1, 2 and 3 have not been shown in this Figure. The overall sequence identities between HDAC8 and HDAC1, HDAC2, HDAC3 and HDLP are 40%, 41%, 41% and 31%, respectively.

The role of Na^+ ion has not been fully elucidated, but it is thought to play a structural role in stabilizing the geometry of the active site. This is presumably the reason of conservation of the Na^+ ion binding site among class I HDACs.

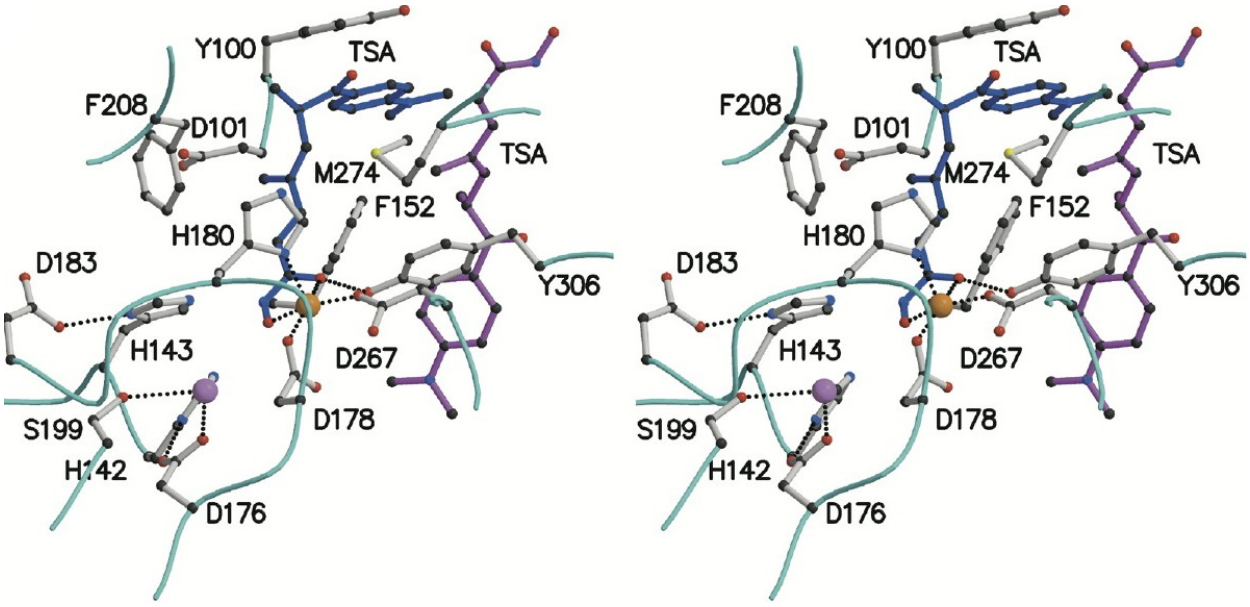

Figure 1.11. Stereo figure exhibiting key residues in HDAC8 active site with two TSA molecules (blue and pink), the zinc ion (orange) and the sodium ion (purple).
Dashed lines represent the potential hydrogen bonds. The zinc ion is bound to the carboxylate oxygens of D178 and D267, and to the Nδ1 atom of H180. Two other co-ordination sites are occupied by the carbonyl and hydroxyl oxygen atoms of the inhibitors' hydroxamate. Sodium ion is bound at the second metal binding site (7Å from the zinc) buried in the protein interior in the vicinity of the active site. It is co-ordinated in an octahedral fashion by six oxygen ligands in the protein: the carboxylate of D176, the side chain hydroxyl oxygen of S199, and the backbone carbonyl oxygen atoms of the amino acid residues 176,178, 180 and 200. Figure adapted from reference (83).

The sodium ion has been shown to co-ordinate and stabilizes a tight loop on the interior of the protein that is important in presenting the key residues at the active site pocket. Due to crystallization conditions, Na^+ was replaced by K^+ in the crystal structure of HDAC8 determined by Vannini et al.(70). They found two potassium binding sites in HDAC8: Site 1 in close proximity (7 Å) to the zinc-binding site, and site 2 situated towards the periphery of the molecule, nearly 15 Å away from site 1 (Figure. 1.14). The presence of the potassium ion increases the positive electrostatic potential within the active site pocket, leading to stabilization of the oxyanion species formed during the transition state of the deacetylation reaction. Potassium binding site 2 (Figure. 1.14) is formed by the coordination of the main chain carbonyl oxygens of F89, T192, V195, and Y225 and two water molecules. Though its relevance in the catalysis is not obvious, the site 2 metal ion is thought to play a role in maintaining the native conformational state of the enzyme.

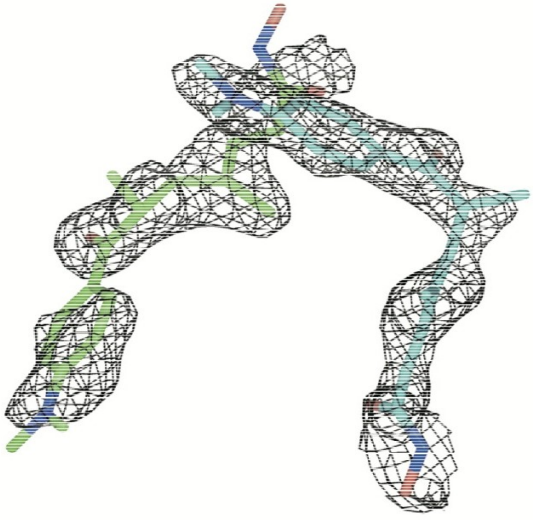

Figure 1.12. Electron density maps for two molecules of TSA when bound to HDAC8.
Fo – Fc simulated annealing omit maps exhibiting the electron density for the TSA molecules upon binding to HDAC8 active site. These maps have been shown within 1.8 Å of the TSA molecules and were contoured at 2.5σ. Figure adapted from reference (83).

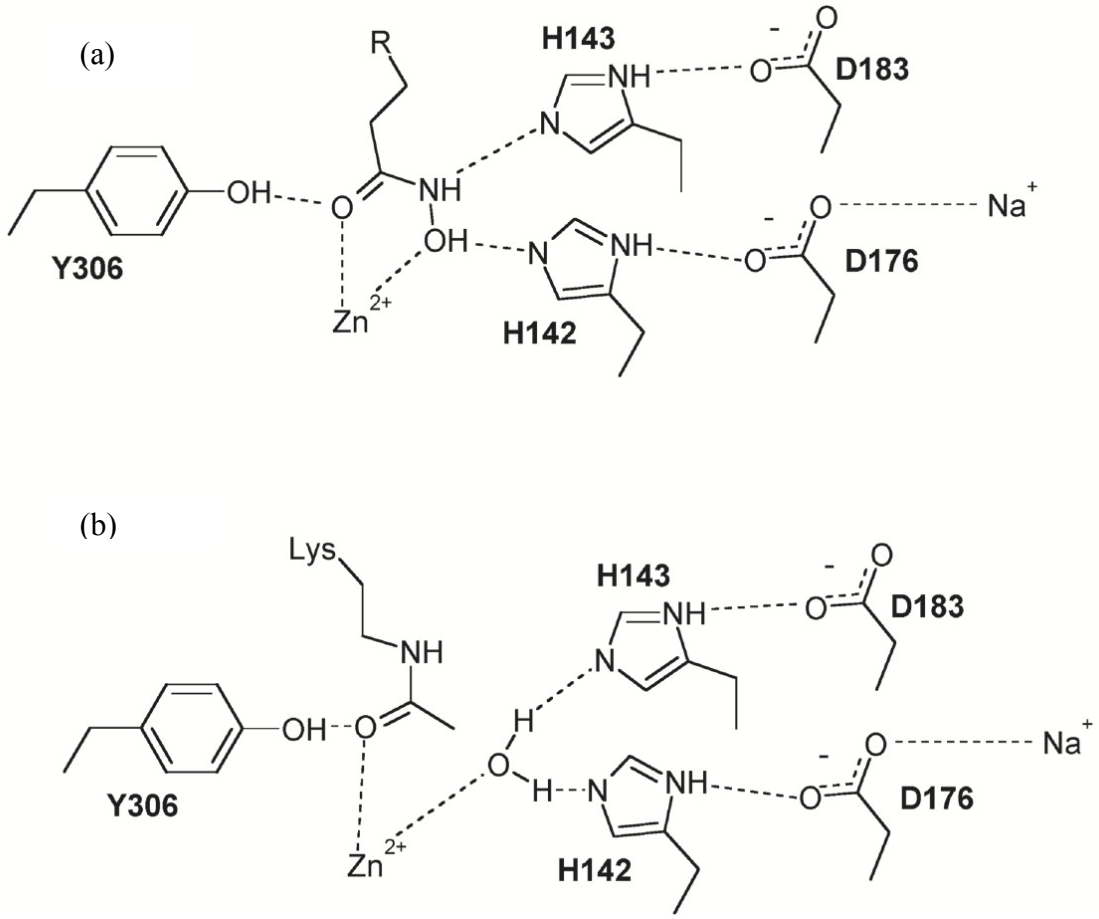

Figure 1.13. Schematic diagram showing the binding of the hydroxamate inhibitors to HDAC8 (upper panel) and the proposed binding mechanism of acetylated lysine to HDAC8 active site (lower panel).
(a) The zinc ion is bound to the carboxylate oxygen atoms of D178 and D267, and to the Nδ1 atom of H180. Two other co-ordination sites are occupied by the carbonyl and hydroxyl oxygen atoms of the inhibitors' hydroxamate. (b) Upon binding of the natural substrate, the above mentioned co-ordination points are proposed to be occupied by the carbonyl oxygen of the acetyl moiety and by a water molecule, respectively. The carboxylate moieties of the D176 and D183 form hydrogen bonds with the Nδ1 atom of each histidine (H142 and H143), similar to Aspartate-Histidine charge relay system found in serine proteases. This is known to increase the basicity of the imidazole Nε2 atom. Figure adapted from reference (83).

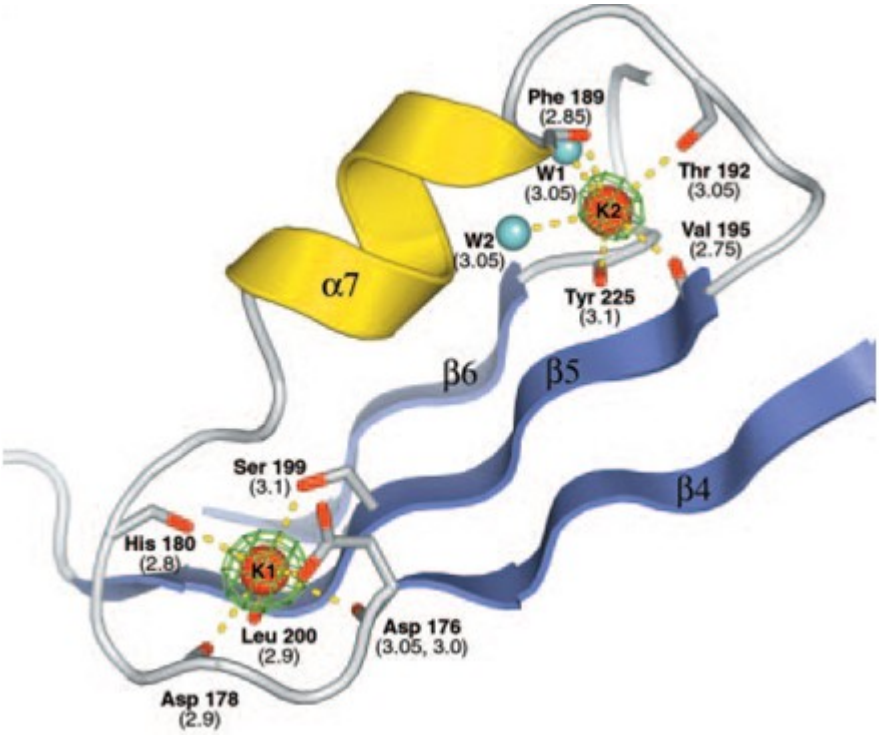

Figure 1.14. Architecture of the two potassium-binding sites, namely K1 and K2.
Red spheres represent the potassium ions. Residues coordinating the potassium ions are drawn in the stick representation. W1 and W2 are the water molecules. Dashed lines represent the co-ordination bonds. Site 1 potassium ion (K1) is in close proximity (7 Å) to the zinc binding site, whereas site 2 potassium ion (K2) is located towards the periphery of the molecule, 15 Å away from site 1. Site 1 potassium ion is hexa-coordinated with six oxygen ligands from D176 (main chain carbonyl oxygen and Oδ1), D178 (main chain carbonyl oxygen), H180 (main chain carbonyl oxygen), S199 (Oγ) and L200 (main chain carbonyl oxygen), arranged in a distorted octahedral geometry. Figure adapted from reference (70).

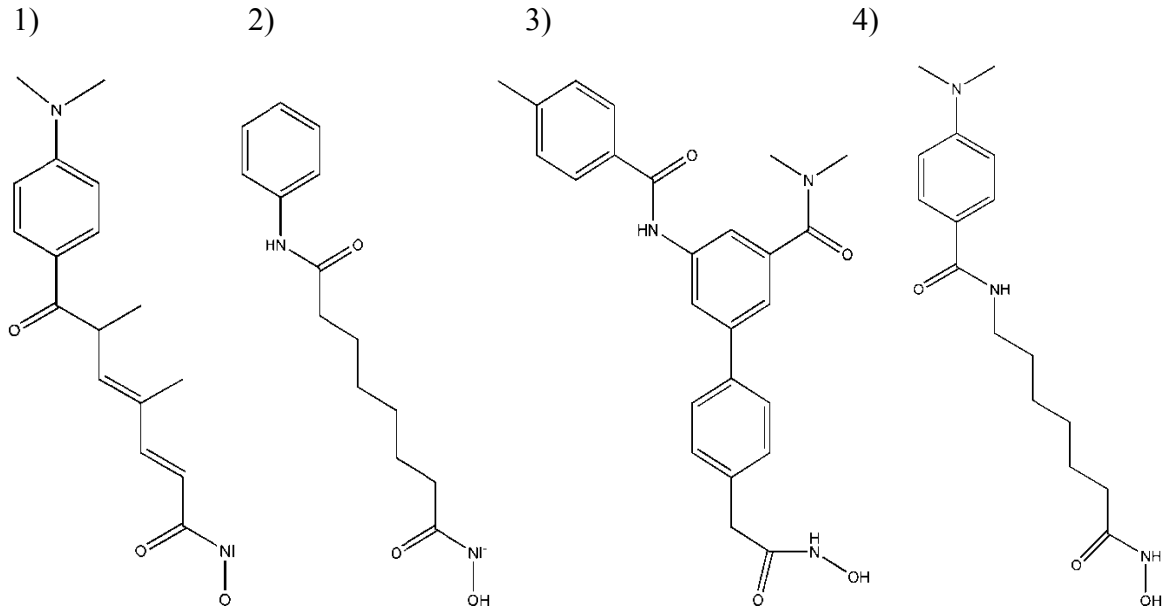

Figure 1.15. Chemical structures of HDAC8 inhibitors.
The inhibitors from left to right are TSA (1), SAHA (2), CRA-A (3) and MS-344 (4). These inhibitors are active against class I and class II HDACs, and have the ability to induce multiple effects within cells, including cell differentiation, cell cycle arrest, and tumor growth suppression (84–88). Figure adapted from reference (83)**.**

1.1.4.4.2. Comparison of HDAC8 with Other Class I HDACs

HDACs 1, 2 and 3 are the other members of class I HDACs which unlike HDAC8 function in association with other protein complexes. HDACs 1 and 2 are found in three repression complexes: NuRD (23,95), CoREST (96,97) and Sin3A (98,99). HDAC3, however, appears to be uniquely recruited to the SMRT/NCoR complex where it interacts with a conserved DAD domain within SMRT/NCoR assembly(33–35,76–78). The HDACs 1, 2 and 3 structures are similar with certain differences in the active site pocket which contributes to their substrate specificity. For example, a solvent- exposed tyrosine residue is located on the surface of HDAC3, adjacent to the active site. This position of the tyrosine is unique for HDAC3 and hence

is important in determining its substrate (74) . The SMRT-DAD interacts with the amino terminal of HDAC3 (residues 9-49) that form helices H1 and H2, loop L2 and strand S1. This region is different in case of HDAC8 and likely explains its ability to be active in the absence of a co-repressor. There are also additional differences in the region where HDAC3 interacts with inositol tetraphosphate (74). In HDAC8, H1 helix is not disordered as in the case of HDAC3. Also, loop L1 is shorter by 2 amino acids (as specified above) and loop L6 contains a proline residue that causes the loop to orient away from the active site. These differences are suggestive of a better access of substrate to the active site pocket of HDAC8 as compared to un-complexed HDAC3.

1.1.5. Enzymatic Assays for Determining the Activity of Class I HDACs

The modulation in the level of histone acetylation by HDAC inhibitors, activators, or certain mutations results in differentiation and/or apoptosis in cancerous cells. Thus, determination of the histone deacetylase activity and the methods for screening potential ligands (inhibitors and/or activators) has become increasingly important due to the integral involvement of HDAC in global transcriptional regulation. Over the past several years a lot of research effort has been invested into developing highly sensitive assays for HDAC activity to facilitate high throughput screening of potential inhibitors/activators of the enzyme. Earlier HDAC assays based on radioisotopes have largely been replaced now by the fluorescence or bioluminescence based assays as the latter are safer and exhibit higher sensitivity. A brief review of the assays that have been used to measure the HDAC activity, including those utilized in the present study is provided below.

1.1.5.1. Fluorescence-labeled Octapeptides-based HDAC Activity Assay to Determine the Deacetylation Site

This assay was developed to replace the radioisotope- based activity assays for HDACs. Traditionally, histone N-terminal peptide sequences have been used in the HDAC activity and inhibition assays. The substrates were labeled with [^{3}H]-acetic acid and the liberation of the tritiated acid was quantitated by either scintillation counting or the scintillation proximity assay (100).However, problems associated with radioactivity led to the development of alternate assays.

Hoffman et al. (1999) introduced the first non-radioactive in-vitro assay for HDAC involving fluorescein-labeled acetyl lysine 1 (101). This assay was widely used to determine the HDAC activity and screening of HDAC inhibitors (102). The assay utilized an octapeptide containing two acetyl-lysine residues, labeled with fluorescein carboxylic acid at the N-terminus and applied HPLC and fluorescence detection to determine the deacetylation site preference. The octapeptide is gradually deacetylated at the acetyl-lysine C-terminus and eventually leads to the formation of some bis-deacetylation product that can be observed. HPLC-chromatography in addition to fluorescence detection and mass spectroscopy were able address questions pertaining to regioselective deacetylation in HDAC substrates (103).

1.1.5.2. Non-isotopic Histone Deacetylase Activity Assay

1.1.5.2.1. Histone Deacetylase Assay-Homogeneous (HDASH)

The Histone deacetylase assay-homogeneous (HDASH) is a non-isotopic HDAC assay. The working principle of this assay is incubation of the fluorescent acetylated HDAC8 substrate [MAL; (N-(4-methyl-7-coumarinyl)-N-α-(*tert*.-butyloxycarbonyl)-N-Ω-acetyllysinamide)] with

HDAC8. Following incubation, deacetylated product [ML; (N-(4-methyl-7-coumarinyl)-N-α-(*tert*.-butyloxy-carbonyl)-lysinamide) is obtained. The deacetylated product is subjected to a derivatization reaction using NDA as a derivatizing agent (Scheme1.1). This is done to convert the deacetylated substrate (ML) to a compound with spectroscopic properties different from the acetylated substrate. This is important as it helps in a selective determination of one of the two, bypassing the need for extraction. The benzisoindole group present in derivatized ML molecules selectively extinguishes only the emission light of these molecules at 390 nm. The emission produced by the remaining substrate is not affected. The homogeneity of this assay lies in it being able to quantify the remaining fluorescent substrate instead of the fluorescent product. This assay allows for high-throughput screening as it can be performed on multi-well plate readers(104) .

1.1.5.2.2. Fluorogenic Histone Deacetylase Assay

This assay has been used in the evaluation of a number of novel histone deacetylase substrates that allow the detection of HDAC activity via a highly sensitive fluorogenic assay(105). The novelty of this assay lies in it combining the specificity of a deacetylation reaction with the advantages of a homogeneous fluorogenic assay in a two-step process. This assay utilizes a peptidic substrate containing a ε-acetylated lysine residue conjugated with 4-methylcoumarin-7-amide moiety at its carboxy terminus. The assay involves a two-step (coupled) enzymatic reaction (Figure. 1.16). The first step is catalyzed by HDAC which results in the cleavage of acetatefrom ε-acetylated lysine residue of the substrate. In the second step, the deacetylated peptide acts as a substrate for trypsin that cleaves only after the deacetylation of lysine residue has occurred, liberating free 7-amino-4-methylcoumarin (AMC) as fluorogenic

product. Since the acetylated peptide substrate is not cleaved by trypsin, 7-amino-4-methylcoumarin (AMC) is only released when HDAC is present in the reaction media. This is a highly sensitive assay that does not require acetylated histone as the enzyme substrate, and it is useful for high throughput screening of HDAC inhibitors (105). This assay has been widely used as it combines the specificity of the deacetylation reaction with the advantages of a homogeneous fluorogenic assay in a two-step process (105).

1.1.5.2.3. Bioluminogenic HDAC Activity Assay

The most recent HDAC activity assay has been developed by Halley et al. (106). This assay is homogeneous, single-step, bioluminogenic assay that can be widely used to monitor the activity of a range of HDAC class I/II and SIRT enzymes. In this assay, as presented in Figure 1.17, the proluminogenic substrate, Boc-GAK(Ac)-aminoluciferin, contains an acetylated lysine peptide sequence derived from histone 4 conjugated to aminoluciferin. HDAC-mediated deacetylation of the acetylated lysine residue facilitates the luminogenic substrate becoming susceptibleto specific proteolytic cleavage by trypsin in the developer reagent. The developer constitutes of luciferase and trypsin enzymes at concentrations that are not rate-limiting. The free aminoluciferin product of the above mentioned cleavage acts as a substrate for luciferase which produces oxyluciferin and light as products. The amount of light produced from this reaction is directly proportional to HDAC enzyme activity.

1.1.6. HDAC Inhibitors Screening Assays

HDACs have been recognized as being the key targets of cancer therapeutics, and thus there has been ongoing progress towards large scale screening of HDAC inhibitors via convenient enzyme assay system.

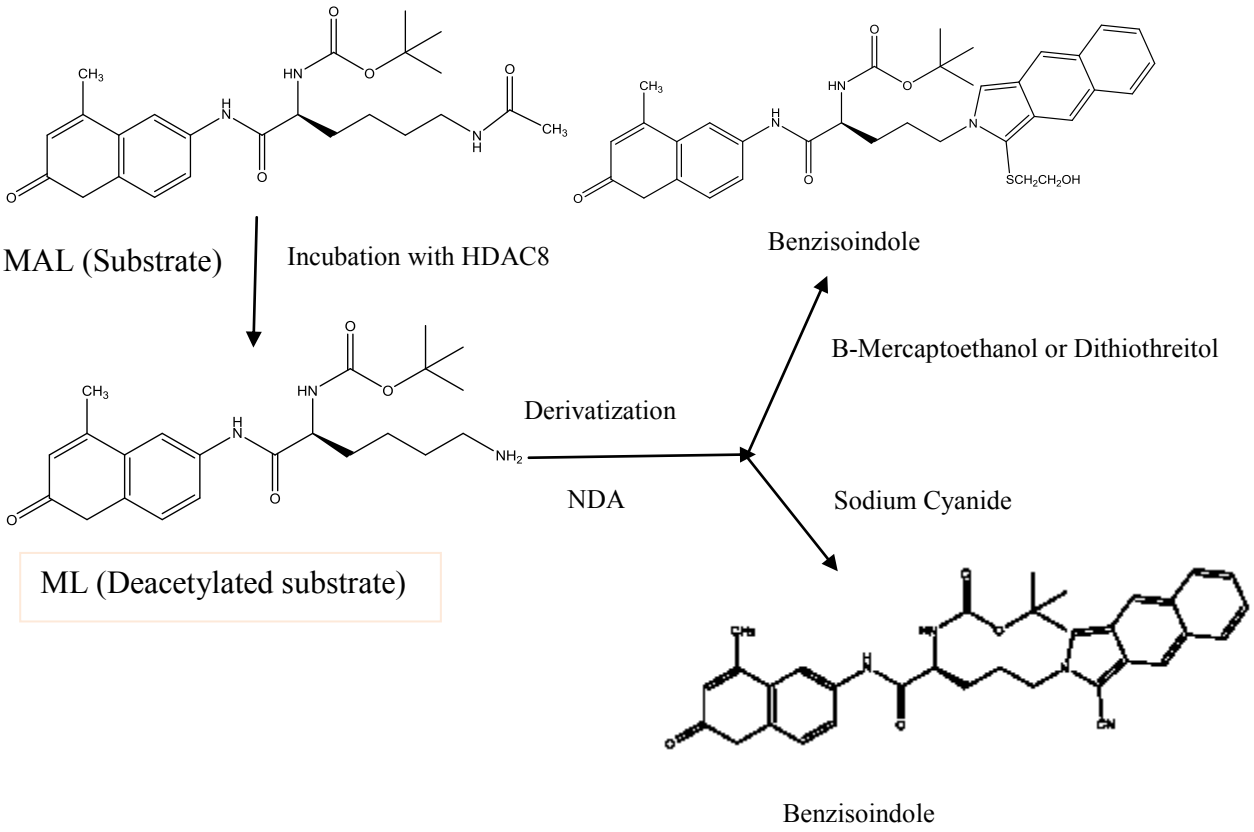

Scheme 1.1. Non-isotopic histone deacetylase activity assay.
Benzoisoindole group present in derivatized ML molecules selectively extinguishes only the emission light of these derivatized molecules at 390 nm. The emission produced by the remaining substrate is not affected. The homogeneity of this assay lies in it being able to quantify the remaining fluorescent substrate instead of the fluorescent product.

Examples of such assays that have been specifically designed for high throughput screening of compounds as inhibitors of HDACs are provided in the following sections.

1.1.6.1. Fluorescence Resonance Energy Transfer (FRET) based Assay

This assay involves a fluorescent inhibitor upon whose binding there is a fluorescence resonance energy transfer between the tryptophan residues of the HDAC enzyme and the fluorescent inhibitor. The enzyme used in the assay is a HDAC-homolog FB188 histone deacetylase-like amidohydrolase (HDAH) from Bordetella species FB188.

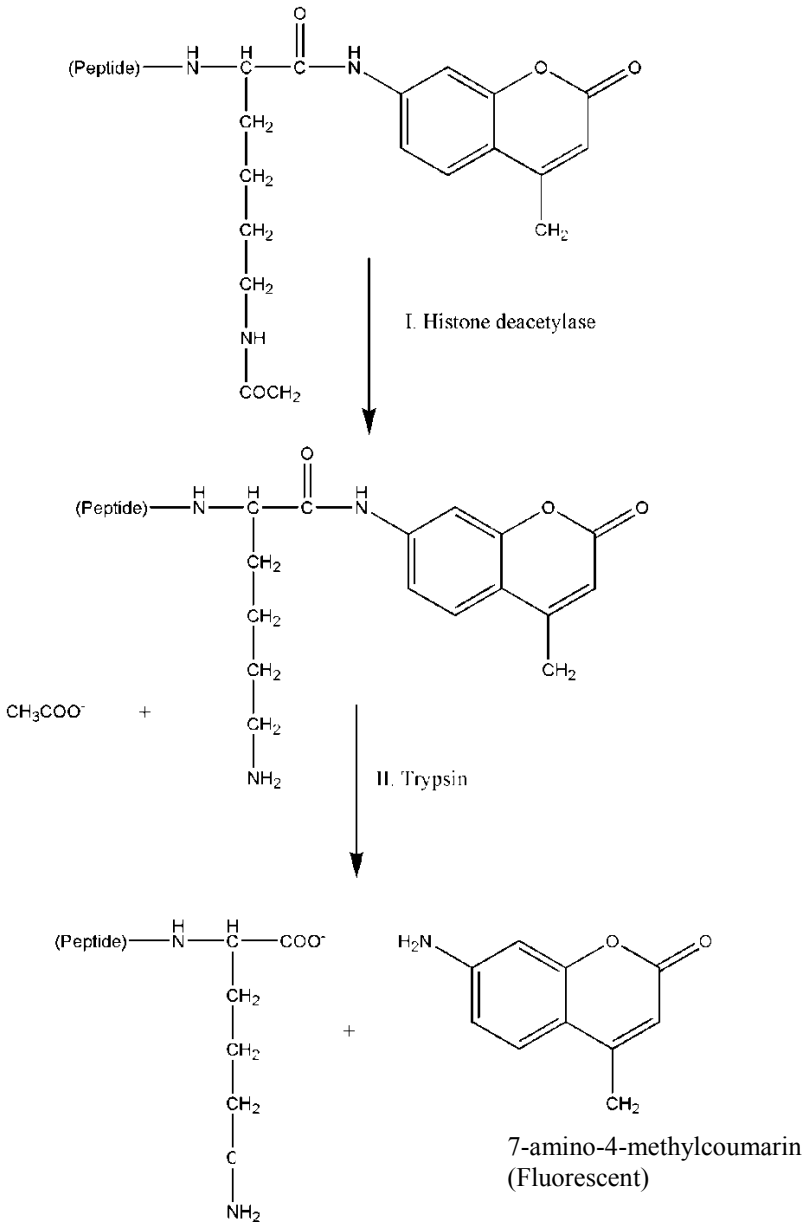

Figure 1.16. Histone deacetylase assay.
Step 1- Deacetylation of ε-acetylated lysyl moieties in peptidic substrates. Step 2- Cleavage of the deacetylated products by trypsin followed by the release of fluorescent 7-amino-4-methylcoumarin (AMC). Fluorescence measurements at λ_{exc}= 390 nm and λ_{em}= 460 nm. Figure adapted from Wegener et al (105).

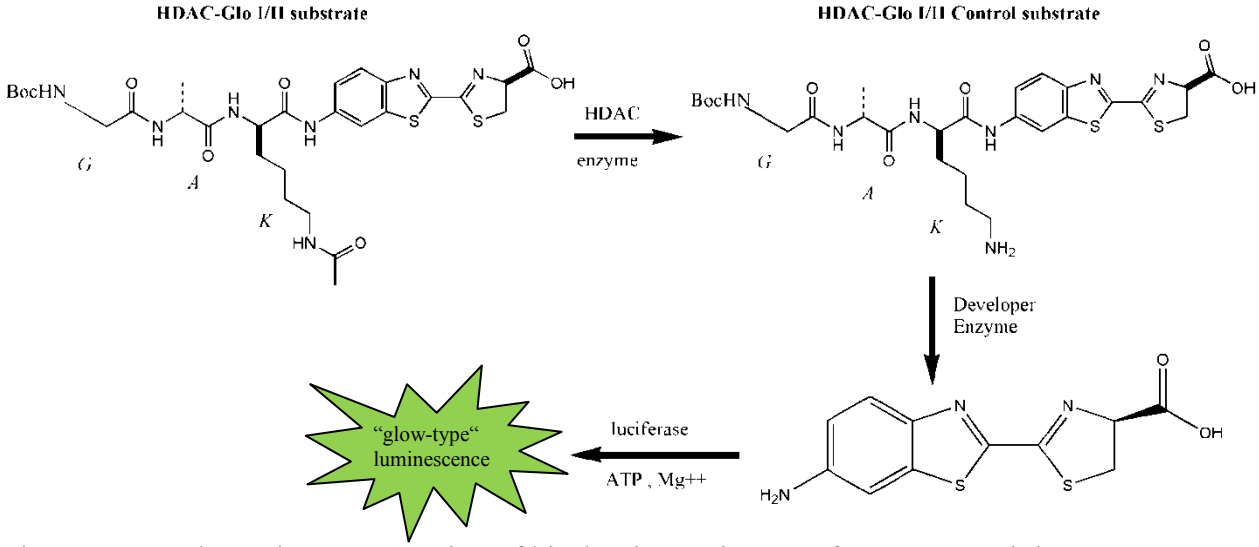

Figure 1.17. Schematic representation of bio-luminogenic assay for HDAC activity. Deacetylation of the luminogenic peptide by HDAC, makes it sensitive to specific proteolytic cleavage that liberates aminoluciferin. The free aminoluciferin is measured using a luciferase reaction to produce a stable emission of light in this overall coupled-assay system. Figure adapted from reference (106).

The inhibitor used in this assay is 2-furylacryloylhydroxamate (FAHA) which is a hydroxamate derivative of 2-furylacrylic acid. 2-furylacryloyl derivatives have an absorption maximum around 350 nm which overlaps with the tryptophan emission maximum. Upon binding, FAHA causes an efficient FRET to take place from the tryptophans of HDAH to the chromophoric system of FAHA. This manifests in strong quenching of the fluorescence emission of the tryptophan residues of HDAH upon binding(107). The second step of this assay involves the displacement of FAHA-HDAH complex by a more potent inhibitor like, cyclopentylpropionyl hydroxamate (CYPX). When FAHA is displaced in competition with CYPX, it shows a decrease in fluorescence resonance energy transfer(107). This displacement is easily monitored as reduced quenching of fluorescence. FAHA in the competition assay works as an important tool to screen compound libraries for new HDAC inhibitors. This assay has an

advantage of being a one-step assay and can offer a possibility to test binding mode of new inhibitors (107).

1.1.6.2. Fluorescence Anisotropy and Lifetime based Assay

This assay has been developed in order to minimize the limitations of the previous assays developed for measurement of HDAC activity. The limitations were the auto-fluorescence of compounds in the FRET-based assay, as described previously (107). To avoid the simultaneous excitation of compounds, a dye was used with strongly red-shifted excitation and emission wavelengths: 1-(3-carboxypropyl)-11-ethyl-2,2,8,10,10-pentamethyl-4-(sulfomethyl)-2,10-dihydro-1H-13-oxa-1,6,11-triazapentacen-11-ium, called Atto700. This dye was conjugated to an aminohexanoyl-spacer which was further conjugated to a hydroxamate moiety. During the assay, the above mentioned Atto700-HA conjugate is bound by HDAH (HDAC-homolog). This results in the increase of fluorescence anisotropy due to the increase in mass upon complex formation. Also, during this time a simultaneous increase in fluorescence lifetime is observed as well. This may be attributed to the changed microenvironment of the Atto700 fluorophore which is more hydrophobic in the complex as compared to the free Atto-HA conjugate(108). Due to the reversible nature of the binding of Atto-HA to HDAH, other non-fluorescent inhibitors (like SAHA or TSA) are able to displace Atto-HA from its binding site at HDAH. Increasing concentrations of non-fluorescent inhibitors displace Atto700-HA from its binding site at HDAH in a dose-dependent manner resulting in a decrease of fluorescence anisotropy and lifetime. Both fluorescence read outs are utilized to calculate the amount of free and bound Atto-HA. Using appropriate equations, the dissociation constants for Atto-HA and HDAH can be determined (108). This is a dual parameter competition assay which involves a fluorescent inhibitor probe

(Atto-HA) that shows an increase in both, fluorescence anisotropy and fluorescence lifetime upon binding to the HDAC enzyme (108).

1.1.6.3. Substrate- Independent TR-FRET (Time resolved-Fluorescence Resonance energy Transfer) Histone Deacetylase Inhibitor Assay

This assay format is based on the direct measurement of the binding affinity of inhibitors to HDAC rather than measurement its enzyme activity. In this assay designed by Marks et al.(109), they have eliminated the need of utilizing a substrate for HDAC activity assay. This alleviates the need of utilizing non-specific substrates for HDAC assays. The assay here involves utilization of GST or His-tagged (epitopes) HDAC enzymes. The other component of this assay is an Alexa Fluor ® 647-labeled HDAC inhibitor or 'tracer", which has a high affinity to Class I(HDAC tracer 1) and IIb (HDAC tracer 2) HDACs(109). This is also a competition assay where the tracer is displaced by a known inhibitor. Therefore, it is very important in this assay to determine the binding affinity of the tracer for each target of interest. The binding affinity of HDAC-tracer is determined by incubating it with an epitope-labeled HDAC (either GST or His-tagged) enzyme along with an anti-epitope antibody and known HDAC-inhibitor, TSA. Control experiments are set up with similar composition except without TSA. After an incubation period at room temperature, TR-FRET values are measured. These TR-FRET values obtained from the TSA-containing experiment are subtracted from those without it. This was done to calculate a correct TR-FRET ratio. The dissociation constant is determined by plotting the corrected TR-FRET values versus the tracer concentration and fitting the data utilizing a one-site binding model equation (109).

1.1.7. HDACs (Classes I and II): Mechanism of Catalysis and Substrate Specificity

As described before, HDAC enzymes modulate the gene expression via deacetylation of acetylated lysine residues on histones. Below is a general reaction catalyzed by all HDACs(110).

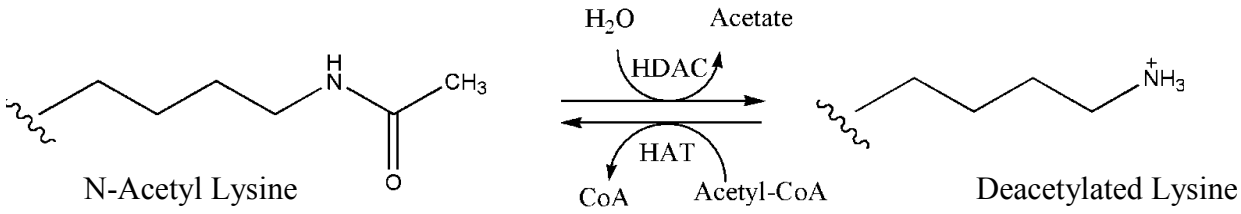

The mechanism of catalysis of HDAC8 has been elucidated in the light of the crystal structure of the catalytically inactive mutant (Y306F) of HDAC8 with bound acetylated peptidic substrate (111). The structural data clearly demonstrated the role of the active site residues in substrate recognition and the deacetylation reaction of the enzyme. The active site of HDAC8 appears to harbor properties of both serine and zinc proteases, and it contains two Histidine-Aspartate dyads where both histidine residues supposedly work as a general acid-base catalytic pair. A study by Vanommeslaeghe et al., (2005) indicated that simultaneous protonation of both histidine residues is unlikely(112). The most likely mechanism has been explored by Vannini et al (111) by solving the crystal structure of HDAC8 in complex with the p53-derived acetylated peptide substrate ((acetyl)-L,Arg-L,His-L,Lys(ε-acetyl)-L,Lys(ε-acetyl), containing a fluorogenic coumarin group at its carboxyl terminus. The substrate corresponds to the sequence Arg379-His380-Lys381(ε-acetyl)-Lys382(ε-acetyl) of the p53 tumor suppressor protein, located in the C-terminal, basic regulatory domain of p53 (113). K382 is deacetylated by class I HDACs resulting in repression of the transcriptional activity of p53 (114). The overall crystal structure of the complex showed a dimeric arrangement (Figure 1.18a and 1.18b).

The structure shows that the K4 (Ac) moiety of the substrate protrudes into the narrow cavity of the active site and co-ordinates with a zinc ion through its carbonyl oxygen (Figure 1.18c). There also lies a catalytic water molecule that is zinc-co-ordinated and interacts with His142 and His143, which lies on the opposite side of the substrate with respect to Y306 (Figure 1.18d).There are two charge-relay dyads in the HDAC8 active site pocket: H142 is a part of the buried and conserved charge- relay system whereas H143 belongs to the exposed putative system which is not conserved in other HDACs. The zinc ion is penta-coordinated with D178 (Oδ2, 1.97 Å), H180 (Nδ1, 2.07 Å) and D267 (Oδ2, 1.97 Å) as ligands, in addition to the water molecule (2.07 Å) and the carbonyl oxygen (2.02 Å) of the acetyl group of the substrate (Figure 1.18d). The carbonyl carbon of the substrate lies in close proximity to the catalytic water molecule and also to the zinc ion which polarizes the carbonyl group and orients the water molecule in the active site such that its nucleophilicity is further increased upon hydrogen bonding to His142 and H143.The hydrophobic amino acid residues lining the active site tunnel stabilize the alkyl chain of the K4(Ac) by forming hydrophobic interactions with F152 and F208, and a hydrogen bond to G151 (Figure 1.18d). Most residues contacting K4(Ac) are highly conserved in all HDACs except for Y306, which is replaced by a histidine in Class II HDACs, causing a decrease in their catalytic activity on peptidic substrates (17).

The basic mechanism of catalysis involves a nucleophilic attack by the active site water molecule on the carbonyl carbon of the substrate (Figure 1.18d and Figure 1.20). The H142 is oriented in an enabling manner to allow extraction of a proton from the water molecule, thereby acting as a general base. The interaction of the carbonyl oxygen of the substrate with the zinc ion results in enhanced polarization of the carbonyl bond, and hence, increases its susceptibility to a

nucleophilic attack. Following a nucleophilic attack and considering no rearrangement at the active site, H143 would not be able to protonate the amine leaving group while Y306 would be able to do so due to its proximity to the amine, thereby breaking down the intermediate to release two products, acetate and lysine. Thus, mutation of Y306 results in the substrate being trapped at the active site of the enzyme, thereby preventing its catalysis.

Vannini et al (2007) also described the role of D101 in HDAC8 catalysis(111). From its presence on the rim of the active site, D101 establishes two directional hydrogen bonds with two adjacent nitrogen atoms of the substrate backbone constraining the substrate in a cis-conformation (Figure 1.19). The integral role of this residue was confirmed by mutating it to alanine that resulted in a complete loss of the HDAC8 enzyme activity on a peptidic substrate and also on purified histones, although the 3D structure of the protein was not affected. This indicated that the interaction of D101with the substrate is important for the correct positioning of the enzyme/substrate and full HDAC8 activity. In addition, this interaction also results in the two main chain oxygen atoms of the substrate to form a number of water-mediated hydrogen bonds with multiple amino acids at the rim of the HDAC8 active site, enhancing the immobility of the substrate in the active site pocket. In 2008, Dowling et al.(115) also confirmed its importance in substrate binding where they created number of D101 variants- D101A, D101E, D101N and D101L. Studies with these variants determined that D101 is critical for the function of the L2 loop and any amino acid substitutions of it can trigger conformational changes of Y111 and W141 that perturbs the site for the substrate binding. The scheme of the mechanism of catalysis of HDACs in presence of the substrate is shown in Figure. 1.21.

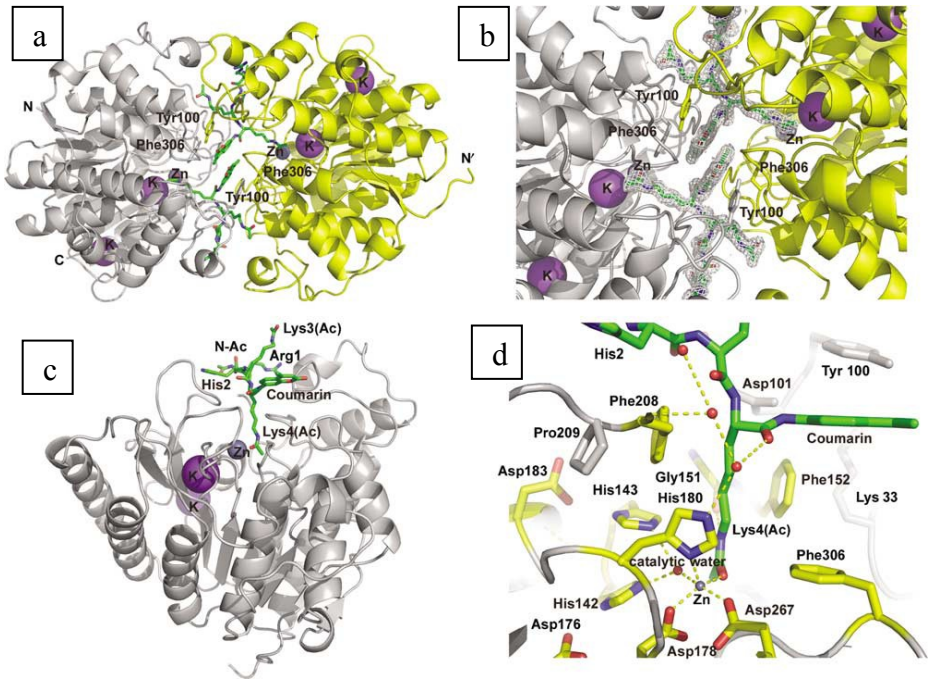

Figure 1.18. Crystal structure of the HDAC8-substrate complex.
Upper left panel shows the ribbon diagram of two HDAC8-substrate complexes in an asymmetric unit. The substrate and the enzyme residues involved in head to head packing are represented as stick Figures. Zinc and potassium ions are represented as purple spheres. The substrate's carbon, nitrogen and oxygen are represented as green, blue and red, respectively. The upper right panel represents the close-up view of the substrate binding site with the 1.0σ-contoured 2Fo-Fc electron density map. The lower left panel shows a single unit of HDAC8-substrate complex. The close-up view of the active site is shown in the lower right panel. Dashed yellow lines represent polar interactions between the residues. Figure adapted from reference (111).

1.1.7.1. Acetate Release Channel of HDAC8

The crystal structure of HDAC8 reveals a tubular internal cavity that extends from the base of the acetyl-lysine binding tunnel towards the rear end of the active site pocket of HDAC8, through which the acetate product is released after the deacetylation reaction. This cavity is the acetate -release channel or the exit-tunnel of HDAC8. This tubular cavity is filled with several water molecules which may act like a shuttle for the acetate ion (70) (Figure. 1.22).

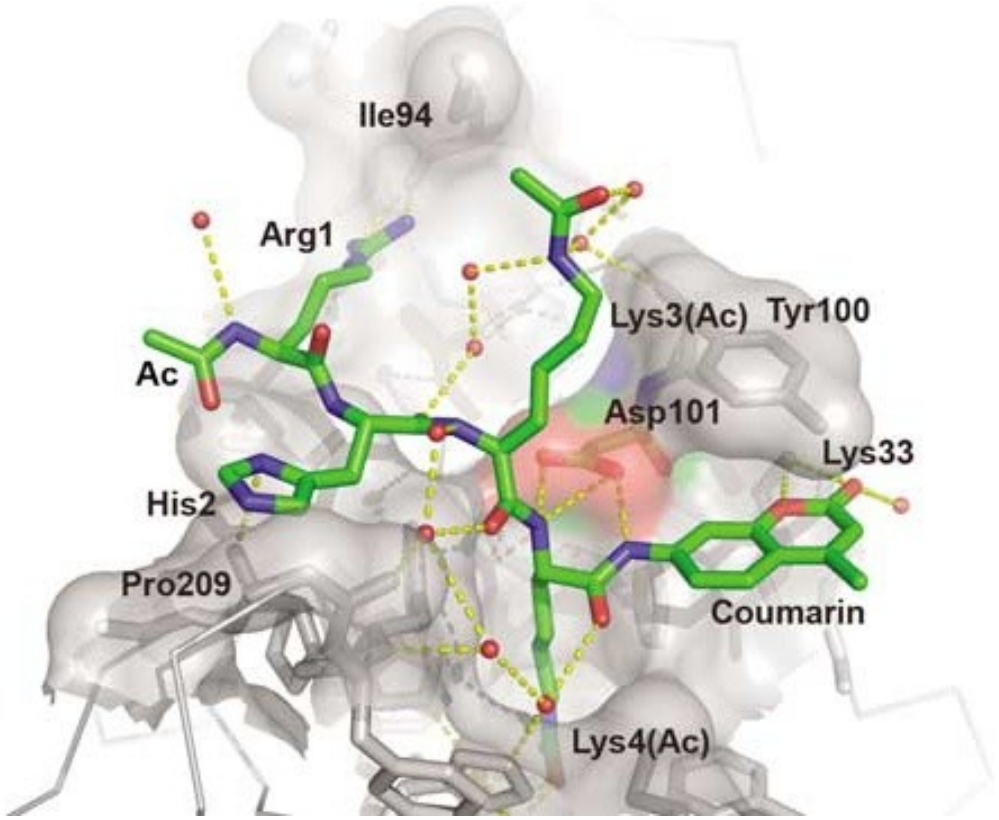

Figure 1.19. Molecular surface of the HDAC8-substrate complex at the active site entrance. Red spheres represent water molecules. This Figure shows that the side chain carboxylate of D101 establishes two directional hydrogen bonds with the two adjacent nitrogen atoms (blue) of the substrate backbone (green), constraining the substrate in an unusual cis-conformation. Also, the two main chain oxygen atoms of the substrate form a network of water-mediated hydrogen bonds with various enzyme residues. The polar interactions at the rim of the active site keep the substrate in place during the deacetylation reaction. Figure adapted from reference (111).

This pocket is also present in HDLP but it has a different shape due to the presence of different amino acid residues (vis a vis those found in HDAC8) residues that line the pocket. It has been proposed that R37 and C153, highly conserved among class I & II HDACs, could be the hydrogen-bonding partners for acetate once the latter is released following the deacetylation of the substrate (70).

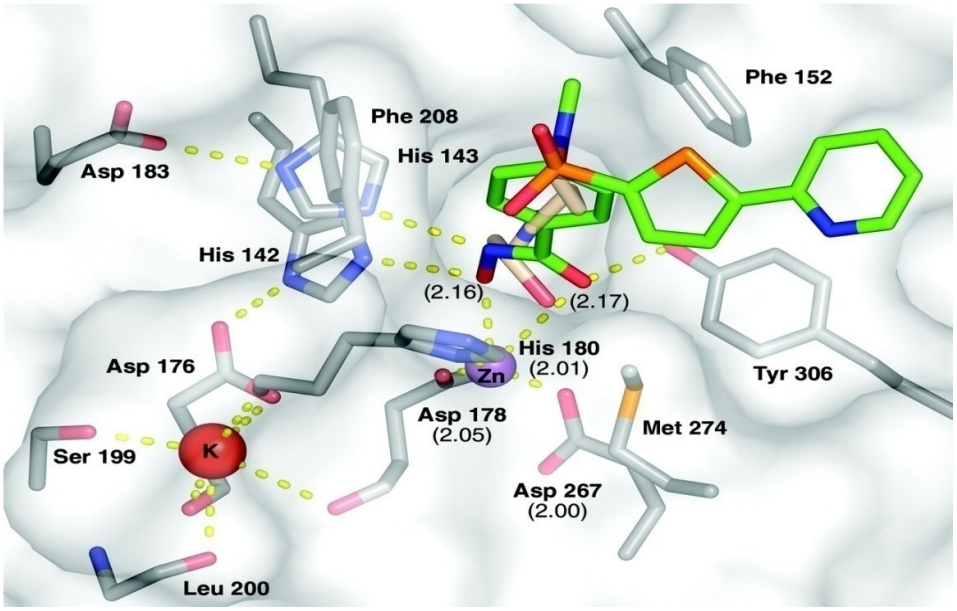

Figure 1.20. Architecture of the HDAC8 active site.
This Figure shows the residues important in HDAC8 catalysis and binding of the inhibitor. The residues, inhibitor and the modeled acetyl-lysine are shown in a stick representation. The carbon is colored green for the inhibitor and wheat colored for the docked acetyl-lysine. The orange, blue, gray and red represent sulfur, nitrogen, carbon and oxygen, respectively. The potassium and zinc cations are represented as red and purple spheres, respectively. Figure adapted from reference (70).

It has also been proposed that Y18, Y20 and H42 play a very important role in the release of acetate and its exchange with the bulk water by virtue of their side chains. These residues are present at the distal end of the exit tunnel (Figure 1.23) and may act as a gate for the release of the acetate, concomitant with signaling the active site to bind another molecule of the substrate. In the present study, the role of these three residues of HDAC8 during enzyme catalysis as well as their contributions in binding of selected ligands has been investigated herein.

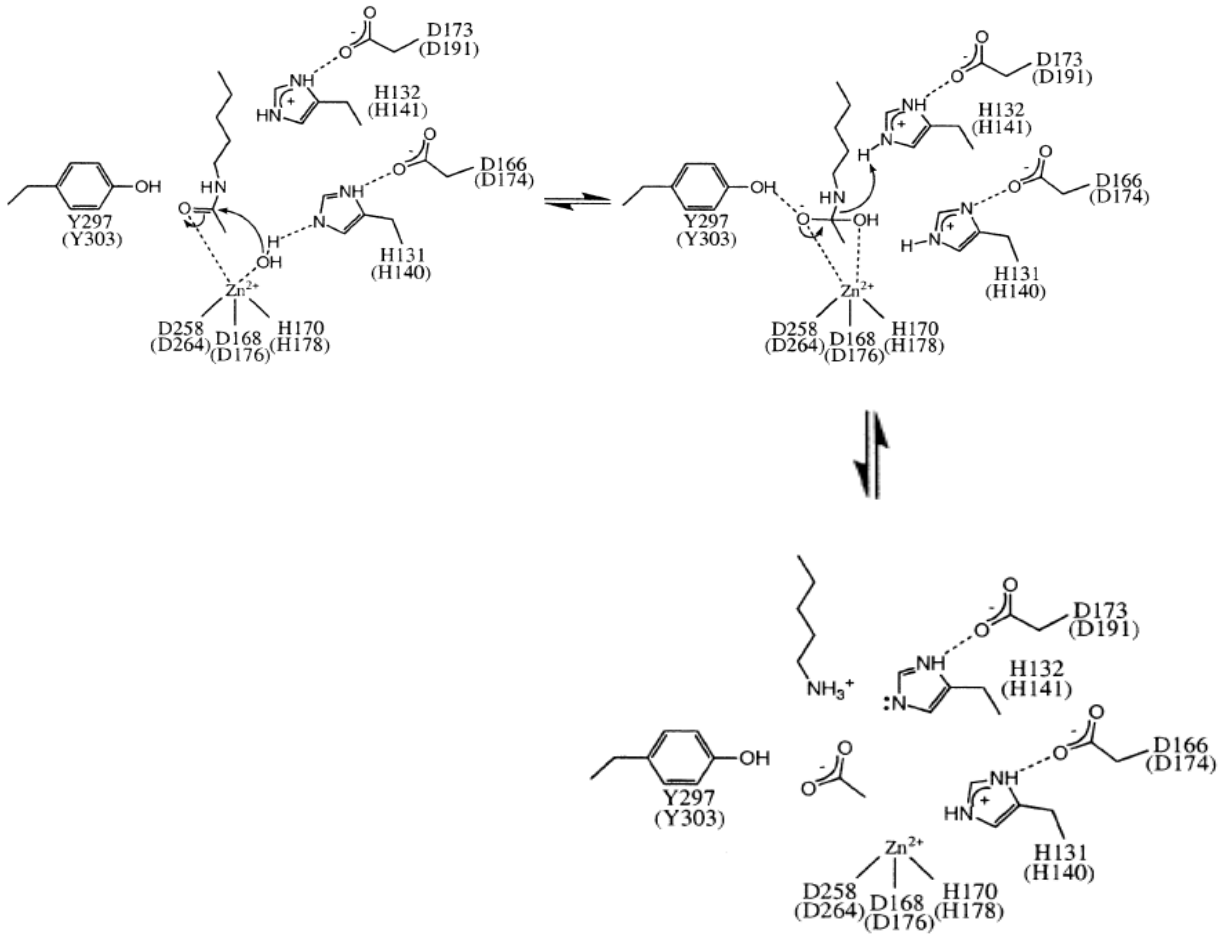

Figure 1.21. The proposed catalytic mechanism for HDLP and HDAC1 catalyzed deacetylation of the acetylated lysine.
The HDLP active site residues involved in the catalysis along with their HDAC1 counterparts (in parenthesis) are shown in this Figure. The Zn^{2+}cation here is bound to the carbonyl oxygen of the N-acetyl amide bond which makes the carbonyl carbon to be positioned in close proximity to the water molecule. Polarization by the zinc cation makes the carbonyl carbon a better electrophile and helps re-orient a water molecule. D166-H131 charge-relay system enhances the nucleophilicity of the water molecule which further aids in the catalysis. Figure adapted from ref (71).

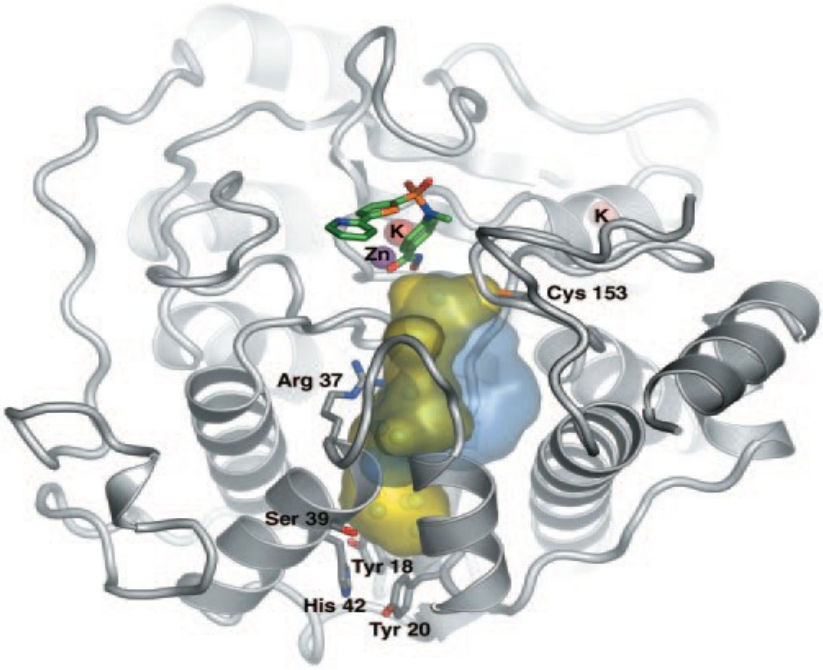

Figure 1.22. Surface representation of HDAC8 (yellow) and HDLP (light blue) internal cavities. The HDAC8 backbone is shown in gray and the water molecules in the buried cavity of the enzyme are shown as cyan spheres. Stick representation of the inhibitor, ions and other active site residues is shown. The architecture of the active site and its immediate surroundings are conserved between HDLP and HDAC8. Immediately below the active site, a tube-like internal cavity (yellow and light gray) filled with several water molecules could act as a shuttle conduit for the acetate reaction product, released after deacetylation. Figure adapted from reference (70).

The internal acetate release channels of HDAC8 and HDLP have been compared previously (70,90) as shown in Figures 1.22 and 1.24. This has provided greater insights into the mechanism of acetate release from histone deacetylases. Comparison of the shape and size of the 14 Å acetate release channels between HDLP and HDAC8 clearly shows that the channel in HDAC8 has a smaller volume (Figures 1.24 and 1.25) (90). Further, the acetate release channel cavity in HDAC8 appears to be divided at the point between amino acid residues L31, I34, R37, S138 and W141, creating a pair of 12 Å and 14 Å channels (90).

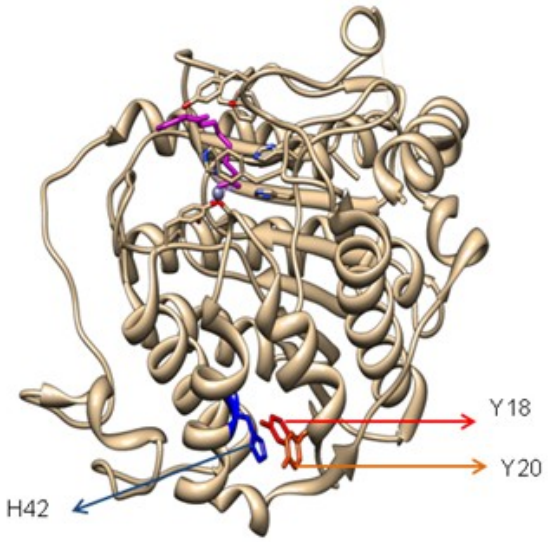

Figure 1.23. HDAC8-SAHA co-complex structure (PDB ID: 1T69) modeled using UCSF Chimera software®.
The HDAC8 backbone is shown in wheat color while the SAHA molecule is shown in pink. Y18, Y20 and H42 are the exit tunnel residues which are proposed to play an important role in the release of the acetate.

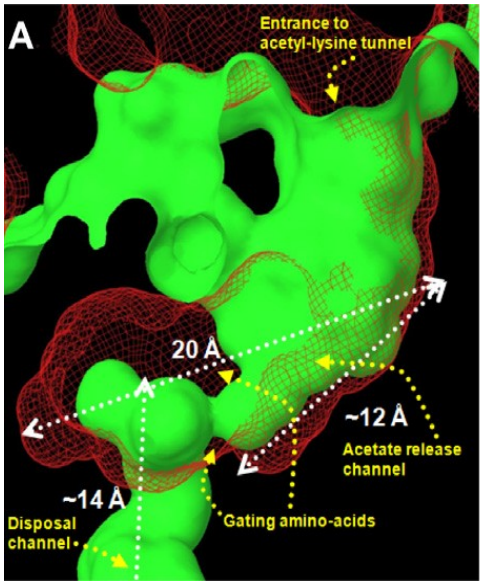

Figure 1.24. Comparison between the HDLP acetate release channel (red mesh) with the reported HDAC8 structure (green solid surface).
The gating amino acids include L31, I34, R37, S138 and W141.The acetate release channel in HDAC8 (12 Å) has a smaller volume compared to the HDLP (20 Å). Figure adapted from reference (90).

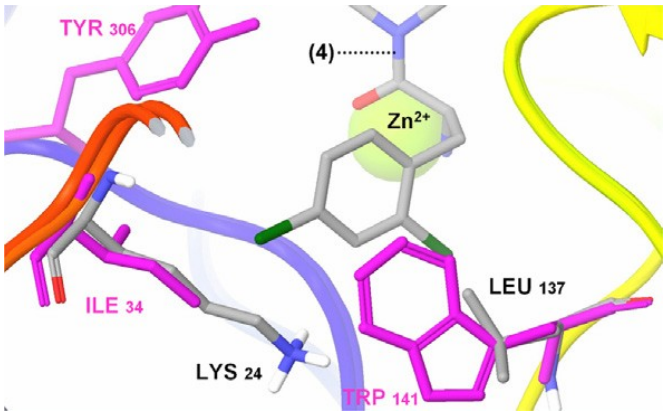

Figure 1.25. Comparison of the amino acid side chains in the acetate release channel in HDAC8 (magenta) and HDAC1 (gray backbone) enzymes.
Crystal structure co-ordinates of HDAC8 have been aligned with the HDAC1 homology model. The most prominent amino acid differences between HDAC8 and HDAC1 in the acetate release channel are W141 to L137 and I34 to K24, creating a smaller binding area. Figure adapted from reference (90).

This 14 Å channel in HDAC8 is the second channel in addition to the 11 Å hydrophobic channel that binds the substrate or the competitive inhibitors and leads to the active site (116). This acetate release channel (exit tunnel), lies adjacent to the metal active site that is lined by charged residues on one side and hydrophobic residues on the other (Figure. 1.26). It has been suggested that this exit tunnel has a role in tunneling the cleaved acetate product (produced after the deacetylation reaction) to the exterior media(117). A similar cavity is apparent in the crystal structure of HDAC8, which accepts the hydrolyzed acetate. This acetate is released upon the movement of the residues at the end of the cavity. This internal cavity is exposed to the outside environment in one of the X-ray structures of HDAC8 (70) but is closed (83,111) in the other structures. This may be indicative of some inherent flexibility of this side of the cavity(118). Additionally, it has been reported that like the active site tunnel, the residues surrounding the

acetate release channel are also highly conserved in HDACs 1, 2, 3, 8 and HDLP (70), suggesting its important function in all class I HDACs.

Whitehead et al. (90) have proposed the mechanism of acetate release via the exit tunnel, elaborating on the role of certain key and conserved residues in the entire process of acetate release. A schematic of the HDAC8 catalyzed deacetylation reaction in Figure 1.27 shows that the acetyl lysine tunnel is re-populated with water molecules from the solvent accessible surface after the release of the deacetylated lysine product. When the next molecule of the acetylated lysine approaches, the acetic acid product from the previous reaction is shunted into the 14 Å disposal channel presumably by active diffusional process. Certain conserved residues, such as R37 and W141 have been suggested to play a role in charge stabilization of acetic acid and closing of the acetyl lysine binding channel by relocating the side-chain indole moiety of W141. Both the residues are suggested to play an integral role in transporting the acetic acid into the disposal channel. Figures 1.28 and 1.29, illustrate the process of acetic acid disposal and preparation of HDAC for the next round of catalytic cycle. The acetic acid hydrogen bonds with the carbonyl oxygen of I19 and amide hydrogen of W137 at the base of the disposal channel. Acetic acid also makes hydrophobic bonds via its methyl group to the side chain moieties of I45, A38 and V41.

This may be the final resting place of the acetic acid in the enzyme before it is released via a concerted movement between Y18, Y20, A38, V41 and H42 side chains and exchange with the bulk water. The detailed mechanism and the individual roles of these residues is yet to be ascertained and the present study attempts to unravel the importance of Y18, Y20 and H42 in terms of the catalytic activity of the enzyme.

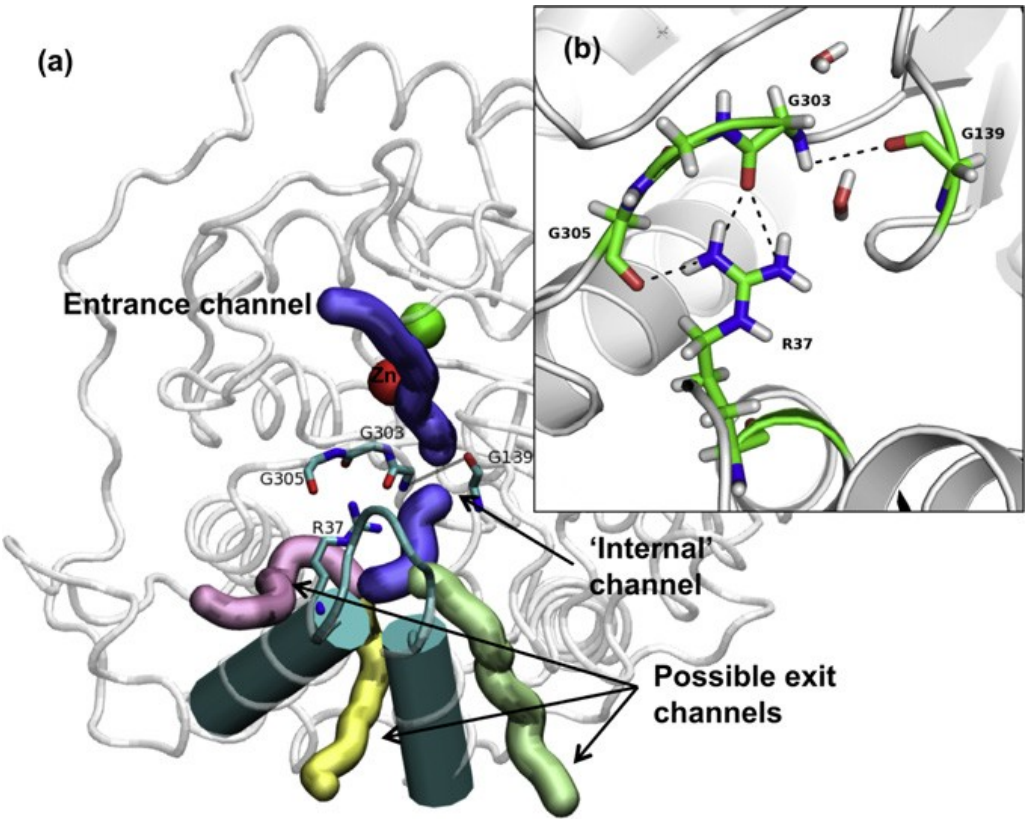

Figure 1.26. HDAC8 structure depicting the channels and the residues R37, G139, G303 and G305.
(a) The entrance channel (long blue spaghetti) is a hydrophobic 11Å tube-like channel that binds the substrate or the competitive inhibitors and leads to the active site. The internal channel (short blue spaghetti) is a 14 Å channel identified adjacent to the metal active site. It is lined by charged residues on one side and hydrophobic residues on the other side, imparting a role in accepting the cleaved acetate and releasing it on the far side of the cavity. Three possible exit channels (green, yellow and purple spaghettis) which traverse the β3 and α6-helix downstream of the internal channel are shown. (b) The inset is a magnified view showing the role of R37 in tethering the loop between β8 and α10-helix as it forms multiple hydrogen bonds (dotted lines) with the backbone carbonyl oxygen atoms of conserved G303 and G305. Amide of G303 forms a hydrogen bond with carbonyl oxygen of G139, blocking the channel and preventing the movement of water across it. Figure adapted from reference (116).

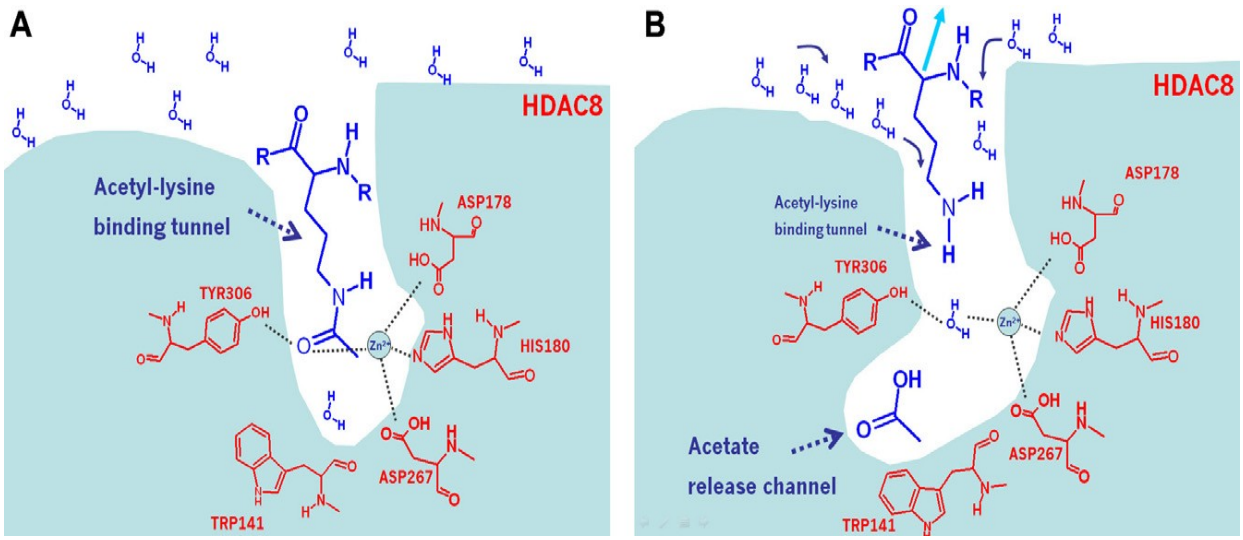

Figure 1.27. Schematic representation of the HDAC8 enzymatic process.
(A) Acetylated lysine binds into the HDAC8 active site tunnel and co-ordinates with Zn^{2+}, D178 and Y306. (B) Bulk solvent water molecules inhabit the entrance tunnel upon release of deacetylated lysine and acetic acid is transferred into the acetate release channel. Figure adapted from reference (90).

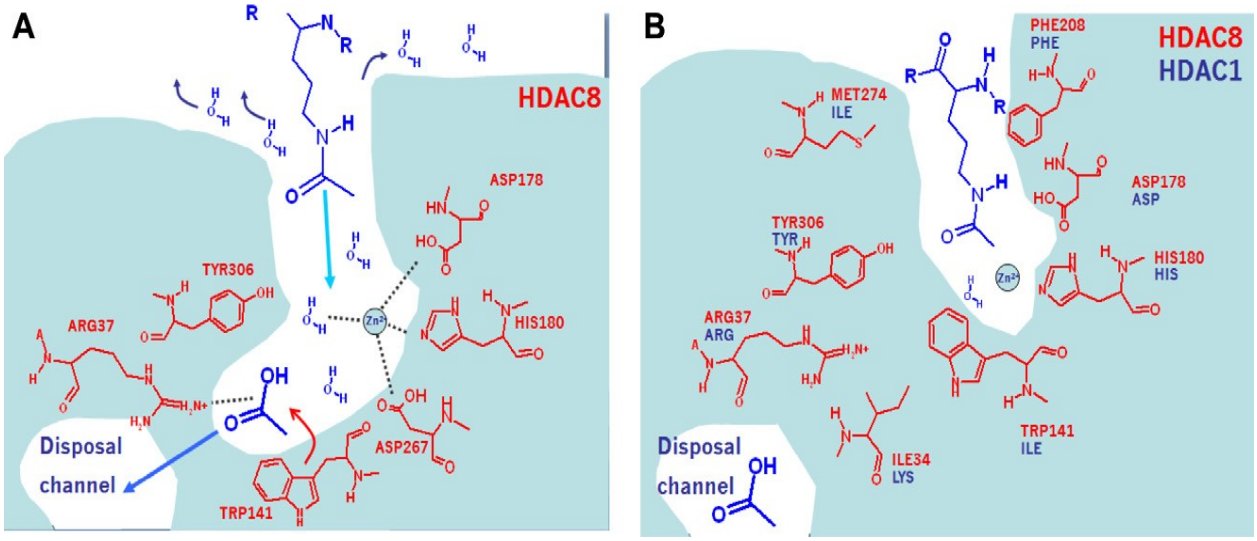

Figure 1.28. Schematic representation of the proposed HDAC8 catalytic process and the acetate release mechanism.
(A) This representation shows the acetic acid switching between channels and entering the disposal channel in order for HDAC8 to prepare for next catalytic cycle. At the same time, the acetylated lysine re-occupies the active site tunnel along with the water molecules. (B) Acetic acid released from the prior cycle enters the 14 Å disposal channel which is its final resting place before being released. Figure adapted from reference (90).

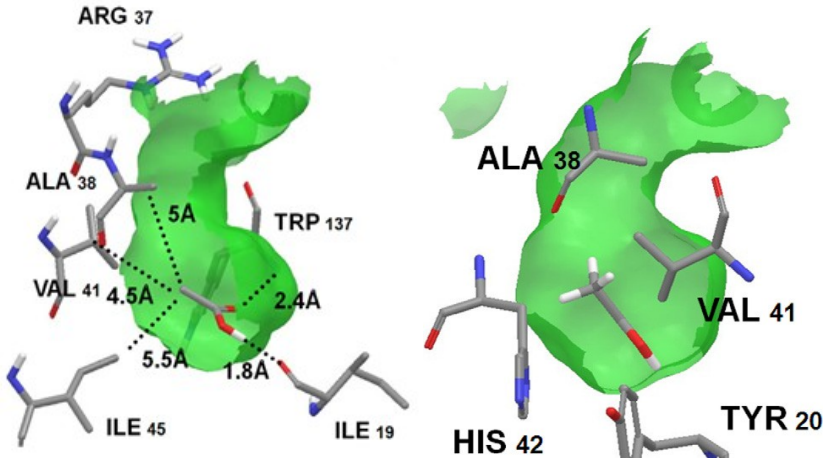

Figure 1.29. Proposed docking model of acetic acid in the 14 Å disposal channel of HDAC8. The Figure on the left shows the acetic acid released from the prior HDAC8 catalytic cycle entering into the disposal channel (green) where it forms hydrogen bonds and hydrophobic contacts with the lining residues (dotted lines). The amino acid residues Y20, A38, V41 and H42 form the barrier between the enzyme interior and the exterior solvent, as shown by the Figure on the right. Figure adapted and modified from reference (90).

The specific role of R37 in the acetate release mechanism has been delineated by Haider et al. (116). Their inspection of the crystal structure of HDAC8 (PDB ID: 2V5W) revealed a conserved R37 residue present at the center of the internal channel, which leads to the release of acetate. This R37 residue forms multiple hydrogen bonds with the backbone carbonyl oxygen atoms of G303 and G305, which are also conserved, causing the tethering of the loop between β3 and α10 helix. The latter results in another hydrogen bond formation between the backbone amide of G303 and the carbonyl oxygen atom of the G139 (conserved and located in the loop between β3 and α6-helix; Figure 1.26). The above bond causes the blocking of the channel in the absence of the acetate moiety. When R37 is mutated to Alanine or Glutamate, HDAC8 enzymes show significantly lower catalytic activity. The specificity constant (k_{cat}/K_m) of R37A mutation is

decreased by 530-fold while that of R37E mutation is decreased by $4X10^5$ fold. These data clearly demonstrated the importance of the positively charged R37 in maintaining the catalytic activity of HDAC8.

The effect of mutations on the interaction of HDAC8 with the acetate ion was determined by measuring the IC_{50} value of the acetate ion in both wild-type and R37 mutants. In the case of R37A mutant, the IC_{50} value increases by 160-fold as compared to the wild-type enzyme, assuming complete inhibition at saturating concentration of the acetate ion (116). The effect of R37 mutation on the secondary structure of HDAC8 was determined by circular dichroism (CD) studies. The CD spectrum of R37A was nearly identical to that of the wild type HDAC8 but the molar ellipticity was significantly decreased in case of R37E mutant. These experimental data led to the suggestion that the decrease in the specificity constant of R37A mutant was primarily due to the impairment of catalytic efficiency of the enzyme, whereas that of R37E mutation was partially due to altered conformational state of the enzyme. These findings led to the conclusion that R37 is a crucial residue for the enzyme catalysis, and this is accomplished via facilitating the release of the reaction product, acetate, via the internal cavity. However, the indirect role of R37 in promoting enzyme catalysis cannot be ruled out, and such feature remains to be elucidated.

1.1.8. Therapeutic Potential of Class I HDACs Inhibitors

HDAC inhibition holds great therapeutic potential in leukemia and some neurodegenerative diseases, including solid tumors and aberrant hormonal signaling. Class I HDACs are over-expressed in certain cancers and inhibiting those results in apoptosis of cancerous cells but not normal cells. The activities of HDAC 1-3 are modulated by post-translational modifications and their association with certain proteins to form complexes. This

makes them targets for the inhibitors (119). HDAC inhibitors fall into six structurally diverse classes (Figure 1.30 and Table 1.2). The first HDAC inhibitor to be identified was butyrate (120) and its derivative phenylbutyrate has already been successfully employed in experimental cancer therapy (121). However, there has been many limitations of using butyrates: Firstly, its potency is very low; it inhibits at a millimolar concentration via a not fully understood non-competitive mechanism (122). Secondly, it is not entirely specific for HDACs but it also affects processes like DNA methylation as well as in phosphorylation and methylation of proteins (122). Thirdly, it has a very short serum half-life in humans (123–125).

Other HDAC inhibitors are more specific and active at lower concentrations (126). Hydroxamate inhibitors, for instance TSA and SAHA and other HDAC inhibitors except for trapoxin and depudecin reversibly inhibit HDAC enzymes (127,128). The Structural data, elucidating the mode of binding of hydroxamate inhibitors (including TSA and SAHA) to the catalytic pocket of HDAC8 have been published by several laboratories (71,83,111). These structures have been very helpful in understanding the structure-activity relationship of the hydroxamate inhibitors as well as aiding in developing improved specific HDAC inhibitors of strong therapeutic potency with high bioavailability and reduced side effects and toxicity. It has been observed that some HDAC inhibitors are more specific only for certain HDAC isozymes, and such selectivity does not appear to be encoded by the architecture of the enzyme's active site pockets (129). Hydroxamates with rigid linker displays better inhibition properties than those with linear and flexible aliphatic linkers. For instance, N-hydroxycarboxamide derivatives were found to be better inhibitors for HDAC8 than N-hydroxyacetamide derivatives. These linkers form greater number of hydrophobic contacts with the active site tunnel(130).Since, the HDAC

inhibitors modulate apoptosis, growth arrest, differentiation and altered gene expression in tumor cells, normal cells are less sensitive to the enzyme inhibitors(131).

It has been found that in the cells treated with HDAC inhibitors, $p21^{WAF1}$, level (a cyclin dependent kinase inhibitor) is consistently induced, resulting in the arrest of cell division at the G_1phase and continuous blockage of the G_2/M phase (132). HDAC inhibitors cause altered expression of a variety of cellular genes including those coding for the proteins triggering apoptosis and cell cycle-regulating factors, molecules with immunological functions, and factors relevant to tumor development (70,132).

Histone deacetylase inhibitors (HDACi) comprise a group of targeted anti-cancer agents that are structurally diverse and have different modes of action. However, most HDACi selectively affect a relatively small proportion of expressed genes (2-10 %) in transformed (e.g., cancerous) cells (133–137). Vorinostat (suberoylanilide hydroxamic acid), a HDACi is the first HDAC inhibitor to get a Food and Drug administration (FDA) approval for the treatment of cutaneous T-cell lymphoma.

Largazole, is another potential cancer therapeutic cyclic depsipeptide that potently inhibits Class I HDACs and preferentially targets transformed over non-transformed cells (138). Largazole is a natural product, found in marine cyanobacterium, with a unique chemical scaffold (Figure 1.31b). Tripeptidomimetics are another novel series of compounds which function as Class I HDAC inhibitors. The latter are constituted of spiro-ring containing sulfur atoms as the cap group and linear carbon chains as linker, and have been found to have a higher potency over SAHA by two orders of magnitude (139).

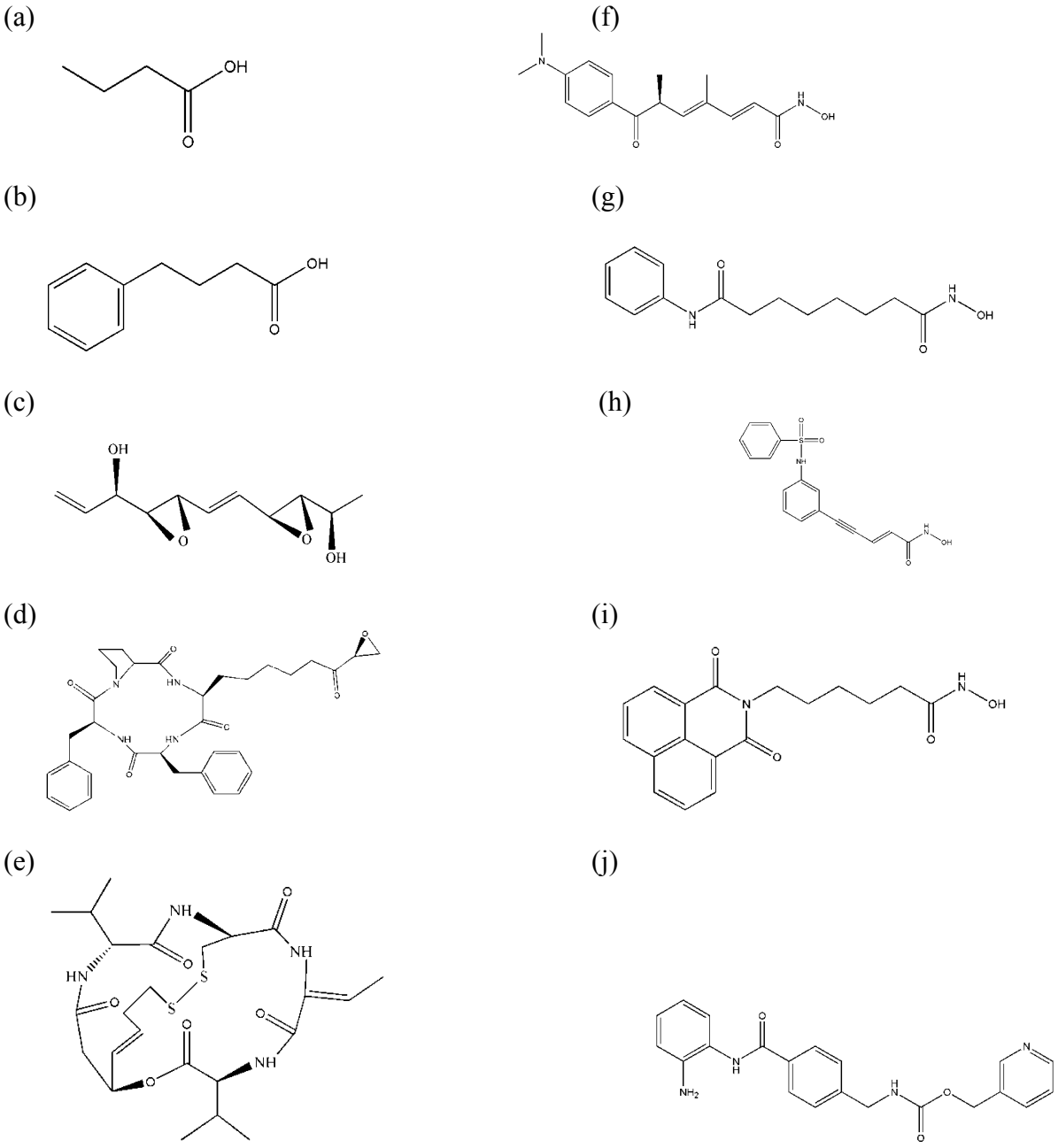

Figure 1.30. Compounds from the six structurally diverse classes of HDAC inhibitors.
(a) Butyrate was the first HDAC inhibitor to be identified followed by (b) phenyl butyrate. (c) Depudecin and (d) Trapoxin bind to HDAC8 irreversibly (e) Depsipeptide and (j) MS-27-275 are being tested in phase I clinical trials. (f) TSA and (g) SAHA belong to hydroxamic acids class of inhibitors which bind to HDACs reversibly. (h) Scriptaid and (i) Oxamflatin have been used in experiments designed to treat melanoma. Figure modified from reference (132).

Table 1.2. Molecular weight, Structural Class and Effective Inhibitory Concentration Range of the HDAC Inhibitors shown in Figure 1.30. Table modified from reference (123).

Inhibitor	MM (Da)	Structural Class[a]	Effective inhibitory concentration range
a Butyric acid	88.1	SCFAs and derivatives	mM
b Phenylbutyrate	165.2	SCFAs and derivatives	mM
c Depudecin	210.2	Epoxides	μM: irreversible binding
d Trapoxin	589.3	CTs containing an AOE moiety	nM: irreversible binding
e Depsipeptide	541.7	CTs lacking an AOE moiety	μM
f TSA	302.4	HAs	μM
g SAHA	264.3	HAs	μM
h Scriptaid	326.4	HAs	μM
i Oxamflatin	342.4	HAs	μM
j MS-27-275	376.4	Benzamides	μM

[a]Abbreviations: SCFA: Short chain fatty acids, CT: Cyclic tetrapeptide, HA: Hydroxamic acid, MM: Molecular mass, AOE: 2-amino-8-oxo-9,10-epoxy-decanoyl.

Chemistry of HDAC inhibitors: HDACi fall in several classes of structures such as aliphatic acids, benzamides, cyclic peptides and hydroxamates.

(a) **Aliphatic acids** like butyrate and phenylbutyrate, valproic acid is an aliphatic acid which is also a known HDAC inhibitor. Its millimolar range of activity makes it a weak inhibitor(140–142). AN-9 (pivaloyloxymethyl butyrate) by Titan Pharmaceuticals is a novel prodrug of butyric acid (142).

(b) **Benzamides** like 5 NOX-275 (MS-275) and MGCD0103 show selective HDAC inhibition (143). The inhibitor coordinates to the catalytic Zn^{2+} ion through both the carbonyl and amino groups to form an unusual 7-membered ring chelate complex. It has been shown MS-275 preferentially inhibits HDAC1 compared to HDAC3 and has little to no effect against HDAC6 and HDAC8(144).

(c) **Cyclic peptide HDACi** are a structurally complex group including Romidepsin (a natural product depsipeptide), apicidin, and the cyclic hydroxamic acid containing peptide group of molecules. These drugs have been found to be active at nanomolar concentration range (145).

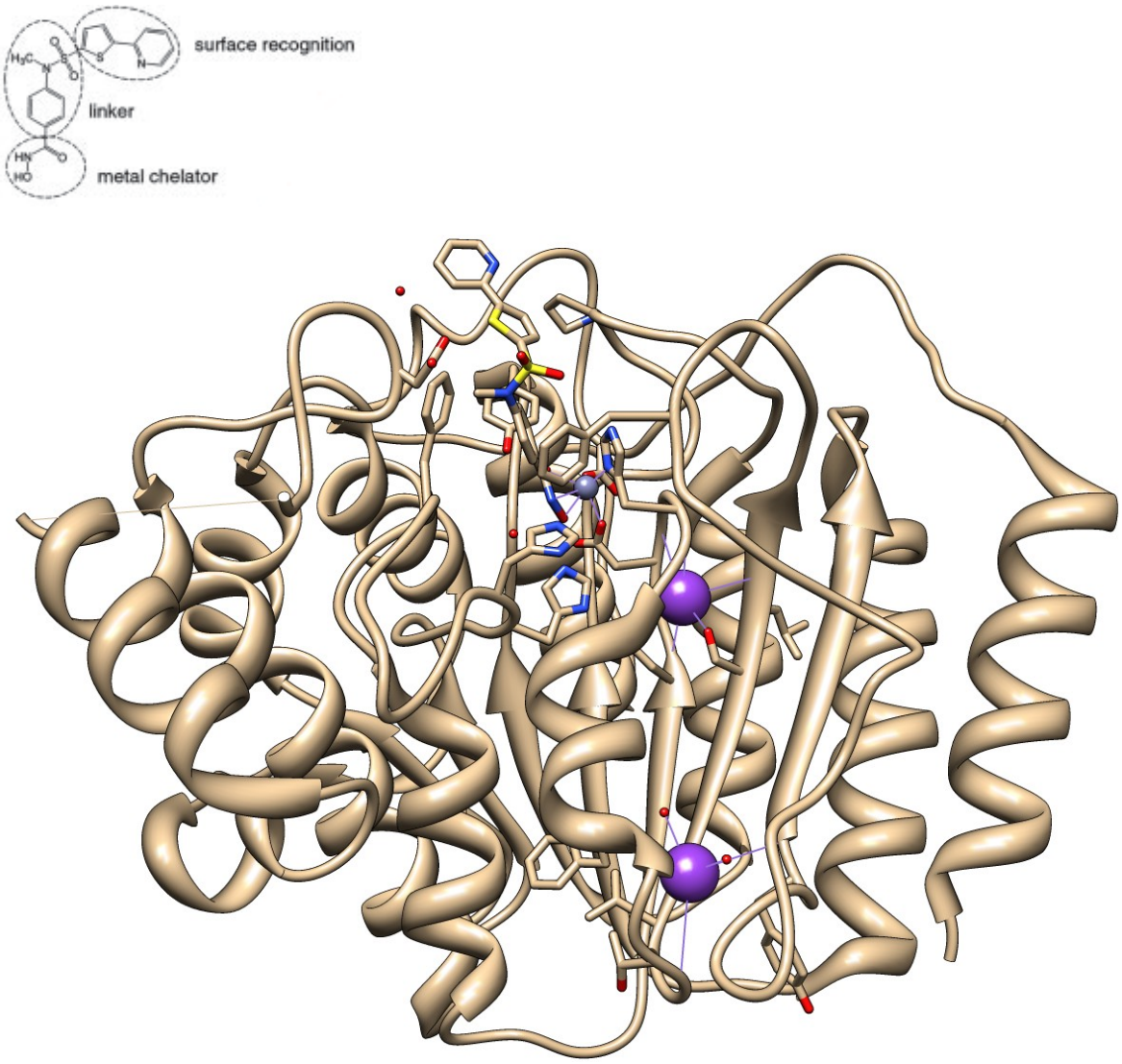

Figure 1.31a. HDAC8 crystal structure in complex with compound 1.
The upper left corner shows the chemical structure of the inhibitor bound to the HDAC8. A stick representation of the inhibitor bound to HDAC8 is shown in the ribbon diagram. The HDAC8: compound 1 structure (PDB ID: 1W22) has been modeled using UCSF Chimera® software.

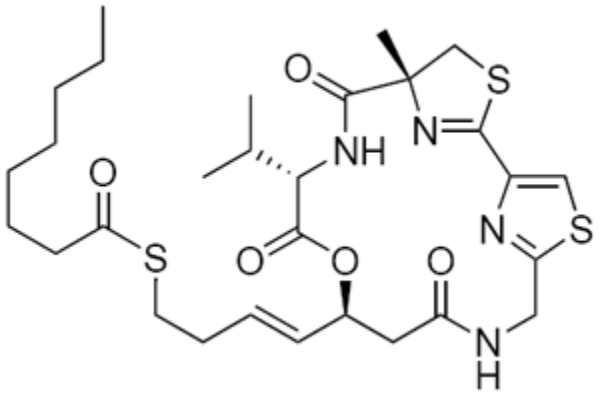

Figure 1.31b. Largazole, a HDACi found in marine cyanobacterium

(d) **Hydroxamate inhibitors** include TSA (first natural hydroxamate HDACi discovered) (87) and Vorinostat or SAHA (86). As mentioned above, a hydroxamate inhibitor consists of a metal-binding domain, a linker domain, and a hydrophobic capping group. The mechanism of inhibition of HDAC8 by hydroxamate inhibitors has been elucidated by Vannini et al. and Somoza et al. (70, 83). Somoza et al. solved the first crystal structures of HDAC8 complexed to trichostatin A (TSA), SAHA, 4-dimethylamino-N-(6-hydroxycarbamoyethyl)benzamide-N-hydroxy-7-(4-dimethylaminobenzoyl)aminoheptanamide (MS-344), and 5-(4-methyl-benzoylamino)-biphenyl-3,4_-dicarboxylic acid 3-dimethylamide 4_-hydroxyamide (CRA-A) (Figure 1.15 and 1.32).Comparison of the structures of the four HDAC:inhibitor complexes suggests that the vicinity of the active site pocket of HDAC8 is highly malleable and undergoes changes to accommodate binding of a variety of different ligands. These inhibitors inhibit HDAC (primarily class I & II) at nanomolar range and block

cancer cell proliferation (146).They exert multiple effects within the cells, including cell differentiation, induction of cell cycle arrest, and suppression of tumor growth(84–88).

Mechanism of action of hydroxamate inhibitors involves a bidentate coordination of its carbonyl and hydroxyl groups with the zinc ion. This chelation of zinc by the hydroxamate inhibitors renders HDAC8 catalytically inactive (Figure 1.32b). In addition to the above, zinc ion is coordinated to active site D178 (Oδ1), H180 (Nδ1) and D267 (Oδ1).The hydroxamic acid inhibitor also hydrogen bonds with both charge-relay histidines (H142 and H143) and the Y306 hydroxyl group and replaces the zinc-bound water molecule of the active structure with its hydroxyl group (Figure 1.15 and 1.20). The cyclic linker region of the inhibitor fits in the hydrophobic channel, with its aromatic aryl moiety stacked between side chains of F152 and F208. Additional *Van der Waals* interactions occur between the linker region, the side chain of M274 and the main chain of G151.

The effects of TSA were studied in MOLT-4 cells by He et al (147) where they found out that TSA-treatment caused the inhibition of the proliferation of MOLT-4 cells in a time and dose-dependent manner. It was concluded by them that TSA decreased the HDAC8 expression in MOLT-4 cells which inhibited the proliferation and caused the cell cycle arrest at the G2/M phase.

a

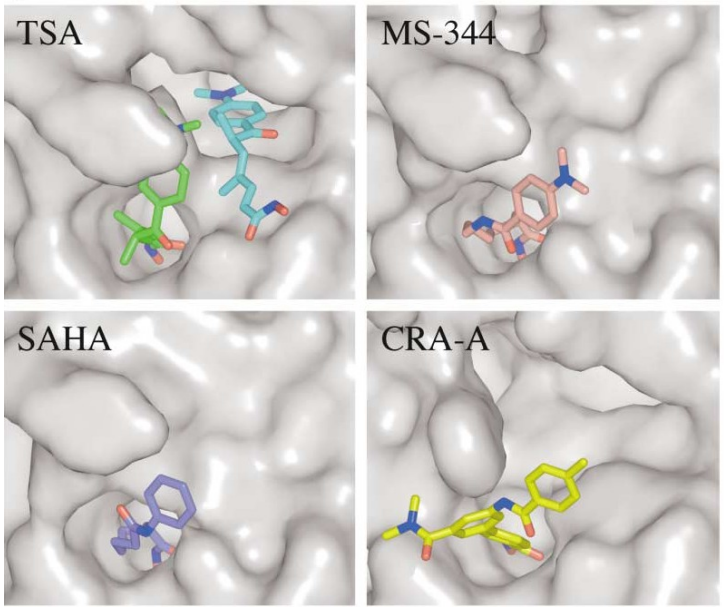

b

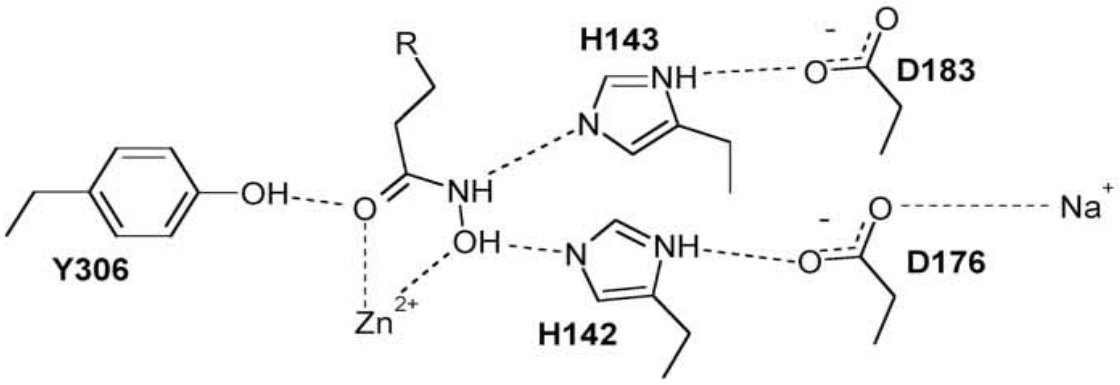

Figure 1.32. (a) Solvent accessible surface of active site areas of the HDAC8:TSA, HDAC8:MS-344, HDAC8-SAHA and HDAC8-CRA-A complexes. (b) Schematic diagram showing the binding of hydroxamate inhibitor to HDAC8.

For TSA and CRA-A, there is an adjacent binding pocket in addition to the catalytic pocket. In HDAC8-CRA-A complex, this is due to the peeling away of the L1 loop away from the enzyme that exposes a deep binding groove immediately adjacent to the active site pocket. In HDAC8: TSA complex, several of the residues that line the groove collapse inwards, and loop L2 (97-103), which is poorly ordered in the CRA-A complex with HDAC8, becomes ordered to the JI-JI stacking interactions between the dimethyl aniline group of TSA and the Y100. Figure adapted from reference (83).

Alpha-amino ketone inhibitors: As mentioned above, hydroxamic acids are the most commonly recognized class of chemical inhibitors for class I HDACs. These acids bind to the catalytic zinc ion at the base of the acetyl-lysine tunnel via an electrostatically favorable bi-dentate binding mode with two oxygen atoms, leaving the amide (NH) to form an additional hydrogen bonding interaction with a histidine. This metal chelating strength of the hydroxamic acid moiety, is believed to be responsible for most of their side-effects like anemia, thrombocytopenia and nausea amongst others (148). Therefore, scientists have long been interested in finding alternative molecules with weaker metal binding potential. Towards this end, Whitehead et al. were successful in synthesizing two novel chiral α-amino-ketone HDAC-binding molecules(90).

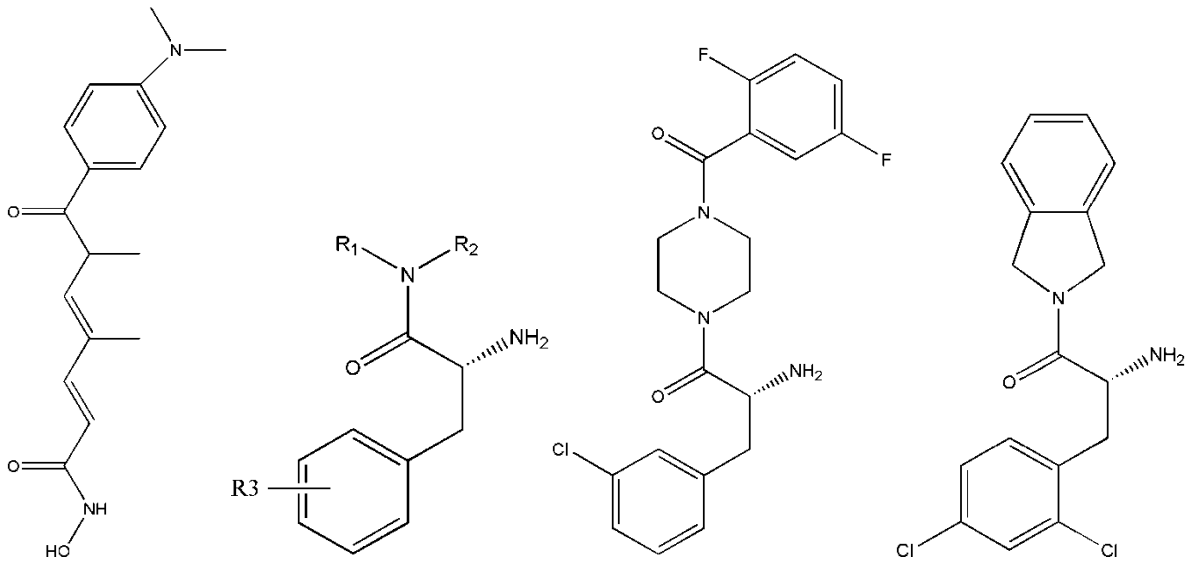

1 **2** **3** **4**

Figure 1.33. Chemical structures of histone deacetylase inhibitors and related ligands. (1) Trichostatin A (2) Generic representation of the (R)-α-amino-ketone moiety. (3) & (4) are class I HDAC binding ligands that are derivatives of (R)-α-amino ketone.

The R-chirality of these molecules (Figure 1.33, molecules 3 & 4) was found to be an important feature in their HDAC-binding. The core of the inhibitors is a primary amine moiety that completes the pseudo-tetrahedral co-ordination with the active site zinc ion, also co-ordinated by D178, H180 and D267. In addition, the central amino group donates a proton to the N (2) atom of H142 resulting in a hydrogen bond formation. The adjacent carbonyl oxygen in 3 & 4 compounds (Figure 1.33) participate in a weakened electrostatic interaction with the zinc ion. Apart from this, both species form a water –mediated hydrogen bond with the backbone amide of G305. The difluoro-benzyl-piperazine and the dihydro-isoindole moieties of compounds 3 & 4 form van der Waals interactions with H143, G151, F152, H180 and F208 of the acetyl-lysine substrate tunnel. The important thing about these inhibitors is that they form additional interactions with the enzyme which are not observed in the binding mode of hydroxamate inhibitors. The 3-chlorophenyl and the 2,4-dichlorophenyl moiety of compounds 3 and 4, respectively, form interactions with side-chains of I34, W141, G303, G304 and Y306 of the acetate product release channel. Specifically, the phenyl rings of these molecules Л-stack with the indole ring of W141. This novel mode of binding of these compounds to HDAC8 is shown in Figures 1.34 and 1.35 (90).

1.1.9. Activators of HDAC8

While the discovery of new inhibitors for HDAC is a major area of research, there has been limited effort in identifying the enzyme activators. It has been reported that chronic obstructive pulmonary disease (COPD), caused by an increased expression of pro-inflammatory factors is due to reduced HDAC8 activity (149). A flavonoid, theophyllin, has been reported to alleviate COPD symptoms by activating HDAC2 indirectly (149,150).

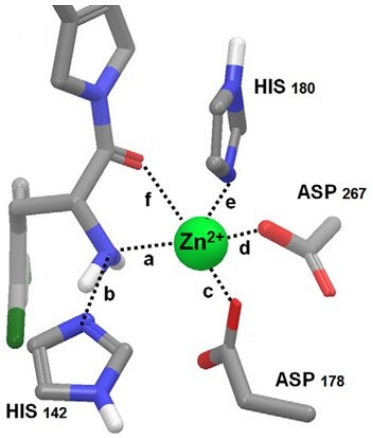

Figure 1.34. The novel binding mode of the α-amino-ketone binding motif in HDAC8.
Letters a-f correspond to intermolecular distances from either the Zn2+ cation or between the amino acid residues, and have the following values: a = 2.2 Å,b = 2.9 Å, c = 2.0 Å, d = 2.0 Å, e = 2.3 Å, f = 2.95 Å. The pseudo-tetrahedral co-ordination with the active site Zn2+ cation is also co-ordinated by D178, H180 and D267. Figure adapted from reference (94).

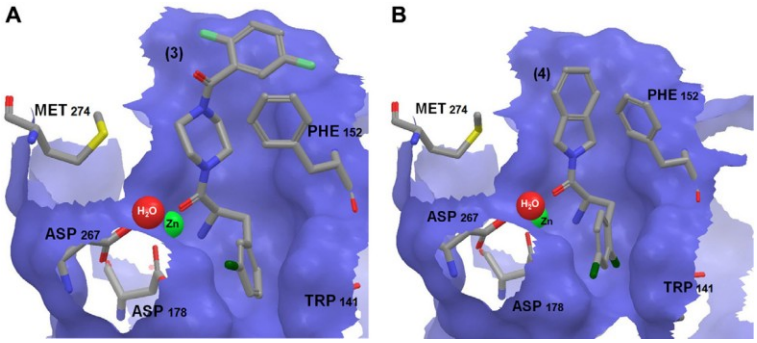

Figure 1.35. Position of the α-amino-ketone inhibitors 3 (panel A) and 4 (panel B) in the HDAC8 active site.
The inhibitors make interactions with HDAC8 on both sides of the catalytic Zn^{2+} ion, occupying volume in both the acetyl-lysine binding tunnel and the acetate product release channel. The central amino group of the inhibitor donates a proton to the N(2) of the His142 forming a H-bond. The adjacent carbonyl oxygen in the inhibitors forms a weak electrostatic interaction with Zn^{2+}.The inhibitors also form a water mediated hydrogen bond with the backbone amide of G305. The difluoro-benzyl-piperazine and the dihydro-isoindole moieties of the inhibitors form Van der Waals interactions with H143, G151, F152, H180 and F208 of the acetyl-lysine binding tunnel. The novel interactions between these inhibitors and the HDAC8 are observed between the 3-chlorophenyl and the 2, 4-dichlorophenyl moieties of compounds 3 &4 respectively, with the side chains of I34, W141, G303, G304 and Y306 of the acetate release channel. Figure adapted from reference (94).

Table 1.3. Catalytic IC_{50} Values of the *in vitro* Activity of Inhibitors 1, 3 and 4 against HDAC isoforms 1, 2, 6 and 8 (modified from reference 96)

Molecule	HDAC1	HDAC2	HDAC6	HDAC8 (nM)
1	3 nM	4 nM	51 nM	960
3	>30 μM	>30 μM	>30 μM	200
4	1.7 μM	3.9 μM	>30 μM	90

More recently, the mutant forms of HDAC8 with a reduced enzyme activity has been linked with Cornelia de Lange syndrome. An HDAC activator has a potential to alleviate the above disease condition associated with a reduced HDAC activity under such patho-physiological conditions (153). Additionally, HDAC8 selective activator could be used for the treatment of COPD and Cornelia de Lange syndrome, by enhancing the enzyme activity. Because of high therapeutic potential of isozyme selective HDAC8 activators, there has been of a growing interest in designing isozyme selective activators of different HDAC isozymes. There have also been additional reports suggesting that activation of HDACs can have a potential role in mitigating the severity of certain diseases. Singh et al. (2011) (151) reported certain derivatives of N-acetyl thiourea to be potential activators of HDAC8. The compound, N(phenylcarbothiol) benzamide (TM-2-51), was found to be the best activator and enhanced the activity of HDAC8 by 12-fold. It decreased substrate K_m by 3-fold and enhanced HDAC8 K_{cat} by 5-fold. Molecular docking studies proposed that this activator interacted at the active site pocket, thereby influencing the enzyme catalysis (151). This study was novel in that previous work with HDAC activators has focused only on Sirtuins (Class III HDACs), especially on Resveratrol, an activator for Sirtuin 1. Sirtuins have been found to link nutrient availability and energy metabolism. Calorie restriction, which has a role in extending the life-span and is found to be beneficial in age-related disorders, activates Sirtuin 1 (152). Accordingly, Sirtuin 1 has emerged

as a therapeutic target for the development of activators to treat diseases of aging. HDAC8 activators, therefore, hold a very high potential for a new generation of therapeutics.

1.1.10. Functional Roles of Selected Site-specific Mutations in HDAC8

A number of studies have been done to investigate the effect of specific mutations on HDAC8 structure and function. As described earlier, Y306 mutation of HDAC8 enzyme impairs its catalytic activity (83,111) and substitution of D101 in HDAC8 by any other amino acid impairs the binding of the substrate to the enzyme (111,115). Dowling et al.(115) solved the structure of H143A HDAC8 mutant complexed with an intact acetylated tetrapeptide substrate molecule. The H143A mutation makes the enzyme catalytically inactive as H143 acts as a general base in HDAC8 catalysis, as described above. This mutation was performed to trap the substrate in the HDAC8-substrate crystal. This structure was then used to study and confirm the importance of D101 for substrate binding. Their studies also revealed how the Y306 and the active site zinc ion together bind and activate the scissile amide linkage of acetyl-lysine (substrate).

In an attempt to identify the residues important for the release of the acetate by-product from HDAC8, Haider et al (2011), mutated the R37 residue (strictly conserved in class I& II HDACs) to either alanine or glutamate (116). These studies revealed that R37 is the binding partner for the acetate by-product generated following the deacetylation reaction of acetyl lysine (substrate) catalyzed by HDAC8.W141, acting as a gating residue, has also been proposed to be important in acetate release (90). Residues in close proximity to the external surface -Y18,Y20 and H42 may also help in the release of acetate and its exchange with the bulk water by movements of their side chains (70). Additional amino acid residues like I19, W137, I45, A38

and V41, that form the exit tunnel, have also been hypothesized to be important in the exit mechanism of acetate (90). However, the precise role of any of the above residues awaits experimental confirmation. Therefore, the present study attempts to experimentally verify the role of these residues in acetate release. Mutations at Y18, Y20 and H42 were created and their effect on kinetics and other biophysical characteristics of HDAC8 was studied. The detailed procedures and the outcomes of these mutations have been presented in the present study.

Recently, certain HDAC8 loss-of-function mutations have been reported in patients with Cornelia de Lange syndrome (153). Cornelia de Lange syndrome is a dominantly inherited congenital malformation disorder, caused mainly by mutations in the cohesin loading protein, NIPBL, and at other times, by mutations in the core cohesion components SMC1A (~ 5%) and SMC3 (<1%)(153). Deacetylation of SMC3 is required for normal functioning. Loss of HDAC8 activity results in increased SMC3 acetylation and incomplete dissolution of the cohesion complex released from chromatin in mitosis. Deardoff et al. (2012) demonstrated that p.H180R mutation severely impairs HDAC8 activity (153). Significant loss in HDAC8 activity was also witnessed in the p.G320R, p.T311M and p.H334R mutations. These residues have been found to be conserved in their position and structure of HDAC8-substrate complexes (153).

Conservatively substituted tunnel forming amino acid residues have been identified in different Class I HDACs. While these are quite conserved, subtle differences exist. Such differences can in turn be exploited in the isoform-selective inhibitor design. M274 of HDAC8 is a critical tunnel forming residue that has been replaced by E272 in HDAC10 and by L268 in HDAC11 over the course of evolution. Based on this, L268 in HDAC11 was mutated to mimic the corresponding residue in either HDAC8 or HDAC10, and the effect of this change on

HDAC11 function was analyzed (154). The HDAC8-like (L268M) mutation in the tunnel forming residue, largely maintained the deep and narrow tunnel as present in HDAC8 whereas HDAC10-like (L268E) mutation caused the tunnel to become wider and shallower as was observed in HDAC10. Thus, this study highlights the importance of even a single amino acid change in the tunnel formation in different HDAC isoforms. The observations from this study can be utilized in the development of isoform-selective HDAC inhibitors and also form the basis of studying the effects of point mutations on the overall functionality of the HDAC proteins(154).

1.1.11. Regulation of HDAC8

HDACs are key regulators of many cellular events, including cell proliferation and cancer, highlighting the critical importance of regulation of HDAC activity. Lee et al. (2004) reported that HDAC8 is negatively regulated by cyclic-AMP dependent protein kinase A (PKA)(91). The PKA phosphor-acceptor site of HDAC8 is Ser39, a non-conserved residue among class I HDACs. Mutation of S39 to Alanine enhances the deacetylase activity of HDAC8. In contrast, mutation of S39E or induction of HDAC8 phosphorylation by forskolin, a potent activator of adenyl cyclase, decreases enzymatic activity of HDAC8. Remarkably, inhibition of HDAC8 activity by hyperphosphorylation leads to hyperacetylation of histones H3 and H4, suggesting that PKA-mediated phosphorylation of HDAC8 plays a central role in the overall acetylation status of histones.

1.1.12. Biophysical Characterizations of HDAC8 mutants

1.1.12.1. Circular Dichroism Analysis of HDACs

Circular dichroism (CD) is one of the best techniques available for the rapid determination of the secondary structure, folding and binding properties of proteins (155). CD is commonly used to determine if a recombinant protein purified from an expression system is folded. The intrinsic circular dichroic properties of proteins can be used to follow their folding and unfolding patterns as a function of time, providing an excellent spectroscopic tool for following the unfolding and folding of proteins as a function of temperature (156). The CD spectra obtained as a function of temperature can also be utilized to determine if a protein has any unfolding intermediates (155). Analysis of the data obtained can be utilized to determine the rate constants and the order of the folding/unfolding reactions. CD can also be utilized to determine the effects of mutations and ligands on protein stability (156). Apart from this, CD can also be used to determine protein interactions (155). Structural changes in proteins originating from the binding of ligands are an integral part in understanding the mechanism of action and their biological activity. CD helps in detecting these changes which can be monitored in different spectral regions (157). CD is an extremely valuable technique in studying proteins especially peptides that cannot be crystallized. Vannini et al., (2004) performed a thermal denaturation experiment on HDAC8 and recorded CD spectra at 12°C in the far UV from 250 nm-190 nm (70). They observed a super imposable folding and unfolding curves upon a temperature scan from 12-54°C performed at 222 nm. This experiment showed the reversibility of the thermal melting curves and regaining of greater than 90 % of the signal upon cooling (70).

1.1.12.2. Isothermal Titration Calorimetry (ITC)

ITC is a highly sensitive thermodynamic technique that directly measures the heat released or absorbed during a biomolecular binding reaction. This heat measurement allows for the accurate determination of the association or the binding constants (K_a), stoichiometry (n), enthalpy (ΔH) and entropy (ΔS) (159). ITC can also be instrumental in determining the mechanism of molecular interaction. Various interactions like protein-small molecule, protein-protein, target-drug, enzyme-inhibitor, antibody-antigen, protein-DNA, protein-lipid and small molecule-small molecule can be studied extensively utilizing this technique. Its applications include assessment of the effect of molecular structure changes on the binding mechanisms, determination of the biological activity of certain molecules, characterization and optimization of the lead compound in the drug discovery. This technique was utilized to determine the effect of mutations on the binding constants (K_a), stoichiometry (n), enthalpy (ΔH) and entropy (ΔS) of HDAC8 and SAHA.

CHAPTER 2. STATEMENT OF PROBLEM

Unlike other enzymes, histone deacetylases harbors a separate "exit" tunnel for release of one of the reaction products (namely acetate), and the residues of the surrounding acetate tunnel have been found to be intimately involved in the enzyme catalysis. To investigate the specific contributions of the amino acid residues on the surface of the exit tunnel, site-specific mutations were created and the roles of such mutations on the binding of HDAC8 selective ligands as well as the enzyme catalysis were investigated. In this pursuit, the activity of mutant HDAC8 enzymes was investigated via *Fluor-de-lys*® HDAC8 assay. Fluorescence spectroscopy and fluorescence lifetime studies were performed to determine the variation in binding of SAHA and c-SAHA to mutant HDAC8 as compared to the wild type. Furthermore, circular dichroism studies were designed to determine a change in the secondary structure as well as the thermal stability and kinetics of unfolding of mutant HDAC8 enzymes. ITC analyses were performed to investigate the change in the substrate-binding pocket with mutant enzymes and HDAC8 inhibitor, SAHA. Ligand-binding studies (involving both the steady state and the time-resolved fluorescence) as well as *Fluor-de-lys*® HDAC8 activity assay involving the newly discovered activator of HDAC8, TM-2-51, were performed for HDAC8 mutants. These studies with the activator were performed to determine the change/enhancement in the mutant enzyme activity, activation constants and dissociation constants. These studies have been summarized as:

1. Steady state kinetic studies for the wild type and mutant HDAC8 enzymes to determine the change in the activity of the enzyme due to mutations.

2. Ligand binding studies (involving both the steady state and the time-resolved fluorescence) for the interaction of both the wild type HDAC8 and mutants with hydroxamate inhibitors.
3. ITC studies for the binding of SAHA to both the wild type and mutant HDAC8 enzymes to ascertain the change in their thermodynamic properties.
4. Circular Dichroism studies to determine the conformational and thermal stability of the wild type and mutant HDAC8 enzymes.
5. Steady state kinetics and ligand binding studies of mutant enzymes in the presence of the activator, TM-2-51, to determine an enhancement in the catalytic efficiency, if any.

These studies were designed to give valuable insights into the role of exit tunnel residues in the structure and catalytic efficiency of HDAC8. This information will allow better understanding of the HDAC8 catalytic mechanism, rate-limiting step, effects of mutations on its secondary structure and substrate-binding pocket. This information, subsequently, would be instrumental in the design of selective inhibitors and activators of HDAC8, which may potentially have lesser side effects.

CHAPTER 3. MATERIALS

The wild type HDAC8 cloning (pLIC-His-HDAC8) was performed in Dr. Srivastava's laboratory at North Dakota State University. Mutagenic primers were ordered from Integrated DNA Technologies (Coralville, IA). The Quikchange Site-directed Mutagenesis kit was purchased from Agilent Technologies (Santa Clara, CA). DNA sequencing was performed at MC lab (San Francisco, California). Molecular-weight standards for SDS-PAGE and agarose gel electrophoresis were obtained from Bio-Rad (Hercules, CA). The coumarin SAHA inhibitor was synthesized by Tanmay Mandal and Ganesh Balasubramanium in Dr. Gregory Cook's laboratory in Department of Chemistry and Biochemistry at NDSU. The 22-micron filters were purchased from VWR (Radnor, PA). Sodium chloride, tryptone, yeast extract, IPTG and ampicillin were purchased from Research Products International Corporation (Mt. Prospect, Illinois). Zinc chloride, magnesium chloride, Tris, imidazole and PMSF were purchased from Calbiochem (Philadelphia, PA). TCEP and bovine serum albumin (BSA) were obtained from Sigma-Aldrich (St.Louis, MO). Plasmid DNA mini-prep kits were purchased from Qiagen (Valencia, CA). The DH5α cells andBL21 Star^{TM} (DE3) *E. coli* cells were purchased from Invitrogen (Grand Island, NY). The His-Trap pre-packed columns for protein purification were purchased from GE Life sciences (Pittsburgh, PA). The substrate, *Fluor de lys*®, was obtained from Enzo life sciences (Farmingdale, NY). Molecular graphics and analyses were performed with the UCSF Chimera package. Chimera is developed by the Resource for Biocomputing, Visualization, and Informatics at the University of California, San Francisco (supported by NIGMS P41-GM103311). All other chemicals were of reagent grade, and were used without further purification.

CHAPTER 4. METHODS

4.1. Cloning, Expression and Purification of HDAC8 mutants

4.1.1. Construction of HDAC8 Mutants: Y18A, Y20A, H42A, E65Q, E66Q, E6566Q, H71Q, Y100A and Y100V

Site-specific mutations of selected amino acid residues in HDAC8 were performed in order to assess the roles of surface residues of acetate release channel. In addition to this, other HDAC8 mutants were created in order to determine the roles of other conserved amino acid residues among HDAC class 1 and 2 enzymes. These mutations were created using the Quikchange site-directed mutagenesis kit (Stratagene), using pLIC-His-HDAC8 DNA encoding wild type HDAC8 (that had previously been cloned in Dr. Srivastava's laboratory) as template. The overall protocol for site-directed mutagenesis, as detailed by Stratagene, involved designing of forward and reverse primers containing the desired mutation, polymerase chain reaction (PCR), cleavage of the parent DNA by DpnI restriction endonuclease and transformation of the mutant plasmid in *E. coli* DH5α cells. Table 4.1 shows the primers used for site-directed mutagenesis of HDAC8. All primers were obtained from Integrated DNA Technologies (IDT) as lyophilized powders and were reconstituted in nuclease-free water to a final concentration of 100 µM. The primer length ranged from 30-35 nucleotides with the desired mutation/s in the center, flanked on each side by approximately 15 nucleotides of correct sequence, to yield an overall melting temperature greater than or equal to 70°C. Polymerase chain reaction (PCR) was set up in dome-capped thin-walled tubes with 5 µl of 10X reaction buffer (Stratagene Kit), 60 ng of wt-HDAC8, 125 ng each of forward and reverse primers, 1 µl of dNTP mix (Stratagene Kit) and 1 µl of Pfu Turbo DNA polymerase (2.5 U/µl) in a 51 µl final reaction volume . The mutagenesis

reaction was performed in an Applied Biosystems Thermocycler, housed in the NDSU Core Biology Facility, IACC, Room 316. The cycling parameters for PCR were as follows: initial denaturation for 30s at 95°C followed by 16 cycles of 30s at 95°C, 1 min at 55°C for annealing and 14 min at 68°C for extension. Upon completion of the PCR reaction, the tubes were cooled by placing them at 4^0C. The reaction mixtures were added with 1 µl of Dpn1 restriction enzyme (10 U/ µl) and the tubes were incubated at 37°C for 2 hours to digest the parental wt-HDAC8 template DNA. The reaction was stopped by placing the reaction tubes on ice. Amplification of mutant DNA was ascertained by electrophoresis of 10 µl of the amplified product on a 1 % agarose gel.

Following DpnI digestion, mutant HDAC8 plasmid DNAs were used to transform *E. coli* DH5α cells using standard molecular biology methods. Briefly, 2 µl of the PCR-amplified mutant HDAC8 plasmid DNA was added to 50 µl of DH5α cells previously aliquoted into autoclaved eppendorf tubes set on ice. Following 30 min incubation on ice the cells were briefly heat-shocked for 45s at 42°C and immediately cooled on ice thereafter. After 5 min, 200 µl of Luria-Broth (LB) was added to each tube containing cells with the transformed plasmid and incubated at 37°C for 1 hour with continuous shaking in an incubator-shaker, followed by plating on LB agar plates containing 100 µg/ml ampicillin. The plates were incubated at 37°C for 16-18 hours to obtain the bacterial colonies transformed with mutant pLIC-His-HDAC8 DNA.

For each HDAC8 mutant, two independent cultures were grown by inoculating single colonies into 5 ml LB media containing 100 µg/ml of ampicillin. After growing at 37^0C in an incubator shaker, cells were pelleted and plasmid DNA was extracted using the Qiaquick® mini-prep kit (Qiagen, Valencia, CA). DNA concentration was measured using the Thermo Scientific

NANODROP 2000c housed in the Core Biology facility, IACC, Room 316. Mutant plasmid DNA was sequenced at the MC lab (San Francisco, CA), to confirm the presence of mutations.

Table 4.1. HDAC8 Mutant Primers: F-Forward Primer, R-Reverse Primer

Mutant	Primers
Y18A	F-5'-TCGCTGGTCCCGGTTGCTATCTATAGTCCCGAG-3' R-5'-CTCGGGACTATAGATAGCAACCGGGACCAGCGA-3'
Y20A	F-5'-GTCCCGGTTTATATCGCTAGTCCCGAGTATGTC-3' R-5'-GACATACTCGGGACTAGCGATATAAACCGGGAC-3'
H42A	F-5'-CGGGCCAGTATGGTGGCTTCTTTGATTGAAGCA-3' R-5'-TGCTTCAATCAAAGAAGCCACCATACTGGCCCG-3'
E66Q	F-5'AAGCCTAAAGTGGCCTCCATGGAGCAGATGGCCACCTTCCACACTGAT-3' R-5'ATCAGTGTGGAAGGTGGCCATCTGCTCCATGGAGGCCACTTTAGGCTT-3'
E65Q	F-5'AAGCCTAAAGTGGCCTCCATGCAGGAGATGGCCACCTTCCACACTGAT-3' R-5'ATCAGTGTGGAAGGTGGCCATCTCCTGCATGGAGGCCACTTTAGGCTT-3'
E6566Q	F-5'AAGCCTAAAGTGGCCTCCATGCAGCAGATGGCCACCTTCCACACTGAT-3' R-5'ATCAGTGTGGAAGGTGGCCATCTGCTGCATGGAGGCCACTTTAGGCTT-3'
H71Q	F-5'GAGATGGCCACCTTCCAGACTGATGCTTATCTG-3' R-5'CAGATAAGCATCAGTCTGGAAGGTGGCCATCTC-3'
Y100A	F-5'GAATATGGGCTAGGTGCTGACTGCCCAGCCACT-3' R-5'AGTGGCTGGGCAGTCAGCACCTAGCCCATATTC-3'
Y100V	F-5'GAATATGGGCTAGGTGTTGACTGCCCAGCCACT-3' R-5'AGTGGCTGGGCAGTCAACACCTAGCCCATATTC-3'

4.1.2. Expression and Purification of Mutant HDAC8 Proteins using pLIC-His-Y18A-HDAC8, pLIC-His-Y20A-HDAC8 and pLIC-His-H42A-HDAC8 Constructs

For expression and purification of recombinant HDAC8 proteins, mutant HDAC8 encoding plasmids (pLIC-His-Y18A-HDAC8, pLIC-His-Y20A-HDAC8 and pLIC-His-H42A-HDAC8) were transformed into BL21 Star™ (DE3) *E. coli* cells using the standard molecular biology protocol. Mutant HDAC8 proteins were purified as described by Vannini *et al*.,(70) with only minor modifications. Transformed BL21 Star^{TM} (DE3) *E. coli* cells were inoculated in LB medium containing 100 µg/mL of ampicillin and grown at 37 ºC in an incubator shaker with a rotation speed of 200 RPM until A_{600} was 0.8 (measured on MD Spectramax M2/M2e spectrophotometer). At this stage, the cells were induced by addition of 0.4 mM IPTG and 100 µM $ZnCl_2$ .Following this, the cells were grown overnight for 14-16 hours in an incubator shaker at 18°C at a rotating speed of 200 RPM. Next day, the cells were pelleted by centrifugation at 5000 RPM at 4°C for 15 min in a refrigerated Sorvall RC-5B. The resulting pellet was resuspended in a lysis buffer containing 50 mM Tris-HCl, pH 8.0, 3 mM $MgCl_2$, 150 mM KCl, 5% glycerol, 1mM β-mercaptoethanol, 0.25 % Triton-X-100 and 20 mM PMSF (dissolved in iso-propanol) for 45 min, by continuous stirring at 4°C. The cells were lysed by sonication using Branson Bath Sonifier (power level 5, 40% duty cycle) on ice for 20 min with 2 min cycle interspersed with 1 min pause. Following sonication, the cell debris was removed by centrifugation (15000 RPM for 90 min) in Sorvall RC-5B. The supernatant was filtered through a 0.22 µm filter and 10 mM imidazole was added to the filtrate prior to the purification of the mutant HDAC8 enzymes by Immobilized Metal Affinity Chromatography (IMAC) using AKTApurifier UPC 100. For this, a 1 ml Nickel-IDA column was equilibrated first with 50 mM

Tris-HCl, pH 8.0, 3 mM $MgCl_2$, 150 mM KCl, 5% glycerol and1mM β-mercaptoethanol, followed by a second equilibration step with 10 column volumes of the above HDAC8 purification buffer containing 10 mM imidazole. Finally the sample was loaded onto the pre-equilibrated nickel-IDA column and run at a flow rate of 0.7 ml min^{-1}. Next, the column was washed with 15 column volumes of a wash buffer containing 25 mM imidazole, 50 mM Tris-HCl, pH 8.0, 3 mM $MgCl_2$, 150 mM KCl, 5% glycerol and 1mM β-mercaptoethanol, to remove the non-specific binding proteins. The specifically bound recombinant HDAC8 protein was then eluted (in 2 ml fractions) by applying a 50 ml gradient of 10-350 mM imidazole in elution buffer containing 50 mM Tris-HCl, pH 8.0, 3 mM $MgCl_2$, 150 mM KCl, 5% glycerol and 1 mM β-mercaptoethanol and protein elution monitored by the chromatogram. The peak fractions, as evident from the chromatogram obtained, were analyzed by gel electrophoresis to determine the purity of the enzyme. Briefly, a resolving gel containing 12% acrylamide + 0.1% SDS and a stacking gel containing 4% acrylamide plus 0.1 % SDS were prepared in 1.5 M Tris-HCl, pH 8.8 and 0.5 M Tris-HCl, pH 6.8, respectively. The column eluate containing recombinant HDAC8 enzyme and 2X loading dye containing 10% SDS, 25% glycerol, 5 mM β-Mercaptoethanol, 0.015% bromophenol blue and 300 mM Tris-HCl, pH 6.8 were mixed together in a 1:1 ratio and denatured by boiling for 5 minutes at 95°C in a water bath. The denatured protein samples were then loaded on the gel and electrophoresed at 200 V in a Tris-HCl-glycine buffer containing 0.1% SDS, 25 mM Tris-HCl and190 mM glycine, pH 8.3. Staining of the gels was performed with 0.1% Coomassie blue in 10% acetic acid and 10% methanol for 20 min followed by destaining for nearly 45 min in a solution containing 10% acetic acid and 40% methanol. The intensity of the protein of interest as compared to other bands in the gel provided

a qualitative indicator of the enzyme purity. The concentration of recombinant HDAC8 enzyme in the eluate was determined by Bradford assay using BSA as a standard protein (158). The assays were performed in a microplate using enzymes diluted in Bradford reagent. This mixture was incubated for 10 min at room temperature and the absorbance was measured at 595 nm using the MD Spectramax M2/M2e spectrophotometer. The peak fractions containing recombinant HDAC were pooled thereafter and dialyzed overnight against the HDAC8 storage buffer (10 mM Tris-HCl, pH 7.5, 3 mM $MgCl_2$, 100 mM NaCl, 10% glycerol, 1mM TCEP) at 4°C. The protein was re-dialyzed in a fresh batch of HDAC8 storage buffer for 5 hours and the purified protein was stored at -80°C. Recombinant wild-type HDAC8 as well as Y18A-HDAC8, Y20A-HDAC8 and H42A-HDAC8 mutant proteins were purified in an identical manner as described above.

4.2. Steady-state Kinetic Methods

4.2.1. Assay of HDAC8 Activity using *Fluor de lys*® as Substrate

The deacetylase activity of HDAC8 was measured on a routine basis by using the *Fluor de lys*® assay system as detailed by Wegner et al., (2003)(105) in standard assay buffer containing 50 mM Tris-HCl, pH 8.0, 137 mM NaCl, 2.7 mM KCl, 1 mM $MgCl_2$ and 1 mg/ml BSA. This is a coupled assay system utilizing a small peptide substrate containing a C-terminal lysine residue conjugated to, 7-amino-4-methylcoumarin (AMC) as a fluorophore. The assay relies on the initial deacetylation of lysine by HDAC8 followed by cleavage of the lysine-AMC amide linkage by trypsin (coupling enzyme) to produce the fluorescent AMC product, which absorbs at 365 nm and emits at 500 nm. The assay was performed on a Molecular Devices SpectraMax® Plus microplate reader (using polystyrene microplates) at room temperature (about 25 ºC) for 3 hours.

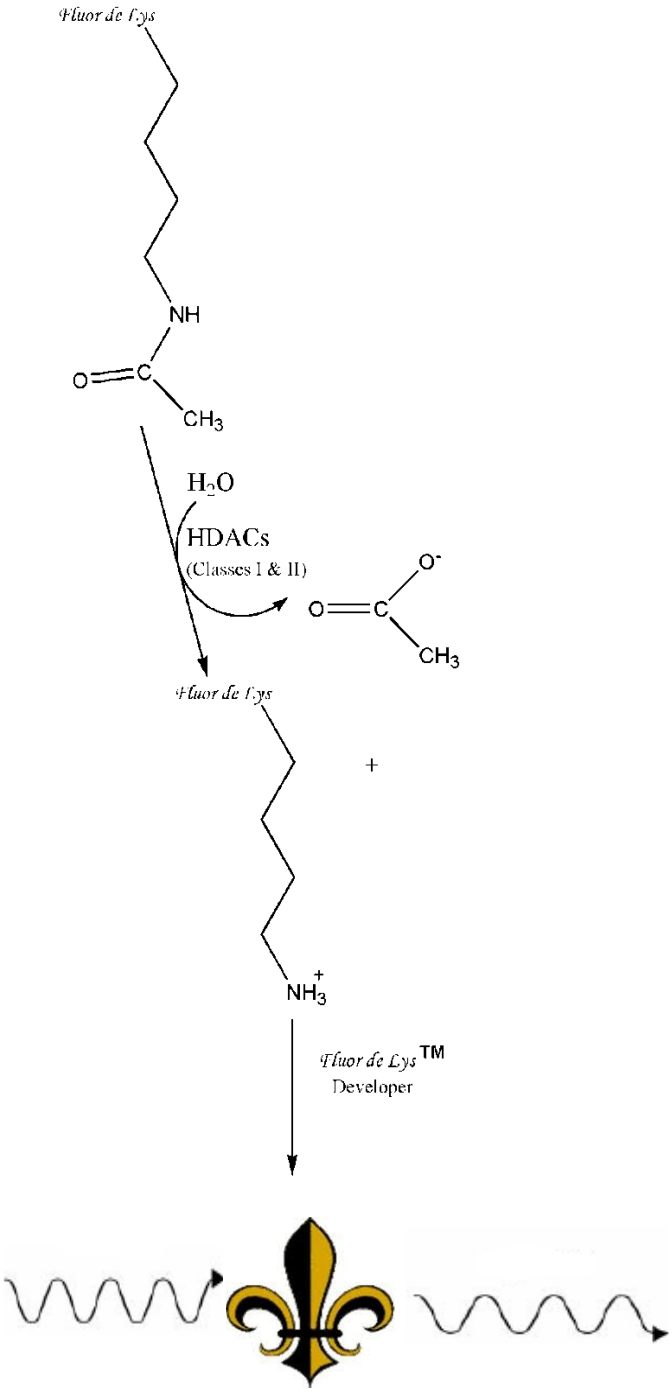

Scheme 4.1. HDAC8 activity assay

Due to impaired rate of catalysis of mutant enzymes (yielding lower signal) a High PMT voltage setting was chosen for measuring the enzyme activity. Reactions were set up in polystyrene microplate wells, where each assay well contained 60-2000 µM *Fluor de lys*® substrate, 250 nM trypsin and 250 nM HDAC8 enzyme (either wild type or mutant) in a total volume of 0.2 ml. Reactions were initiated by the addition of the enzyme and progress curves were monitored at 500 nm (λ_{exc}= 365 nm with cut off filter at 455 nm). The initial rates were plotted as a function of substrate concentration. The initial rate of the enzyme catalysis was determined by the slope of the linear portion of the reaction progress curve following the initial lag phase. The magnitude of the product formation was calculated using AMC (the reaction product of the HDAC8 and trypsin catalyzed reactions) as standard. The increase in fluorescence emission intensity (λ_{exc}= 360 nm and λ_{em}= 460 nm) as a function of AMC concentration was measured to generate a standard plot that was used to convert the rate of the reaction from relative fluorescence units (RFU) per sec to µmoles of the product formed per sec. The value of k_{cat} of HDAC8 was determined using AMC standard plot using the following calculation. The value of V_{max} obtained as RFU/s from the trypsin-coupled assay was converted into µM/s using a standard plot (Figure 4.1).The latter was generated by measuring the increase in fluorescence of the reaction product of the HDAC8 assay as a function of fluorophore concentration. The fluorophore was prepared by treatment of the deacetylated standard (available from the Enzo Life Sciences) with 50 µM of trypsin for 10 minutes. The value of k_{cat} was calculated by dividing the V_{max} (µM/s) value by the concentration of HDAC8 used in the assay. A unit of HDAC8 activity is defined as the amount of enzyme required to convert one micromole of substrate into product per min in standard assay buffer.

To determine the K_m and k_{cat} values of HDAC8, initial rates were plotted as a function of the substrate concentration. The data were analyzed via the classic Michaelis-Menten equation (equation 4.1):

$$v = V_{max} / (1 + K_m / [S]) \qquad \text{Eq. 4.1}$$

where v is the initial rate, K_m is the apparent binding constant of the substrate with the enzyme (expressed in μM) and V_{max} is the maximal steady-state rate (expressed in μM s^{-1}). The k_{cat} value was calculated by dividing V_{max} by the total concentration of the enzyme, and was represented in the units of sec^{-1}. All data analysis was performed using GRAFIT software (ver. 4.0) unless specifically mentioned otherwise.

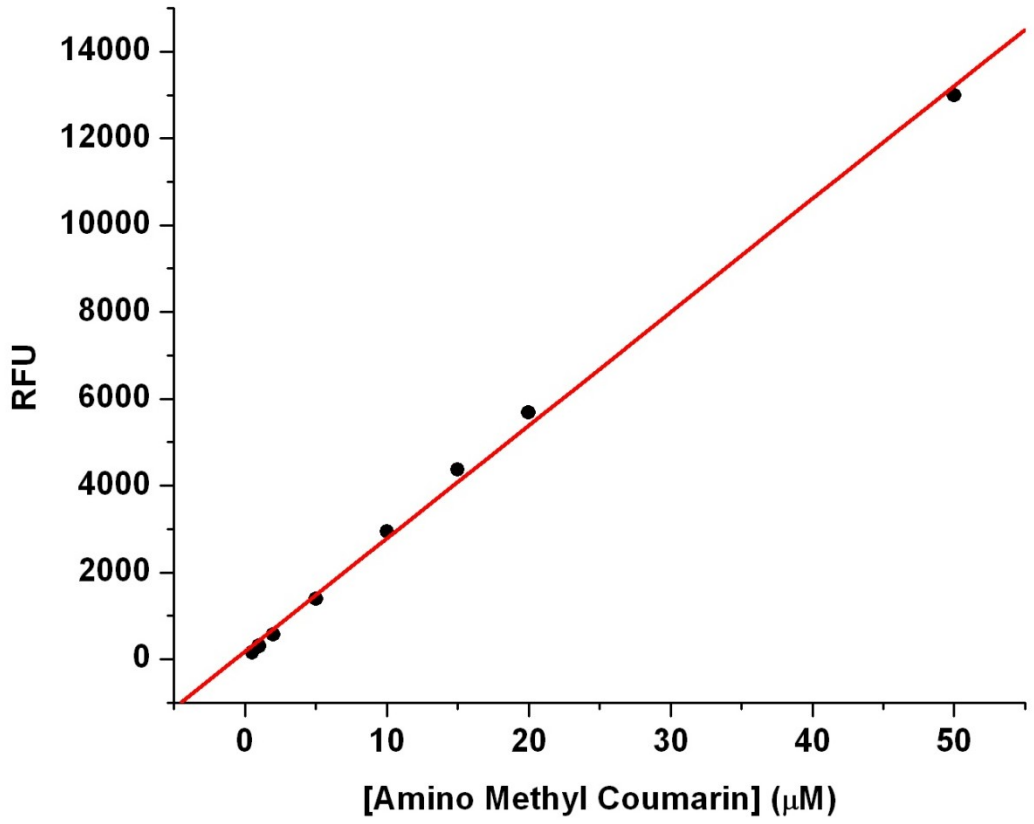

Figure 4.1. Standard plot of amino methyl coumarin (AMC).
A microplate was set up with different concentrations of AMC-deacetylated standard in each well and 50 μM of trypsin was added to each well. The corresponding RFU values for the known concentrations of AMC were determined using the end-point assay with λ_{exc}= 365 nm and λ_{em}= 500 nm. A standard plot of deacetylated AMC was generated to determine the amount of the product formed per second (nM per second) after each catalytic cycle of the enzyme. The fluorescence signal (measured in RFU) was converted into the concentration units of product (nM/s) using this standard curve. These values were fit using a linear equation of the line and were used to convert the fluorescence signal (measured in RFU) into the concentration units of the product formed (nM of product formed per second) per unit time for the wild type and the mutants of HDAC8.

4.2.2. Activation of Wild Type and Mutant HDAC8 Enzymes by TM-2-51

It has been known that a variety of N-acetylthiourea derivatives activate the HDAC8 catalyzed reaction. Singh et al., 2011 (151) has described the effects of the TM-2-51 on the K_m and k_{cat} of the wild type HDAC8. It was determined that the K_m for *Fluor de lys*® for wild type HDAC8 was reduced by 3-fold whereas k_{cat} had increased by 5-fold.To probe the effect of one such N-acetylthiourea (namely, TM-2-51), on the K_m and k_{cat} of wild-type and mutant HDAC8 enzymes, the deacetylase activity of HDAC8 was measured in the presence of 50 μM TM-2-51 by using the *Fluor de lys*® assay system as described above.

The enzyme reaction was measured in a standard assay buffer constituted of 50 mM Tris-HCl, pH 8.0, 137 mM NaCl, 2.7 mM KCl, 1 mM $MgCl_2$ and 1 mg/ml BSA. Reactions were set up for Y18A-HDAC8, Y20A-HDAC8 and H42A-HDAC8 in a polystyrene microplate where each assay well contained 60-2000 μM *Fluor de lys*® substrate, 50 μM activator, 250 nM trypsin and 250 nM wild-type or mutant HDAC8 enzyme in a total volume of 0.2 ml. Reactions were initiated by the addition of the enzyme and the time course of increase in fluorescence as a function of time was monitored. The initial rates of HDAC8 reactions were obtained by the slope of the linear portion of the reaction progress curve after the initial lag-phase time. The calculation of the product formation (or the quantitative determination of the HDAC8 activity) was performed using AMC (HDAC8 deacetylated standard) standard plot as described above. To determine the K_m and k_{cat} values of wild type and mutant HDAC8 in the presence of the activator, the initial rates were plotted as a function of the substrate concentration. The data was analyzed via the classic Michaelis-Menten equation (equation 4.1). The k_{cat} value was calculated by dividing V_{max} by the total concentration of the enzyme and expressed in unit of sec^{-1}. All data

analyses were performed using GRAFIT software (ver. 4.0) unless specifically mentioned otherwise.

4.2.3. Steady-state Kinetic Experiments for the Inhibition of Wild Type and Mutant HDAC8 Enzymes

The spectrofluorometric experiments for the determination of the inhibition constants of selected inhibitors were performed on a Molecular Devices SpectraMax® Plus microplate reader using polystyrene microplate. The assay conditions were set as follows: λ_{exc} = 365 nm, λ_{em} = 500 nm and $\lambda_{cut\ off}$ = 455 nm, at room temperature for 3 hours. Due to impaired rate of catalysis of mutant enzymes (yielding lower signal) a High PMT voltage setting was chosen for measuring the enzyme activity. The reactions were performed utilizing the *Fluor de lys*® assay system as described above in the standard assay buffer. Reactions were started by addition of the respective HDAC8 enzyme and the reaction progress was monitored for 3 hours at 500 nm.

4.2.3.1. Determination of the Inhibition Constant (K_i) of Acetate for Wild Type and the Mutant HDAC8 Enzymes

Based upon the proposed mechanism of the HDAC8 catalysis (83) the deacetylation leads to the formation of the deacetylated lysine product and the acetate by-product. Mutations at the exit tunnel were hypothesized to interfere with the release of the acetate. Therefore, it was important to measure the inhibition constant of the acetate for both the wild type and the mutant HDAC8 to ascertain any difference in each of the enzymes. The inhibition constant for acetate (K_i) was determined utilizing the *Fluor de lys*® assay system, as described, via Molecular Devices Spectra Max plus micro plate reader in a polystyrene microplate in the presence of varying concentrations of acetate in the HDAC8 standard assay buffer. Stock solutions of

potassium acetate in the HDAC8 standard assay buffer (50 mM Tris-HCl, pH 8.0, 137 mM NaCl, 2.7 mM KCl, 1 mM $MgCl_2$ and 1 mg/ml BSA) were prepared with the following concentrations: 200 mM, pH 8.0, 500 mM, pH 8.0 and 1M, pH 8.0. Reactions were set up for wt-HDAC8, Y18A-HDAC8, Y20A-HDAC8 and H42A-HDAC8 in a polystyrene microplate. Each assay well contained 150 μM *Fluor de lys*® substrate (except for Y18A it was 500 μM), varying concentrations of acetate (0-120 mM), 250 nM trypsin and 250 nM wild-type or mutant HDAC8 (except in case of Y18A-HDAC8, which was used at 500 nM) enzyme in a total volume of 0.2 ml. Reactions were initiated by the addition of the enzyme and the time course of increase in fluorescence as a function of time was monitored. The initial rates of HDAC8 reactions were obtained by the slope of the linear portion of the reaction progress curve after the initial lag-phase time. The rate of enzyme catalysis was determined as described above and was plotted as a function of inhibitor concentration. To reliably measure the enzyme activity, relatively high concentrations of the HDAC8 enzymes were taken. In this scenario, there is a possibility that a part of the substrate and/or inhibitor is bound to the enzyme site. The Michaelis-Menten relies on the free concentrations of the substrates and inhibitors, rather than their total concentrations. Therefore, the fraction of the bound species must be subtracted from their total concentrations for data analysis. But in this particular scenario, this constraint is not of a major concern since the K_m for HDAC8 is about 600 μM, and as long as the substrate concentration is maintained at 150 μM or higher, the total concentration of the substrate could be taken as the measure of the free concentration. In case of tight binding inhibitors, the free concentrations must be calculated from the total concentration by complete solution of the quadratic equation describing the

enzyme-inhibitor interaction. Equation 4.2 below is a classic steady-state equation for following the competitive inhibition of the enzymes:

$$v = V_{max}/1 + K_m/[S](1 + [I]_f/K_i) \qquad \text{Eq: 4.2}$$

where v is the initial velocity and V_{max} is the maximal velocity of the enzyme catalyzed reaction, $[I]_f$ is the free concentration of the inhibitor which in this case will be the total concentration as the inhibitor concentration will be much higher than the enzyme, [S] is the concentration of *Fluor de lys*®, K_m is the amount of *Fluor de lys*® required to half saturate HDAC8 enzymes and K_i is the inhibition constant to be determined. The eq. 4.2 can be further simplified to a form of eq. 4.3, if in the reaction the substrate concentration can be maintained considerably lower than the K_m. This simplifies Eq: 4.2 as follows

$$v = V_{max} * [S]/K_m/(1 + [I]_f/K_i) \qquad \text{Eq: 4.3}$$

In the absence of any inhibitor, the numerator of Eq. 4.3 can be taken as the measure of initial velocity (V_o) of the enzyme catalyzed reaction. Also, $[I_f]$, can be represented in the form of total concentration of the enzyme and inhibitor by a complete solution of the quadratic equation describing their interaction. Therefore, with these solutions the data was analyzed with the final form of the competitive steady-state model which is given as follows, using the GRAFIT software (ver.4)

$$v = \frac{v_o * K_i}{K_i + ([I]_t - 0.5(([I]_t + [E]_t + K_i - \sqrt{([I]_t + [E]_t + K_i)^2 - 4 * [I]_t * [E]_t)})} \qquad \text{Eq: 4.4}$$

4.2.3.2. Determination of the Inhibition Constant (K_i) of SAHA and Coumarin-SAHA for Wild Type and Mutant HDAC8 Enzymes

SAHA (Suberoyl Anilide Hydroxamic Acid) is a known competitive inhibitor of different HDAC isozymes including HDAC8, and the structural data reveals that it binds to the active site pocket of the enzyme. Recently, a fluorescent analogue of SAHA (namely coumarin-SAHA, c-SAHA) has been synthesized to serve as the reporter group for determining the binding affinity of several HDAC8 inhibitors. To probe whether mutations in the exit tunnel of HDAC8 influenced the binding affinities of SAHA and c-SAHA, steady-state kinetic experiments were performed to determine their K_i values. This was accomplished using the *Fluor de lys*® assay system as described previously. The stock solutions of SAHA and c-SAHA were prepared in the HDAC8 standard assay buffer, and the reactions were set up for wt-HDAC8, Y18A-HDAC8, Y20A-HDAC8 and H42A-HDAC8 in a polystyrene microplate. Each assay well contained 150 μM *Fluor de lys*® substrate, varying concentrations of SAHA or c-SAHA (0-10 μM), 250 nM trypsin and 250 nM wild-type or mutant HDAC8 (except in case of Y18A-HDAC8, which was used at 1 μM) enzyme in a total volume of 0.2 ml. Reactions were initiated by the addition of the HDAC8 enzyme and the time course of increase in fluorescence as a function of time was monitored. The initial rates of HDAC8 reactions were obtained by the slope of the linear portion of the reaction progress curve after the initial lag-phase time. The rate of enzyme catalysis was determined as described previously in section 4.2.4, and was plotted as a function of the inhibitor concentration. To reliably measure the enzyme activity, relatively high concentrations of the HDAC8 enzymes were used, and the data were analyzed by Eq 4.4.

4.2.4. Determination of the Activation Constant of an Activator (TM-2-51) for the HDAC8 Mutants- Y18A, Y20A and H42A

The activation constants (K_a) for TM-2-51of wild type and the mutant HDAC8 were ascertained using the *Fluor de lys*® assay system (as described) via the Molecular Devices Spectra Max plus micro plate reader, using varying concentrations of TM-2-51 in the HDAC8 standard assay buffer. The activator's stock was prepared in 100% DMSO. Working solutions for the substrate and the HDAC8 enzymes were prepared in 50 mM Tris-HCl, pH 8.0, 137 mM NaCl, 2.7 mM KCl, 1 mM $MgCl_2$ and 1 mg/ml BSA (HDAC8 standard assay buffer). Reactions were set up for wt-HDAC8, Y18A-HDAC8, Y20A-HDAC8 and H42A-HDAC8 in a polystyrene microplate where each assay well contained 150 µM *Fluor de lys*® substrate, varying concentrations of TM-2-51 (0-50 µM), 250 nM trypsin and 250 nM wild-type or mutant HDAC8 enzyme in a total volume of 0.2 ml. The enzyme catalyzed reactions were initiated by the addition of the specific HDAC8 enzymes and the initial rates were plotted as a function of TM-2-51 concentration. The reactions were monitored at 500 nm for 3 hours at room temperature in the microplate reader and the reaction progress curves were analyzed utilizing the Hill equation (Eq 4.5):

$$v = V_{max} * x^n / (k^n + x^n) + \text{offset} \qquad \text{Eq: 4.5}$$

where v is the rate of reaction, V_{max} is the maximum velocity of the reaction, x is the activator concentration, k is the activation constant (K_a) and n is the Hill coefficient.

4.2.5. Determination of the equilibrium Dissociation Constants (K_d) of SAHA, c-SAHA and TM-2-51 (Activator) for the Wild type and Mutant HDAC8 Enzymes

To determine the K_d of SAHA for the wild-type and mutant HDAC8 enzymes, a fixed concentration of the HDAC8 enzyme (1 μM, 250 μl volume) was titrated against increasing concentrations of the inhibitor SAHA (1-10 μM) in a square-bottomed 4 mm path length quartz cuvette. The excitation and emission wavelengths were maintained at 280 nm and 340 nm, respectively, to monitor the change in the intrinsic fluorescence (mainly contributed by tryptophan and tyrosine residues) of HDAC8. For all experiments, the excitation and emission slits were maintained at 12 mm and 10 mm, respectively, and the PMT voltage was set at 800. All the stock and working solutions were made in 10 mM Tris-HCl, pH 7.5, 3 mM $MgCl_2$, 100 mM NaCl, 10% glycerol and 1mM TCEP. The decrease in fluorescence intensity of the wild type and the mutant HDAC8 enzymes was measured at 340nm and the observed fluorescence intensity after correcting for the dilution effect, was plotted as a function of the inhibitor concentrations. The dissociation constants of the enzyme-inhibitor complexes were determined by analyzing the data via the classical binding model (given by a complete solution of the underlying quadratic equation) using GRAFIT (ver.4.0)

$$\Delta F = (C * (L_{tot} + K_d + n * E_{tot} - \sqrt{\{(E_{tot} * n + L_{tot} + K_d)^2 - 4 * n * [E_{tot}] * [L_{tot}]\}} / 2 \quad \text{Eq: 4.6}$$

Here, ΔF is the change in the protein fluorescence upon binding to SAHA or c-SAHA, E_{tot}, and L_{tot} refer to the total enzyme and total ligand concentration, respectively. K_d is the dissociation constant of the enzyme-ligand complex and n is the stoichiometry of the enzyme-ligand complex. C is amplitude of signal changes at saturation concentration of the ligand, and it is normalized with respect to signal changes between 0 and 1. In the case of Coumarin-SAHA (c-

SAHA), the experiment for determination of the dissociation constant was performed in a similar fashion but by exciting the ligand (0.5 μM, 250 μl volume) at 325 nm, and monitoring the fluorescence emission at 397nm. All the settings were kept the same as mentioned above for the SAHA analysis. The change in the fluorescence emission intensity of c-SAHA at 397 nm (after correcting for the dilution effect) was plotted as a function of the increasing enzyme concentration and the dissociation constant was determined by analyzing the data with eq. 4.6 with the help of GRAFIT (ver.4.0).

In the case of activator TM-2-51, the dissociation constant was determined by exciting a fixed concentration (1 μM, 250 μl volume) of the HDAC8 mutants (Y18A, Y20A and H42A) at 280 nm and measuring the fluorescence emission intensity of the protein at 340 nm. All the settings were kept the same as mentioned above. The change in the fluorescence emission intensity of the protein at 340 nm (after correcting for the dilution effect) was plotted as a function of increasing activator concentration and the dissociation constant was determined by analyzing the data with eq. 4.2 with the help of GRAFIT (ver.4.0).

4.3. Fluorescence Lifetime Measurements

Fluorescence lifetime measurements were performed on a custom design Photon Technology International (PTI) Fluorescence-Lifetime instrument. The excitation sources for measuring the time resolved fluorescence decay were the Light Emitting Diodes (LEDs) with maximum power outputs at 280 nm and 340 nm, respectively. The 340 nm LED was utilized to excite c-SAHA while the 280 nm LED was used to excite the intrinsic fluorescence of the protein (contributed primarily by the tyrosine and tryptophan residues). The emitted light was detected (at a right angle to the excitation source) by means of a stroboscopic emission

monochromator configured at appropriate wavelengths (340 nm for protein fluorescence and 400 nm for c-SAHA fluorescence). Diluted starch suspensions (prepared in de-ionized water) were used to collect the instrument response function (IRF). The data were collected in 200 channels and the integration time was set as 1 second. Depending on the signal obtained, 20-30 averages were acquired for the samples to obtain a better resolution of the fluorescence traces. For all experiments, a 250 µl sample volume prepared in HDAC8 storage buffer was used in a 1 cm path length cuvette and contained 4 µM HDAC8 or 500 nM c-SAHA.

The time resolved fluorescence decay curves were analyzed using PTI's software, Felix 32 to calculate the lifetimes of the fluorophores under different conditions. The kinetic traces obtained were fitted by the following single and double exponential rate equations (Eq 4.7)

$$I(t) = \sum_{i=1}^{n} \alpha_i \exp(-t/\tau_i) \qquad \text{Eq: 4.7}$$

where α_i and τ_i are amplitude and fluorescence lifetime for the i^{th} component, respectively. The following relationship (Eq. 4.8) was used to calculate the relative contribution (f_i) of the i^{th} component.

$$f_i = (\alpha_i \tau_i / \sum_{i=1}^{n} \alpha_i \tau_i) * 100\% \qquad \text{Eq: 4.8}$$

The goodness of the exponential fit of the fluorescence curves was determined by the reduced chi-square, the Durbin-Watson, and Z values.

4.4. Isothermal Titration Calorimetry (ITC)

ITC is a highly sensitive thermodynamic technique that directly measures the heat released or absorbed during a bio-molecular binding reaction. This heat measurement allows for the accurate determination of the association or the binding constants (K_a), stoichiometry (n),

enthalpy (ΔH) and entropy (ΔS) (159). ITC can also be instrumental in determining the mechanism of molecular interaction. Various interactions like protein-small molecule, protein-protein, target-drug, enzyme-inhibitor, antibody-antigen, protein-DNA, protein-lipid and small molecule-small molecule can be studied extensively utilizing this technique. The thermodynamic parameters of the binding of SAHA to wild-type and mutant HDAC8 enzymes were analyzed by ITC using a VP-ITC isothermal titration calorimeter. Given the exquisite sensitivity of these experiments, single buffer diluents were used for both the enzyme and the ligand, to minimize errors. For this, a 20 mM stock solution of SAHA in 100% DMSO was used to prepare a working concentration of 200 μM SAHA (containing 1% DMSO) in a 0.2 micron filtered buffer containing 10 mM Tris-HCl, pH 7.5, 3 mM $MgCl_2$, 100 mM NaCl, 10% glycerol and 1mM TCEP. A 10 μM HDAC8 solution also containing 1% DMSO was prepared in the same buffer. Both the solutions were thoroughly degassed for 15-20 min in a Thermo vacuum. The enzyme was loaded into a pre-washed and pre-equilibrated sample cell (1.8 ml) and the ligand into a pre-washed and pre-equilibrated syringe (300 μl). Injections were made in 45 X 4μl increments with the constant rotation of the syringe at 310 RPM throughout the experiment for a thorough mixing of both the solutions. Before the titration, the reference cell was washed and loaded with a freshly prepared and filtered 0.03% sodium azide solution to eliminate any contaminants. The detailed instrumentation, experimental design and analysis for these experiments is described in a comprehensive review by Wiseman at al (159).

As the HDAC8 is titrated with the ligand, heat is either released or absorbed due to the formation of the enzyme-ligand complex. A thermoelectric device present in the ITC measures the difference in the temperature between the sample and the reference cells. This difference is

compensated by the heating or cooling of the sample cell, thereby maintaining a constant temperature difference between the two cells. The heat released or absorbed upon titration of the ligand is directly proportional to binding and as the reaction progresses a decrease in the heat signal is observed for exothermic reactions. Towards the end of the reaction, the heat produced is due to the heat of dilution and is considered as background signal. The raw calorimetric data is thus presented as the amount of heat produced per second (following the subtraction of the background signal) upon injection of the ligand. These heat signals are automatically integrated by the analysis software to calculate the amount of heat produced per injection. Thereafter, these calculated heat values are plotted as a function of ligand concentration and analyzed by a single binding-site model, inbuilt in the Origin 7.0 software. The average of heat produced per injection for the last 5 injections was taken as the heat of dilution and subtracted as background from all 45 injections. The final data represents the background corrected amount of molar heat produced per injection as a function of molar ratio of ligand to the HDAC8 enzyme.

For data analysis, all the parameters to be calculated (n, K_a and $\Delta H°_{obs}$) were allowed to vary and the standard errors were derived following the best fit of the experimental data. These experiments were performed so as to compare the difference in the heat signal upon binding of SAHA to the mutant HDAC8 enzymes versus the wt-HDAC8.

4.5. Circular Dichroism of the Wild Type and Mutant HDAC8 Enzymes

Circular dichroism (CD) is one of the best techniques available for the rapid determination of the secondary structure, folding and binding properties of proteins. Circular dichroic (CD) spectra of the wild type and mutant HDAC8 enzymes were measured on a J-815 spectropolarimeters (Tokyo, Japan) using a 1 mm path length quartz cuvette and nitrogen flow

rate of 40 ft^3 $hour^{-1}$. A total volume of 150 µL containing 8 µM HDAC8 enzyme (either wild type or mutant) prepared in a buffer containing 5 mM Tris-HCl (pH 8.0), 0.5 % glycerol, 0.1 mM DTT and 15 mM KCl was used. This buffer composition was important to minimize the background CD signal and the spectrum of the buffer was subtracted from the spectra of protein. An average of 5 scans taken at room temperature, were collected for each sample and the data was smoothed by the Fast Fourier Transform (FFT) utility of the Jasco analysis software.

4.5.1. Thermal Denaturation of the Wild Type and Mutant HDAC8 Enzymes

To determine the effect of exit tunnel mutations on the overall thermal stability of the wild type and mutant HDAC8 enzymes, the equilibrium unfolding of the HDAC8 enzymes induced by rising temperatures was measured by CD spectroscopy. For these studies, a temperature range of 12–60°C was used except in case of Y18A, where the temperature ranged till 95°C. The unfolding was monitored in terms of changes in the ellipticity of HDAC8 enzymes at 222 nm. For this, a total volume of 150 µL containing 8 µM HDAC8 enzyme (either wild type or mutant) prepared in a buffer containing 5 mM Tris-HCl (pH 8.0), 0.5 % glycerol, 0.1 mM DTT and 15 mM KCl was used. The experiment was performed on a J-815 spectropolarimeter equipped with a Peltier temperature control, in a 1 mm path-length cuvette with a nitrogen flow rate of 40 ft^3 $hour^{-1}$. The cuvette containing the enzyme was placed in the cuvette holder which was pre-equilibrated at the initial temperature of 12^0C. The experiment was started after an initial delay period of 25 seconds. During the course of the experiment, the temperature was increased in increments of 1°C min^{-1}. The changes in the ellipticity of the HDAC8 enzymes were monitored and plotted as a function of the temperature.

The minimal model for the unfolding of the HDAC8 enzyme was an equilibrium two-state transition between native and denatured forms of the enzyme:

$$\text{Native} \underset{}{\overset{K}{\rightleftharpoons}} \text{Denatured}$$

Scheme 4.2. Equilibrium two-state transition between native and denatured forms of the enzyme.

According to this model, no stable intermediates are present between the native and the denatured states at equilibrium and each state exhibits distinct experimental signals. This two-state transition can be described by the Santoro and Bolen equation (160) (Eq: 4.9):

$$y = \frac{(y_N + m_N T + (y_D + m_D T)\ \exp[\Delta H_{vh}/R(1/T_m - 1/T)\ ]}{1 + \exp[\frac{\Delta H_{vh}}{R\left(\frac{1}{T_m} - \frac{1}{T}\right)}]} \qquad \text{Eq: 4.9}$$

where y is the observed signal, y_N and y_D are the native and the denatured baseline intercepts, m_N and m_D are the native and the denatured baseline slopes, T is the temperature, ΔH_{vh} is the van't Hoff enthalpy, R is the gas constant and T_m is the temperature of the transition mid-point. This two-state transition was observed with all the HDAC8 enzymes under consideration, except Y18A-HDAC8, where predominance of a stable intermediate was witnessed between the native and the denatured states. The thermal denaturation data for Y18A-HDAC8 was analyzed using the Boltzmann 2 equation as follows:

$$y = A2 + (A1 - A2)/(1 + \exp\left(\frac{x - x_0}{dx}\right)) \qquad \text{Eq: 4.10}$$

where A1 and A2 are the amplitudes of the first and second denatured states, respectively, x and x_o refer to the melting temperatures of the first and second phase, respectively.

4.5.2. Kinetic Studies for the Unfolding of Wild Type and Mutant HDAC8 Enzymes

To determine the kinetic profile for unfolding of the wild type and mutant HDAC8 enzymes as a function of temperature (ranging from 35-55°C except for Y18A-HDAC8, which ranged from 35-90°C), the time-dependent changes in the secondary structure were measured on a Jasco J-815 CD instrument with the temperatures maintained by the Peltier temperature controller. The quartz cuvette (1 mm path-length), containing 8 μM HDAC8 enzyme prepared in a buffer containing 5 mM Tris-HCl (pH 8.0), 0.5 % glycerol, 0.1 mM DTT and 15 mM KCl, in a total volume of 150 μL, was placed in the cuvette holder and the temperature was allowed to stabilize (~25 seconds). The time-dependent ellipticity at 222 nm (θ_{222}) at a fixed temperature was monitored for up to 1 hour and the data was analyzed by either the double-exponential rate equation (Eq. 4.11) or the single-exponential rate equation (Eq 4.12):

$$Signal = 1 - (A_1 * e^{-k_1 * t} + A_2 * e^{-k_2 * t}) + \text{offset} \qquad \text{Eq. 4.11}$$

$$Signal = A * (1 - e^{-k_{obs} * t}) + \text{offset} \qquad \text{Eq. 4.12}$$

where the experimental signal is θ_{222}, A is the amplitude of the signal and k_{obs} is the observed single exponential rate constant. For the double exponential rate equation, A1 and A2 are the amplitudes of the first and the second phase respectively, k_1 and k_2 are the observed rate constants of the first and the second phase, respectively.

Following this, Arrhenius plots were generated by plotting the natural log of k_{obs} as a function of 1/T and data was fitted by a linear form of the Arrhenius equation as follows:

$$\ln(k_{obs}) = \ln(A) - \Delta E / RT \qquad \text{Eq: 4.13}$$

where *A* is the Arrhenius pre-exponential factor, ΔE is the observed activation energy (kcal/mol), R is the gas constant and T is the temperature in Kelvin. The following relationship was used for the conversion of ΔE into the observed transition state enthalpy ($\Delta H^{\ddagger}_{obs}$):

$$\Delta H^{\ddagger}_{obs} = \Delta E + RT \qquad \text{Eq: 4.14}$$

With the exception of Y20A-HDAC8, for all other HDAC8 enzymes, only the first phase rate constants were used for the Arrhenius plot as the second rate constants remained largely unchanged. The Y20A-HDAC8, on the other hand, displayed a single exponential fit.

4.5.3. Temperature Dependent Changes in the Activity of the Wild type and Mutant HDAC8 Enzymes

Aliquots of 10 µM HDAC8 enzyme in eppendorf tubes were subjected to temperatures ranging from 35-95°C for 25 seconds in a water bath. Following the thermal denaturation, the enzyme aliquots were quickly placed on ice and an HDAC8 activity assay was set up in a microplate as described in section 4.2.1. Each well contained 500 µM *Fluor de lys*® substrate, 1 µM HDAC8 enzyme and 250 nM trypsin in a total volume of 0.2 ml in the HDAC8 standard assay buffer. Each well of the microplate corresponded to a different temperature to which that specific HDAC8 aliquot had been exposed. The progress of the HDAC8 reaction was plotted as a function of temperature using the Origin 8.5 software.

4.5.4. Time Dependent Change in the Activity of the Wild Type and Mutant HDAC8 Enzymes

To perform this, 50 µl aliquots of 10 µM HDAC8 enzyme were prepared and were subjected for different time intervals to a temperature of 35°C in a water-bath. A stop watch was used. Following the temperature treatment, each enzyme aliquot was immediately placed on ice.

Upon completion of the above process, the HDAC8 enzyme activity assay was set up in a similar fashion as described before in the section 4.2.1.

The experiment was set up in a microplate where each well corresponded to a different time interval for one specific HDAC8 enzyme. The assay conditions in each well included, 500 µM *Fluor de lys*® substrate, 250 nM trypsin, 1 µM HDAC8 enzyme in the HDAC8 standard assay buffer in a total volume of 0.2 ml. Following the completion of the assay, the percent residual activity of the HDAC8 enzyme was plotted as a function of time utilizing the Origin 8.5 data analysis software.

CHAPTER 5. RESULTS

5.1. Cloning of Histone Deacetylase 8 (HDAC8) Mutants

HDAC8 is a 377 residue protein and is expressed in multiple organs including heart, lung, kidney and pancreas. Using human kidney as a source, Hu et al.,(1999) were the first to clone HDAC8 and purify it as an active recombinant enzyme following expression in *Escherichia coli* (13). Active HDAC8 was cloned in Srivastava's lab using a pLIC-His-plasmid according to the procedure and protocol developed and detailed by Cabrita et al.,(161). The vector encodes for a hexa-His peptide (His-tag) followed by a TEV (Tobacco Etch Virus) protease recognition site and an LIC (Ligation-independent cloning) site. The aforementioned His-tag served as a purification tag for Immobilized Metal Affinity Chromatography. Based on a review of the background literature, a comprehensive analysis of the HDAC8 sequence and available structural data led to the identification of the conserved amino acid residues in HDAC8 to elucidate their functional properties. These residues were targeted for mutagenesis to evaluate the structure-functional features of HDAC8. The residues E65, E66 and H71 (Figures 1.10 and 5.1 (a)) are conserved among class I and class II HDACs and were targeted for mutation to determine their importance in the functionality of the protein. Further, Y100 was mutated primarily to understand its role in the inhibitor binding to HDAC8. Three additional residues, Y18, Y20 and H42, were mutated based upon their conservation amongst class I HDACs (Figure 5.1 (a)) and also their presumed role in the release of reaction product, acetate, from the enzyme pocket following catalysis (70,90). Figure 5.1(b) shows the localization of these residues on the HDAC8 structure. Crystal structure superimpositions of HDAC2 with HDAC8 and HDAC4 with HDAC8 are shown in Figures 5.2 and 5.3 to highlight the conservation of the amino acid

residues in the tertiary structure. The localization of the residues: E65, E66, Y100 and H71 on the HDAC8 crystal structure have been represented in Figure 5.1 (b).

The residues mentioned above were mutated using a site-directed mutagenesis kit from Stratagene (La Jolla, CA, USA). Mutagenesis reactions were set up in thin-walled PCR tubes. Each reaction constituted of reaction buffer, 50 ng of the wild type HDAC8 plasmid, 125 ng of each forward and backward primer, 1 µl of dNTP mix and nuclease free water to make up the final volume to 50 µl. Finally, 1 µl of *PfuTurbo* DNA polymerase was added to each reaction mix. Polymerase chain reaction was performed as per the procedure described in the Methods section. In order to test the presence of the mutated HDAC8 genes, the PCR product was loaded on to an agarose gel and the DNA was separated by electrophoresis (Figure 5.5).The size of the PCR product was nearly 7 kb which corresponds to the size of wild type HDAC8 plasmid size. The presence of specific mutations E65Q, E66Q, E6566Q, H71A, Y100A, Y100V, Y18A, Y20A and H42A (Figure 5.5) was confirmed by pyro-sequencing at MC LAB (California). The PCR product was then transformed into DH5α cells to amplify the mutated HDAC8 plasmids. Of the above mutations, Y18A, Y20A and H42A mutations were of special interest since these residues gate the exit tunnel. Therefore, these mutants were selected for detailed biophysical studies to unravel their roles in the catalytic mechanism of HDAC8.

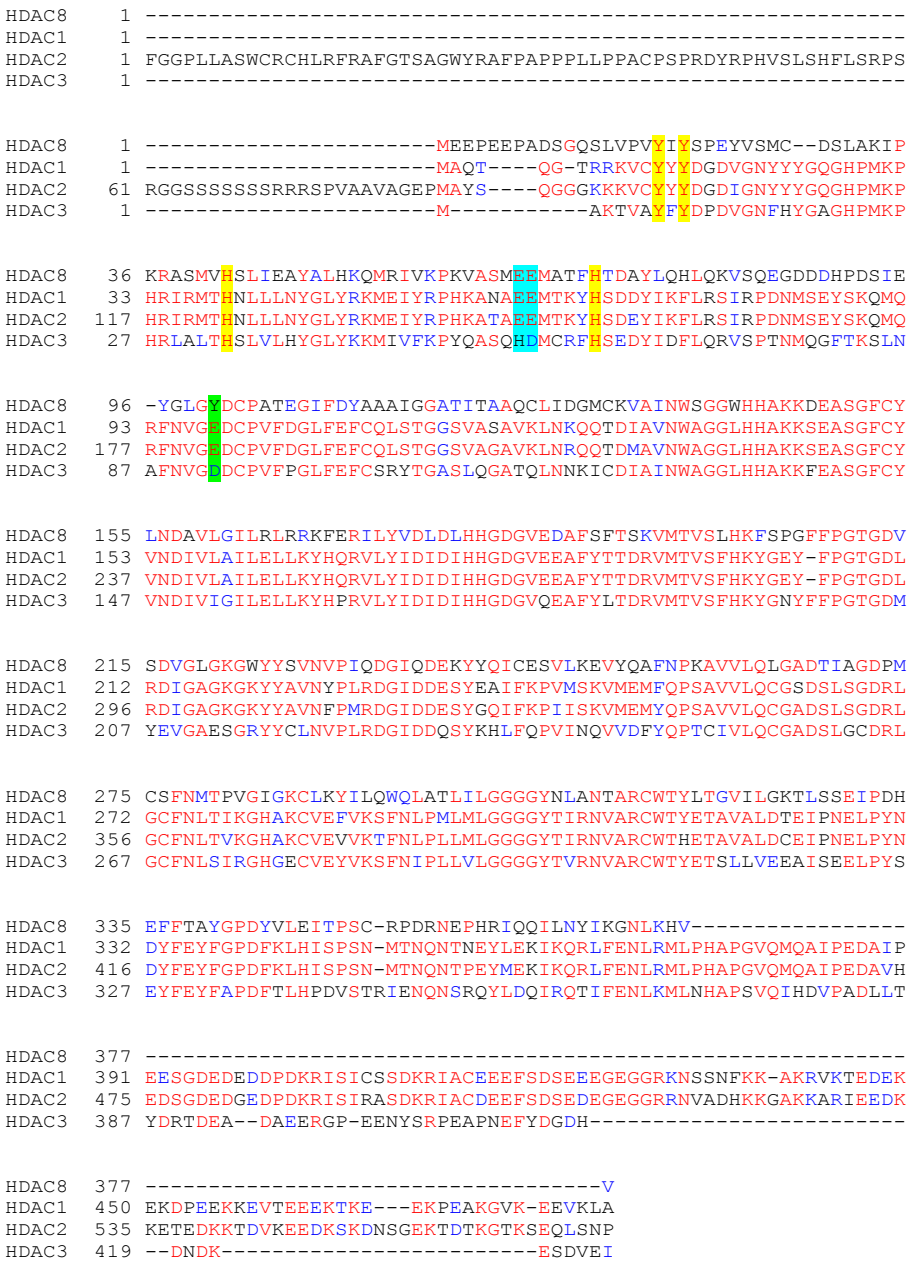

Figure 5.1a. Sequence alignment of class I HDACs showing conservation of the amino acid residues selected for mutations.
The exit tunnel residues- Y18, Y20 and H42 (highlighted in yellow) are conserved among Class I HDACs.E65, E66 (Blue highlight) and H71 (Yellow highlight to the right of E66) are also highly conserved among class I as well as Class II HDACs (Figure 1.10 and 5.3). Y100 in HDAC8 (green highlight) is not conserved but it is interesting to note that in other Class I HDACs it is a negatively charged residue (E in HDAC1 and HDAC2; D in HDAC3). Therefore, this residue was mutated to study its importance in the structure-functional aspect of HDAC8. This figure was generated using TCOFFEE online sequence alignment tool.

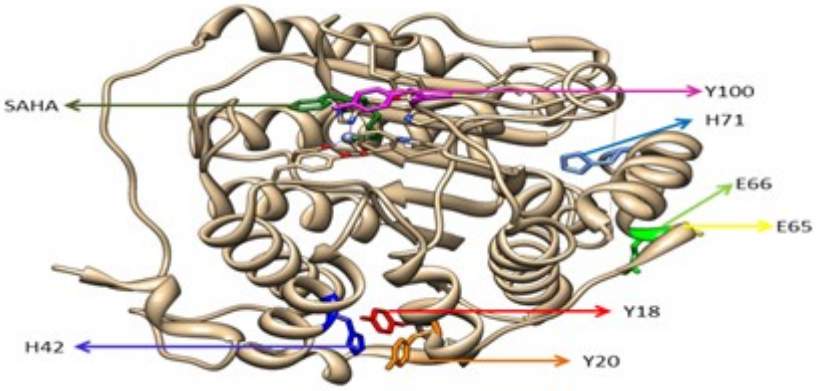

Figure 5.1b. A ribbon diagram of HDAC8 displaying the location of the highly conserved residues E65, E66, H71 amongst class I & II HDACs and exit tunnel residues Y18, Y20 and H42 targeted for mutagenesis.
The HDAC8 active site pocket is marked by bound ligand SAHA (forest green). The residue Y100 (magenta) present in the vicinity of the HDAC8 active site pocket was mutated to understand its role in the substrate binding to HDAC8. The figure (PDB ID. 1T69) was generated using the UCSF-Chimera® software**.**

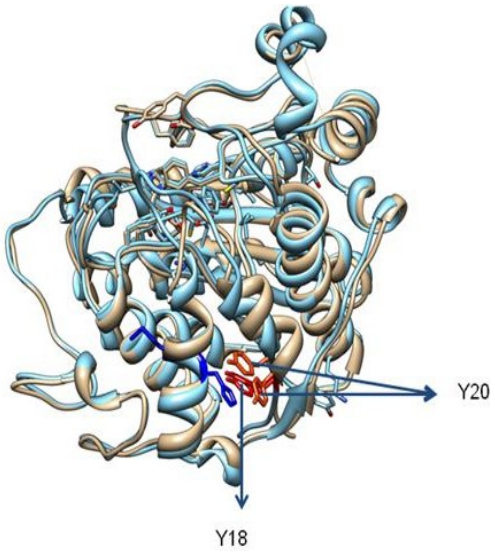

Figure 5.2. A ribbon diagram showing the superimposition of the class I HDACs: HDAC2 (PDB ID. 3MAX; Blue ribbon) and HDAC8 (PDB ID. 1T69; Light brown ribbon).
This figure shows that Y18 and Y20 are not only conserved in the primary sequence but also are conserved in terms of their 3-D localization amongst the class I HDACs. The figure was generated using the UCSF-Chimera® software.

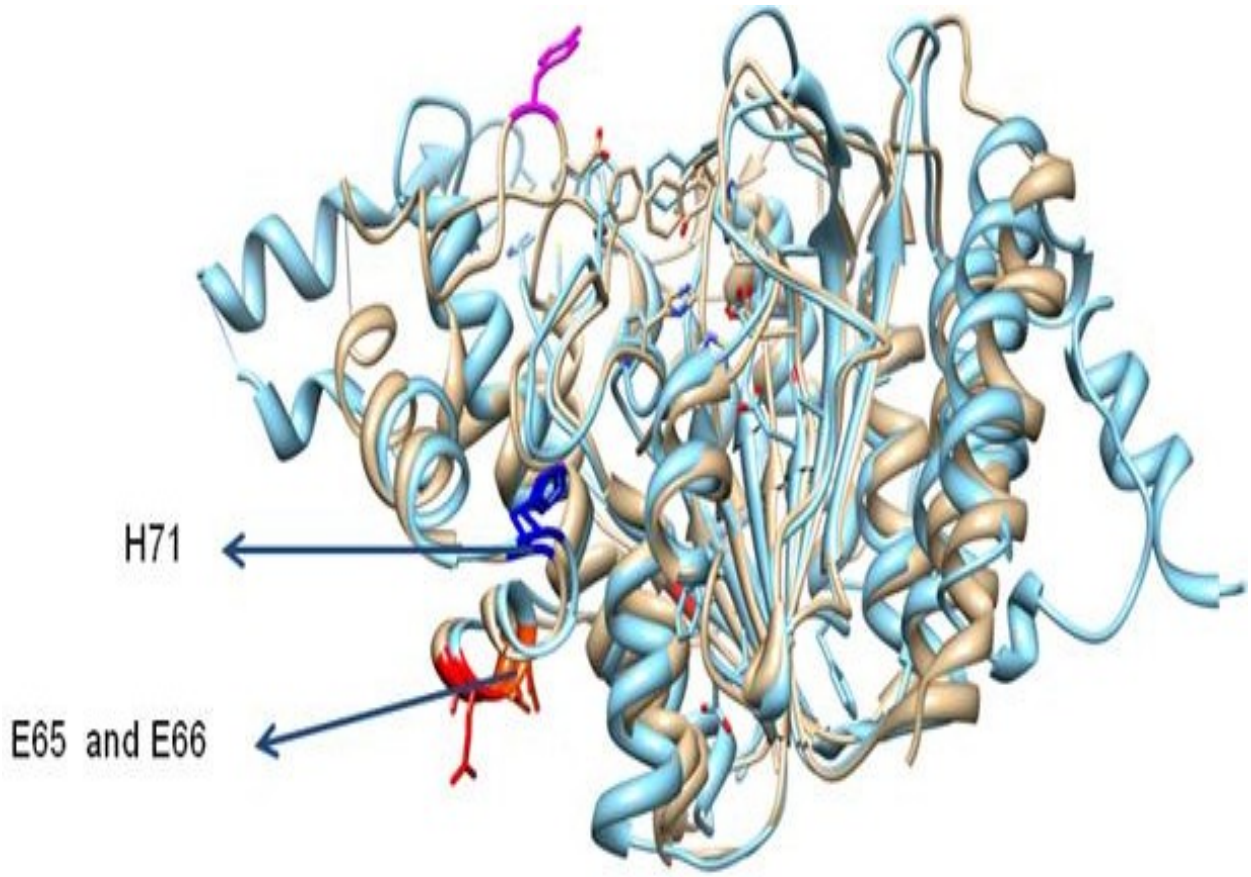

Figure 5.3. A ribbon diagram showing the superimposition of the class I & II HDACs :HDAC8 (PDB ID. 1T69; Light brown ribbon) and HDAC4 (PDB ID. 2VQM; Blue ribbon).
This figure shows that E65, E66 and H71 residues are conserved in the primary sequence as well as in the 3-D structure amongst Class I & II HDACs. This made them potential candidates for the mutation analysis. The figure was generated using the UCSF-Chimera® software.

Figure 5.4. Sequence alignment of class I and II HDACs showing an overall sequence identity and conservation.
In this alignment, Y18 and Y20 (yellow highlight) do not show sequence conservation amongst class II HDACs which is in contrast to Class I HDACs. E65 and E66 (blue highlight), on the other hand are mostly conserved except in HDAC3. E65 in HDAC3 is Histidine which may be an indicative of its specialized function. E66 is conservatively substituted with aspartate in HDAC3. The residue Y100 (gray highlight) is unique to HDAC8 and may contribute to its substrate specificity. Overall, the residues colored in red are highly conserved among both the classes while blue colored residues are conservatively substituted. The overall sequence identity among all the six sequences was calculated to be 39 %.

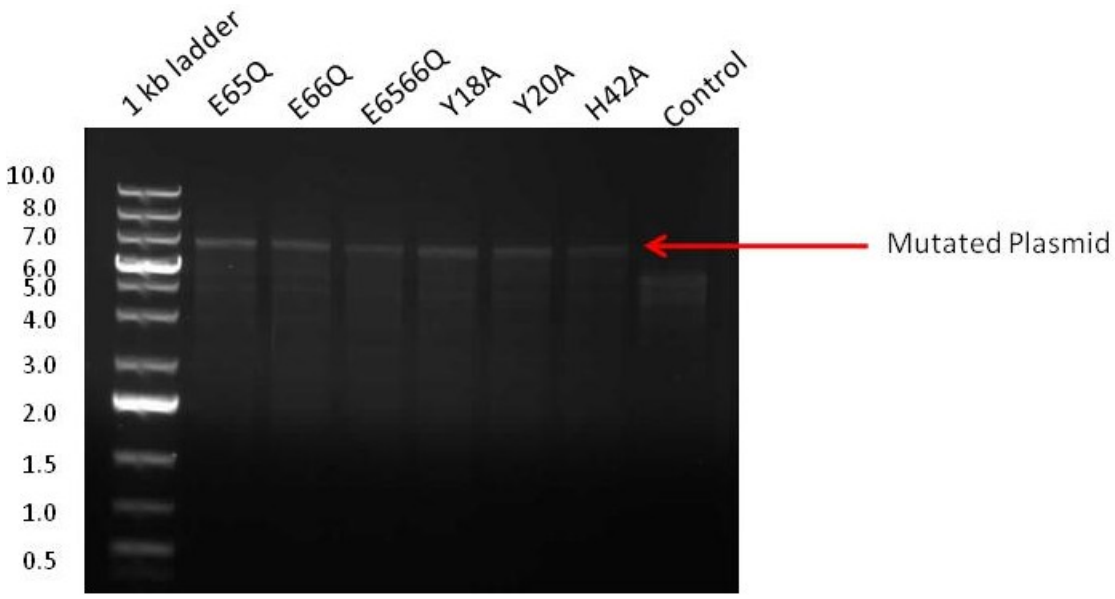

Figure 5.5. Agarose gel electrophoresis of DNA from the intermediate PCR step for site-directed mutagenesis.
A 20% aliquot of the PCR resolved on 1% agarose gel is shown. The conspicuous band (arrow) in each lane corresponds to the expected amplification product containing the desired HDAC8 mutation as confirmed by DNA sequencing. The control lane did not show such a band.

5.2. Expression and Purification of Y18A-HDAC8, Y20A-HDAC8 and H42A-HDAC8 Recombinant Proteins

The mutant HDAC8 plasmids were transformed into DH-5α cells for amplification of the plasmid. Following this, plasmid DNAs encoding mutant HDAC8 enzymes were isolated using a Qiagen miniprep kit. Following verification of the mutation by DNA sequencing, the plasmids encoding the respective mutations were transformed into BL21-DE3 cells, an optimized *E.coli* host strain for protein expression. The procedure for transformation and growth of the bacterial cultures has been detailed in section 4.1.1. The mutant HDAC8 proteins were over-expressed by induction of the *lac* promoter with IPTG (a lactose analogue). Following induction, the bacterial cultures were grown further in a temperature-controlled incubator-shaker at 18°C with constant

shaking at 200 RPM for 16-18 hours. Cells were harvested by centrifugation and the harvested cells were lysed by suspension in the 100 ml of lysis buffer (50 mM Tris-HCl pH 8.0, 3 mM $MgCl_2$, 150 mM KCl, 5% glycerol ,1mM β-mercaptoethanol, 0.25 % Triton-X-100) followed by sonication. The bacterial lysate was clarified by centrifugation to remove the debris since the expressed HDAC8 mutants were expected to be present in the soluble fraction of the cell extract. Next, the crude bacterial extract supernatant containing 10 mM imidazole in the purification buffer (50 mM Tris-HCl pH 8.0, 3mM $MgCl_2$, 150mM KCl, 5% glycerol and 1mM β-mercaptoethanol) was filtered using a 0.2 μm filter and loaded on to a pre-equilibrated 1 ml Ni^{2+}-IDA column (a HisTrap column made up of highly cross-linked agarose containing Iminodiacetic acid (IDA) as a chelating group) connected to an AKTApurifier UPC10 (GE Healthcare lifesciences) for purification of the recombinant proteins. Addition of 10 mM imidazole to the crude extract helps prevent the non-specific binding of the contaminant proteins. The recombinant proteins were retained selectively in the column due to their 6-Histidine tag (particularly the imidazole ring) binding to the Ni^{2+}- beads while the other proteins failed to bind the column and flowed through. The column was washed with 15 column volumes (15 ml) of wash buffer (4-6 % of buffer B containing 500 mM imidazole i.e. 20-30 mM of imidazole in the purification buffer) to elute any non-specifically bound proteins from the HisTrap column. In the case of Y20A-HDAC8 and H42A-HDAC8 mutants, the wash buffer contained 30 mM imidazole (6% of Buffer B) while in the case of Y18A-HDAC8 mutant imidazole concentration in the wash buffer was reduced to 20 mM (4 % of buffer B) based upon a test wash profile. Finally, the bound proteins were eluted with a linear gradient of increasing imidazole concentration (20-150 mM imidazole) over a range of 50 ml (50 column volume) elution volume. The eluted protein

was collected in 2 ml fractions and the peak fractions with maximal absorbance at 280 nm were analyzed by SDS-PAGE to determine purity. After determination of the purity, specific fractions were pooled together and dialyzed against the dialysis buffer (section 4.1.2.). Figures 5.7, 5.9 and 5.11 show the elution profiles of Y18A-HDAC8, Y20A-HDAC8 and H42A-HDAC8 mutant proteins, respectively, generated by plotting the absorbance of the eluted protein at 280 nm across different fractions of the eluate. The peak fractions for Y18A-HDAC8 (6-14) (Figure 5.8), Y20A-HDAC8 (6-13) (Figure 5.10) and H42A-HDAC8 (7-14) (Figure 5.12) were analyzed by SDS-PAGE to determine their homogeneity and were found to be substantially pure. The molecular weight of the mutant HDAC8 recombinant proteins was expected to be identical to that of the wild-type HDAC8 since each mutant protein contained only a single amino acid substitution from the wild-type HDAC8 sequence. This was indeed the case as all three HDAC8 mutants exhibited a single 42 kD band on SDS-PAGE, corresponding to the reported molecular weight for wild-type HDAC8 (70,83). The peak fractions containing pure protein were pooled and dialyzed against the dialysis buffer. The purified recombinant proteins were stored in 1 ml aliquots at -80°C. The protein concentration was determined by Bradford assay using BSA as a standard (Figure 5.6) (158). The total yield for each recombinant protein was as follows: Y18A-HDAC8, 0.4 mg/L of bacterial culture: Y20A-HDAC8, 1.1 mg/L of bacterial culture: H42A-HDAC8, 0.6 mg/L of bacterial culture.

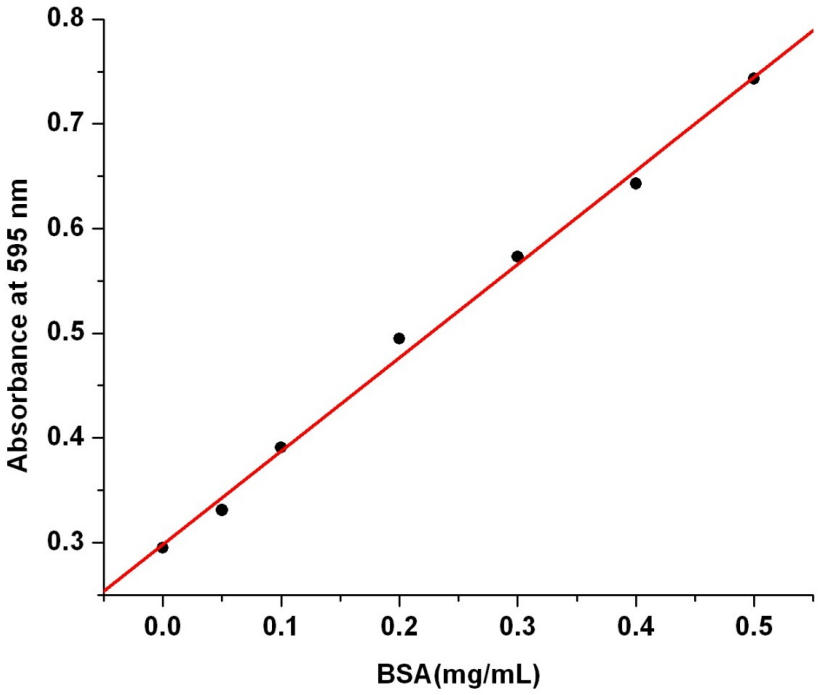

Figure 5.6. Standard plot of absorbance from serial dilutions of bovine serum albumin (BSA) used to determine the enzyme concentration.
A stock solution of 2 mg/ml BSA was prepared using de-ionized water. This stock was serially diluted to concentrations of 0.05 mg/ml, 0.1 mg/ml, 0.2 mg/ml, 0.3 mg/ml, 0.4 mg/ml and 0.5 mg/ml. A microplate was set up to perform the Bradford Assay with 200 µl of Bradford reagent (diluted 1:5 in de-ionized water) per well and 10 µl of each concentration of BSA. Unknown samples were processed in an analogous manner with 10 µl of the unknown sample per well mixed with 200 µl Bradford reagent. The plate was incubated at room temperature and the absorbance was measured at 595 nm. Absorbance (A_{595}) values were plotted as a function of known concentration of BSA and fitted by the linear equation. This equation was used to calculate the enzyme concentration in unknown samples and the total yield of each recombinant protein**.**

Table 5.1. Composition of the Bradford Assay for Determining a Standard Curve

Well No.	1	2	3	4	5	6
[BSA] (mg/ml)	0.05	0.1	0.2	0.3	0.4	0.5
Volume of BSA (µl)	10	10	10	10	10	10
Volume of Bradford reagent (µl)	200	200	200	200	200	200

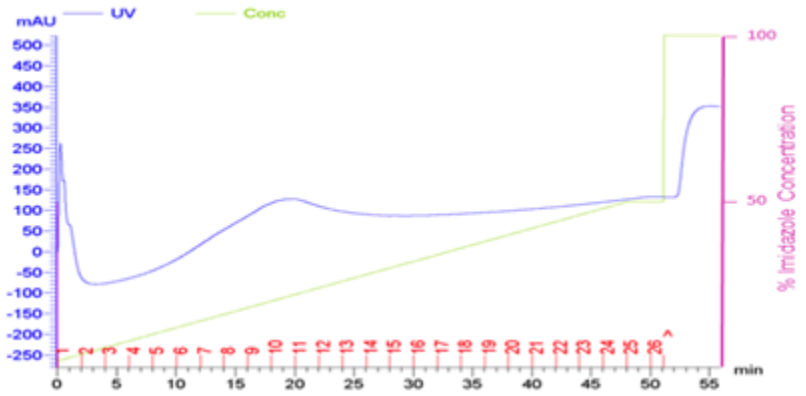

Figure 5.7. Elution profile of Y18A-HDAC8 from a 1 ml Nickel-IDA affinity column.
The crude bacterial extract supernatant containing the 10 mM imidazole in the purification buffer (50 mM Tris-HCl pH 8.0, 3mM $MgCl_2$, 150 mM KCl, 5% glycerol and 1mM β-mercaptoethanol) was loaded on to the 1 ml Nickel-IDA affinity column. AKTApurifier UPC10 connected to AKTA purifier. Following loading process, the column was washed with 15 column volumes of 20 mM imidazole in purification buffer. The linear gradient of 50 column volumes from 20-150 mM imidazole was used to elute the protein from the column. The recombinant protein was eluted with a linear gradient of imidazole (4 %-30 % Buffer B containing 500 mM imidazole).The fraction numbers are labeled in red in the above figure.

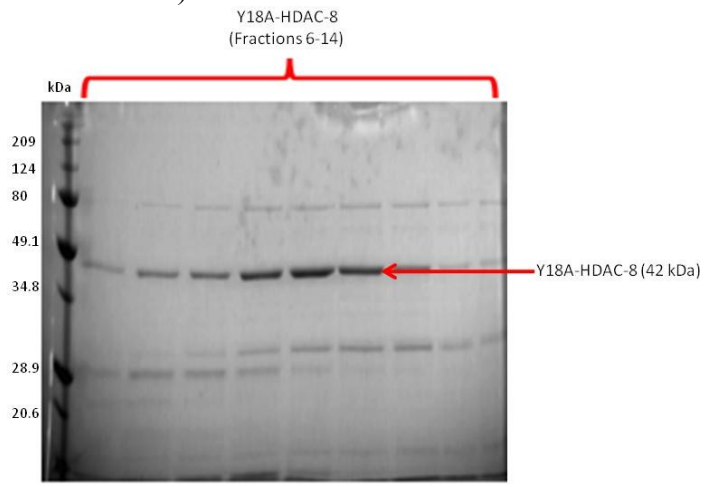

Figure 5.8. Electrophoretic analysis of Ni^{2+}- IDA affinity purified recombinant Y18A-HDAC8 protein by discontinuous SDS-PAGE.
The peak fractions from the purification process were run on an SDS-polyacrylamide gel to determine purity and were pooled thereafter. The protein gel was stained with Coomassie blue followed by destaining with a solution containing methanol and acetic acid, and photographed. All the fractions were pooled and protein concentration was determined to be 7.6 µM by Bradford assay.

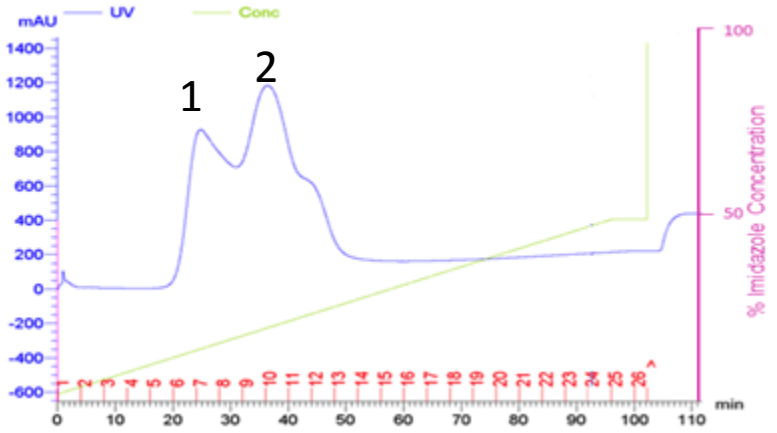

Figure 5.9. Elution profile of Y20A-HDAC8 from a 1 ml Nickel-IDA affinity column.
The crude bacterial extract supernatant containing the 10 mM imidazole in the purification buffer (50 mM Tris-HCl pH 8.0, 3 mM $MgCl_2$, 150 mM KCl, 5% glycerol and 1mM β-mercaptoethanol) was loaded on to the 1 ml Nickel-IDA affinity column. AKTA purifier UPC10 connected to AKTA purifier. Following loading process, the column was washed with 15 column volumes of 30 mM imidazole in purification buffer. The linear gradient of 50 column volumes from 20-150 mM imidazole was used to elute the protein from the column. The recombinant protein was eluted with a linear gradient of imidazole (4 %-30 % buffer B containing 500 mM imidazole).The fraction numbers are labeled in red in the above figure.

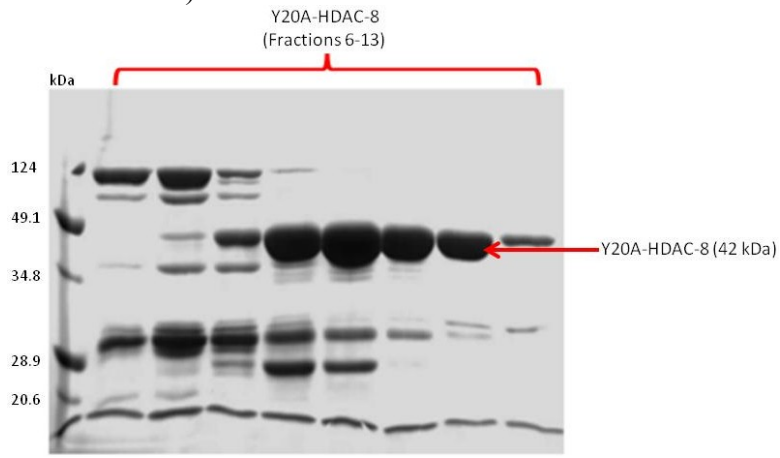

Figure 5.10. Electrophoretic analysis of Ni^{2+}-IDA affinity purified recombinant Y20A-HDAC8 protein by discontinuous SDS-PAGE.
The peak (1&2) fractions from the purification process were run on an SDS-polyacrylamide gel to determine purity and were pooled thereafter. The protein gel was stained with Coomassie blue followed by destaining with a solution containing methanol and acetic acid, and photographed. Fractions 9-13 (lanes 5-9) were pooled and protein concentration was determined to be 27.6 µM by Bradford assay.

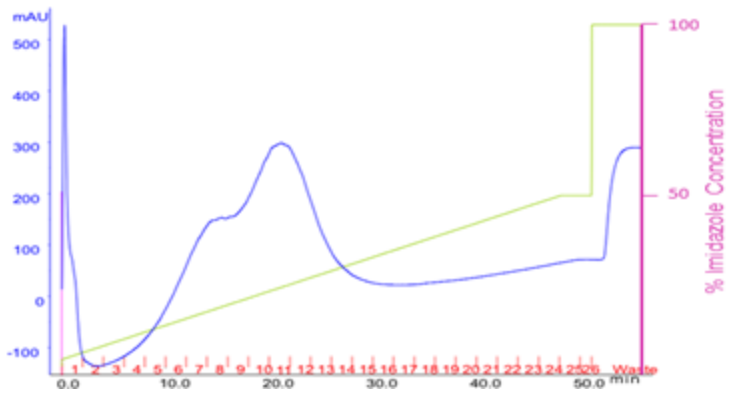

Figure 5.11. Elution profile of H42A-HDAC8 protein from a 1 ml Nickel-IDA affinity column. The crude bacterial extract supernatant containing the 10 mM imidazole in the purification buffer (50 mM Tris-HCl pH 8.0, 3mM $MgCl_2$, 150 mM KCl, 5% glycerol and 1mM β-mercaptoethanol) was loaded on to the 1 ml Nickel-IDA affinity column. AKTA purifier UPC10 connected to AKTA purifier. Following loading process, the column was washed with 15 column volumes of 30 mM imidazole in purification buffer. The linear gradient of 50 column volumes from 20-150 mM imidazole was used to elute the protein from the column. The recombinant protein was eluted with a linear gradient of imidazole (4 %-30 % buffer B containing 500 mM imidazole).The fraction numbers are labeled in red in the above figure.

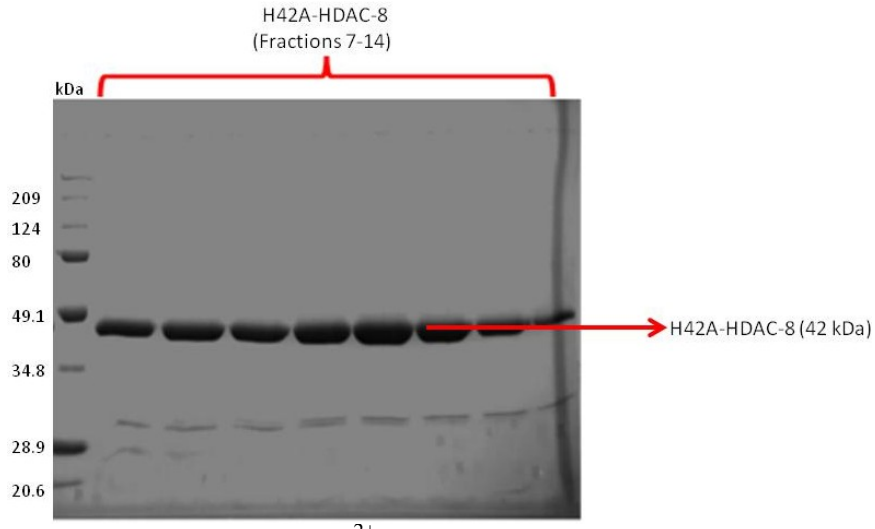

Figure 5.12. Electrophoretic analysis of Ni^{2+}-IDA affinity purified recombinant H42A-HDAC8 protein by discontinuous SDS-PAGE.
The peak fractions from the purification process were run on an SDS-polyacrylamide gel to determine purity and were pooled thereafter. The protein gel was stained with Coomassie blue followed by destaining with a solution containing methanol and acetic acid, and photographed. Fractions 7-14 were pooled and the protein concentration was determined to be 10.5 µM by Bradford assay.

5.3. Steady State Kinetics for Wild Type and Mutant HDAC8

HDAC8 is a metallo-enzyme that requires binding of a single metal ion for optimal activity (66). Studies have shown that HDAC8 activity was maximal when bound to iron, thereby identifying iron as the likely metal cation that is physiologically present in the enzyme (13,162,163). However, Dowling et al., (2010) determined that the preference for zinc binding by HDAC8 is consistent with the higher lewis acidity of zinc ion (164). Therefore, for all practical experiments we have utilized zinc as the metal ion for purification of mutant HDAC8 enzymes.

HDAC8 is over expressed in cancer and neuro-degenerative diseases(165). HDAC8 mutations were designed to test the role of three specific exit tunnel residues, namely Y18, Y20 and H42, in the normal functioning of the enzyme. This information would be helpful not only in enhancing our mechanistic understanding of HDAC8 but also aid the development of novel drugs targeting HDAC8.

To determine the effect of the three single amino acid substitutions mentioned above on the rate of reaction of HDAC8, a series of experiments was set up to assess the functionality of the mutated HDAC8 enzymes and to perform a comparative analysis of the activities of the three HDAC8 mutant enzymes. For this, the experiment was set up in a microplate using the commercially available *Fluor de lys*® HDAC8 assay system (Biomol) that utilizes a non-physiological peptide substrate to measure HDAC8 activity, as described in section 4.2.1. This substrate contains AMC (7-Amino Methyl Coumarin) group attached to the acetyl lysine moiety. Upon catalysis by HDAC8, the deacetylated product is generated which is cleaved by trypsin. The following settings were used as the standard assay condition: λ_{ex} = 365 nm, λ_{em} = 500 nm,

PMT = High. These wavelengths were chosen in order to minimize the inner filter effect caused by high concentrations of the *Fluor de lys*® substrate. A lag phase, representative of the delay in the fluorescence signal, was observed prior to attainment of the steady state phase. The lag phase (3000 s in case of mutant HDAC8 and nearly 1500 s in case of wild type HDAC8) was the time required to reach the steady state concentration of the deacetylated substrate (*Fluor de lys*®), formed due to the HDAC8 catalyzed reaction. The cleavage of the deacetylated *Fluor de lys*® by trypsin, liberated the highly fluorescent product (AMC) which was monitored (λ_{ex} = 365 nm, λ_{em} = 500nm) as a function of time. This lag phase was subtracted from the reaction progress curve to calculate the initial steady-state rate of the enzyme catalysis.

To determine the K_m value, initial velocities of the enzyme (both the wild type and mutant HDAC8) catalyzed reactions were measured as a function of the substrate concentration. The profile showed a hyperbolic dependence of the initial velocity on the substrate concentration. The reaction of wild-type HDAC8 with the *Fluor de lys*® substrate proceeded with relatively low values of k_{cat}/K_m and high K_m values compared to most other enzymes that react with their physiological substrates near the diffusion-controlled limit (166). The steady state kinetic parameters of K_m, k_{cat} and k_{cat}/K_m values for the wild-type and mutant HDAC8 enzymes were calculated from initial reaction rates measured under conditions of sub-saturating substrate (60-2000 μM) and enzyme (0.25 μM) utilizing the AMC standard plot and have been listed in Table 5.2. The values computed for K_m were 593.06 ± 76.29 μM, 669.54 ± 174.43 μM, 599.16 ± 134.22 μM and 706.58 ± 93.94 μM, for wild type HDAC8, Y18A-HDAC8, Y20A-HDAC8 and H42A-HDAC8, respectively. The values computed for k_{cat} were 120 x $10^{-4}s^{-1}$, 3.52 x $10^{-4}s^{-1}$, 7.6 x 10^{-4} s^{-1} and 1.4 x 10^{-3} s^{-1} for wild type HDAC8, Y18A-HDAC8, Y20A-HDAC8

and H42A-HDAC8, respectively. From the values presented in Table 5.2 and Figures 5.13 and 5.14, the effect of mutations on the K_m, k_{cat} and k_{cat}/K_m is quite clear. As the first order rate constant, k_{cat} is a measure of the initial velocity and was the highest for wt-HDAC8 and declined by 34 fold, 16 fold and 9 fold in case of Y18A, Y20A and H42A HDAC8 mutants, respectively. The K_m values, on the other hand, were quite comparable for the wild type and mutant HDAC8 enzymes. These results indicate that the above point mutations did not disrupt the active site pocket and hence, the binding of substrate was not affected significantly. However, these mutations did have a drastic effect on the velocity of the reaction that may in turn be related to the inhibition of the release of acetate. These results suggest that release of the acetate by-product via the exit tunnel may be a rate-limiting step and may determine the overall rate of reaction by HDAC8.

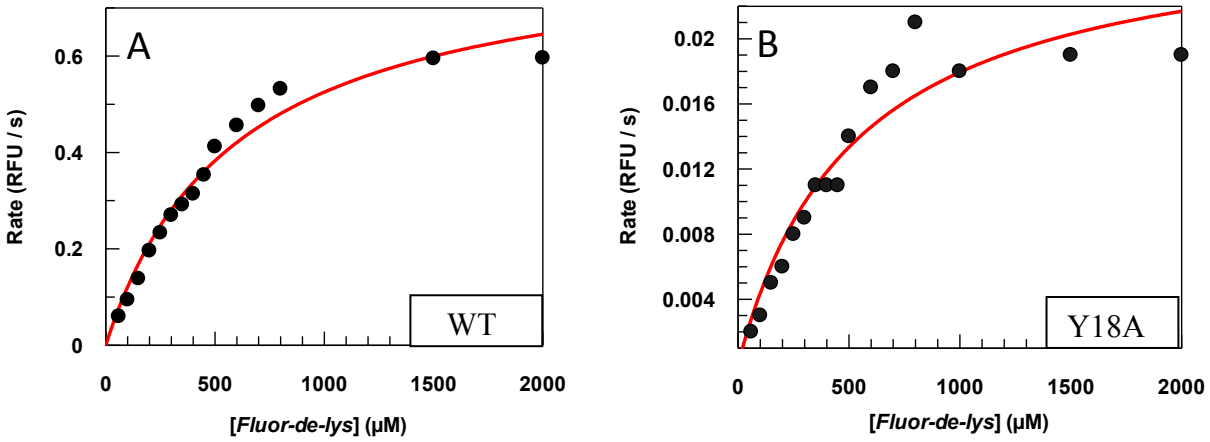

Figure 5.13. Michaelis-Menten plot of constitutive enzymatic activities of WT-HDAC8 (panel A) and Y18A-HDAC8 mutant (panel B).
The reactions were performed in HDAC8 assay buffer (buffer composition described in section 4.2.1) in a microplate at room temperature using λ_{exc}= 365 nm and λ_{em}= 500 nm with a cut off filter at 455 nm. Each reaction consisted of 250 nM enzyme, 60-2000 µM substrate and 250 nM trypsin in the assay buffer. Panel A shows the constitutive activity of wt-HDAC8, displaying k_{cat} = 0.012 s^{-1} and K_m= 593.06 ± 76.29 µM. Panel B shows the constitutive activity of Y18A-HDAC8, displaying k_{cat} = 3.52 x $10^{-4}s^{-1}$ and K_m= 669.54 ± 174.43µM (also see table 5.2).

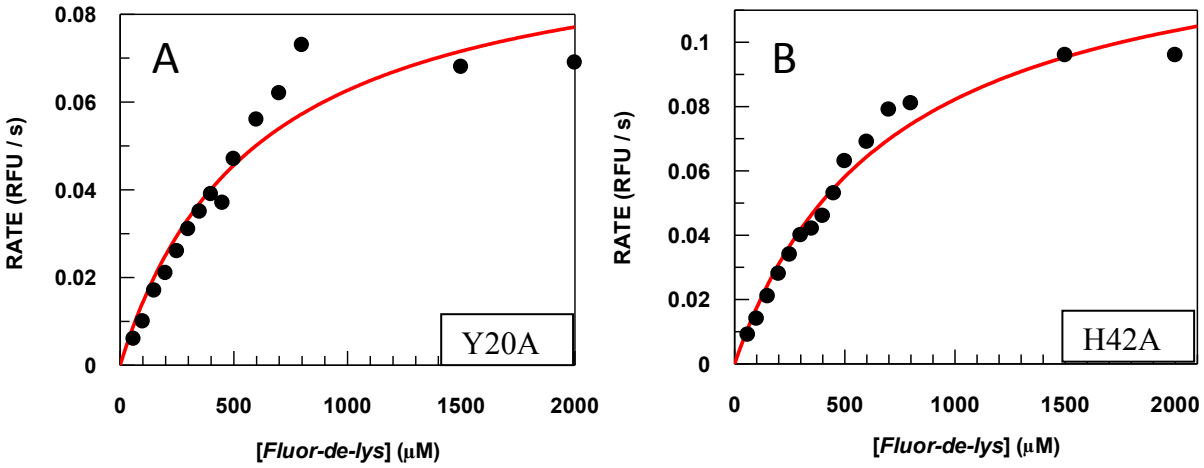

Figure 5.14. Michaelis-Menten plot of constitutive enzymatic activities of Y20A-HDAC8 (panel A) and H42A-HDAC8 mutants (panel B).
The reactions were performed in HDAC8 assay buffer (buffer composition described in section 4.2.1) in a microplate at room temperature using λ_{exc}= 365 nm and λ_{em}= 500 nm with a cut off filter at 455 nm. Each reaction consisted of 250 nM enzyme, 60-2000 µM substrate and 250 nM trypsin in the assay buffer. Panel A shows the constitutive activity of Y20A-HDAC8, displaying $k_{cat} = 7.6 \times 10^{-4} s^{-1}$ and K_m= 599.16 ± 134.22 µM. Panel B shows the constitutive H42A-HDAC8 activity, displaying $k_{cat} = 1.4 \times 10^{-3} s^{-1}$ and K_m= 706.58 ± 93.94µM (also see table 5.2).

Table 5.2. Kinetic Parameters for the Constitutive Activity of Wild Type and Mutant HDAC8

HDAC8	**k_{cat} (s^{-1})**	**K_m (µM)**	**k_{cat}/K_m ($M^{-1}s^{-1}$)**
Wild Type	120×10^{-4}	593.06 ± 76.29	20.2
Y18A	3.52×10^{-4}	669.54 ± 174.43	0.52
Y20A	7.6×10^{-4}	599.16 ± 134.22.	1.26
H42A	1.4×10^{-3}	706.58 ± 93.94	1.98

K_m (Michaelis-Menten constant)
s (seconds),
M (molar),
k_{cat} (first order rate constant)

5.3.1. Inhibitory Potency of Acetate (CH_3COO^-) for the Wild Type and Mutant HDAC8 Enzymes

As described previously, acetate is a by-product of the deacetylation reaction catalyzed by HDAC8 and is released via the exit tunnel. Since the mutations were created at the exit tunnel, it was important to determine the inhibition constant (K_i) of acetate for each of the three HDAC8 mutants. The inhibition constant (K_i) of the above inhibitor were determined by measuring the initial rates of the HDAC8 catalyzed reaction as a function of inhibitor concentrations. The experiment was performed utilizing the *Fluor de lys*® assay system, as described in section 4.2.3 and 4.2.4. Stock solutions of potassium acetate in the HDAC8 standard assay buffer (50 mM Tris-HCl, pH 8.0, 137 mM NaCl, 2.7 mM KCl, 1 mM $MgCl_2$ and 1 mg/ml BSA) were prepared with the following concentrations: 200 mM, pH 8.0, 500 mM, pH 8.0 and 1M, pH 8.0. Reactions were set up for wt-HDAC8, Y18A-HDAC8, Y20A-HDAC8 and H42A-HDAC8 in a polystyrene microplate. Each assay well contained 150 μM *Fluor de lys*® substrate (except for Y18A it was 500 μM), varying concentrations of acetate (0-120 mM), 250 nM trypsin and 250 nM wild-type or mutant HDAC8 (except in case of Y18A-HDAC8, which was used at 500 nM) enzyme in a total volume of 0.2 ml. Reactions were initiated by the addition of the enzyme and the time course of increase in fluorescence as a function of time was monitored. The data were analyzed by competitive binding model using equation 4.4, and the inhibition constant (K_i) for acetate was determined. Figure 5.15 shows the acetate inhibition profile for wild type HDAC8 and mutants where the solid lines represent the best fit of the experimental data using the above mentioned binding model. The K_i value for acetate for the wild type

HDAC8, Y18A-HDAC8, Y20A-HDAC8 and H42A-HDAC8 were computed as 0.477 ± 0.058 mM, 0.903 ± 0.056 mM, 1.649 ± 0.109 mM and 0.920 ± 0.657 mM (Table 5.3.).

The overall values for the equilibrium inhibition constant of acetate (K_i) for the HDAC8 mutants were found to be not much different from that of the wild-type HDAC8. Compared to wt-HDAC8, the three exit-tunnel HDAC8 mutants exhibited a 1.9-3.4 fold increase in the K_i of acetate (Fig. 5.15 and Table 5.3). The key determinant of acetate binding in HDAC8 has been reported to be the R37 residue(116). Given that the three exit tunnel mutations are all localized in the vicinity of R37, they may influence the interaction of R37 with acetate. However, since the above three HDAC8 mutants contain an intact R37, there may only be a minor impact on acetate binding in these mutants, consistent with the observed partial resistance of the three HDAC8 mutants to acetate inhibition. Short-chain fatty acids, such as phenyl butyrate and phenyl acetate, inhibit HDAC activity and affect the expression of numerous genes with disparate cellular functions (167,168). These agents have been tested in the clinic, but they suffer from a short plasma half-life as well as from the relatively high (millimolar) concentrations that are required for their action. Acetate has also been found to be one of the least potent inhibitors of HDAC activity in an earlier study involving short chain fatty acids (SCFAs) (169).

5.4. Physiochemical Properties of Recombinant Human HDAC8 Mutants

The steady state kinetic analysis of HDAC8 mutants showed a decreased enzymatic activity. These results were further substantiated by performing spectral, kinetic and thermodynamic studies on the above three mutants, both in ligand-free and ligand-bound conditions. The latter studies were performed in combination with known inhibitors and activators of HDAC8.

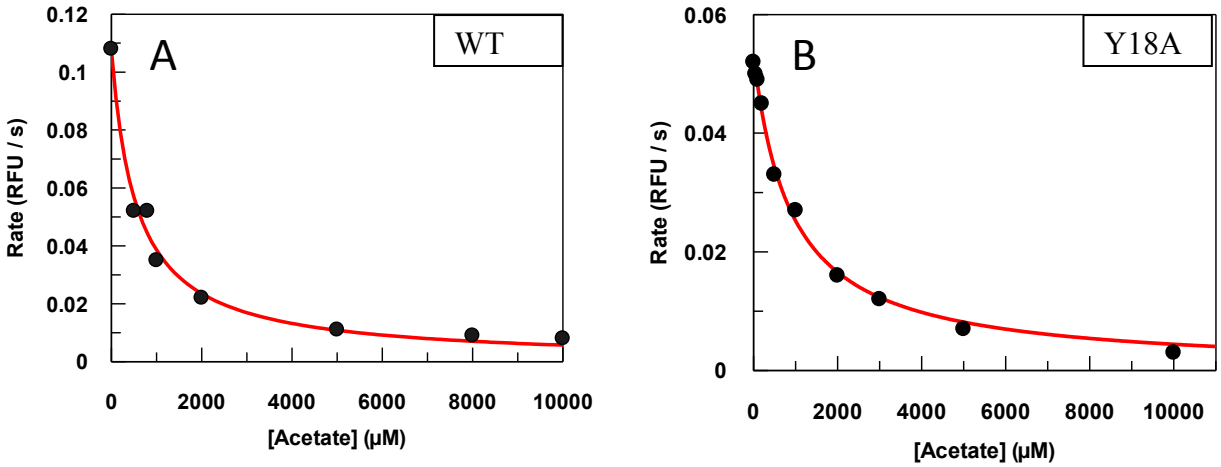

Figure 5.15. Inhibition of WT-HDAC8 (A) and Y18A-HDAC8 (B) by acetate.
The reaction was set up with varying concentration of acetate in each well and HDAC8 activity was monitored until an asymptote was reached at room temperature. As evident from the shape of the curves in panels A & B, acetate is a weaker inhibitor for Y18A-HDAC8 enzymatic activity (K_i= 0.903 mM) compared to the wild type HDAC8 enzymatic activity (K_i= 0.477 mM). Similar analysis was performed for other HDAC8 mutants (profiles not shown) and the summarized data are shown in Table 5.3.

Table 5.3. Equilibrium Inhibition Constant (K_i) for Acetate in Wild Type and Mutant HDAC8 Enzymes

HDAC8	**K_i of Acetate (mM)**
Wild Type	0.477 ± 0.058
Y18A	0.903 ± 0.056
Y20A	1.649 ± 0.109
H42A	0.920 ± 0.657

These studies were designed to further test the following hypothesis of: a) The exit tunnel and exit tunnel residues are important in the normal functioning of the enzyme. b) The exit tunnel residues can serve as a potential site for HDAC8 inhibition or activation. c) These

mutations may have an impact on the structure of the enzyme, hence affecting its structure-activity relationship.

5.4.1. Inhibitory Potency of SAHA and its Fluorescent Analog- Coumarin-SAHA (c-SAHA) for the Wild Type and Mutant HDAC8 Enzymes

Suberoylanilide hydroxamic acid (SAHA) is a well characterized and FDA approved inhibitor of HDACs for the treatment of T-cell lymphoma. It is known to cause growth arrest, differentiation, and/or apoptosis of many tumor types *in vitro* and *in vivo* (70,83). It belongs to the class of hydroxamate inhibitors containing a metal-binding hydroxamate, linker and cap regions. The linker and the cap groups interact with the surface and the rim of the active site pocket of the HDAC8 enzymes, respectively. Referring to the importance of SAHA as an inhibitor of HDAC8, it was imperative to determine its inhibition constant for the mutant HDAC8 enzymes to understand the effect of mutations on the functionality of the HDAC8 enzyme. Any change in the inhibition constant for mutant HDAC8s compared to the wild type would be an indicative of the disruption of the binding site for SAHA as a result of mutation.

The inhibition constant of HDAC8–inhibitor complexes (both for wild type and mutant HDAC8 enzymes) was determined using the trypsin-coupled assay (Schultz et al., 2004)(170) as described in section 4.2.4.1. The stock solutions of SAHA were prepared in the HDAC8 standard assay buffer (50 mM Tris-HCl, pH 8.0, 137 mM NaCl, 2.7 mM KCl, 1 mM $MgCl_2$ and 1 mg/ml BSA) and the reactions were set up for wt-HDAC8, Y18A-HDAC8, Y20A-HDAC8 and H42A-HDAC8 in a polystyrene microplate. Each assay well contained 150 μM *Fluor de lys*® substrate, varying concentrations of SAHA (0-10 μM), 250 nM trypsin and 250 nM wild-type or mutant HDAC8 (except in case of Y18A-HDAC8, which was used at 1 μM) enzyme in a total volume

of 0.2 ml. Reactions were initiated by the addition of the HDAC8 enzyme and the time course of increase in fluorescence as a function of time was monitored. The initial velocity of the enzyme-catalyzed reaction in each case was determined by monitoring the time-dependent change in the fluorescence intensity at 500 nm (λ_{ex}= 365 nm) in the absence or presence of inhibitors. The inhibition constant (K_i) values of the inhibitors were determined as described by Morrison (171) (see section 4.2.4). The data were analyzed by competitive binding model using equation 4.4, and the inhibition constant (K_i) for SAHA was determined and are listed in Table 5.4. Figure 5.16 shows the representative inhibition profiles of wild type and the Y18A-HDAC8 enzymes with SAHA. The solid line is the best fit of the experimental data using Equation 4.4 yielding the K_i values of 287.55 ± 22.41 nM, 632.75 ± 48.56 nM, 570.32 ± 70.11nM and 267.44 ± 25.56 nM for wild type HDAC8, Y18A HDAC8, Y20A HDAC8 and H42A HDAC8, respectively. No significant differences were observed in the inhibition constant values between wild type HDAC8 and the above three mutant HDAC8 enzymes.

Coumarin-SAHA (c-SAHA) inhibition studies were done in comparison to the studies performed with wild-type HDAC8 and SAHA. c-SAHA is an ideal fluorescent probe for determining the binding affinity and dissociation off-rates of selected HDAC inhibitors (172). The experiment was set up in a microplate and the inhibition constants for both wild-type and HDAC8 mutants were determined using the trypsin-coupled assay (Schultz et al., 2004) as described in sections 4.2.3 and 4.2.4. The stock solutions of c-SAHA were prepared in the HDAC8 standard assay buffer (50 mM Tris-HCl, pH 8.0, 137 mM NaCl, 2.7 mM KCl, 1 mM $MgCl_2$ and 1 mg/ml BSA) and the reactions were set up for wt-HDAC8, Y18A-HDAC8, Y20A-HDAC8 and H42A-HDAC8 in a polystyrene microplate. Each assay well contained 150 μM

Fluor de lys® substrate, varying concentrations of c-SAHA (0-10 μM), 250 nM trypsin and 250 nM wild-type or mutant HDAC8 (except in case of Y18A-HDAC8, which was used at 1 μM) enzyme in a total volume of 0.2 ml. Reactions were initiated by the addition of the HDAC8 enzyme and the time course of increase in fluorescence as a function of time was monitored. The initial rates of the HDAC8 catalyzed reaction (both wild type and the mutants) were measured as function of inhibitor concentrations. The solid lines shown in figure represent the best fit of the experimental data using the competitive binding model (equation 4.4). Figures 5.16 and 5.17 show the representative inhibition profiles of wild type and Y18A-HDAC8 enzymes with SAHA and c-SAHA, respectively. Similar analysis was also performed for the other two HDAC8 mutants (profiles not shown). Table 5.4 shows comprehensive data collected from these experiments. The analysis of the experimental data using Equation 4.4 yielded the K_i values of 210.77 ± 26.47 nM, 473.30 ± 64.70 nM, 449.90 ± 38.40 nM and 126.22 ± 22.60 nM for wild type HDAC8, Y18A HDAC8, Y20A HDAC8 and H42A HDAC8, respectively. Results show that c-SAHA is a more potent inhibitor of HDAC8. It is presumably because of the presence of the bulky coumarin cap group which may interact with the residues around entry region of the enzyme's active site pocket. There were no significant differences between HDAC8 mutants and the wild type HDAC8 for K_i values of either SAHA or c-SAHA. This indicated that the mutations at the exit tunnel did not alter the active site structure to an appreciable extent.

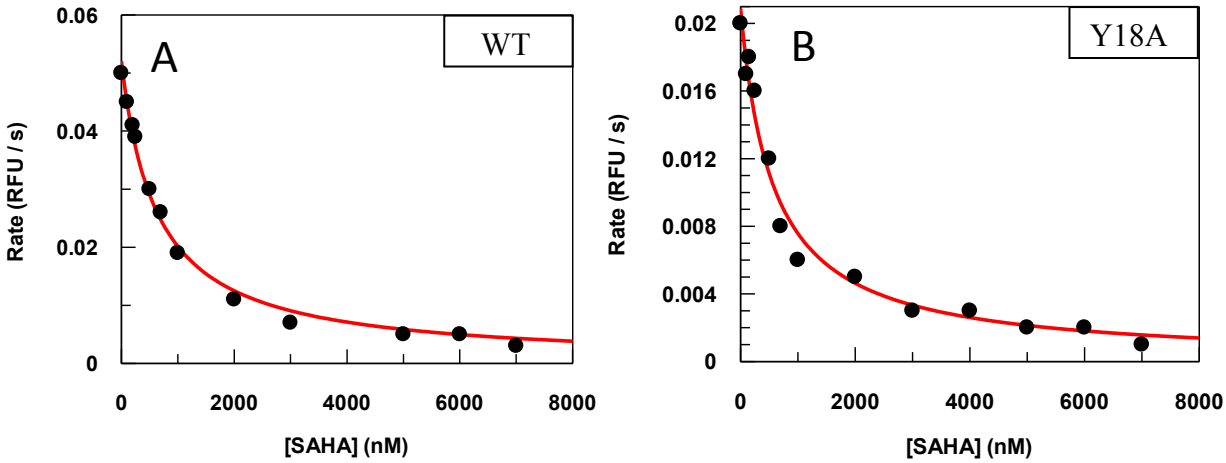

Figure 5.16. Inhibition of WT-HDAC8 (A) and Y18A-HDAC8 (B) by SAHA.
The reaction was set up with varying concentration of SAHA in each well and HDAC8 activity was monitored till the asymptote was reached at room temperature. The K_i of SAHA for WT-HDAC8 was =287.55 ± 22.41 nM and that for Y18A-HDAC8 was=632.75 ± 48.56 nM. Similar SAHA inhibition profiles (not shown) were also obtained for the other HDAC8 mutants, and the K_i values of SAHA for HDAC8 mutants were not significantly different from that of wild type HDAC8 (shown in Table 5.4).

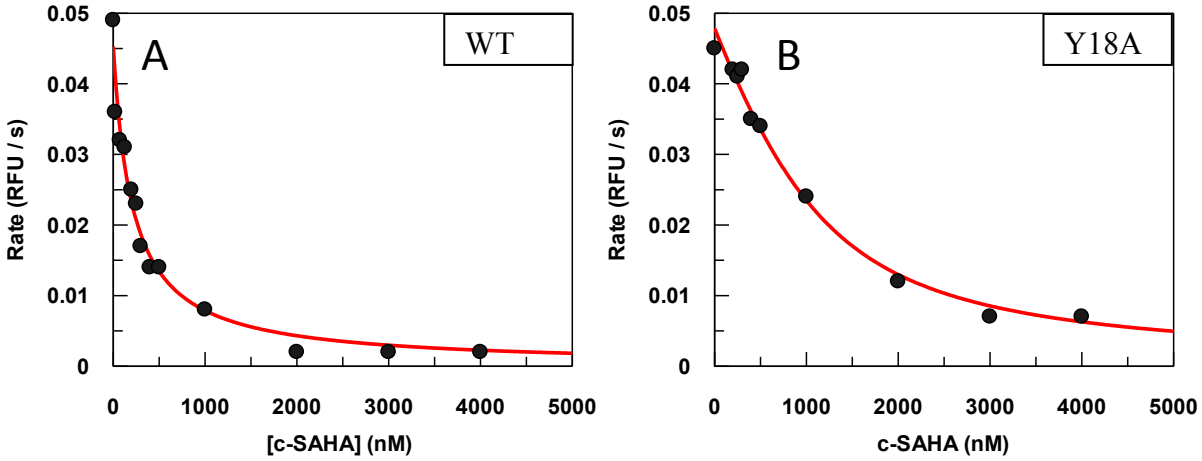

Figure 5.17. Inhibition of WT-HDAC8 (A) and Y18A-HDAC8 (B) by coumarin SAHA (c-SAHA).
The reaction was set up with varying concentration of c-SAHA in each well and HDAC8 activity was monitored till the asymptote was reached at room temperature. The K_i of c-SAHA for WT-HDAC8 was= 210.77 ± 26.47 nM and that for Y18A-HDAC8 was= 473.30 ± 64.70 nM. Similar c-SAHA profiles (not shown) were also obtained for the other HDAC8 mutants, and the Ki values of c-SAHA for HDAC8 mutants were not significantly different from that of wild type HDAC8 (shown in Table 5.4).

Table 5.4. Inhibition Constant (K_i) for SAHA and c-SAHA in Wild Type and Mutant HDAC8 Enzymes

HDAC8	K_i of SAHA (nM)	K_i of c-SAHA (nM)
Wild Type	287.55 ± 22.41	210.77 ± 26.47
Y18A	632.75 ± 48.56	473.30 ± 64.70
Y20A	570.32 ± 70.11	449.90 ± 38.40
H42A	267.44 ± 25.56	126.22 ± 22.60

5.5. Direct Binding of Inhibitors to the Wild Type and HDAC8 Mutants

5.5.1. Equilibrium Dissociation Constant (K_d) of SAHA for Wild Type and Mutant HDAC8 Enzymes

All the proteins containing amino acids- phenylalanine, tyrosine and tryptophan have an intrinsic fluorescence contributed by the above mentioned residues. The fluorescence properties of these residues are very sensitive to any changes in their local environment. Any change accrued upon by binding of an effector (inhibitor/ activator) can lead either to enhancement or quenching in their fluorescence. Therefore, interaction of HDAC8 enzymes (both the wild type and mutants) with the known inhibitors-SAHA and c-SAHA was studied via the steady state fluorescence spectroscopic measurement of the protein. The K_d of SAHA for wild type and mutant HDAC8 enzymes was determined by titration of a fixed concentration of the HDAC8 enzyme (1 μM, 250 μl volume) by increasing concentrations of the inhibitor SAHA (1-10 μM) in a square-bottomed 4 mm path length quartz cuvette. The excitation and emission wavelengths were maintained at 280 nm and 340 nm, respectively, to monitor the change in the intrinsic fluorescence (mainly contributed by tryptophan and tyrosine residues) of HDAC8. For all

experiments, the excitation and emission slits were maintained at 12 mm and 10 mm, respectively, and the PMT voltage was set at 800. All the stock and working solutions were made in 10 mM Tris-HCl, pH 7.5, 3 mM $MgCl_2$, 100 mM NaCl, 10% glycerol and 1mM TCEP. Upon binding of SAHA to wt-HDAC8 and mutants, quenching of protein fluorescence was observed. The change in HDAC8 fluorescence signal at 340 nm (λ_{ex} = 280 nm) was plotted as a function of the ligand concentration (Figure 5.18 shows the representative binding isotherms for determining the K_d of SAHA). The solid line is the best fit of the experimental data using the quadratic Equation 4.6 yielding the K_d values of 500.55 ± 35.44 nM, 123.42 ± 11.86 nM, 143.67 ± 17.03 nM and 124.03 ± 15.05 nM for wild type HDAC8, Y18A HDAC8, Y20A HDAC8 and H42A HDAC8, respectively. Table 5.5 lists the values for the dissociation constant for each of the HDAC8 enzymes. The difference in K_d values for SAHA between the mutant HDAC8 enzymes and the wild-type enzyme were smaller than an order of magnitude, and were considered to be largely similar. Hence, these results were indicative of unchanged active site or substrate binding pocket in case of HDAC8 mutants.

5.5.2. Equilibrium Dissociation Constant (K_d) of c-SAHA for Wild Type and Mutant HDAC8 Enzymes

The dissociation constants for c-SAHA for the wild type and mutant HDAC8 enzymes were determined by titration of a fixed concentration of c-SAHA (500 nM) with increasing concentrations of the respective enzymes. Here we titrated the ligand (0.5 µM, 250 µl volume) with the enzyme. All the settings were kept the same as mentioned above for the SAHA analysis. Fluorescence intensity was monitored at 397 nm (λ_{ex} = 325 nm) and quenching of the

fluorescence was observed in each case. Figure 5.19 shows the representative binding isotherms for the determination of K_d for c-SAHA. The change in c-SAHA fluorescence signal at 397 nm (λ_{ex} = 325 nm) was plotted as a function of the HDAC8 enzymes concentration (Figure 5.19 shows the representative binding isotherms for determining the K_d of c-SAHA). The solid line is the best fit of the experimental data using the quadratic Equation 4.6 yielding the K_d values of 225.46 ± 20.56 nM, 336.59 ± 54.09 nM, 496.51 ± 85.43 nM and 217.61 ± 29.28 nM for wild type HDAC8, Y18A HDAC8, Y20A HDAC8 and H42A HDAC8, respectively. Table 5.5 lists the values for the dissociation constant for each of the enzymes. As in case of SAHA, the difference in K_d values for c-SAHA between the mutant HDAC8 enzymes and the wild-type enzyme were smaller than an order of magnitude, and were considered to be largely similar.

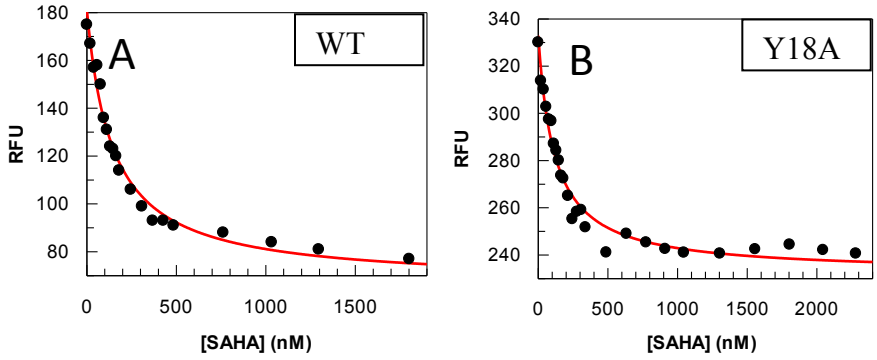

Figure 5.18. Binding isotherm for the determination of the equilibrium dissociation constant (K_d) of SAHA with WT-HDAC8 (A) and Y18A-HDAC8 (B) determined by fluorescence spectroscopy.
Formation of HDAC8-SAHA complex was measured by monitoring the quenching of protein fluorescence upon addition of SAHA. The experiment was performed with 1 µM HDAC8 in a 4mm quartz cuvette and aliquots of SAHA were added at regular intervals. Following excitation at 280 nm, fluorescence emission was monitored at 340 nm. The quenching of fluorescence was plotted as a function of increasing concentration of SAHA and data were analyzed by equation 4.6 to determine K_d. The K_d values of wild type HDAC8 and Y18A-HDAC8 mutant for SAHA ligand were determined to be 500.55 ± 35.44 nM (A) and 123.42 ± 11.86 nM (B), respectively.

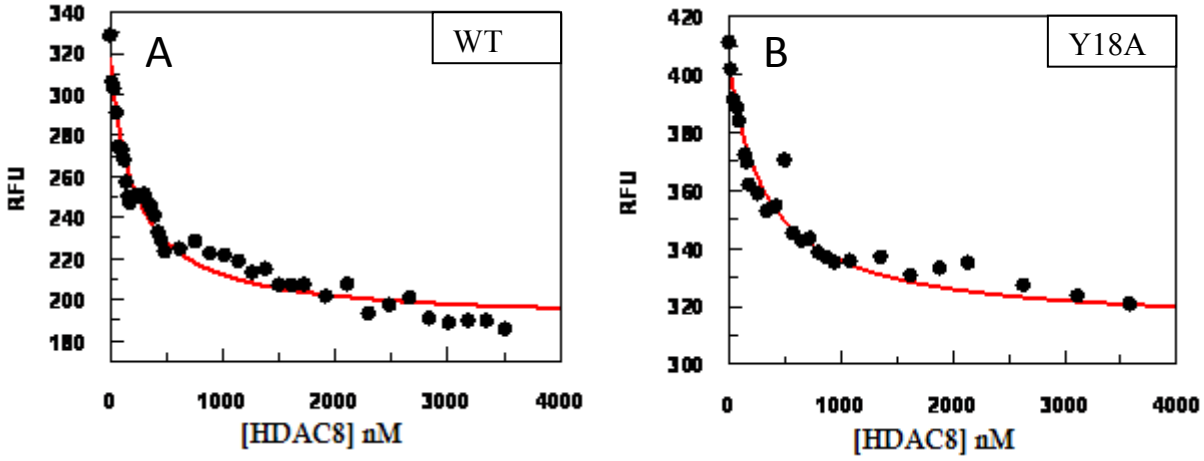

Figure 5.19. Binding isotherm for the determination of the equilibrium dissociation constant (K_d) of c-SAHA with WT-HDAC8 (A) and Y18A-HDAC8 (B) determined by fluorescence spectroscopy.

Formation of HDAC8-c-SAHA complex was measured by monitoring the quenching of c-SAHA fluorescence upon addition of wild type or mutant HDAC8 enzyme. The experiment was performed with 500 nM c-SAHA in a 4mm quartz cuvette and aliquots of HDAC8 were added at regular intervals. Following excitation at 280 nm, fluorescence emission was monitored at 340 nm. The quenching of fluorescence was plotted as a function of increasing concentration of HDAC8 enzyme and data were analyzed by eq. 4.6 to determine K_d. The K_d values of wild type HDAC8 and Y18A-HDAC8 mutant for SAHA ligand were determined to be 225.46 ± 20.56 nM (A) and 336.59 ± 54.09 nM (B), respectively. Thus, as in the case of K_i there was not much difference in the K_d values of c-SAHA between wild type and mutant HDAC8 enzymes (Refer table 5.5).

Table 5.5. Equilibrium Dissociation Constant (K_d) Values for Wild Type and Mutant HDAC8 Enzymes for SAHA and c-SAHA Ligands

HDAC8	**K_d of SAHA (nM)**	**K_d of c-SAHA (nM)**
Wild Type	500.55 ± 35.44	225.46 ± 20.56
Y18A	123.42 ± 11.86	336.59 ± 54.09
Y20A	143.67 ± 17.03	496.51 ± 85.43
H42A	124.03 ± 15.05	217.61 ± 29.28

5.6. Time-resolve Fluorescence Spectroscopic Measurements of Both the Wild Type and Mutant HDAC8 Enzymes

5.6.1. Fluorescence Decay Curve of c-SAHA in the Presence or Absence of Wild Type and Mutant HDAC8 Enzymes

The fluorescence lifetime properties of c-SAHA (λ_{ex} = 340 nm, λ_{em} = 400 nm) and the mechanism of the fluorescence quenching of c-SAHA upon binding to HDAC8 enzymes were investigated using free c-SAHA, wild type HDAC8 and the three HDAC8 mutant enzymes. Fluorescence Lifetime measurements were performed on a custom design Photon Technology International (PTI) Fluorescence-Lifetime instrument. The excitation source for measuring the time resolved fluorescence decay for c-SAHA was the Light Emitting Diode (LED) with maximum power output at 340 nm. The emitted light was detected (at a right angle to the excitation source) by means of a stroboscopic emission monochromator configured at appropriate wavelengths (400 nm for c-SAHA fluorescence). Diluted starch suspensions (prepared in de-ionized water) were used to collect the instrument response function (IRF). The data were collected in 200 channels and the integration time was set as 1 second. Depending on the signal obtained, 20-30 averages were acquired for the samples to obtain a better resolution of the fluorescence traces. For all experiments, a 250 µl sample volume prepared in HDAC8 storage buffer (composition as described above) was used in a 4mm path length cuvette and contained 500 nM c-SAHA. The time resolved fluorescence decay curves were analyzed using PTI's software, Felix 32 to calculate the lifetime of c-SAHA under different conditions. Figure 5.20 shows the decay curve of free c-SAHA which conform to a single exponential rate equation as described in the Methods section. Figure 5.21 shows the decay curves of c-SAHA bound to

wild type HDAC8 (panel A), c-SAHA bound to Y18A-HDAC8 mutant (panel B), c-SAHA bound to Y20A-HDAC8 mutant (panel C) and c-SAHA bound to H42A-HDAC8 mutant (panel D) which also conformed to the single-exponential rate equation as explained in the Methods section. The data were analyzed using Equation 4.5 yielding the fluorescence life-time. The fluorescence lifetime values of free c-SAHA and c-SAHA combined with either the wild type or mutant HDAC8 enzyme have been listed in Table 5.6.The values obtained for c-SAHA-HDAC8 complex, c-SAHA-Y18A HDAC8, c-SAHA-Y20A HDAC8 and c-SAHA-H42A HDAC8 were 1.86 ns, 1.90 ns, 1.89 ns and 1.89 ns, respectively**.** It is evident that c-SAHA lifetimes remain unchanged irrespective of binding to either wild type or mutant HDAC8 enzymes. The results can be explained as occurring due to the phenomenon of static fluorescence quenching. Quenching can also occur as a result of the formation of a non-fluorescent ground state complex between the fluorophore and the quencher. When this complex absorbs light it immediately returns to the ground state without emission of a photon. The only observed fluorescence is from the uncomplexed fluorophore. This process, hence, does not change the lifetime of the sample as uncomplexed fluorophores have normal excited state properties. Quenching occurs due to the reduced number of fluorophores.

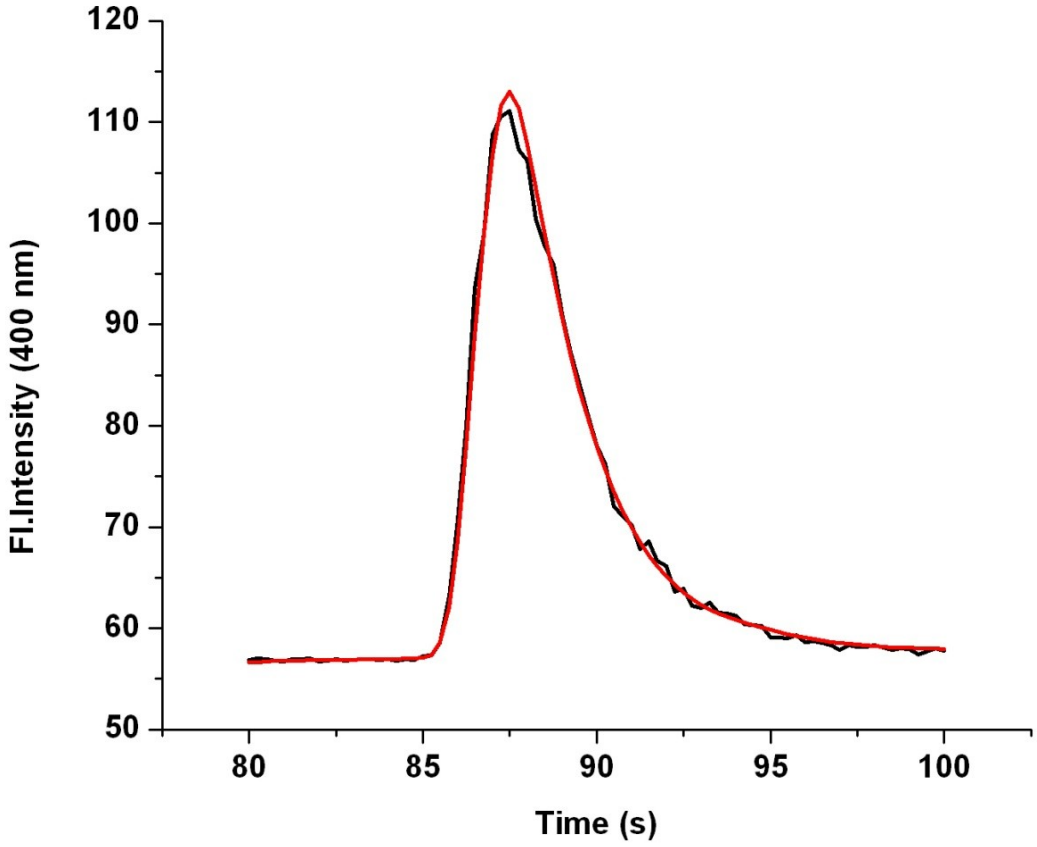

Figure 5.20. Fluorescence decay curve of c-SAHA.
The experiment was performed in a 4mm path length square quartz cuvette using a 340 nm LED light source and emission was monitored at 400 nm. In this case 500 nM of c-SAHA was used and a total of 30 scans were obtained. Instrument response factor (IRF) was acquired using a dilute solution of starch for the same time window under identical experimental conditions. The data were analyzed using the single exponential equation inbuilt in the Felix software which yielded a lifetime of 1.90 ns. The black curve represents the acquired decay associated spectra and the red curve is the best fit of the data after analysis. The lifetime values from this experiment are shown in Table 5.6.

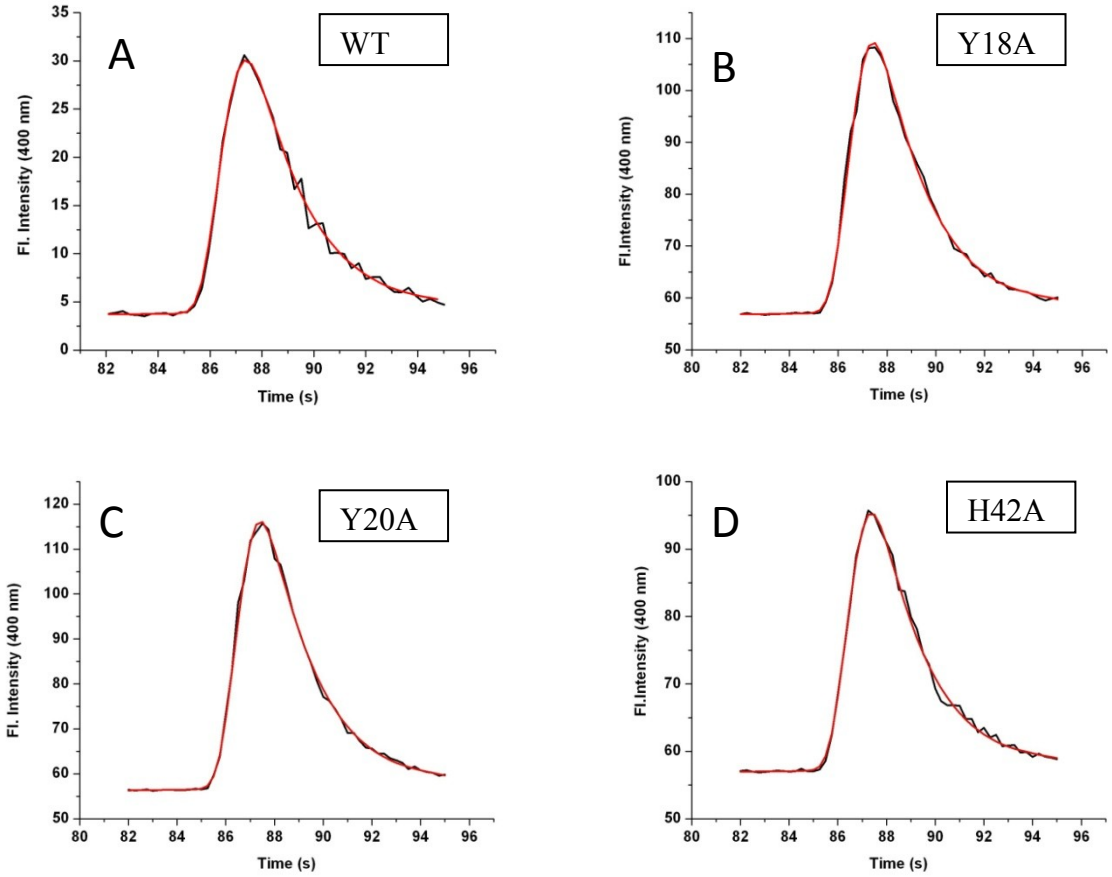

Figure 5.21. Fluorescence decay curves of c-SAHA in the presence of wild type or mutant HDAC8 enzymes: (A) WT-HDAC8 plus c-SAHA (B) Y18A-HDAC8 plus c-SAHA (C) Y20A-HDAC8 plus c-SAHA (D) H42A-HDAC8 plus c-SAHA.
The experiment was performed in a 4mm path length square quartz cuvette using a LED (340nm) light source and emission was monitored at 400 nm. In each case, 500 nM of c-SAHA was used with 4 μM HDAC8 and a total of 30 scans were obtained. Instrument response factor (IRF) was acquired using a dilute solution of starch for the same time window under identical experimental conditions. The data were analyzed using the single exponential equation inbuilt in the Felix software. In each panel, the black curve represents the acquired decay associated spectra and the red curve is the best fit of the data after analysis. The values obtained for c-SAHA-HDAC8 complex, c-SAHA-Y18A HDAC8, c-SAHA-Y20A HDAC8 and c-SAHA-H42A HDAC8 were 1.86 ns, 1.90 ns, 1.89 ns and 1.89 ns, respectively. The lifetime values for all the samples are shown in Table 5.6.

Table 5.6. Fluorescence Decay Lifetime of c-SAHA in the Absence or Presence of Wild Type and Mutant HDAC8 Enzymes

Protein	Lifetime (ns)
c-SAHA	1.90 ± 0.01
HDAC8 + c-SAHA	1.86 ± 0.02
Y18A + c-SAHA	1.90 ± 0.01
Y20A + c-SAHA	1.89 ± 0.02
H42A + c-SAHA	1.87 ± 0.02

ns: nano-seconds

5.6.2. Fluorescence Decay Curve of the Tryptophan Residues in Wild Type and Mutant HDAC8 Enzymes

The fluorescence lifetime properties of the wild type and mutant HDAC8 enzymes were determined by monitoring their decay curve at 340 nm (λ_{ex} = 280nm). Specifically, this experiment sought to identify if the HDAC8 mutations resulted in a change in the lifetimes of tryptophan residues. Fluorescence lifetime measurements were performed on a custom design Photon Technology International (PTI) Fluorescence-Lifetime instrument. The excitation source for measuring the time resolved fluorescence decay for HDAC8 (both the wild type and mutants) was the Light Emitting Diode (LED) with maximum power output at 280 nm. The emitted light was detected (at a right angle to the excitation source) by means of a stroboscopic emission monochromator configured at appropriate wavelengths (340 nm for protein fluorescence). Diluted starch suspensions (prepared in de-ionized water) were used to collect the instrument response function (IRF). The data were collected in 200 channels and the integration time was set as 1 second. Depending on the signal obtained, 20-30 averages were acquired for the samples

to obtain a better resolution of the fluorescence traces. For all experiments, a 250 µl sample volume prepared in HDAC8 storage buffer (composition as described above) was used in a 4 mm path length cuvette and contained 4 µM HDAC8 enzyme (for both the wild type and mutant proteins). The time resolved fluorescence decay curves were analyzed using PTI's software, Felix 32 to calculate the lifetime of tryptophan under different conditions. Figure 5.23 depicts the fluorescence decay profiles of the wild type and the HDAC8 mutants. The red curves are the best fit of the experimental data using the double exponential rate equation (in case of mutants) and single exponential rate equation (in case of wild type HDAC8). Panels A-D show the fluorescence decay profiles of the wild type HDAC8, and Y18A, Y20A and H42A HDAC8 mutants, respectively. The fluorescence decay curves of the mutant HDAC8 enzymes fit to a bi-exponential in contrast to the wild type HDAC8.The lifetime values obtained for wild type HDAC8, Y18A-HDAC8, Y20A-HDAC8 and H42A-HDAC8 were 2.941 ± 0.196 ns, 0.36 ± 0.20 ns &3.00 ± 0.00 ns, 0.54 ± 0.25 ns & 3.00 ± 0.00 ns and 0.01ns & 2.2 ± 0.00 ns, respectively. HDAC8 has 4 tryptophan residues: W137, W141, W294 and W315. Of these W137, W315 and W141 are present in close proximity (Figure 5.22) to the exit tunnel residues. Therefore, we can attribute the change in the lifetime of these residues to their altered environment due to mutations. Also, mutations allow the adoption of additional conformations relative to the wild type (173). These values are shown in Table 5.7 which was computed using the Felix32 software from Photon Technology International (see section 4.4).

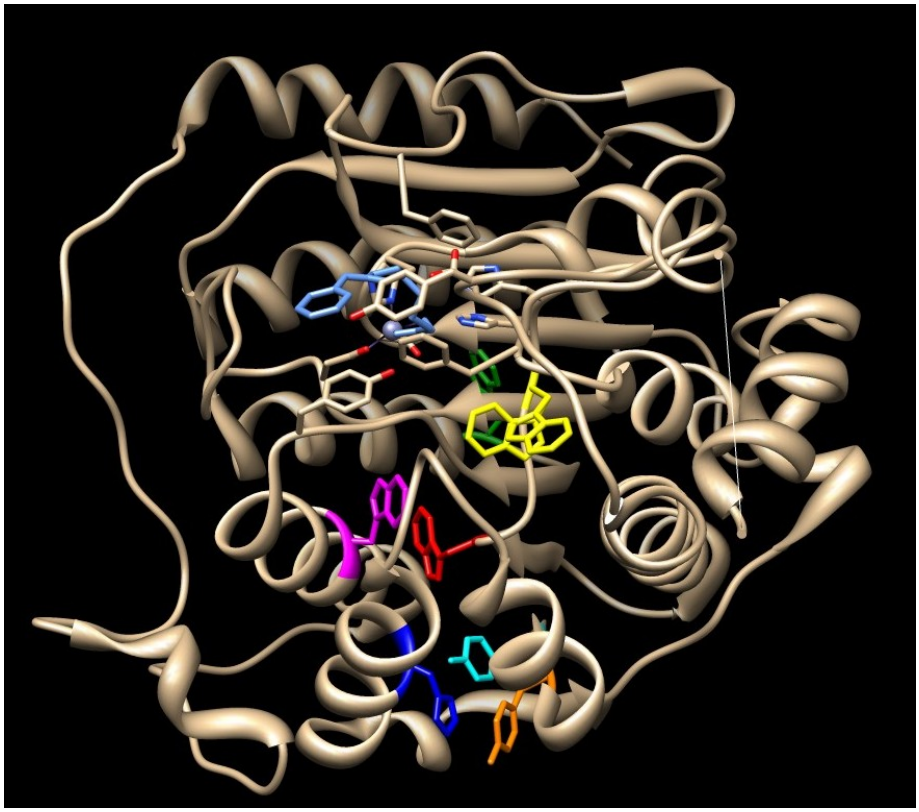

Figure 5.22. Ribbon diagram showing the position of four tryptophan residues relative to the Y18 (cyan), Y20 (orange) and H42 (blue) residues in HDAC8 crystal structure.
W315 (magenta) and W137 (red) are seen in close proximity to the mutated residues of HDAC8 enzyme. W141 (yellow) is the gating residue of the exit tunnel. W294 (green) is present away from both the active site and the exit tunnel. The figure (PDB ID. 1T69) has been modeled using UCSF Chimera® software.

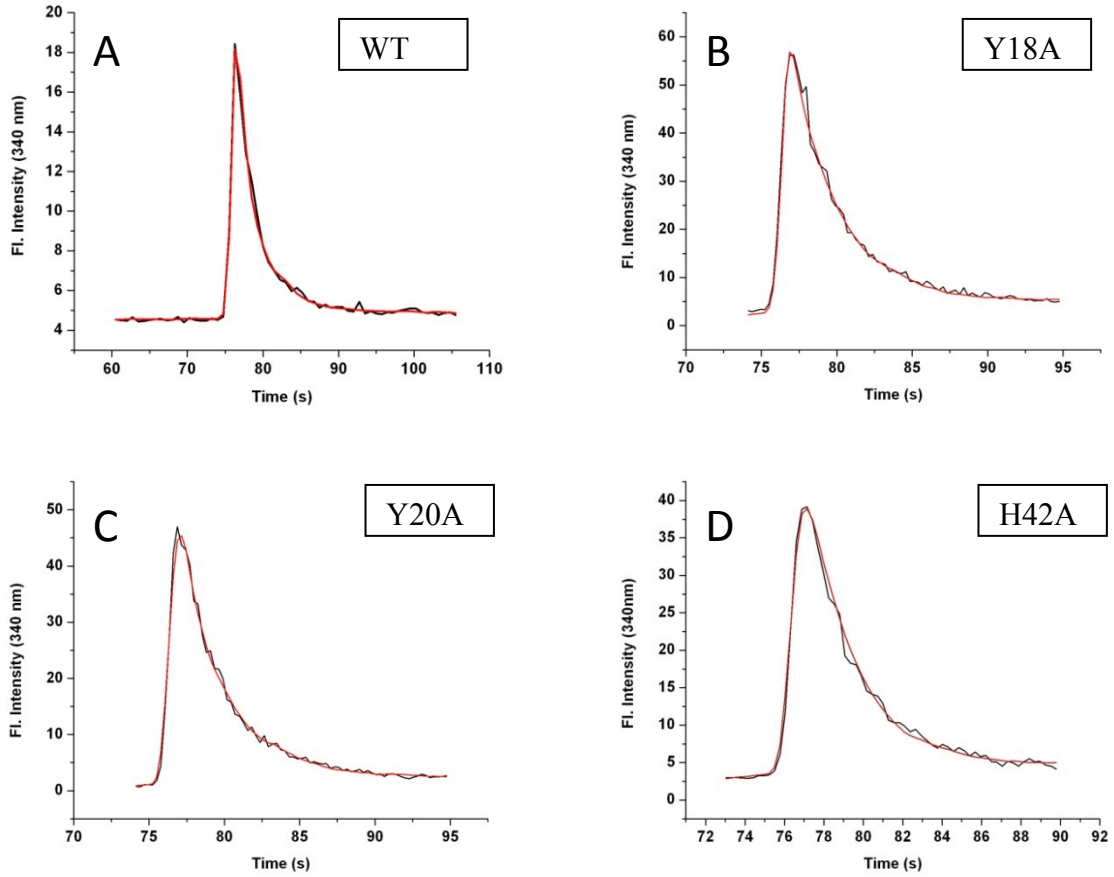

Figure 5.23. Fluorescence decay curves of wild type and mutant HDAC8 enzymes.(A) WT-HDAC8 (B) Y18A-HDAC8 (C) Y20A-HDAC8 (D) H42A-HDAC8.
The experiment was performed in a 4mm path length square quartz cuvette with a LED (280 nm) light source and emission was monitored at 340 nm. In each case, 4 µM HDAC8 was used and a total of 30 scans were obtained in each case. Instrument response factor (IRF) was acquired using a dilute solution of starch for the same time window under identical experimental conditions. The data were analyzed using the double exponential equation inbuilt in the Felix32 software. In each panel, the black curve represents the average of acquired decay associated spectra and the red curve is the best fit of the data after analysis. The lifetime values obtained for wild type HDAC8, Y18A-HDAC8, Y20A-HDAC8 and H42A-HDAC8 were 2.941 ± 0.196 ns, 0.36 ± 0.20 ns & 3.00 ± 0.00ns, 0.54 ± 0.25 ns & 3.00 ± 0.00 ns and 0.01ns & 2.2 ± 0.00 ns, respectively. The lifetime values for all samples are tabulated in table no. 5.7.

Table 5.7. Fluorescence Decay Lifetimes of Wild Type and Mutant HDAC8 Enzymes

HDAC8	Lifetime 1 (ns)	Lifetime 2 (ns)
Wild type	2.941 ± 0.196	-
Y18A	0.36 ± 0.20	3.00 ± 0.00
Y20A	0.54 ± 0.25	3.00 ± 0.00
H42A	0.01(negligible)	2.2 ± 0.00

ns: nano-seconds

5.7. Isothermal Titration Calorimetric (ITC) Studies for the Binding of SAHA (HDAC8 inhibitor)

Determination of the binding affinity of wild type and mutant HDAC8 enzymes was performed primarily using the fluorescence spectroscopy methods. In order to investigate the thermodynamics of the binding of SAHA to HDAC8 mutants, the ITC studies were performed. Protein-Ligand interaction is usually associated with either absorption or release of heat. It was of interest, therefore, to study interaction of SAHA with the wild type HDAC8 and mutant HDAC8 to unravel if there was a difference in the heat signals produced by the wild type and mutant HDAC8 enzymes. These experiments were performed using an isothermal titration calorimeter (Microcal) to determine parameters such as change in enthalpy, entropy, stoichiometry and the apparent binding affinity. The wild type or mutant HDAC8 enzymes (10 μM) were loaded into the sample cell and were titrated with 200 μM SAHA in 50 mM Tris-HCl, pH 7.5, containing 100 mM NaCl, 3 mM $MgCl_2$, 10 % Glycerol and 1 mM TCEP (loaded in the syringe- 45 injections of 4 μl each) at room temperature (25°C). As shown in top panel of figure 5.24(representing the raw calorimetric data), the heat signal produced (exothermic peaks) during the titration decreases progressively, as the enzyme active site gets saturated with each injection

of the ligand, i.e., SAHA. The heat signals from the last five injections were primarily due to the heat of dilution. The average of the heat contribution from these five injections (background heat signal) was subtracted from all the prior injections so as to eliminate its effect on the calculation of the parameters. The bottom panel represents the graph of the amount of heat generated per injection as a function of the molar ratio of the ligand. The solid, smooth lines shown in the figures 5.24-5.27 are the best fit of the data using the model proposed by Wiseman et al (159). Figures 5.24 through 5.27 show the raw and fitted data for the wild type and the three mutant HDAC8 enzymes. To reiterate here for each reaction, 10 μM of HDAC8 enzyme (wild type or mutant) was titrated with 45 x 4 μl injections of 200 μM SAHA inHDAC8 storage buffer (50 mM Tris-HCl, pH 7.5, containing 100 mM NaCl, 3 mM $MgCl_2$, 10 % Glycerol and 1 mM TCEP). In these figures, the upper panel represents the raw calorimetric data of titration indicating the amount of heat produced per injection. The lower panel depicts the fit of the data using the single site binding model where each data point corresponds to the integration of the area under the peak (see section 4.2). This area corresponds to the heat generated in kcal/ mole of the injectant. The values for the change in enthalpy and entropy upon binding are listed in Table 5.8. The values obtained for the stoichiometry of SAHA with wild type HDAC8, Y20-HDAC8 and H42A-HDAC8 were 0.755 ± 0.0439, 0.644 ± 0.016 and 0.361 ± 0550, respectively. The association constants (K_a) obtained were 1.10E6 ± 2.34E5 M^{-1}, 1.10E6 ± 1.18E5 M^{-1} and 1.37E6 ± 3.73E5 M^{-1} for wt-HDAC8, Y20A-HDAC8 and H42A-HDAC8, respectively. The third parameter determined was standard enthalpy change (ΔH^0) for wt-HDAC8, Y20A-HDAC8 and H42A-HDAC8 as-1.009E4 ± 751.8 cal mol^{-1}, -1.135E4 ± 379.6 cal mol^{-1} and -1.047E4 ± 204.6 cal mol^{-1}, respectively. Strikingly, efforts to determine the above mentioned parameters for the

Y18A-HDAC8 mutant were unsuccessful as there was no detectable heat signal generated upon the binding of SAHA to this mutant enzyme. In contrast, the values for the above parameters for Y20A and H42A HDAC8 mutants were not much different from those of the wild type HDAC8.

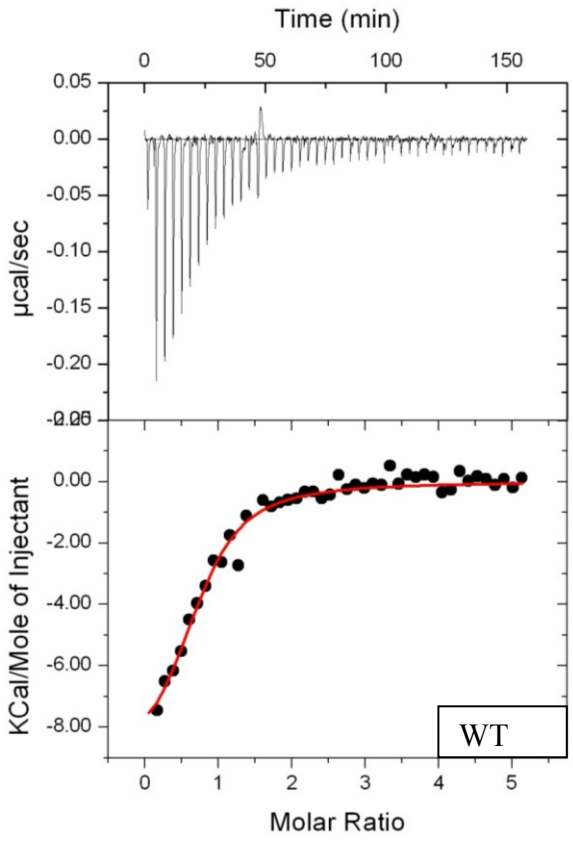

Figure 5.24. Isothermal titration calorimetry of WT-HDAC8.
Titration of 10 µM wild type HDAC8 with 200 µM SAHA was carried out at 25 °C. The top panel shows the raw calorimetric data as a function of time in minutes whereas the bottom panel shows the integrated heat per injection versus the molar ratio of SAHA to wild type HDAC8. The solid smooth line corresponds to the best fit of the experimental data to a single binding site model, providing parameters of enthalpy change and binding affinity as shown in Table 5.8.

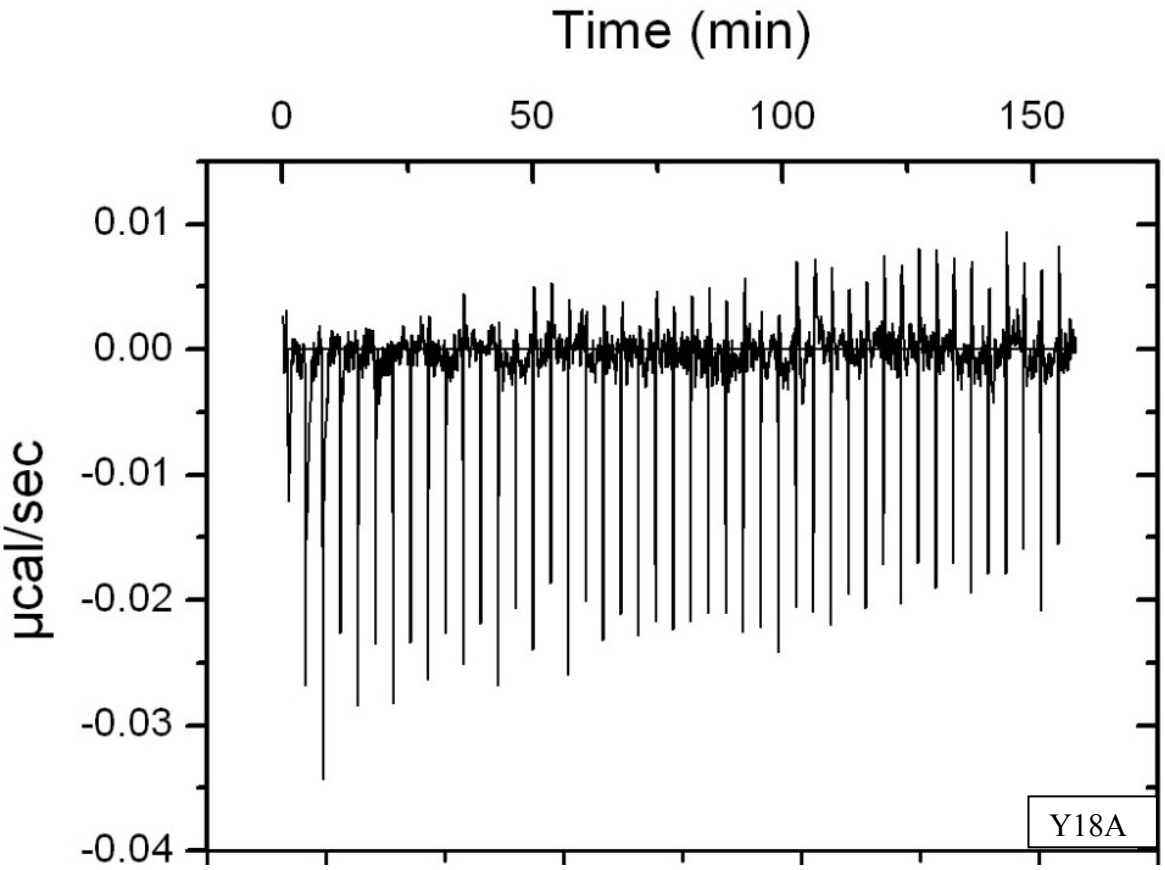

Figure 5.25. Isothermal titration calorimetry of Y18A-HDAC8.
Titration of 10 µM Y18A-HDAC8 enzyme with 200 µM SAHA was carried out at 25 °C. The top panel shows the raw calorimetric data as a function of time in minutes whereas the bottom panel shows the integrated heat per injection versus the molar ratio of SAHA to mutant enzyme in each case. The solid smooth line corresponds to the best fit of the experimental data to a single binding site model, providing parameters of enthalpy change and binding affinity as shown in Table 5.8.

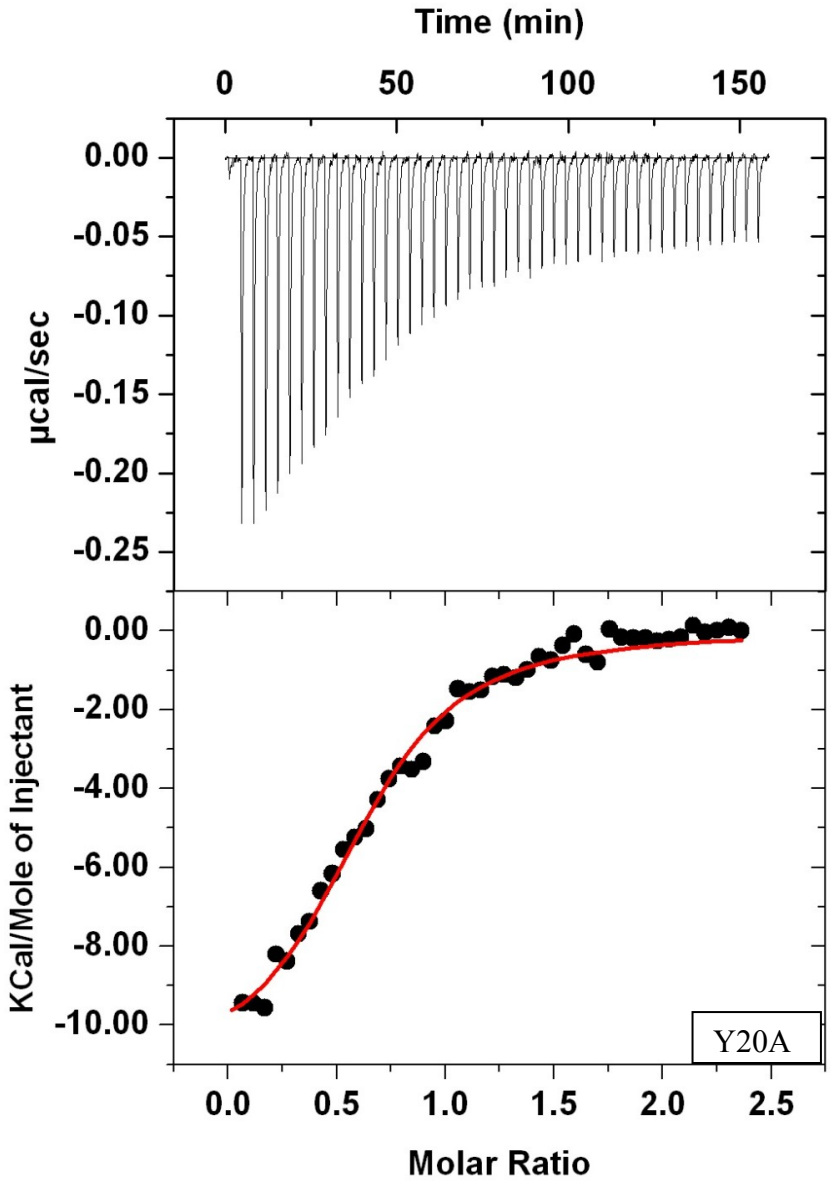

Figure 5.26. Isothermal titration calorimetry of Y20A-HDAC8.
Titration of 10 µM Y20A-HDAC8 enzyme with 200 µM SAHA was carried out at 25 °C. The top panel shows the raw calorimetric data as a function of time in minutes whereas the bottom panel shows the integrated heat per injection versus the molar ratio of SAHA to mutant enzyme in each case. The solid smooth line corresponds to the best fit of the experimental data to a single binding site model, providing parameters of enthalpy change and binding affinity as shown in Table 5.8.

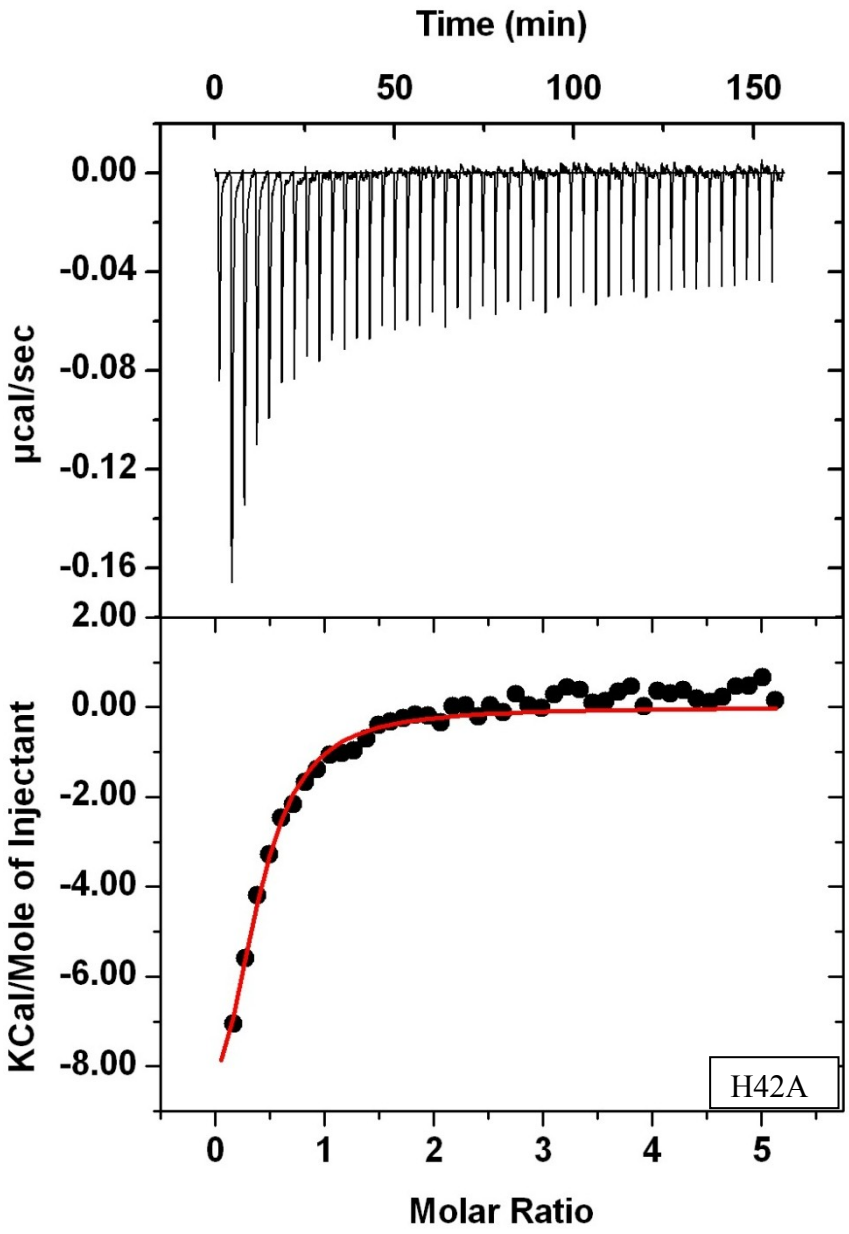

Figure 5.27. Isothermal titration calorimetry of H42A-HDAC8.
Titration of 10 µM H42A-HDAC8 enzyme with 200 µM SAHA was carried out at 25 °C. The top panel shows the raw calorimetric data as a function of time in minutes whereas the bottom panel shows the integrated heat per injection versus the molar ratio of SAHA to mutant enzyme in each case. The solid smooth line corresponds to the best fit of the experimental data to a single binding site model, providing parameters of enthalpy change and binding affinity as shown in Table 5.8.

Assuming the standard state, the free energy changes (ΔG^0) for the binding of wt-HDAC8, Y20A-HDAC8 and H42A-HDAC8 were calculated ($\Delta G^0 = -RT \ln K_a$) as -8.2, -8.2 and -8.3 kcal/mole, respectively.

Table 5.8. Isothermal Titration Calorimetry (ITC) Analysis of Wild Type and Mutant HDAC8 Enzymes with SAHA

HDAC8	K_a (M^{-1})	N	ΔH (cal mol^{-1})	ΔS (cal $mol^{-1}deg^{-1}$)
Wild type	1.10E6 ± 2.34E5	0.755 ± 0.0439	-1.009E4 ±751.8	-6.19
Y18A	n.d.	n.d	n.d.	n.d.
Y20A	1.10E6 ± 1.18E5	0.644 ± 0.016	-1.135E4 ±379.6	-10.4
H42A	1.37E6±3.73E5	0.361 ± 0550.	-1.047E4 ±204.6	-7.03

Thus, the casual perusal of data suggested that Y18A-HDAC8 mutant appeared to display significantly different characteristics as compared to either the wild type HDAC8 or the other two HDAC8 mutants.

5.8. Circular Dichroism Studies to Determine the Conformational Stability of the Wild Type and Mutant HDAC8 Enzymes

5.8.1. Circular Dichroic Spectra of Wild Type and HDAC8 Mutant Enzymes

Due to the striking behavior of the Y18A-HDAC8 mutant, its circular dichroism (CD) spectrum was recorded in the far-UV region to ascertain if the altered behavior was due to a change in the secondary structure. Circular dichroic (CD) spectra were measured on a J-815 spectropolarimeters (Tokyo, Japan) using a 1 mm path length quartz cuvette and nitrogen flow rate of 40 ft^3 $hour^{-1}$. A total volume of 150 µL containing 8 µM HDAC8 enzyme (either wild type or mutant) prepared in a buffer containing 5 mM Tris-HCl (pH 8.0), 0.5 % glycerol, 0.1 mM DTT and 15 mM KCl was used. As control, similar analysis was also performed for the wild type HDAC8 as well as Y20A and H42A HDAC8 mutants, for comparative studies. Figure 5.28

depicts far-UV CD spectra for wild type and the Y18A, Y20A and H42A HDAC8 mutants. For each enzyme, the spectrum displays a maximum at approximately 195 nm as well as two minima at 223 nm and 208 nm. The observed spectra are the characteristic of the proteins rich in α-helix. The wild type spectrum obtained was found to be quite similar to the one reported earlier by Vannini et al. (70). The CD spectra shown in the Figure 5.28 are largely identical except for the Y18A mutant that displays a different profile at 222 nm. The CD spectra of the wild type HDAC8 and Y18A-HDAC8 were subjected to the *Dichroweb* analysis (an online tool for the secondary structure analysis of proteins) utilizing the K2D algorithm to determine the secondary structural composition of both the enzymes. The analysis provided the percentages of the α-helical, β-sheet and the random coil content of these proteins. The experimental and the fitted spectra (obtained from the analysis of the CD data) are represented by the green and blue lines, respectively. According to this analysis (Figure 5.28 (b)), wt-HDAC8 comprised of 50% α-helix, 8% β-sheets and 42% random coil (NRMSD= 0.065). Similar analysis for Y18A-HDAC8 (Figure 5.28 (c)) computed values of 45% α-helix, 19% β-sheet and 36% random coil (NRMSD= 0.089). According to the analysis of HDAC8 crystal structure (PDB ID. 1T69)(70),these values were found to be 37% α-helix, 11% β-sheet and 52% random coil, closely matching the HDAC8 values obtained above . The above analysis thus reveals differences in secondary structure content of the wild type HDAC8 and the Y18A-HDAC8 mutant, with the latter displaying a higher content of β-sheets compared to wild type HDAC8. This altered secondary structure may in turn affect the enzymatic activity of Y18A-HDAC8 while contributing to its higher stability.

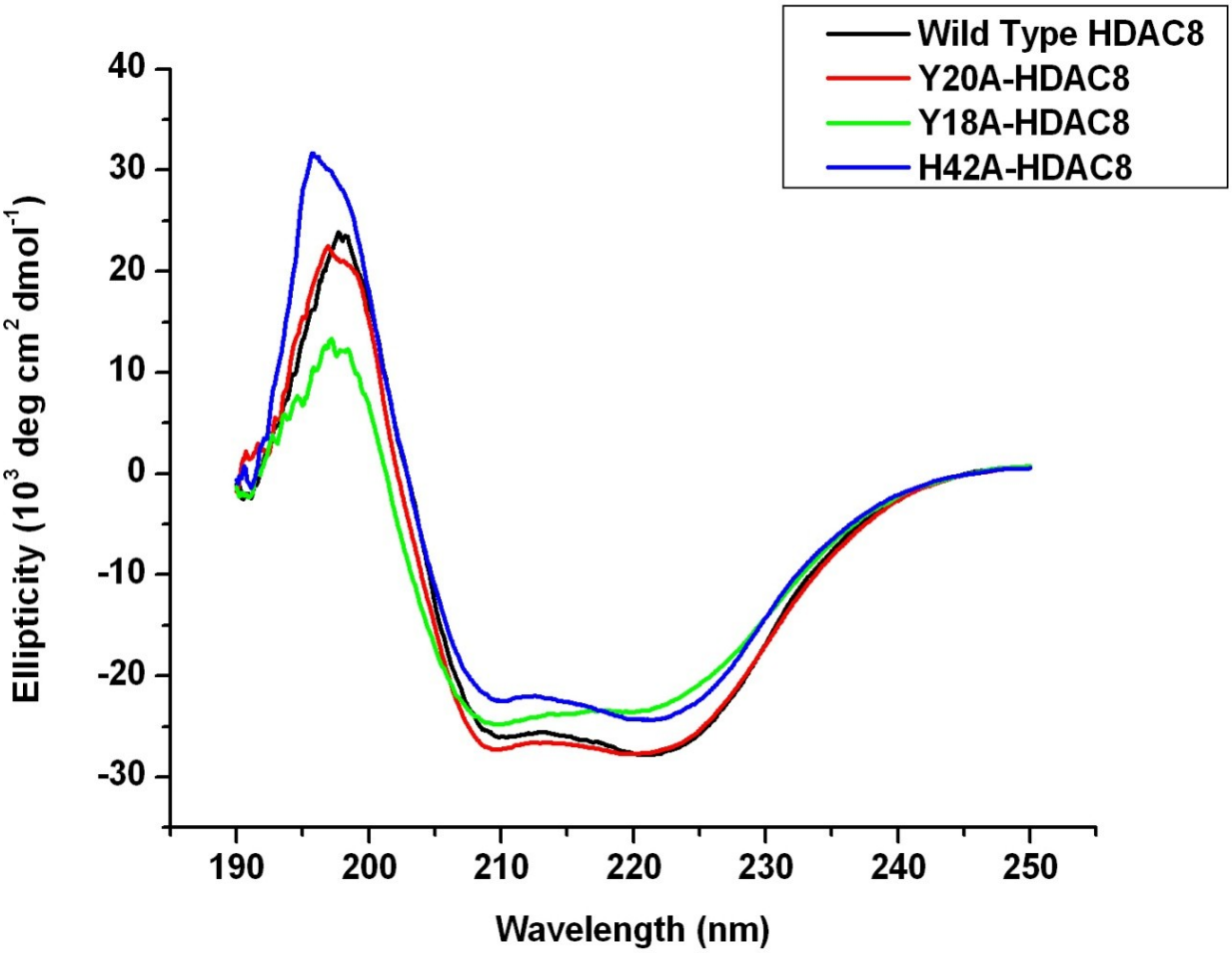

Figure 5.28a. Comparison of circular dichroism (CD) spectra of the wild type and mutant HDAC8 enzymes.
For each enzyme, 8 µM protein was dialyzed into 5 mM Tris-HCl (pH 8.0), 0.5 % glycerol, 0.1 mM DTT and 15 mM KCl. The dialyzed protein (150 µl) was pipetted into a 0.1 cm path length quartz cuvette and spectra were measured at 25 °C. The profiles shown above reflect the average of five CD scans for each enzyme under identical experimental conditions. The Y-axis here shows the ellipticity of the HDAC8 enzymes at each wavelength.

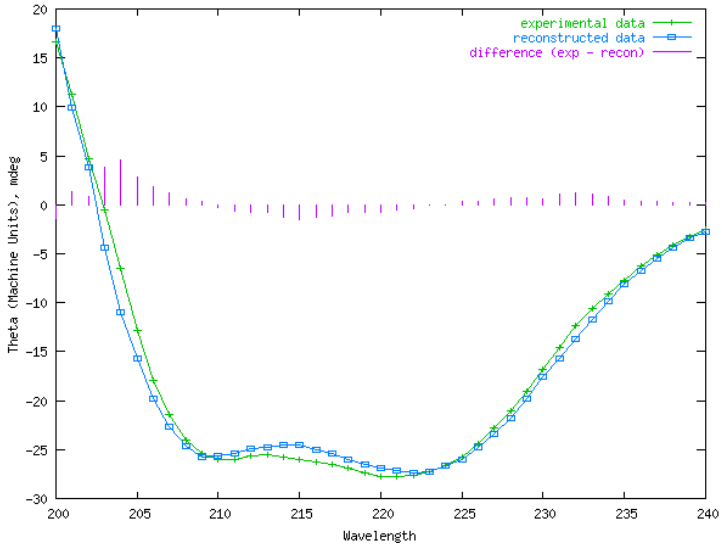

Figure 5.28b. Dichroweb analysis of the circular dichroism spectra of WT-HDAC8 enzyme. The data obtained were analyzed using a K2D analysis algorithm, which provided a theoretical estimate of the secondary structure composition of the wild type HDAC8 as 50% α-helix, 8% β-sheets and 42% random coil with NRMSD = 0.065. The green and blue curves represent the experimental and the fitted results, respectively.

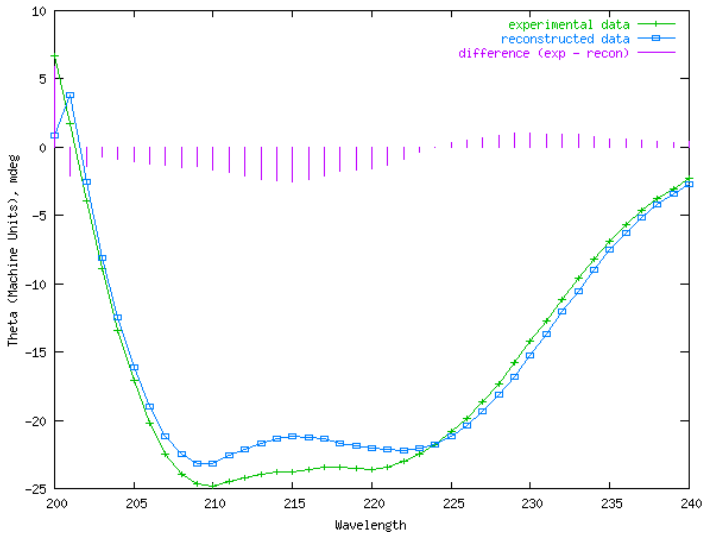

Figure 5.28c. Dichroweb analysis of the circular dichroism spectra of Y18A-HDAC8 enzyme. The data obtained were analyzed using a K2D analysis algorithm, which provided a theoretical estimate of the secondary structure composition of the Y18A- HDAC8 as 45% α-helix, 19% β-sheets and 36% random coil with NRMSD = 0.089. The green and blue curves represent the experimental and the fitted results, respectively.

5.8.2. Thermal Denaturation of Wild Type and Mutant HDAC8 Enzymes

Circular dichroic spectra revealing a change in the profile of the HDAC8 enzymes (especially Y18A-HDAC8) were suggestive of further experiments to monitor the equilibrium unfolding of each enzyme as a function of temperature at 222 nm, the wavelength at which differences in CD spectra of wild type HDAC8 and Y18A-HDAC8 were detected. This wavelength of 222 nm is monitored for the proteins which have a higher α-helical content such as HDAC8, in the present study. These experiments were important to determine the effect of exit tunnel mutations on the overall stability of the wild type and mutant HDAC8 enzymes. These experiments were performed with 8 μM HDAC8 enzyme (both wild type and the mutants) in CD buffer (see section 4.6 for composition of buffer). The thermal denaturation profiles of the wild type HDAC8, Y20A-HDAC8 and H42A-HDAC8 enzymes are shown in Figure 5.29. The thermal denaturation profile for Y18A-HDAC8 is shown in Figure 5.30. The increase in ellipticity accompanying the increase in temperature was monitored over a range of temperatures as follows: 12 °C-55 °C for wild type HDAC8 (Figure 5.29, panel A) and H42A-HDAC8 (Figure 5.29, panel C), 12 °C-42 °C for Y20A-HDAC8 (Figure 5.29, panel B) and 12 °C-90 °C for Y18A-HDAC8 (Figure 5.30, panel A). The data for wild type, Y20A and H42A HDAC8 enzymes was fitted according to the Santoro-Bolen equation (Eq. no. 4.9) based on a two- phase transition between the native and denatured forms for each enzyme. However, it was evident from the profile of Y20A-HDAC8 that this mutant enzyme was relatively unstable compared to the wild type and H42A-HDAC8. In initial experiments, the Y20A-HDAC8 enzyme precipitated as the temperature was raised over 45 °C. Therefore, the Y20A-HDAC8 experiment was repeated with a lower final temperature of 42 °C. Interestingly, the Y18A-HDAC8 mutant

showed a 3-phase transition, indicating its unusual stability compared to the other HDAC8 enzymes. Since the Santoro-Bolen equation is good only for fitting data acquired from a bi-phasic transition, the Boltzmann 2 equation (Eq. 4.10) was used instead to fit the thermal denaturation profile of Y18A-HDAC8. However, panel B of Figure 5.30 shows the Santoro-Bolen fit of the first transition of Y18A-HDAC8, from where the enthalpy of the unfolding was calculated for the first transition. This was not possible for the second transition as the amplitude of the change was too short and data appeared to be too noisy to be fitted with Santoro-Bolen equation. The melting temperatures (T_m) of the wild type and the mutant HDAC8 enzymes as well as their van't -Hoff enthalpies of unfolding have been listed in Table 5.9. The van't –Hoff enthalpies were computed to be 74.06 ± 1.40 kJ/mol, 39.11 ± 0.94 kJ/mol (phase 1 only), 73.72 ± 3.38 kJ/mol and 82.65 ± 3.57 kJ/mol for wt-HDAC8, Y18A-HDAC8, Y20A-HDAC8 and H42A-HDAC8, respectively. The T_m for wild type HDAC8, Y20A-HDAC8 and H42A-HDAC8 was calculated to be 312.10 ± 0.07 K, 309.34 ± 0.16 K and 310.56 ± 0.12 K. As is clear from these data, the melting temperatures forY20A-HDAC8 and H42A-HDAC8 are slightly lower than that of the wild type. Therefore, we can say that these two mutants have become slightly thermally unstable. Y18A-HDAC8, on the other hand has two melting temperatures (T_{m1} = 306.66 ± 0.12 K and T_{m2} =383.55 ± 0.11 K) indicative of two populations of this mutant enzyme. First population is somewhat similar to wild type in stability but the second population shows a very high thermal stability as revealed by a higher melting temperature for this phase.

Table 5.9. Thermal Denaturation of Wild Type and Mutant HDAC8 Enzymes using CD Spectroscopy Signal to Compute van't-Hoff enthalpy and the Melting Temperatures

HDAC8	H (kJ mol^{-1})	T_m (Kelvin)
Wild Type	74.06 ± 1.40	312.10 ± 0.07
Y18A	39.11 ± 0.94 (phase 1 only)	306.66 ± 0.12, 383.55 ± 0.11
Y20A	73.72 ± 3.38	309.34 ± 0.16
H42A	82.65 ± 3.57	310.56 ± 0.12

5.8.3. Temperature-induced Unfolding of Wild Type and Mutant HDAC8 Enzymes as a Function of Time Monitored by Circular Dichroic Spectroscopy

Following the analysis of equilibrium thermal unfolding of the wild type and mutant HDAC8 enzymes, it was of interest to ascertain the kinetic profiles for their thermal denaturation. The kinetic profiles of unfolding were determined as a function of a specific temperature. The time-dependent changes in the secondary structure were measured on a Jasco J-815 CD instrument with the temperatures maintained by the Peltier temperature controller. The quartz cuvette (1 mm path-length), containing 8 μM HDAC8 enzyme prepared in a buffer containing 5 mM Tris-HCl (pH 8.0), 0.5 % glycerol, 0.1 mM DTT and 15 mM KCl, in a total volume of 150 μL, was placed in the cuvette holder and the temperature was allowed to stabilize (~25 seconds).

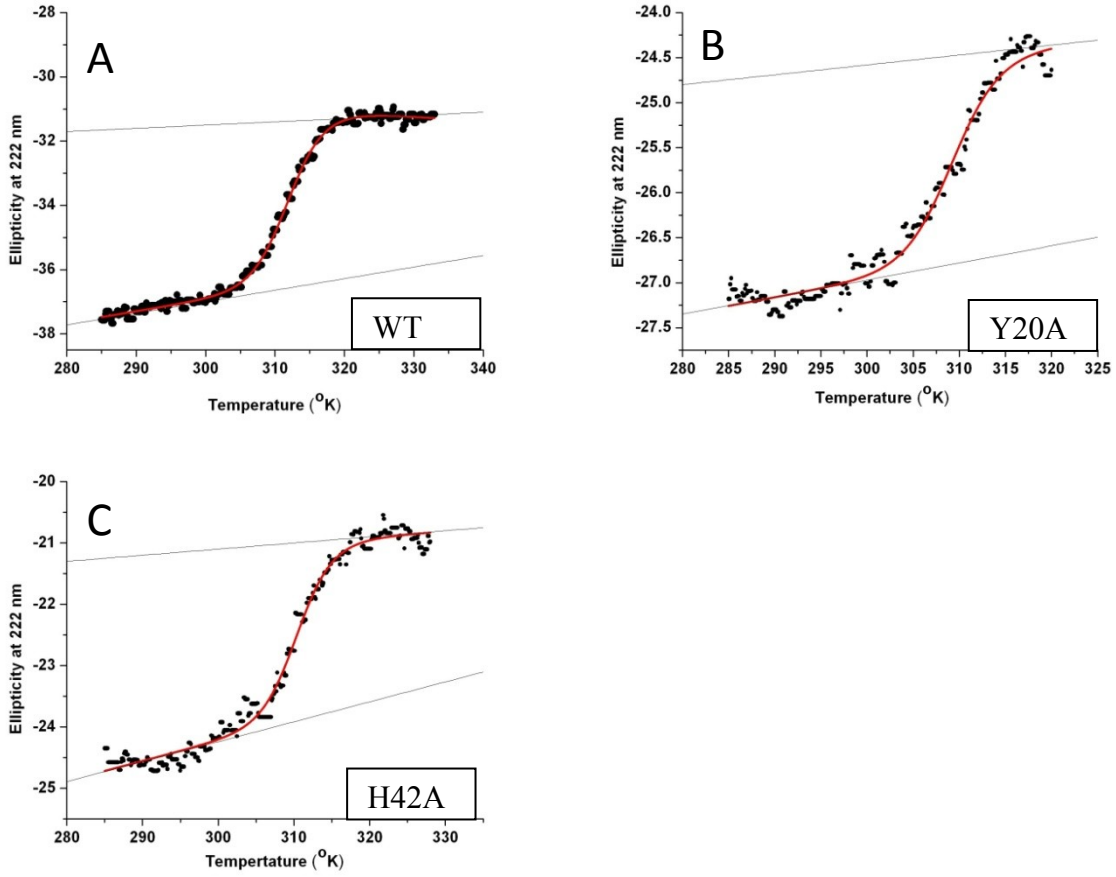

Figure 5.29. Thermal denaturation profiles of WT-HDAC8 (A), Y20A-HDAC8 (B) and H42A-HDAC8 (C).
Each protein (8 µM) was dialyzed into 5 mM Tris-HCl (pH 8.0), 0.5% glycerol, 0.1 mM DTT and 15 mM KCl and 150 µl of the dialyzed protein was pipetted into a 0.1 cm path length quartz cuvette. Data acquisition was started after a delay time of 25 sec. Thermal unfolding at 222 nm was acquired for a range of temperatures (12°C – 55°C) at a scan rate of 1°C min^{-1}. Data were analyzed by Santoro-Bolen equation (Eq. no. 4.9) for wt-HDAC8 (Panel A), H42A-HDAC8 (Panel C) and Y20A-HDAC8 (Panel B) for the 2-phase transition observed in each case, to calculate the van't-Hoff enthalpies of unfolding and the melting temperatures (T_m).

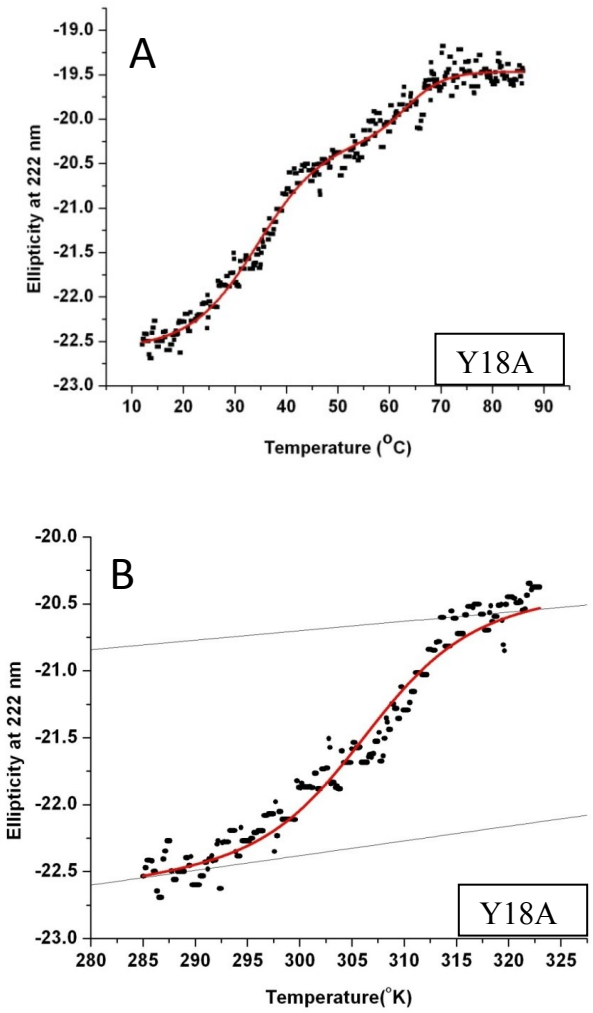

Figure 5.30. Thermal denaturation of Y18A-HDAC8.
The thermal denaturation data of Y18A-HDAC8 was analyzed by the Boltzmann equation (eq. no. 4.10) (Panel A) as it was a 3-phase transition (Folded-intermediate-unfolded) and T_m for each transition was determined. Panel B shows the Santoro-Bolen fit of the first phase of Y18A-HDAC8 denaturation separately but the second phase could not be fitted because it was short and too noisy compared to the first phase.

The time-dependent ellipticity at 222 nm (θ_{222}) at a fixed temperature was monitored for up to 1 hour and the data was analyzed. Consequently, experiments were performed in a standard CD spectrometer by monitoring θ_{222} for the wild type and mutant HDAC8 enzymes as a function of time at a fixed temperature. The time-traces were monitored until the changes in θ_{222} were no longer significant (approximately 1 hour). These experiments were carried out at temperatures ranging from 35 ºC – 50 ºC for wild type HDAC8 and H42A-HDAC8, 35 ºC -65 ºC for Y18A-HDAC8 and 35 ºC -43 ºC for Y20A-HDAC8. Figures 5.31, 5.32, 5.33 and 5.34 depict the representative kinetic profiles of the unfolding of wild-type HDAC8, Y18A, Y20A and H42A HDAC8 mutants, respectively.

The results demonstrated that at all temperatures analyzed, the data for wild type and HDAC8 mutant enzymes conformed to a biphasic kinetic profile except in the case of Y20A-HDAC8 that displayed a single-phase kinetic profile indicating a single step reaction. The fitted parameters for the time-dependent changes in θ_{222} as a function of temperature were generated using equations 4.11 and 4.12 (see section 4.6.2) and are summarized in Tables 5.10, 5.11, 5.12and 5.13 which list the values of the rate constants and the amplitudes at different temperatures for the wild type, Y18A, Y20A and H42A HDAC8 enzymes, respectively.

It was noticed upon inspection of the data in Table 5.10 that the offset and the amplitude of the larger rate constant (A_1) increased as a function of temperature. As is evident from the data in Tables 5.10, 5.11, 5.12 and 5.13 the first amplitudes (A_1) increase linearly with the temperature. In contrast to the behavior of A_1, the amplitude of the slow rate constant (A_2) decreased with the increase in temperature until there was no further change. Similarly, the observed rate constant k_1 exhibited a dependence on the experimental temperature whereas k_2

appeared to remain relatively unchanged and can account for the isomerization step in the catalysis. The increase in k_1 was observed as a function of temperature and was approximately 3.8 fold for wild type, 2.45 fold for Y18A, 7.45 fold for Y20A and 3.90 fold for H42A HDAC8 enzymes. Inspection of the data in Tables 5.10 through 5.13, suggests that wild type and H42A HDAC8 unfolded at nearly the same rate and show a similar increase in k_1,while for the Y20A HDAC8 mutant, the rate of unfolding was very high, indicating its increased susceptibility to the rise in temperature. For Y18A HDAC8, the rate of unfolding was very high to begin with and did not increase much with increase in temperature, indicating its already unfolded conformation due to mutation.

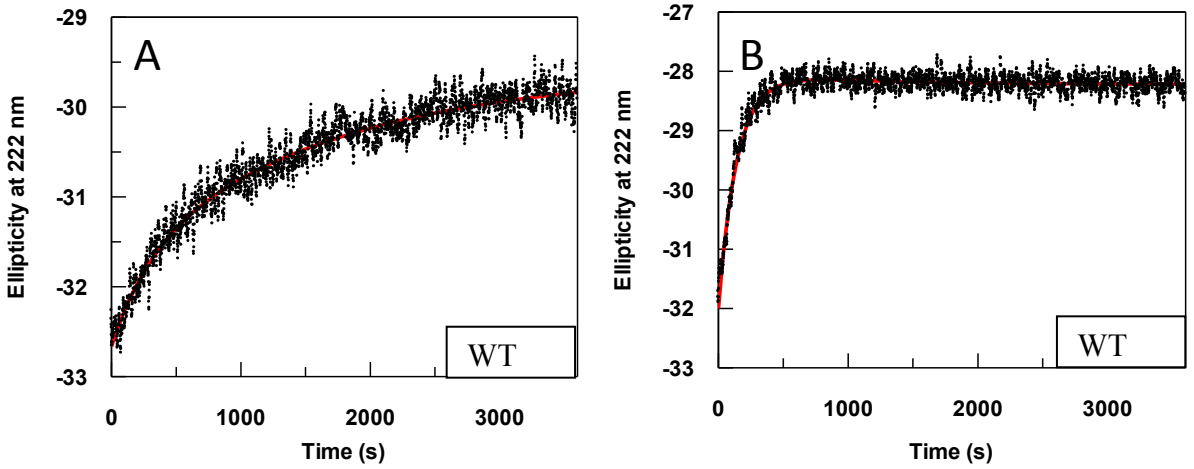

Figure 5.31. Rates of thermal unfolding of WT-HDAC8 at 35 °C (panel A) and 42 °C (panel B). Wild type HDAC8 protein (8 µM) was dialyzed into 5 mM Tris-HCl (pH 8.0), 0.5% glycerol, 0.1 mM DTT and 15 mM KCl and 150 µl of the dialyzed enzyme was pipetted into a 0.1 cm path length quartz cuvette. After equilibration for 2 min at room temperature, the cuvette was placed in a cuvette holder previously equilibrated to the temperature desired for the experiment. Data acquisition was initiated after a delay time of 25 s. The data was analyzed using eq. no. 4.11 and the solid red line represents the best fit of the data. The kinetics of unfolding followed a bi-exponential path. The computed rate constants and the amplitudes have been tabulated in Table 5.10.

Table 5.10. Kinetic Parameters for the Thermal Unfolding of WT-HDAC8 at Different Temperatures

Temperature (^{0}Celsius)	k_1 (s^{-1})	k_2 (s^{-1})	Amplitude 1 (A1) (mdeg)	Amplitude 2 (A2) (mdeg)
35	$3.5e^{-3} \pm 3e^{-4}$	$6e^{-4} \pm 3.9e^{-5}$	0.90 ± 0.07	2.16 ± 0.05
40	$4e^{-3} \pm 7.02e^{-5}$	$3.8e^{-3} \pm 2e^{-4}$	2.76 ± 0.03	0.75 ± 0.03
42	$7e^{-3} \pm 1e^{-4}$	$1e^{-3} \pm 3e^{-4}$	3.9 ± 0.04	-0.19 ± 0.03
45	$8.9e^{-3} \pm 3e^{-4}$	$3.4e^{-3} \pm 3e^{-4}$	4.76 ± 0.10	-1.24 ± 0.11
47	$13.3e^{-3} \pm 3e^{-4}$	$3.4e^{-3} \pm 2e^{-4}$	5.11 ± 0.06	-1.1 ± 0.06
50	$14e^{-3} \pm 3e^{-4}$	$5.5e^{-3} \pm 2e^{-4}$	6.10 ± 0.11	-1.8 ± 0.12

k_1: First rate constant
k_2: Second rate constant
mdeg: Milli degrees
s: seconds

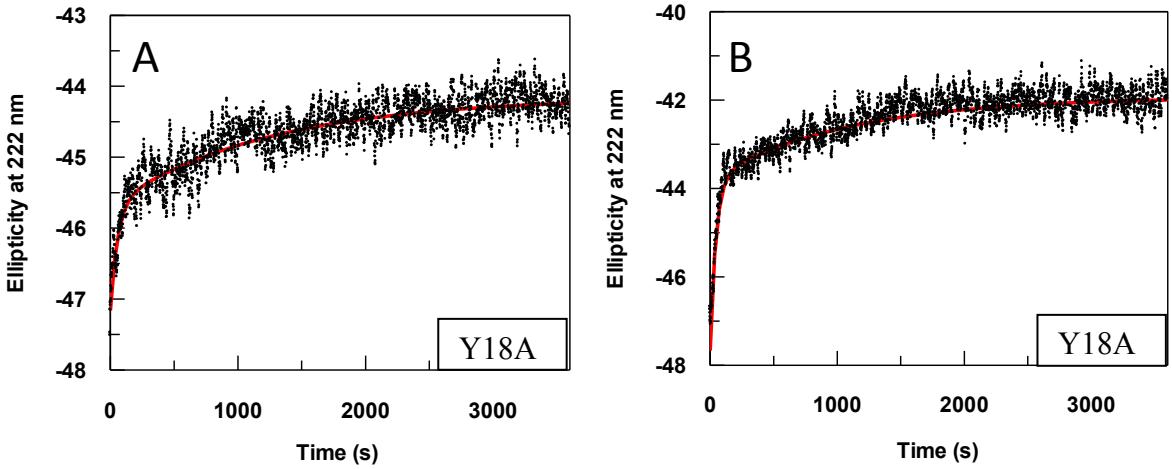

Figure 5.32. Rates of thermal unfolding of Y18A-HDAC8 at 35°C (panel A) and 45°C (panel B). The Y18A-HDAC8 protein (8 µM) was dialyzed into 5 mM Tris-HCl (pH 8.0), 0.5% glycerol, 0.1 mM DTT and 15 mM KCl and 150 µl of the dialyzed enzyme was pipetted into a 0.1 cm path length quartz cuvette. After equilibration for 2 min at room temperature, the cuvette was placed in a cuvette holder previously equilibrated to the temperature desired for the experiment. Data acquisition was initiated after a delay time of 25 s. The data was analyzed using eq. no. 4.11and the solid red line represents the best fit of the data. The kinetics of unfolding followed a bi-exponential path. The computed rate constants and the amplitudes have been tabulated in Table 5.11

Table 5.11. Kinetic Parameters for the Thermal Unfolding of the Y18A-HDAC8 at Different Temperatures

Temperature (^{0}Celsius)	k_1 (s^{-1})	k_2 (s^{-1})	Amplitude (A1) (mdeg)	Amplitude (A2) (mdeg)
35	$1.75e^{-2} \pm 8e^{-4}$	$8e^{-4} \pm 3.32e^{-5}$	1.49 ± 0.04	1.51 ± 0.01
40	$1.80e^{-2} \pm 6e^{-4}$	$4e^{-4} \pm 1.66e^{-5}$	3.40 ± 0.06	2.19 ± 0.01
45	$2.19e^{-2} \pm 6e^{-4}$	$9e^{-4} \pm 2.14e^{-5}$	3.87 ± 0.07	1.86 ± 0.02
50	$2.31e^{-2} \pm 8e^{-4}$	$6e^{-4} \pm 2.49e^{-5}$	4.56 ± 0.09	2.35 ± 0.02
55	$4.29e^{-2} \pm 1.8e^{-3}$	$1.4e^{-3} \pm 2.43e^{-5}$	5.23 ± 0.12	3.34 ± 0.03
60	$4.26e^{-2} \pm 2.5e^{-3}$	$2.3e^{-3} \pm 2.19e^{-5}$	5.46 ± 0.16	7.07 ± 0.04
65	$4.13e^{-2} \pm 1.3e^{-3}$	$2.3e^{-3} \pm 2.76e^{-5}$	6.97 ± 0.12	5.44 ± 0.04

k_1: First rate constant
k_2: Second rate constant
mdeg: Milli degrees
s: seconds

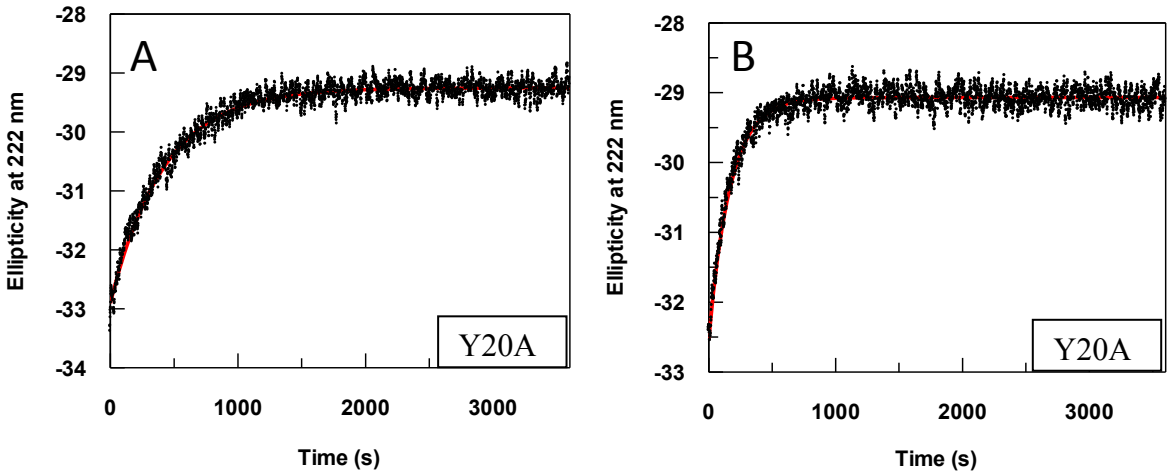

Figure 5.33. Rates of thermal unfolding of Y20A-HDAC8 at 35°C (panel A) and 39°C (panel B). The Y20A-HDAC8 protein (8 µM) was dialyzed into 5 mM Tris-HCl (pH 8.0), 0.5% glycerol, 0.1 mM DTT and 15 mM KCl and 150 µl of the dialyzed enzyme was pipetted into a 0.1 cm path length quartz cuvette. After equilibration for 2 min at room temperature, the cuvette was placed in a cuvette holder previously equilibrated to the temperature desired for the experiment. Data acquisition was initiated after a delay time of 25 s. The data was analyzed using eq. no. 4.12 and the solid red line represents the best fit of the data. The kinetics of unfolding followed a bi-exponential path. The computed rate constants and the amplitudes have been tabulated in Table 5.12.

Table 5.12. Kinetic Parameters for the Thermal Unfolding of Y20A-HDAC8 at Different Temperatures

Temperature (°Celsius)	k_1 (s^{-1})	Amplitude (A1) (mdeg)
35	$2.4e^{-3} \pm 1.48e^{-5}$	3.65 ± 0.01
37	$4.1e^{-3} \pm 3.29e^{-5}$	3.32 ± 0.01
39	$5.9e^{-3} \pm 5.12e^{-5}$	3.46 ± 0.02
41	$11.2e^{-3} \pm 1e^{-4}$	4.17 ± 0.02
43	$17.9e^{-3} \pm 3e^{-4}$	3.96 ± 0.04

k_1: First rate constant
mdeg: mill degrees
s: seconds

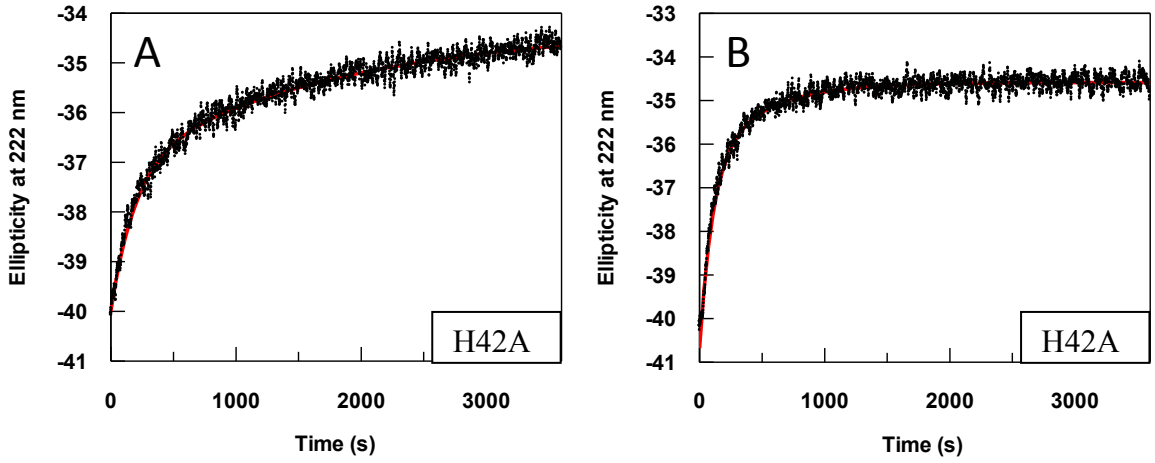

Figure 5.34. Rates of thermal unfolding of H42A-HDAC8 at 35°C (panel A) and 40°C (panel B). The H42A-HDAC8 protein (8 µM) was dialyzed into 5 mM Tris-HCl (pH 8.0), 0.5% glycerol, 0.1 mM DTT and 15 mM KCl and 150 µl of the dialyzed enzyme was pipetted into a 0.1 cm path length quartz cuvette. After equilibration for 2 min at room temperature, the cuvette was placed in a cuvette-holder previously equilibrated to the temperature desired for the experiment. Data acquisition was initiated after a delay time of 25 s. The data was analyzed using eq. no. 4.11 and the solid red line represents the best fit of the data. The kinetics of unfolding followed a bi-exponential path. The computed rate constants and the amplitudes have been tabulated in Table 5.13.

Table 5.13. Kinetic Parameters for the Thermal Unfolding of the H42A-HDAC8 at Different Temperatures

Temperature (^{0}Celsius)	k_1 (sec^{-1})	k_2 (sec^{-1})	Amplitude (A1) (mdeg)	Amplitude (A2) (mdeg)
35	$5.2e^{-3} \pm 1e^{-4}$	$6e^{-4} \pm 2.17e^{-5}$	2.87 ± 0.04	2.82 ± 0.02
37	$6.5e^{-3} \pm 1e^{-4}$	$9e^{-4} \pm 2.2e^{-5}$	3.89 ± 0.03	2.38 ± 0.03
40	$9.5e^{-3} \pm 2e^{-4}$	$5e^{-4} \pm 7.8e^{-5}$	4.14 ± 0.08	1.95 ± 0.09
42	$7.1e^{-3} \pm 8.8e^{-5}$	$5e^{-4} \pm 6.2e^{-5}$	5.39 ± 0.03	0.75 ± 0.01
45	$13.8e^{-3} \pm 1e^{-4}$	$4e^{-4} \pm 4.4e^{-5}$	6.90 ± 0.03	0.48 ± 0.10
47	$13.7e^{-3} \pm 1e^{-4}$	$2e^{-4} \pm 7.05e^{-5}$	6.91 ± 0.03	0.64 ± 0.10
50	$20.3e^{-3} \pm 1e^{-4}$	$9e^{-4} \pm 5.6e^{-5}$	7.12 ± 0.02	0.17 ± 0.01

k_1: First rate constant
k_2: Second rate constant
mdeg: Milli degrees

Since the dependence of the rate constants upon temperature was found to be non-linear, the data were plotted using the natural log of the observed rate constants as a function of the inverse temperature (expressed in Kelvin) to generate an Arrhenius plot. Using this plot, the observed activation energies (E_a) for the processes giving rise to k_1 could be calculated from the slope of the plot (equal to $-E_a / R$) with the Arrhenius pre-exponential factor or the frequency factor (A) given by the Y-axis intercept (equal to ln (A)) using equation 4.13 (see section 4.6.2). An Arrhenius plot was not generated for k_2 since latter remained relatively unchanged.

Figure 5.35 depicts the resulting Arrhenius plots for k_1 for the wild type, Y18A, Y20A and H42A HDAC8 enzymes in panels A, B, C and D, respectively. The dependence of the natural log of k_1 was linear throughout, with calculated activation energies of 19.89 kcal mol^{-1}, 7.28 kcal mol^{-1}, 48.43 kcal mol^{-1} and 16.95 kcal mol^{-1} for the wild type, Y18A, Y20A and H42A HDAC8 enzymes, respectively (also see Table 5.14). As evident from the data, the activation

energies for the wild type HDAC8 and the H42A HDAC8 are quite similar. In contrast, Y18A HDAC8 has lower activation energy, indicating its faster unfolding, consistent with other results shown previously in this section. The only discrepancy arose for Y20A HDAC8, which despite having a low melting temperature appears to have high activation energy. Based upon an extensive search of the relevant literature, the above results were considered unique to Y20A HDAC8 unfolding and there is no precedent of such a feature with other proteins. Although it was possible to use the parameters obtained from the Arrhenius plots to calculate the transition state energies, enthalpies and entropies for the unfolding process, this analysis was not undertaken. According to Eyring theory, the ground and transition states are assumed to be in equilibrium for such calculation (174). However, the unfolding of the wild type and mutant HDAC8 enzymes was not reversible, thus altering the equilibrium between the ground and transition states. Therefore, equilibrium conditions were not met and the calculation of the thermodynamic parameters for the transition states was not pursued.

5.8.4. Determination of Histone Deacetylase Activity in Wild Type and Mutant HDAC8 Enzymes after Heat Treatment at Different Temperatures

Following the characterization of the thermodynamics and the kinetics of the unfolding of the HDAC8 enzymes, it was imperative to correlate the unfolding of the protein to its deacetylase activity at that specific temperature. Aliquots of 10 μM HDAC8 enzyme in eppendorf tubes were subjected to temperatures ranging from 35-95°C for 25 seconds in a water bath. Following the thermal denaturation, the enzyme aliquots were quickly placed on ice and an HDAC8 activity assay was set up in a microplate as described in section 4.2.1

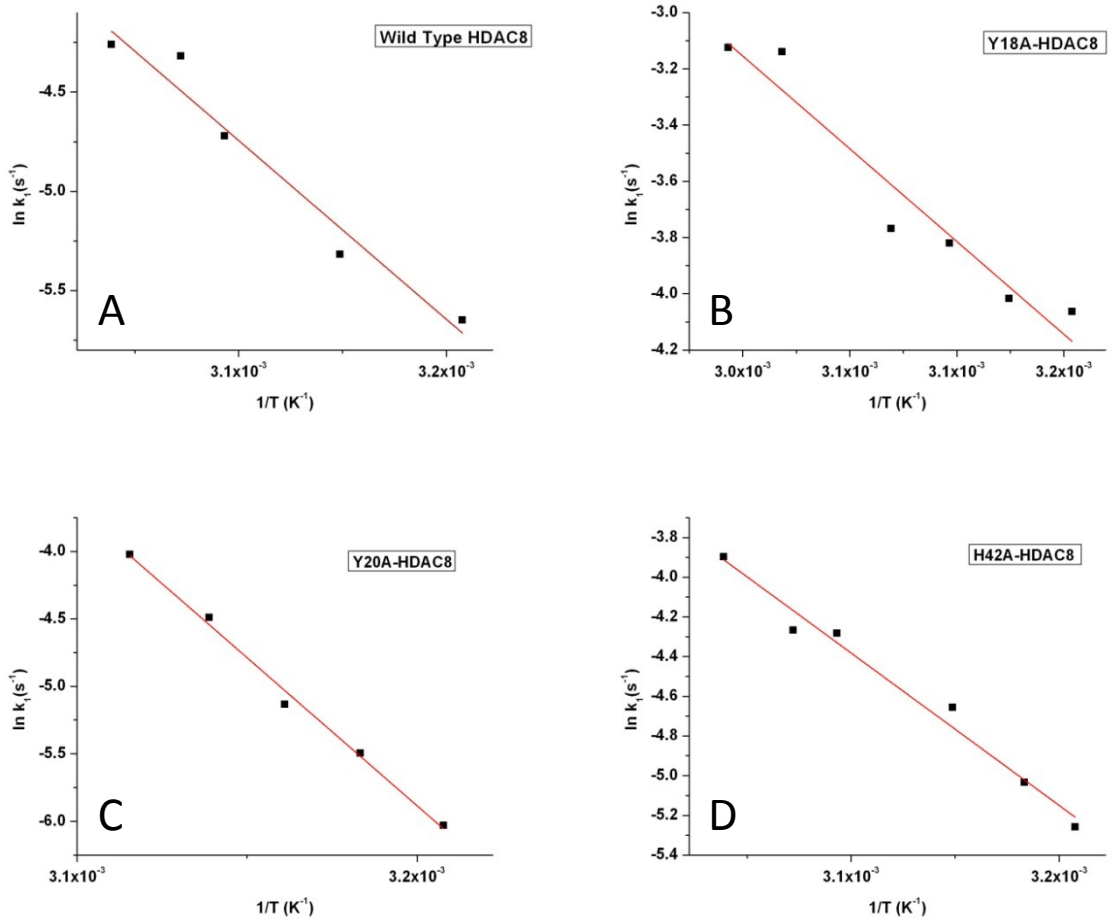

Figure 5.35. Arrhenius plots for the thermal unfolding of wild type and mutant HDAC8 enzymes.
Panel A depicts the Arrhenius plot for WT-HDAC8 faster rate constant k_1 with an E_a of 19.89 Kcal mol-1 provided by the best fit of eq. 4.13 (solid line). Panel B shows the Arrhenius plot for the Y18A-HDAC8 faster rate constant k_1 with E_a calculated as 7.28 kcal mol^{-1} provided from the best fit of eq.4.13 (solid line). Panel C shows the Arrhenius plot for the Y20A-HDAC8 faster rate constant k_1 with E_a calculated as 48.43 kcal mol^{-1} provided from the best fit of eq.4.13 (solid line) and Panel D shows the Arrhenius plot for the H42A-HDAC8 faster rate constant k_1 with E_a calculated as 16.95 kcal mol^{-1} provided from the best fit of eq.4.13 (solid line).

Table 5.14. Activation Energy of Wild Type and Mutant HDAC8 Enzymes as Computed from the Rate Constants of Thermal Denaturation

HDAC8	Activation Energy (E_a) (kcal/mol)	Enthalpy ($\Delta H^{\neq}$)(kcal/mol)	Arrhenius Factor (A) (s^{-1})
Wild Type	19.89	6.69	4.31×10^{11}
Y18A	7.28	19.30	2.275×10^{3}
Y20A	48.43	47.84	5.528
H42A	16.95	16.36	5.91×10^{8}

Each well contained 500 µM *Fluor de lys*® substrate, 1 µM HDAC8 enzyme and 250 nM trypsin in a total volume of 0.2 ml in the HDAC8 standard assay buffer. Each well of the microplate corresponded to a different temperature to which that specific HDAC8 aliquot had been exposed. Figure 5.36 shows the HDAC8 activity (of heat-treated wild type and mutant HDAC8 enzymes) as a function of temperature. As is apparent from the plots, the wild type HDAC8 and H42A-HDAC8 completely lost their activity at approximately 50 °C. This corroborates with their complete unfolding at this temperature as shown by Figure 5.29 in section 5.8.2. In contrast, for Y20A-HDAC8, a drastic fall in enzymatic activity was observed between temperatures 39°C -43°C, consistent with its complete unfolding around this temperature range. Any further increase in temperature was observed to cause precipitation of this protein. Interestingly, for Y18A-HDAC8, a very sharp drop in enzymatic activity was observed between temperatures 25 °C-45 °C, corresponding to the first phase of its tri-phasic unfolding described above. Thus, the second population of Y18A-HDAC8, despite being heat resistant, is enzymatically inactive.

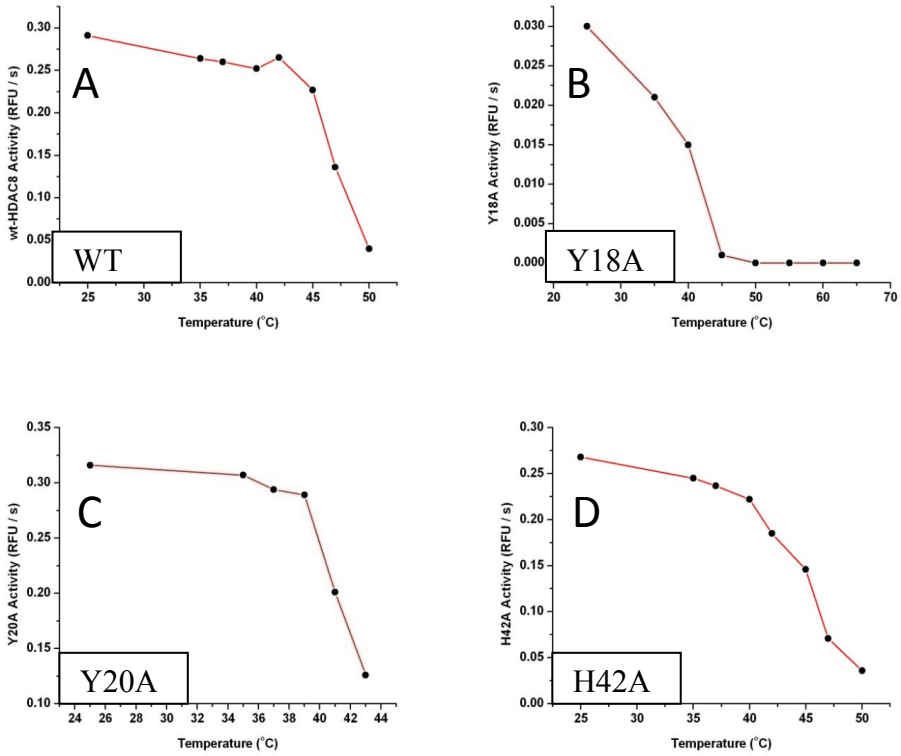

Figure 5.36. Histone deacetylase activity of heat-treated WT-HDAC8 (A) Y18A-HDAC8 (B) Y20A-HDAC8 (C) and H42A-HDAC8 (D).
Aliquots of each enzyme were treated for 25 s at the test temperature by incubation in water bath and immediately placed on ice. The activity measurement was performed in a microplate at room temperature using the HDAC8-coupled assay system (as described before) with 1 µM enzyme, 500 µM substrate, and 250 nM trypsin in HDAC8-assay buffer in each well. The deacetylase activity of each enzyme was plotted as a function of temperature to generate the enzymatic activity profile across a temperature gradient.

5.8.5. Temporal Change in Deacetylase Activity in Wild Type and Mutant HDAC8 Enzymes at a Specific Temperature (35 °C)

Both wild type and mutant HDAC8 enzymes displayed loss in deacetylase activity upon their unfolding over a range of elevated temperatures. To understand the kinetics of the enzyme unfolding at a particular temperature, it was important to perform a temporal analysis of protein unfolding at a fixed temperature. The experiment was designed based upon the kinetic profile of

each HDAC8 (section 5.8.3), and was carried out at 35 °C. To perform this, 50 µl aliquots of 10 µM HDAC8 enzyme were prepared and were subjected for different time intervals to a temperature of 35°C in a water-bath. Based upon their faster rate constants, the time intervals for Y18A-HDAC8 and Y20A-HDAC8 were designed very close to each other to enable detailed capture of the change in enzymatic activity in that time range. For the wild type and H42A-HDAC8, on the other hand, these intervals were broadly spaced as the rate constants for their unfolding were slower compared to the other two mutants. The experiment was set up in a microplate where each well corresponded to a different time interval for one specific HDAC8 enzyme. The assay conditions in each well included, 500 µM *Fluor de lys*® substrate, 250 nM trypsin, 1 µM HDAC8 enzyme in the HDAC8 standard assay buffer in a total volume of 0.2 ml. Following the completion of the assay, the percent residual activity of the HDAC8 enzyme was plotted as a function of time. A close look at figure 5.37 shows that for the same time interval of 3000 seconds, the wild type HDAC8 was more resistant to the loss of activity at 35^0C compared to H42A-HDAC8. This clearly indicates that H42A-HDAC8 mutant is more susceptible to heat-denaturation at a particular temperature for a specific time compared to the wild type HDAC8. In case of Y18A and Y20A HDAC8 mutants, a sharp drop in temporal enzymatic activity was noticed. In Y18A-HDAC8, this drop was steeper compared to Y20A-HDAC8 which relates back to the faster rate constants and the kinetic profile of the former. Thus, Y18A-HDAC8 exhibited complete loss of enzymatic activity at 500 seconds while in the case of Y20A-HDAC8 complete loss of activity occurred at 1500 seconds. These results are further indicative of the faster unfolding of the Y18A mutant in its first phase.

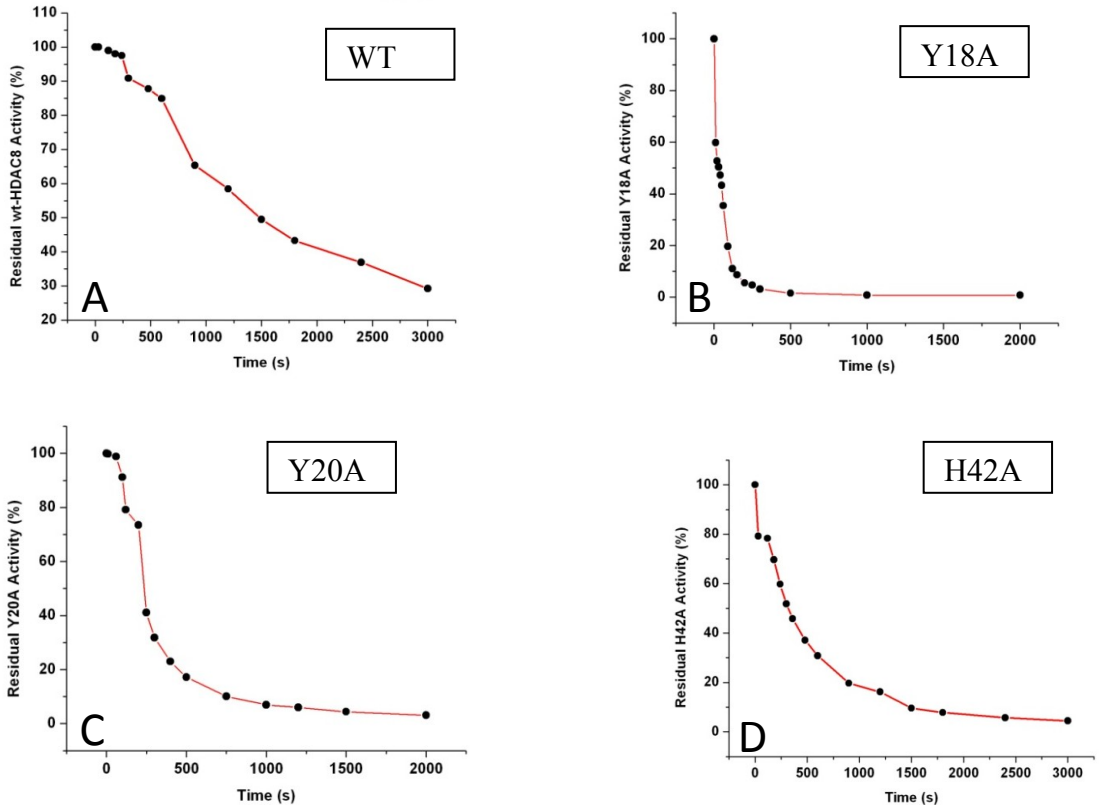

Figure 5.37. Temporal change in the deacetylase activity of the wild type and mutant HDAC8 enzymes at 35°C.
Aliquots of wt-HDAC8 and mutant HDAC8 enzymes were subjected to heat shock at 35^0C for specific time intervals, over a total period of 3000 s for WT-HDAC8 and H42A-HDAC8 (panels A & D, respectively), 2000 s for Y18A-HDAC8 and Y20A-HDAC8 (panels B & C, respectively). The above time periods were selected based upon the denaturation profile of each enzyme. Every aliquot after heat shock for specific time was placed on ice until the activity was measured. The deacetylase activity measurement was performed in a microplate at room temperature using the HDAC8-coupled assay system (as described before) with 1 µM enzyme, 500 µM substrate and 250 nM trypsin in HDAC8-assay buffer in each well. The enzyme activity was plotted as a function of time and the trend of denaturation was followed to determine the stability of the enzyme after being subjected to a particular temperature.

5.9. Studies of Wild Type and Mutant HDAC8 Enzymes with the Activator- TM-2-51

5.9.1. Modulation of Steady-state Kinetic Parameters of the Wild Type and Mutant HDAC8 by TM-2-51 and Determination of its Activation Constant for the HDAC8 Mutants- Y18A, Y20A and H42A

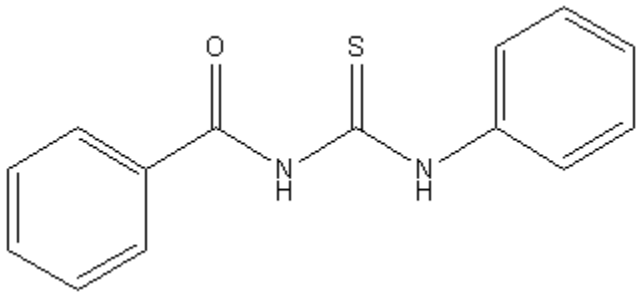

Figure 5.38. Structure of TM-2-51 (Activator of HDAC8)

TM-2-51, N-acetylthiourea-derivative, a novel activator of HDAC8 (Figure 5.38) identified recently in Srivastava lab, is the first isozyme selective activator reported for HDAC8 (151). It has been shown to activate wild type HDAC8 with an apparent activation constant of 12.5 μM. It achieves this activation by reducing K_m by 3-fold and enhancing k_{cat} by 5-fold (151). In view of delineating the mechanism of the mutant HDAC8 activation byTM-2-51, the K_m and k_{cat} values of the mutant HDAC8 catalyzed reactions were determined in the presence of saturating concentration of the activator using *Fluor de lys*® as the substrate. Figure 5.39 shows the Michaelis-Menten plot for the HDAC8-catalyzed reaction for wild-type and Y18A-HDAC8 mutant in the presence of the activator (TM-2-51). Similar, analysis was also performed for other two HDAC8 mutant enzymes. Table 5.15 lists the values for the kinetic parameters for all three HDAC8 mutants, revealing considerable changes upon the addition of the activator. The solid

smooth line is the best fit of the experimental data. In the presence of the activator, HDAC8 k_{cat} was enhanced by 7-fold in wild type, 25-fold in Y18A, 23-fold in Y20A and 11-fold in H42A mutant. The decrease in K_m values in the presence of the activator was 4-fold, 2-fold, 1.2-fold and 2.3-fold in wild type HDAC8, Y18A, Y20A and H42A mutant, respectively. Since, this change in K_m values is comparable to the wild type HDAC8, these results suggest that the above mutations may not have had a significant impact on the HDAC8 active site pocket given that the activator binds in the vicinity of the active site pocket as reported previously by AutoDock vina modeling studies (151). This information may be useful in designing compounds that can inhibit/modify the above exit-tunnel residues and thereby function as effective HDAC8 inhibitors.

As evident from the results below, TM-2-51 serves as a potent activator of mutant HDAC8 enzymes. It was of interest to determine the detailed kinetic mechanism of the enzyme catalysis in the presence of TM-2-51. To do that, apparent activation constant for TM-2-51 (activator) for Y18A, Y20A and H42A HDAC8 mutant enzymes was determined by measuring the initial velocity of the mutant HDAC8 (Y18A-HDAC8, Y20A-HDAC8 and H42A-HDAC8) catalyzed reactions as a function of the activator concentration utilizing the trypsin-coupled assay system. As evident from the data analysis performed using equation 4.5, mutant HDAC8-catalyzed reactions were sigmoidally dependent on the activator concentration. Figure 5.40 represents the cooperative fit of the activity of the mutant HDAC8 enzymes as a function of increasing activator concentration.

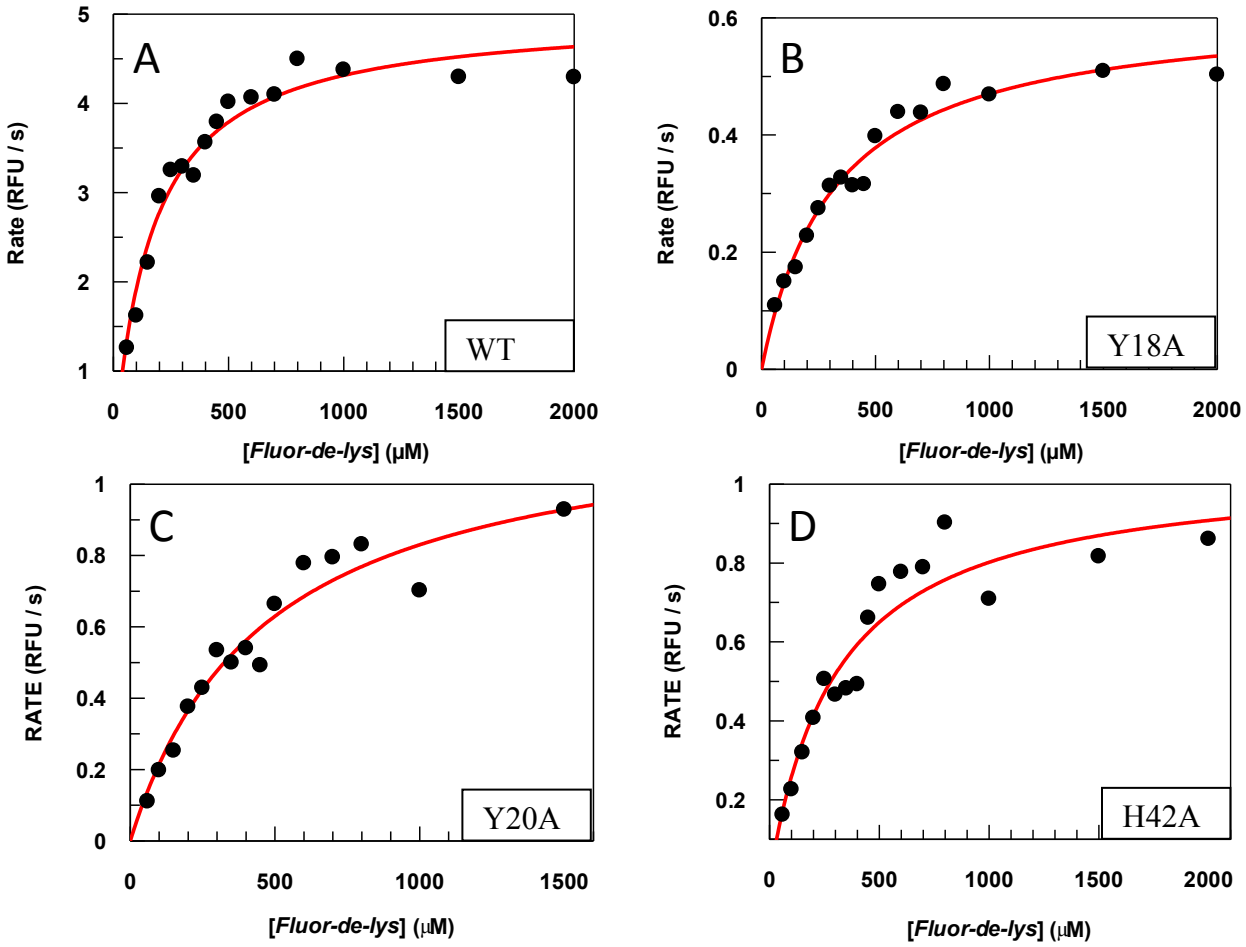

Figure 5.39. Michaelis-Menten plot of agonist-induced (TM-2-51) enzymatic activities of WT-HDAC8 (panel A), Y18A-HDAC8 mutant (panel B), Y20A-HDAC8 (Panel C) and H42A-HDAC8 (Panel D).
The reactions were performed in HDAC8 assay buffer (buffer composition described in section 4.2.1) in a microplate at room temperature using λ_{exc}= 365 nm and λ_{em}= 500 nm with a cut off filter at 455 nm. Each reaction consisted of 250 nM enzyme, 150 μM substrate, and 250nM trypsin in the assay buffer and 50 μM TM-2-51. Panel A shows the enzymatic activity of WT-HDAC8, displaying k_{cat} = 7.6 x 10^{-2} and K_m= 160.55 ± 18.19 μM. Panel B shows the enzymatic activity of Y18A-HDAC8, displaying k_{cat}= 8.72 x $10^{-3}s^{-1}$ and K_m= 320.43 ± 36.76 μM. Panel C shows the enzymatic activity of Y20A-HDAC8, displaying k_{cat}=1.76 x $10^{-2}s^{-1}$ and K_m= 465.96 ± 92.91 μM. Panel D shows the enzymatic activity of H42A-HDAC8, displaying k_{cat}= 1.52 x $10^{-2}s^{-1}$ and K_m= 305.42 ± 61.65 μM. In the presence of the activator, HDAC8 k_{cat} was enhanced by 7-fold in wild type, 25-fold in Y18A, 23-fold in Y20A and 11-fold in H42A mutant. The decrease in K_m values in the presence of the activator was 4-fold, 2-fold, 1.2-fold and 2.3-fold in wild type HDAC8, Y18A, Y20A and H42A mutant, respectively.

Table 5.15. Kinetic Parameters for Wild Type and Mutant HDAC8 Enzymatic Activity in the Presence of 50 μM TM-2-51

HDAC8	k_{cat} (s^{-1})	K_m (μM)	k_{cat}/K_m ($M^{-1}s^{-1}$)
Wild Type	7.6×10^{-2}	160.55 ± 18.19	475
Y18A	8.72×10^{-3}	320.43 ± 36.76	27
Y20A	1.76×10^{-2}	465.96 ± 92.91	37.7
H42A	1.52×10^{-2}	305.42 ± 61.65	49.8

s (seconds),
M (molar),
k_{cat} (first order rate constant)
K_m (Michaelis-Menten constant)

The values of the activation constants as listed in table 5.16 shows that compared to wild type HDAC8, the activation constant was nearly 2-fold higher for Y18A-HDAC8 while those for Y20A and H42A mutants were relatively similar to the wild type HDAC8. This may suggest that even though the activator binds to a similar site on the mutant HDAC8 proteins and activates these at a similar concentration as the wild type, it is somehow able to activate the mutant HDAC8 protein to a far greater extent, consistent with results shown above. This can be due to a tighter binding of the activator to the mutant HDAC8 compared to the wild type HDAC8. The cooperative fit indicated by the Hill coefficients of 1.34, 1.34 and 1.43 for Y18A, Y20A and H42A HDAC8 mutants, respectively, shows that there is more than one binding site for the activator on the mutant HDAC8 proteins. In other words, we can also say that the binding of the first molecule of TM-2-51 enhanced the binding affinity of the subsequent activator molecules. This has also been shown to be the case for wild type HDAC8 (151). Previous experiments done in the lab have shown wild-type to have an activation constant of 12.4 ± 1.2 μM with a Hill coefficient of 1.31.

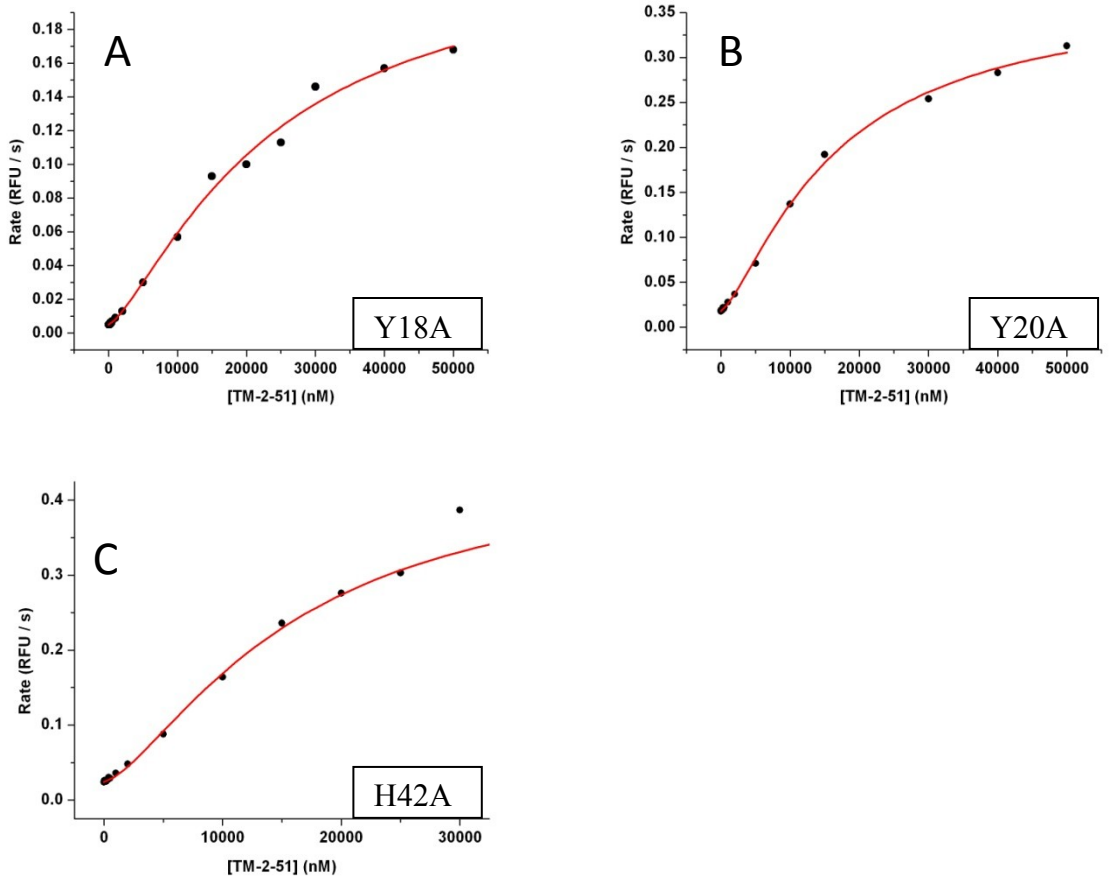

Figure 5.40. Determination of the apparent activation constant for TM-2-51 (activator) for HDAC8 mutants Y18A-HDAC8 (A), H42A-HDAC8 (B) and Y20A-HDAC8(C).
The experiment was performed in a microplate with varying concentrations of the activator (0-100 μM). The *Fluor de lys*® assay system was used as described previously. The enzyme activity was monitored as a function of time and plotted as a function of the concentration of the activator. The data was analyzed by equation no. 4.5 and the solid red line represents the best fit. The K_a and the Hill coefficient were determined in each case (see table 5.16).

Table 5.16. Activation Constants for TM-2-51 and the Hill Coefficients in case of HDAC8 and Mutants

HDAC8	K_a (μM)	Hill Coefficient (n)
WT	12.5 ± 1.2 (Ref: 151)	1.31 ± 0.12 (Ref 151)
Y18A	23.35 ± 3.46	1.34 ± 0.11
Y20A	16.45 ± 1.25	1.34 ± 0.07
H42A	16.08 ± 1.62	1.43 ± 0.07

5.9.2. Direct Binding of TM-2-51 to Y18A, Y20A and H42A Mutant HDAC8 Enzymes

The binding affinity of the activator TM-2-51 for the HDAC8 mutants was determined via the titration of the fixed concentration of mutant protein (1 μM) with an increasing concentration of the activator (TM-2-51) and was monitored using fluorescence spectroscopy. The quenching of the fluorescence was observed upon addition of each aliquot of the activator. The fluorescence signals were measured in a LS-50B spectrofluorometer with the settings described in section 4.3. The quenching of the protein fluorescence was measured at 340 nm (λ_{exc}= 280 nm) and was corrected for the dilution before plotting the data using equation 4.6.

The change in HDAC8 fluorescence signal (at 340 nm) was plotted as a function of activator concentration. Figure 5.41 shows that the fluorescence intensity decreased with each addition of the activator and this decrease followed a hyperbolic profile as a function of increasing concentration of the titrant (activator) until saturation of the enzyme was reached and no further change in fluorescence was detectable. The solid line is the best fit of the experimental data using the quadratic equation 4.6. Table 5.17 lists the values of dissociation constants of the activator TM-2-51 for the wild type and mutant HDAC8 enzymes, obtained from the analysis of the data by fitting with a quadratic equation for a competitive binding model. The dissociation

constants for Y18A, Y20A and H42A HDAC8 enzymes were found to be 81.92 nM, 32.28 nM and 37.48 nM, respectively. Earlier experiments performed in the lab have shown the K_d of wild type HDAC8 for activator to be 0.28 ± 0.05 μM. It is clear from these data that the HDAC8 mutants exhibit a higher binding affinity for the activator compared to the wild type HDAC8. This may potentially explain the increased activation of HDAC8 mutants by the activator though the binding sites that underlie this activation are unclear. Also, another important thing to note here is the difference between the K_d value obtained and the activation constant of the wild type are different by an order of magnitude. But for mutants, that difference is two orders of magnitude. Further study was needed beyond 2.5 μM of the activator concentration, in order to explore other weak binding sites. But the limitation to this study was the significant absorption of light in the UV region leading to inner-filter effect.

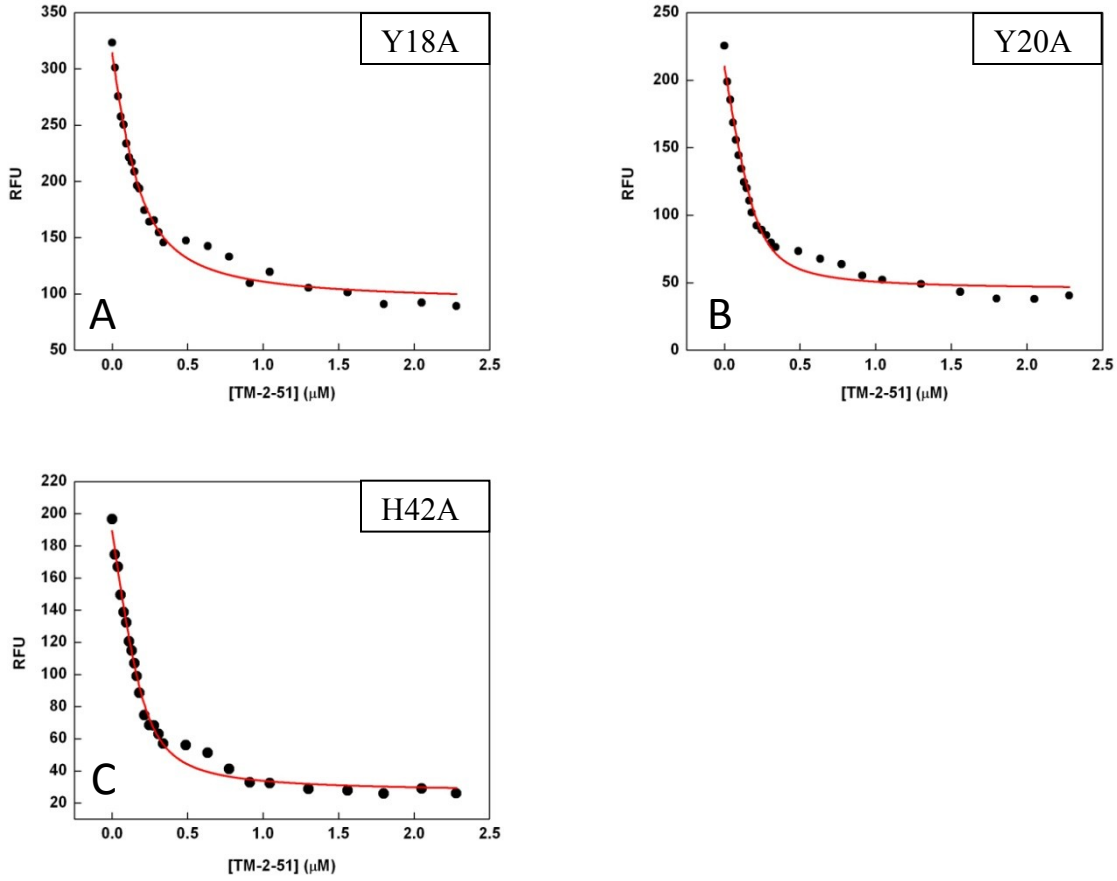

Figure 5.41. Binding isotherm for the determination of the equilibrium dissociation constant (K_d) of TM-2-51(Activator) with Y18A-HDAC8 (A), Y20A-HDAC8 (B) and H42A-HDAC8 (C) determined by fluorescence spectroscopy.
Formation of HDAC8-Activator complex was measured by monitoring the quenching of protein fluorescence upon addition of activator. The experiment was performed with 1 μM HDAC8 in a 4 mm path length quartz cuvette and aliquots of activator were added at regular intervals. The quenching of fluorescence with increasing concentrations of activator was plotted after correcting for the dilution effect to determine K_d. The experiments were monitored at 340 nm after excitation at 280 nm and data were analyzed by eq. 4.6 which provided K_d values as tabulated in Table no. 5.17.

Table 5.17. Equilibrium Dissociation Constant for TM-2-51

HDAC8	K_d for TM-2-51 (nM)
WT	250 ± 13.11
Y18A	81.92 ± 10.54
Y20A	32.28 ± 6.42
H42A	37.84 ± 4.88

5.9.3. Computational Studies on the Binding Sites of the Activator in the Wild Type and the Mutant HDAC8 Enzymes

5.9.3.1. Computer Docking Simulation of TM-2-51 at its Plausible Binding Sites with HDAC8-Substrate Complex

Computational studies in Srivastava lab have also shown that TM-2-51 binds to the active site pocket of HDAC8. Upon discovering the activating effect of TM-2-51 on HDAC8, it was of great interest to speculate on its binding sites. A recent computational study from Srivastava lab (151) involved molecular docking of TM-2-51 performed with the structural coordinates of the HDAC8-substrate complex (PDB ID- 2V5W.pdb) utilizing a program called AutoDock Vina. The study showed the computational models which displayed the clusters of TM-2-51 docked at the active site pocket of HDAC8 as well as its proximity to the active site residues and the bound substrate. The best docked structure of TM-2-51 was found to be stacked between the aromatic residues of F306 and the coumarin moiety of the substrate. Besides π-π stacking interactions, the activator made Van der Waals contacts with side chains of P35, F152, M274 and L308, and in addition also shows potential electrostatic interactions with the backbone carbonyl residues of A32 and K33. These stacking interactions are believed to enhance the binding affinity of the substrate in the presence of the activator (151). It has been reported that TM-2-51 selectively

activates HDAC8 (151) and activation was also observed in the present study in case of both the wild type and mutants. Previous studies (83) have suggested that the malleability of the enzyme surface in the vicinity of the active site is mainly responsible for the selective activation of HDAC8 (151). The assistance of the coumarin moiety of the substrate in causing the activation effect was refuted by determining the direct binding affinity of TM-2-51 and purified HDAC8 (151).

Based on this knowledge, it was important to determine if there are any binding sites for the activator in the exit tunnel or in the proximity of the exit tunnel residues (Y18, Y20 and H42). Collaboration with a computational scientist, Changhui Yan at the Computer Science Department at NDSU helped us generate models of the HDAC8-substrate complex where the activator was docked by a blind docking approach utilizing the PyMol software. Here no assumption was made about the putative docking sites of the ligand. Strikingly, we found an activator-binding site that was present very close to the exit tunnel residues mentioned above (Figure 5.42). This led us to speculate that binding of the activator near the exit tunnel residues may cause a conformational change that helps facilitate the release of the acetate by-product from HDAC8. Upon mutation of these residues, this binding site might have become more accessible, especially in the Y18A-HDAC8 mutant, which consequently might have led to a tighter binding and a greater increase in the k_{cat} value for this mutant.

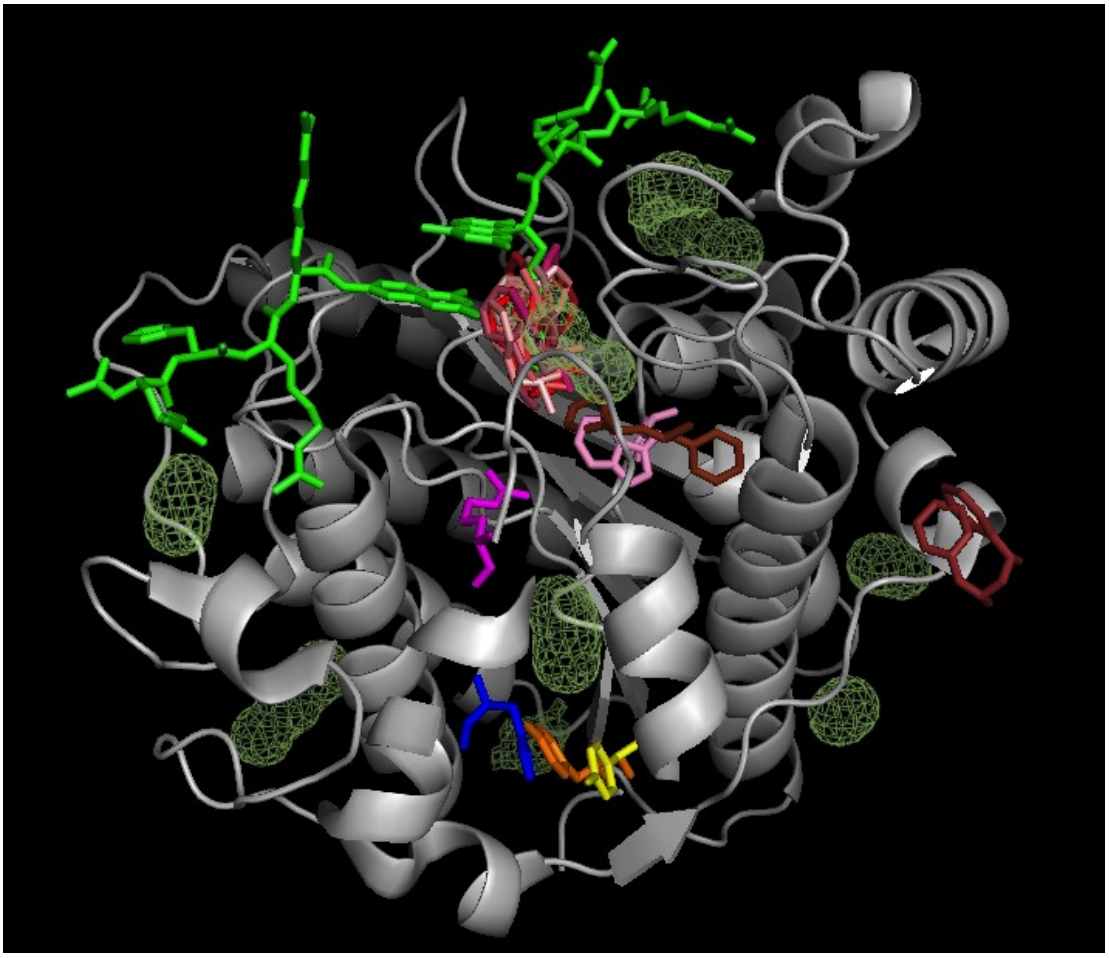

Figure 5.42. HDAC8-substrate complex (PDB ID. 2V5W) showing the plausible sites for the binding of the activator, TM-2-51 (green mesh).
The figure was generated using the Pymol software with a peptidic substrate as ligand (green).The top 10 conformations or the possible binding sites for the activator generated by blind docking approach are shown in shades of wine red (stick conformations). Y18 (orange), Y20 (yellow) and H42 (blue) are present in the vicinity of one of the plausible binding sites (green mesh) for the activator. The other two important residues in the exit tunnel, R37 and W141 (magenta and pink stick representation, respectively) are also in the near surroundings of the two plausible binding sites of the activator.

CHAPTER 6. DISCUSSION

Acetylation of histones can regulate the accessibility of DNA to cellular machinery and thus change the protein expression profiles of cells. Regulation of the acetylation state of proteins is important as aberrant acetylation of both histone and non-histone proteins can contribute to the development of many disease states(175–177). Metal-dependent histone deacetylases (HDACs) catalyze the hydrolysis of acetyl-L-lysine side chains in histone and non-histone proteins to yield L-lysine and acetate. Histone deacetylases (HDACs) catalyze the removal of the acetyl group from the ε-amino group of lysine side chains clustered near the hydrophilic N-terminal ends of the core histones. Deacetylation is often correlated with transcriptional silencing as it makes the promoter element inaccessible to the transcriptional machinery. As proof of their importance to human health, two broad spectrum lysine deacetylase/histone deacetylase (HDAC) inhibitors [suberoylanilide hydroxamic acid (SAHA) and Romidepsin] have been approved by the U.S. Food and Drug Administration and are currently on the market for the treatment of T-cell lymphomas.

HDAC isozymes can be grouped into four classes based on their phylogenetic similarity (178). Class I (HDAC1, 2, 3, and 8), class IIa (HDAC4, 5, 7, and 9), class IIb (HDAC6 and 10), and class IV (HDAC11) enzymes catalyze deacetylation using a metal-dependent mechanism (178,179) while class III (Sirt1-7) enzymes use an NAD^+ cofactor to perform deacetylation (180,181). HDAC8 is a member of the class I histone deacetylase enzyme family and is predominantly expressed in smooth muscle tissue. It has been implicated as a key player in the progression of cancers (182), and is therefore an enzymatic target of tremendous interest to

laboratories around the world concerned with discovering a cure for these life threatening conditions.

Given the abundance and importance of HDAC substrates, some of the foremost questions in the field are the regulation of enzymatic activity and the determination of the substrate specificity of HDACs. Mechanistically and structurally, HDAC8 is the best studied of the HDAC homologs. Furthermore, HDAC8 is proposed to recognize a number of non-histone substrates (110,183,184) and is therefore a good model for developing analytical approaches to unravel HDAC substrate specificity as well as understand its structure-function relationship.

Despite tremendous progress in understanding the biology of HDAC8, a number of key issues remain unresolved, precluding full exploitation of HDAC8 as a drug target. For example, determinants of substrate specificity are still being evaluated for HDAC8 and further identification of binding motifs will be beneficial for understanding the biology of this enzyme. Thus, the poor HDAC8 enzyme kinetics observed with histone H4 and p53 peptide substrates compared to other HDACs makes it doubtful that these proteins are HDAC8 substrates *in vivo* (110,170). Further, the importance of exit tunnel and specific exit-tunnel residues has not been rigorously tested, creating ambiguity over the possibility of the exit tunnel residues being used as a potential site for activation or inhibition of HDAC8. In an effort to address some of these issues, the present study was aimed at investigating the importance of specific exit tunnel residues in HDAC8 enzymatic functioning.

Based upon a review of the available literature, HDAC sequence conservation and available structural data, three residues in HDAC8 sequence, Y18, Y20 and H42, were targeted for mutagenesis and following biophysical studies. These residues had also been hypothesized

previously to play a role in the release of acetate from the HDAC8 pocket following catalysis (70,90). Using a Stratagene Quikchange mutagenesis kit, each of the above three residues was mutated to alanine and the mutation confirmed by DNA sequencing. The resulting mutant HDAC8 enzymes were expressed in *E. coli* using a pLIC-His vector and purified by Ni^{2+}-IDA chromatography to obtain substantially pure recombinant HDAC8 mutant enzymes (Figures 5.7-5.12). The purified recombinant HDAC8 mutant enzymes were then characterized in terms of enzyme catalysis, secondary structure and other biophysical properties, to understand the role of these critical residues on HDAC8 structure-function relationship. Purified recombinant HDAC8 is known to catalyze deacetylation and displays substrate selectivity in the absence of additional protein cofactors (13,15,107,110,115,116,164,170,185–190), suggesting that HDAC8 can catalyze deacetylation *in vivo* in the absence of a protein complex. The steady-state kinetic parameters for catalysis of the deacetylation of peptides can thus provide insight into both the kinetic mechanism and the biophysical parameters of this enzyme.

HDAC8-catalyzed deacetylation of the p53 and H4 coumarin peptides has a low value of k_{cat}/K_m (10^3–10^4 $M^{-1}s^{-1}$) in comparison to enzymes that function near diffusion-controlled limits (10^6–$10^8 M^{-1}s^{-1}$) and a high value for K_m (320 μM, H4 peptide) (110) compared to other HDAC isozymes (~ 30 μM) (170). These data suggest a simple Michaelis–Menten kinetic model whereby substrate binding and dissociation is rapid, and is followed by rate-limiting deacetylation. This conclusion is bolstered by the observed enhancement of the k_{cat} value for deacetylation of peptides labeled with a more reactive trifluoroacetyl group (188,191). Therefore, substrate specificity is determined by both the affinity of HDAC8 for a peptide substrate and the reactivity of the enzyme–substrate complex. Experiments to determine the rate of reaction, K_m

and the specificity constant of the HDAC8 mutant enzymes revealed that compared to the wild type, the Y18A and the Y20A mutants had dramatically reduced rates of reaction while the H42A mutant did not exhibit such a decrease (Figures 5.13, 5.14 and Table 5.2). Thus, the above tyrosine mutations clearly affected the catalytic activity of the enzyme evidenced by the altered rate constant, indicating a role of these residues in the rate determining step of HDAC8 catalysis.

The relative k_{cat}/K_m values are a measure of how efficiently an enzyme converts a substrate into product and indicate the substrate preference of an enzyme when discriminating among multiple substrates (192). The majority of enzymes have k_{cat}/K_m values of 10^5–10^6 $M^{-1}s^{-1}$ (193). These values are generally slower than the diffusion controlled rate constants for substrate binding, which can be as high as 10^7–10^8 $M^{-1}s^{-1}$(187). Consistent with this, the k_{cat}/K_m values for the HDAC8 homolog HDAC1 for deacetylation of the peptide, Ac-Gly-Ala-Lys-AMC, and for the homologous enzyme, arginase I, are on the order of 10^5 $M^{-1}s^{-1}$(170,189). In the present study, the HDAC8 mutants exhibited nearly 10-40 fold reduction in the specificity constant k_{cat}/K_m compared to WT-HDAC8, indicating a defect in enzymatic activity. By comparison, mutation of R37, which is proposed to be important for gating the acetate release channel in HDAC8, decreases the k_{cat}/K_m value for Co^{2+}-HDAC8-catalyzed deacetylation of the *Fluor de lys*® substrate (R-H-K(ac)-K(ac)-methylcoumarin) by 530-fold (116). However, none of the mutants in the present study exhibited any significant change in K_m compared to wt-HDAC8. The Michaelis-Menten constant K_m is the substrate concentration at which the reaction rate is at half-maximum, and is an inverse measure of the substrate's affinity for the enzyme—as a small K_m indicates high affinity, meaning that the rate will approach V_{max} more quickly. Thus, the tyrosine mutations Y18A and Y20A did not impact substrate binding to HDAC8 since the K_m

remained largely unchanged. The loss in HDAC8 catalytic activity due to the above tyrosine mutations implies a block at a later stage in the catalytic cycle of the enzyme. This may be manifested as a defect in acetate by-product release due to a mutation in the exit tunnel.

To substantiate the results obtained in enzymatic activity assay for the three mutant HDAC8 enzymes, additional studies were performed to determine spectral, kinetic and thermodynamic characteristics of these mutants, both in ligand-free and ligand-bound forms. For these studies, the ligands included a known HDAC8 activator, TM-2-51 and previously characterized inhibitors of HDAC8 like SAHA and c-SAHA (172).

One caveat to making conclusions from kinetic parameters measured in *in vitro* experiments is that some enzymes require an activator for optimal activity. As many HDAC isozymes associate with large protein complexes *in vivo*, it is possible that other proteins could activate the catalytic activity or enhance the substrate affinity to increase the value of k_{cat}/K_m for HDAC8 in the cell. Thus, when the enzymatic activity of the HDAC8 mutants was tested in the presence of the known HDAC8-activator TM-2-51, considerable enhancement in enzymatic activity was observed. Strikingly, wt-HDAC8 exhibited a 7-fold enhancement in k_{cat} while the k_{cat} for HDAC8 Y18A, Y20A and H42A mutants was enhanced 25, 23 and 11-fold, respectively (Figure 5.39 and Table 5.15). Despite the apparent higher inducibility of the mutant HDAC8 enzymes by TM-2-51, the k_{cat} as well as the k_{cat}/K_m values for the mutant HDAC8 enzymes in the presence of TM-2-51 were significantly lower compared to those of identically treated wt-HDAC8. Given that the activator TM-2-51 is presumed to bind in the vicinity of the active site pocket of HDAC8 (172), these results imply that the above exit tunnel mutations have a deleterious effect on HDAC8 enzymatic activity without impacting its active site pocket.

Hydroxamic acids are the most prevalent class of chemicals for inhibition of HDACs. These acids bind to the catalytic zinc cation at the base of the acetyl-lysine tunnel via an electrostatically favorable bi-dentate binding mode with two oxygen atoms, leaving the amide NH to form an additional hydrogen bonding interaction with a histidine. In the clinic, hydroxamic acid containing therapeutics are proving to be effective in saving lives, for instance vorinostat (194) is FDA approved for use in T-cell lymphoma, with panobinostat (195) belinostat (196) close to market approval. Analysis of binding of these inhibitors to HDAC8 provides another tool to dissect the effect of mutations in the exit tunnel residues. In binding experiments using SAHA and Coumarin-SAHA, the equilibrium inhibition constants (K_i) for HDAC8 mutants showed only small changes compared to wt-HDAC8 (Figures 5.16, 5.17 and Table 5.4). Further, equilibrium dissociation constants (K_d) for HDAC8 mutants also showed only small changes compared to wt-HDAC8 (Figures 5.18, 5.19 and Table 5.5). The fluorescence lifetime of c-SAHA, indicative of static quenching where binding does not influence the excited state, also remained unchanged upon binding to either wt-HDAC8 or any of the three HDAC8 mutants under study (Figure 5.20, 5.21 and Table 5.6).These results could be interpreted to mean that either the HDAC8 substrate-binding pocket has not been distorted significantly in these mutants. Alternately, this may also reflect the malleability of the HDAC8 active site pocket that is known to accommodate some changes without a significant effect on its binding constant (197).

The structure of HDAC8 yields clues about molecular recognition relevant to substrate selectivity. HDAC8 is the second smallest metal-dependent HDAC at ~ 42 kD, containing little more than the catalytic domain (13–15,178) and folds as a single α/β domain with a core eight-

stranded β-sheet surrounded by eleven α-helices (Figure 1.9). The substrate binding surface, composed of nine loops and an 11 Å tunnel leading to the active site, is proposed to be conformationally flexible based on the poor occupancy and varying positions of the loop residues in crystal structures (70,83,111,115,164) (Figure 1.19).Comparison of all the HDAC8 crystal structures illustrates that the L1 and L2 loops have the most structural variability of the loops in the proposed substrate binding surface, suggestive of a role in ligand binding. Additionally, the L2 loop interacts with inhibitors, suggesting that it may be important for molecular recognition of substrates (Dowling et al., 2008). Loops are a common structure in promiscuous enzymes (198) and examples of proteins, such as chymotrypsin (199) and carboxypeptidase A (200) that use loops to bind a range of substrates are abundant in nature. These loops create a number of different conformations that bind ligands through a combination of induced fit and select fit mechanisms (192,201). The varied conformations and motifs provide a palette of binding sites to accommodate a multiplicity of substrates. Furthermore, long-range allosteric movements propagated through the loops may affect the active site and surrounding areas, potentially altering substrate preferences.

To unravel the effect of the above three mutations on HDAC8 global structure, fluorescence decay curves of the tryptophan residues were analyzed to detect any alterations ascribable to the mutations. In contrast to the wt-HDAC8, the fluorescence decay curves of the mutant HDAC8 enzymes fit to a bi-exponential, indicative of an altered tryptophan environment in the HDAC8 mutants (Figure 5.23 and Table 5.7).

The analysis of enzyme kinetics by fluorescence spectroscopic methods using peptide substrates may be reflective of limited short-range interactions where the binding may be

dominated by a few strong contacts, as observed for the interaction between Y100 of HDAC8 and the methylcoumarin moiety of short *Fluor de lys*® peptides(185,187). However, numerous other short and long-range interactions such as ring stacking, hydrogen bonding, salt bridges, and electrostatic interactions are also involved in HDAC8 functionality as evidenced by HDAC8 crystal structures and biochemical measurements(115,185,187). Thus, to gain an independent perspective on the effect of mutations on HDAC8 structure, a different approach to evaluate ligand-binding to the HDAC8 mutants was utilized. Using SAHA as ligand, isothermal calorimetry experiments were performed to determine thermodynamic parameters for the protein-ligand interactions such as change in enthalpy, entropy, stoichiometry and the apparent binding affinity, by monitoring the heat change as signal. Isothermal titration calorimetry (ITC) revealed a significant change in the amount of heat signal in Y18A HDAC8 mutant compared to the wild type and the other HDAC8 mutants (Figure 5.24-5.27). The ITC profile of the Y18A mutant was completely distorted and was devoid of any reliable signal that could be used to determine the parameters. Thus, the K_a, N, ΔH and ΔS parameters were not discernable for the Y18A mutant compared to the other mutants as well as the wt-HDAC8 (Table 5.8), indicative of a significant impact of the Y18A mutation on HDAC8 structure. The Y20A and H42A mutants, on the other hand, displayed thermodynamic parameters that were not significantly different from those obtained for the wt-HDAC8. These results indicate that mutation of Y18 causes a change in the binding of SAHA to the enzyme, possibly reflecting a global change in the structure of the enzyme. The failure of such a change being manifested in the K_m and fluorescence measurements may be due to multiple factors being involved in these assays (202). However, the exquisite sensitivity of ITC coupled with the unique signature of the heat signal

enable the detection of even small differences that may be missed by other analytical methods. Alteration of the secondary structure of the Y18A mutant was also apparent from the altered CD spectra of the Y18A mutant compared to other HDAC8 mutants as well as wt-HDAC8 (Figure 5.28). Increased ellipticity of the Y18A mutant manifested at 222 nm presumably arose due to a higher content of β-sheets in its secondary structure revealed by *Dichroweb* analysis (Figures 5.28 and 5.29). These results lend strength to the conclusion that the Y18A mutation has an effect on the global structure of the HDAC8 enzyme which was well evident in its functionality.

The thermal denaturation profile obtained by CD spectroscopy for Y18A-HDAC8 also revealed a distinctive pattern with a 3-phase transition (Fig. 5.30) in contrast to the 2-phase transition profiles of WT-HDAC8 and the other two HDAC8 mutant enzymes (Fig. 5.29). The T_m of the Y20A and H42A HDAC8 mutants were marginally lower compared to the WT HDAC8, suggestive of only a slight decrease in their thermal stability (Table 5.9). On the other hand, the Y18A mutant exhibited a profile consistent with the enzyme being comprised of two populations with distinct melting temperatures. The majority of Y18A-HDAC8 molecules, though functionally inactive, appeared to exhibit thermal stability that was slightly different from that of the wt-HDAC8 as it remained soluble even at elevated temperatures that caused wt-HDAC8 to precipitate. An additional coexisting minor population of Y18A-HDAC8 exhibited even higher thermal stability, with T_m that was nearly two-fold higher than that of the WT-HDAC8, with precipitation occurring only past 92°C. Evidently, the Y18A mutation has a dramatic effect on the HDAC8 structure that impacts its thermal stability as well as its functionality. Overall, these results reveal a gradient of effects on thermal stability by the three HDAC8 mutations.

The kinetics of unfolding during thermal denaturation by CD spectroscopy revealed a monophasic profile for the Y20A mutant in contrast to the biphasic profile observed for wt-HDAC8 as well as the other HDAC8 mutants (Figures 5.31 - 5.34). The unfolding rate constant k_1 in general exhibited a dependence on the experimental temperature, showing an increase with increasing temperatures. However, the observed unfolding rate constant k_1 values for the Y18A mutant appeared to be significantly higher compared to k_1 values for the wt-HDAC8 and the other mutants (Tables 5.10 - 5.13), suggesting that the Y18A mutant unfolds much faster. The wt-HDAC8 and H42A-HDAC8 were quite similar in their unfolding kinetics, with the H42A-HDAC8 profile exhibiting a somewhat faster unfolding compared to the wild type. Arrhenius plots generated to determine the activation energy for the wild-type HDAC8 and each of the HDAC8 mutants also showed similar profiles for the wild type HDAC8 and H42A-HDAC8 with significantly different profiles for the other two mutants (Figure 5.35). Together, the unfolding kinetic profiles and the Arrhenius plots indicate that the Y18A-HDAC8 mutant exhibits the fastest unfolding that is also accompanied with greater thermal stability compared to the wt-HDAC8 and the other mutants. It is plausible that thermal denaturation of the Y18A-HDAC8 protein leads it to assume a random coil structure with *de novo* bonding that is thermally resistant (203)(204).On the other hand, the Y20A-HDAC8 mutant displayed the highest activation energy and lower thermal stability (Table 5.14), suggestive of an entropically driven process (205–209).The thermal denaturation induced unfolding of HDAC8 and its mutant derivatives was irreversible, precluding analysis of thermodynamic properties of any transition states.

The correlation of thermal unfolding as a function of deacetylase activity revealed valuable insight into the effect of mutations on enzymatic structure-function relationship. The

wt-HDAC8 and H42A-HDAC8 enzymes exhibited a gradual decline in enzymatic activity with increasing temperature culminating in a complete loss of HDAC activity around 50°C (Figure 5.36), consistent with their complete unfolding at this temperature. In contrast, the Y20A-HDAC8 mutant enzyme exhibited a significant decline in enzymatic activity at lower temperatures (39°C-43°C), as predicted from its complete unfolding at this temperature, with precipitation of the protein occurring in response to any further increase in temperature. Interestingly, the Y18A-HDAC8 protein exhibited a sharp drop in enzymatic activity at even lower temperatures (25°C-45°C), corresponding to the first phase of its triphasic unfolding evidenced by the CD studies described above. Thus, the second population of Y18A-HDAC8 mutant, despite showing greater thermal tolerance, is enzymatically inactive.

Additional insight into the thermal unfolding response of HDAC8 mutants came from a comparative analysis of temporal protein unfolding at a fixed temperature. At 35°C, the wt-HDAC8 exhibited the highest heat resistance compared to mutant HDAC8 enzymes (Figure 5.37), clearly establishing that the native HDAC8 structure is optimized for enzymatic activity, and mutations in the exit tunnel residues have a destabilizing effect. In contrast to wt-HDAC8, the Y18A-HDAC8 mutant exhibited the steepest decline in temporal activity, consistent with its faster rate constant and kinetic profile.

The present study also utilized the activator TM-2-51 to tease out any potential differences in the interaction of HDAC8 mutants with an agonist. Data presented in Fig. 5.39 and Table 5.15 show that the interaction of HDAC8 mutants with TM-2-51 agonist was altered compared to wt-HDAC8. Specifically, HDAC8 mutants exhibited a 2-4 fold higher binding affinity for the activator compared to the wt-HDAC8. The Hill Coefficient values were also

higher for the HDAC8 mutants compared to wt-HDAC8, suggestive of greater cooperative binding of the activator. These results may potentially explain the increased activation of HDAC8 mutants by TM-2-51 shown in Figure 5.40 by a mechanism that remains to be characterized. Determination of activation constant (K_a) of TM-2-51 for the HDAC8 mutants provided another line of evidence suggestive of mutation induced alteration of HDAC8 function. Compared to wt-HDAC8, the K_a of Y18A-HDAC8 was nearly 2-fold higher while the other two mutants showed K_a relatively similar to the wt-HDAC8 (Figure 5.40 and Table 5.16). This may suggest that even though the activator binds to a similar site/s on the mutant HDAC8 proteins and activates these at a similar concentration as the wild type, it is somehow able to activate the mutant HDAC8 protein to a greater extent. This can be due to a tighter binding of the activator to the mutant HDAC8 compared to the wild type HDAC8. Based on the Hill coefficient values, the mutant HDAC8 proteins, like their wild-type counterpart, showed more than one binding site for the activator TM-2-51, although structural evidence for the activator binding site/s is lacking. The HDAC8 mutants also exhibited 2-6 fold lower equilibrium dissociation constant for TM-2-51 compared to wt-HDAC8 (Figure 5.41 and Table 5.17). It can thus be speculated that the above mutations made the HDAC8 binding to the activator TM-2-51 tighter while at the same time increasing the effective concentration required for the activation. Previous computational studies performed with the activator TM-2-51 showed that this molecule docked at the active site pocket(151). In the present study, it was found that the activator has plausible binding site/s close to the exit tunnel (Figure 5.42). This site may have become more accessible due to the mutations under study, leading to higher activation in mutant HDAC8 enzymes compared to wt-HDAC8.

The effect of tyrosine to alanine mutations on HDAC8 activity cannot be ascribed to lack of phosphorylation since Y18 or Y20 are not known substrates for tyrosine phosphorylation. On the other hand, phosphorylation of S39, located on the backside of the HDAC8 surface, 21Å from the catalytic metal ion (70,83,111,115,164) has been suggested to have the potential to affect the subcellular localization, protein–protein interactions, allosteric effects, and HDAC8 activity via conformational changes that propagate to the active site or enzyme–substrate interface. Ser39 lies near the junction with the L1 loop (70,83,111,115,164) that has been implicated in substrate recognition, and therefore phosphorylation at that position may alter enzyme–substrate interactions. The S39 residue is located in a pocket on the enzyme surface surrounded by hydrophobic and acidic residues and also contacts R37, suggesting that phosphorylation of S39 could induce a structural perturbation due to the altered charge. It would be interesting to test if substitution of Y18 or Y20 with a negatively charged residue such as Aspartate or Glutamate has a different outcome on HDAC8 functionality than the one observed in the present study with Y to A mutations. Regulation of histone deacetylation by tyrosine phosphorylation has not been reported previously although numerous examples of HDAC activity regulating the function of transcription factor tyrosine phosphorylation are known. Thus, the role of Y residues in the exit tunnel is likely purely structural.

Due to the metal chelating strength of the hydroxamic moiety, it is believed to be responsible for clinically observed side-effects such as nausea, thrombocytopenia, anemia and other metabolic abnormalities that are detrimental to the health of patients in contrast to their life-saving profile (148). As such, the search for alternative small molecules containing weaker metal binding features has been of great interest to the HDAC community. Recent attempts to

design novel selective HDAC8 inhibitors have also revealed the feasibility of additional approaches to inhibit HDAC8 activity that may impact the active site microenvironment without directly affecting the catalytic pocket. For example, Vaidya et al., (210) reported a novel series of HDAC8 inhibitors without a zinc-chelating hydroxamic acid moiety. Photoaffinity labeling and molecular modeling studies suggested that these ligands are likely to bind in an 'upside-down' fashion in a secondary binding site proximal to the main catalytic site.

Similarly, Suzuki et al., (211) described a compound C149 that interacts with additional loop residues that were not previously reported to be involved in HDAC8-ligand interaction. It was reported that compound C149 has a U-shaped conformation in the active site of HDAC8, and most importantly, the phenylthiomethyl group of compound C149 binds to a hydrophobic pocket formed by W141, I34, and P35, which is thought to be unique to HDAC8 and where the methylthio group can interact with W141 and the phenyl group can bind to P35 and Y306 through hydrophobic interactions (211). Bermudez-Lugo (212) used molecular dynamic (MD) simulations to show that valproic acid (VPA) bound with highest affinity at a site located at the acetyl-releasing channel, termed the hydrophobic active site channel (HASC). The affinity of VPA for HASC was due to its highly hydrophobic properties that allow VPA to take part in van der Waals interactions with Y18, I19, Y20, V25, R37, A38, V41, H42, I135 and W137, while VPA’s carboxylate group has several hydrogen bonding interactions with the backbones of S138, I19, N136 and W137. The VPA side chain moieties also formed hydrophobic interactions with the aromatic cluster of Y18, Y20 and W37 as well as with the side chains of V25, I19 and I135. MD simulations showed that the HASC door continuously opened and closed, which affected the affinity of VPA to the HASC, but the affinity toward the HASC was consistently higher than that

obtained for the CS, suggesting that the HASC could be involved in the mechanism of inhibition. Thus, such studies demonstrate the potential for the identification of compounds with novel modes of interaction with HDAC8 that may involve residues outside of the conventional catalytic site, for example, by targeting the HDAC8 exit tunnel residues.

Acetate is a by-product of the deacetylation reaction catalyzed by HDAC8 and is released via the exit channel. Finnin et al., (71) noted that the origin of the measurement criterion of the internal 14 Å channel has not been reported. For instance, the distance between the amino-acids that define the start and end of the channel (terminal hydroxyl functionality on S29 and His-131 imidazole side-chain) is ~20 Å for the first HDLP reported structure(71).Whitehead et al., (90) reassessed the shape of the HDAC8 acetate release channel that was previously reported to be 14 Å in size. They noted that the volume available in the HDAC8 acetate release channel is considerably smaller than in case of HDLP. There are clearly two volume components in HDAC8, and this internal acetate release channel cavity appears to be divided at a junction between amino-acid residues L31, I34, R37, S138 and W141 into an '12 Å+14 Å' channel pair. The acetic acid settles well at the base of the 14 Å disposal channel making hydrogen bonding contact with I19 and W137. The acidic species also makes favorable hydrophobic contacts via its methyl group with the side-chain residues of I45, A38 and V41. This may indicate the final resting place of the acetic acid group within the histone deacetylase prior to its release via a mechanism mediated between residues Y20, A38, V41 and H42 whose side-chain residues separate the acetic acid moiety in this disposal cavity from the aqueous bulk solvent(90). Compared to WT-HDAC8, the three exit-tunnel HDAC8 mutants exhibited a 1.9-3.4 fold decrease in the K_i of acetate (Fig. 5.15 and Table 5.3). The key determinant of acetate binding in

HDAC8 has been reported to be the R37 residue (116). Given that the three exit tunnel mutations are all localized in the vicinity of R37, they may influence the interaction of R37 with acetate. However, since the above three HDAC8 mutants contain an intact R37, there may only be a minor impact on acetate binding in these mutants, consistent with the observed partial resistance of the three HDAC8 mutants to acetate inhibition.

The present study was performed using peptide HDAC8 substrates that provide a useful analytical tool for investigation of HDAC8 structure function analysis and thus these results can only be interpreted in the context of HDAC8 activity on peptide substrates. It remains to be seen what effect these mutations have on HDAC8 activity on physiological protein substrates that may likely involve additional interactions of HDAC8 exit tunnel residues. Nevertheless, the present study provides novel insight into physicochemical aspects of HDAC8 structure-function relationship and assesses the effect of mutations in the acetate exit tunnel on HDAC8 function. Using multiple independent analytical approaches, the present study demonstrates that single point mutations in HDAC8 acetate exit tunnel at either Y18 or Y20 position have a dramatic effect on its catalytic activity even though the substrate binding pocket is not directly impacted by the mutation. Both Y18 and Y20 are highly conserved, reflecting an evolutionary pressure to maintain the protein secondary structure, for optimal HDAC8 enzymatic function. The present study thus adds to the growing body of evidence highlighting the importance of the by-product release mechanism in the overall catalysis of HDAC8 enzyme. Deeper exploration of this aspect of HDAC8 biology will help pinpoint the actual rate limiting step of the catalysis and aid the development of new inhibitors or activators targeting these residues. This is an important

research area that can be exploited in the design and development of novel therapeutics for cancer and neurodegenerative diseases.

REFERENCES

1. Allfrey VG, Faulkner R, Mirsky AE. Acetylation and methylation of histones and their possible role in the regulation of rna synthesis*. Proc Natl Acad Sci U S A. 1964 May;51(5):786–94.

2. Sternglanz R. Histone acetylation: a gateway to transcriptional activation. Trends Biochem Sci. 1996 Oct;21(10):357–8.

3. Leipe DD, Landsman D. Histone deacetylases, acetoin utilization proteins and acetylpolyamine amidohydrolases are members of an ancient protein superfamily. Nucl Acids Res. 1997 Sep 1;25(18):3693–7.

4. Taunton J, Hassig CA, Schreiber SL. A mammalian histone deacetylase related to the yeast transcriptional regulator Rpd3p. Science. 1996 Apr 19;272(5260):408–11.

5. Yang WM, Inouye C, Zeng Y, Bearss D, Seto E. Transcriptional repression by YY1 is mediated by interaction with a mammalian homolog of the yeast global regulator RPD3. Proc Natl Acad Sci USA. 1996 Nov 12;93(23):12845–50.

6. Rundlett SE, Carmen AA, Kobayashi R, Bavykin S, Turner BM, Grunstein M. HDA1 and RPD3 are members of distinct yeast histone deacetylase complexes that regulate silencing and transcription. Proc Natl Acad Sci USA. 1996 Dec 10;93(25):14503–8.

7. Carmen AA, Rundlett SE, Grunstein M. HDA1 and HDA3 are components of a yeast histone deacetylase (HDA) complex. J Biol Chem. 1996 Jun 28;271(26):15837–44.

8. Vidal M, Gaber RF. RPD3 encodes a second factor required to achieve maximum positive and negative transcriptional states in Saccharomyces cerevisiae. Mol Cell Biol. 1991 Dec;11(12):6317–27.

9. Bjerling P, Silverstein RA, Thon G, Caudy A, Grewal S, Ekwall K. Functional divergence between histone deacetylases in fission yeast by distinct cellular localization and in vivo specificity. Mol Cell Biol. 2002 Apr;22(7):2170–81.

10. Yang WM, Yao YL, Sun JM, Davie JR, Seto E. Isolation and characterization of cDNAs corresponding to an additional member of the human histone deacetylase gene family. J Biol Chem. 1997 Oct 31;272(44):28001–7.

11. Dangond F, Hafler DA, Tong JK, Randall J, Kojima R, Utku N, et al. Differential display cloning of a novel human histone deacetylase (HDAC3) cDNA from PHA-activated immune cells. Biochem Biophys Res Commun. 1998 Jan 26;242(3):648–52.

12. Emiliani S, Fischle W, Van Lint C, Al-Abed Y, Verdin E. Characterization of a human RPD3 ortholog, HDAC3. Proc Natl Acad Sci USA. 1998 Mar 17;95(6):2795–800.

13. Hu E, Chen Z, Fredrickson T, Zhu Y, Kirkpatrick R, Zhang GF, et al. Cloning and characterization of a novel human class I histone deacetylase that functions as a transcription repressor. J Biol Chem. 2000 May 19;275(20):15254–64.

14. Van den Wyngaert I, de Vries W, Kremer A, Neefs J, Verhasselt P, Luyten WH, et al. Cloning and characterization of human histone deacetylase 8. FEBS Lett. 2000 Jul 28;478(1-2):77–83.

15. Buggy JJ, Sideris ML, Mak P, Lorimer DD, McIntosh B, Clark JM. Cloning and characterization of a novel human histone deacetylase, HDAC8. Biochem J. 2000 Aug 15;350 Pt 1:199–205.

16. Johnstone RW. Histone-deacetylase inhibitors: novel drugs for the treatment of cancer. Nat Rev Drug Discov. 2002 Apr;1(4):287–99.

17. Fischle W, Dequiedt F, Hendzel MJ, Guenther MG, Lazar MA, Voelter W, et al. Enzymatic activity associated with class II HDACs is dependent on a multiprotein complex containing HDAC3 and SMRT/N-CoR. Mol Cell. 2002 Jan;9(1):45–57.

18. Fischle W, Dequiedt F, Fillion M, Hendzel MJ, Voelter W, Verdin E. Human HDAC7 histone deacetylase activity is associated with HDAC3 in vivo. J Biol Chem. 2001 Sep 21;276(38):35826–35.

19. Yang W-M, Tsai S-C, Wen Y-D, Fejer G, Seto E. Functional domains of histone deacetylase-3. J Biol Chem. 2002 Mar 15;277(11):9447–54.

20. Kao HY, Ordentlich P, Koyano-Nakagawa N, Tang Z, Downes M, Kintner CR, et al. A histone deacetylase corepressor complex regulates the Notch signal transduction pathway. Genes Dev. 1998 Aug 1;12(15):2269–77.

21. Verdel A, Curtet S, Brocard MP, Rousseaux S, Lemercier C, Yoshida M, et al. Active maintenance of mHDA2/mHDAC6 histone-deacetylase in the cytoplasm. Curr Biol. 2000 Jun 15;10(12):747–9.

22. Cress WD, Seto E. Histone deacetylases, transcriptional control, and cancer. J Cell Physiol. 2000 Jul;184(1):1–16.

23. Zhang Y, Ng HH, Erdjument-Bromage H, Tempst P, Bird A, Reinberg D. Analysis of the NuRD subunits reveals a histone deacetylase core complex and a connection with DNA methylation. Genes Dev. 1999 Aug 1;13(15):1924–35.

24. Knoepfler PS, Eisenman RN. Sin meets NuRD and other tails of repression. Cell. 1999 Nov 24;99(5):447–50.

25. You A, Tong JK, Grozinger CM, Schreiber SL. CoREST is an integral component of the CoREST- human histone deacetylase complex. Proc Natl Acad Sci USA. 2001 Feb 13;98(4):1454–8.

26. Robertson KD, Ait-Si-Ali S, Yokochi T, Wade PA, Jones PL, Wolffe AP. DNMT1 forms a complex with Rb, E2F1 and HDAC1 and represses transcription from E2F-responsive promoters. Nat Genet. 2000 Jul;25(3):338–42.

27. Rountree MR, Bachman KE, Baylin SB. DNMT1 binds HDAC2 and a new co-repressor, DMAP1, to form a complex at replication foci. Nat Genet. 2000 Jul;25(3):269–77.

28. Lai A, Kennedy BK, Barbie DA, Bertos NR, Yang XJ, Theberge MC, et al. RBP1 recruits the mSIN3-histone deacetylase complex to the pocket of retinoblastoma tumor suppressor family proteins found in limited discrete regions of the nucleus at growth arrest. Mol Cell Biol. 2001 Apr;21(8):2918–32.

29. Lai A, Lee JM, Yang WM, DeCaprio JA, Kaelin WG Jr, Seto E, et al. RBP1 recruits both histone deacetylase-dependent and -independent repression activities to retinoblastoma family proteins. Mol Cell Biol. 1999 Oct;19(10):6632–41.

30. Ito K, Barnes PJ, Adcock IM. Glucocorticoid receptor recruitment of histone deacetylase 2 inhibits interleukin-1beta-induced histone H4 acetylation on lysines 8 and 12. Mol Cell Biol. 2000 Sep;20(18):6891–903.

31. Wotton D, Lo RS, Lee S, Massagué J. A Smad transcriptional corepressor. Cell. 1999 Apr 2;97(1):29–39.

32. Choi HS, Lee JH, Park JG, Lee YI. Trichostatin A, a histone deacetylase inhibitor, activates the IGFBP-3 promoter by upregulating Sp1 activity in hepatoma cells: alteration of the Sp1/Sp3/HDAC1 multiprotein complex. Biochem Biophys Res Commun. 2002 Aug 30;296(4):1005–12.

33. Wen YD, Perissi V, Staszewski LM, Yang WM, Krones A, Glass CK, et al. The histone deacetylase-3 complex contains nuclear receptor corepressors. Proc Natl Acad Sci USA. 2000 Jun 20;97(13):7202–7.

34. Li J, Wang J, Wang J, Nawaz Z, Liu JM, Qin J, et al. Both corepressor proteins SMRT and N-CoR exist in large protein complexes containing HDAC3. EMBO J. 2000 Aug 15;19(16):4342–50.

35. Zhang J, Kalkum M, Chait BT, Roeder RG. The N-CoR-HDAC3 nuclear receptor corepressor complex inhibits the JNK pathway through the integral subunit GPS2. Mol Cell. 2002 Mar;9(3):611–23.

36. Galasinski SC, Resing KA, Goodrich JA, Ahn NG. Phosphatase inhibition leads to histone deacetylases 1 and 2 phosphorylation and disruption of corepressor interactions. J Biol Chem. 2002 May 31;277(22):19618–26.

37. Tsai S-C, Seto E. Regulation of histone deacetylase 2 by protein kinase CK2. J Biol Chem. 2002 Aug 30;277(35):31826–33.

38. Thiagalingam S, Cheng K-H, Lee HJ, Mineva N, Thiagalingam A, Ponte JF. Histone deacetylases: unique players in shaping the epigenetic histone code. Ann N Y Acad Sci. 2003 Mar;983:84–100.

39. Grozinger CM, Hassig CA, Schreiber SL. Three proteins define a class of human histone deacetylases related to yeast Hda1p. Proc Natl Acad Sci USA. 1999 Apr 27;96(9):4868–73.

40. Fischle W, Emiliani S, Hendzel MJ, Nagase T, Nomura N, Voelter W, et al. A new family of human histone deacetylases related to Saccharomyces cerevisiae HDA1p. J Biol Chem. 1999 Apr 23;274(17):11713–20.

41. Zhou X, Marks PA, Rifkind RA, Richon VM. Cloning and characterization of a histone deacetylase, HDAC9. Proc Natl Acad Sci USA. 2001 Sep 11;98(19):10572–7.

42. Fischer DD, Cai R, Bhatia U, Asselbergs FAM, Song C, Terry R, et al. Isolation and characterization of a novel class II histone deacetylase, HDAC10. J Biol Chem. 2002 Feb 22;277(8):6656–66.

43. Zhou X, Richon VM, Rifkind RA, Marks PA. Identification of a transcriptional repressor related to the noncatalytic domain of histone deacetylases 4 and 5. Proc Natl Acad Sci USA. 2000 Feb 1;97(3):1056–61.

44. Huang EY, Zhang J, Miska EA, Guenther MG, Kouzarides T, Lazar MA. Nuclear receptor corepressors partner with class II histone deacetylases in a Sin3-independent repression pathway. Genes Dev. 2000 Jan 1;14(1):45–54.

45. Grozinger CM, Schreiber SL. Regulation of histone deacetylase 4 and 5 and transcriptional activity by 14-3-3-dependent cellular localization. Proc Natl Acad Sci USA. 2000 Jul 5;97(14):7835–40.

46. Lemercier C, Verdel A, Galloo B, Curtet S, Brocard MP, Khochbin S. mHDA1/HDAC5 histone deacetylase interacts with and represses MEF2A transcriptional activity. J Biol Chem. 2000 May 19;275(20):15594–9.

47. Miska EA, Karlsson C, Langley E, Nielsen SJ, Pines J, Kouzarides T. HDAC4 deacetylase associates with and represses the MEF2 transcription factor. EMBO J. 1999 Sep 15;18(18):5099–107.

48. Zhang CL, McKinsey TA, Lu JR, Olson EN. Association of COOH-terminal-binding protein (CtBP) and MEF2-interacting transcription repressor (MITR) contributes to transcriptional repression of the MEF2 transcription factor. J Biol Chem. 2001 Jan 5;276(1):35–9.

49. Guarente L. Sir2 links chromatin silencing, metabolism, and aging. Genes Dev. 2000 May 1;14(9):1021–6.

50. Imai S, Armstrong CM, Kaeberlein M, Guarente L. Transcriptional silencing and longevity protein Sir2 is an NAD-dependent histone deacetylase. Nature. 2000 Feb 17;403(6771):795–800.

51. Frye RA. Characterization of five human cDNAs with homology to the yeast SIR2 gene: Sir2-like proteins (sirtuins) metabolize NAD and may have protein ADP-ribosyltransferase activity. Biochem Biophys Res Commun. 1999 Jun 24;260(1):273–9.

52. Luo J, Su F, Chen D, Shiloh A, Gu W. Deacetylation of p53 modulates its effect on cell growth and apoptosis. Nature. 2000 Nov 16;408(6810):377–81.

53. Luo J, Nikolaev AY, Imai S, Chen D, Su F, Shiloh A, et al. Negative control of p53 by Sir2alpha promotes cell survival under stress. Cell. 2001 Oct 19;107(2):137–48.

54. Kuzmichev A, Zhang Y, Erdjument-Bromage H, Tempst P, Reinberg D. Role of the Sin3-histone deacetylase complex in growth regulation by the candidate tumor suppressor p33(ING1). Mol Cell Biol. 2002 Feb;22(3):835–48.

55. Langley E, Pearson M, Faretta M, Bauer U-M, Frye RA, Minucci S, et al. Human SIR2 deacetylates p53 and antagonizes PML/p53-induced cellular senescence. EMBO J. 2002 May 15;21(10):2383–96.

56. Vaziri H, Dessain SK, Ng Eaton E, Imai SI, Frye RA, Pandita TK, et al. hSIR2(SIRT1) functions as an NAD-dependent p53 deacetylase. Cell. 2001 Oct 19;107(2):149–59.

57. Nakagawa M, Oda Y, Eguchi T, Aishima S-I, Yao T, Hosoi F, et al. Expression profile of class I histone deacetylases in human cancer tissues. Oncol Rep. 2007 Oct;18(4):769–74.

58. Warrener R, Beamish H, Burgess A, Waterhouse NJ, Giles N, Fairlie D, et al. Tumor cell-selective cytotoxicity by targeting cell cycle checkpoints. FASEB J. 2003 Aug;17(11):1550–2.

59. Bertrand P. Inside HDAC with HDAC inhibitors. Eur J Med Chem. 2010 Jun;45(6):2095–116.

60. Yamaguchi T, Cubizolles F, Zhang Y, Reichert N, Kohler H, Seiser C, et al. Histone deacetylases 1 and 2 act in concert to promote the G1-to-S progression. Genes Dev. 2010 Mar 1;24(5):455–69.

61. Zupkovitz G, Grausenburger R, Brunmeir R, Senese S, Tischler J, Jurkin J, et al. The cyclin-dependent kinase inhibitor p21 is a crucial target for histone deacetylase 1 as a regulator of cellular proliferation. Mol Cell Biol. 2010 Mar;30(5):1171–81.

62. Senese S, Zaragoza K, Minardi S, Muradore I, Ronzoni S, Passafaro A, et al. Role for histone deacetylase 1 in human tumor cell proliferation. Mol Cell Biol. 2007 Jul;27(13):4784–95.

63. Oh M, Choi I-K, Kwon HJ. Inhibition of histone deacetylase1 induces autophagy. Biochem Biophys Res Commun. 2008 May 16;369(4):1179–83.

64. Huang BH, Laban M, Leung CH-W, Lee L, Lee CK, Salto-Tellez M, et al. Inhibition of histone deacetylase 2 increases apoptosis and p21Cip1/WAF1 expression, independent of histone deacetylase 1. Cell Death Differ. 2005 Apr;12(4):395–404.

65. Cunliffe VT. Eloquent silence: developmental functions of Class I histone deacetylases. Curr Opin Genet Dev. 2008 Oct;18(5):404–10.

66. Waltregny D, Glénisson W, Tran SL, North BJ, Verdin E, Colige A, et al. Histone deacetylase HDAC8 associates with smooth muscle alpha-actin and is essential for smooth muscle cell contractility. FASEB J. 2005 Jun;19(8):966–8.

67. Lee H, Sengupta N, Villagra A, Rezai-Zadeh N, Seto E. Histone deacetylase 8 safeguards the human ever-shorter telomeres 1B (hEST1B) protein from ubiquitin-mediated degradation. Mol Cell Biol. 2006 Jul;26(14):5259–69.

68. Nusinzon I, Horvath CM. Positive and negative regulation of the innate antiviral response and beta interferon gene expression by deacetylation. Mol Cell Biol. 2006 Apr;26(8):3106–13.

69. Gao L, Cueto MA, Asselbergs F, Atadja P. Cloning and functional characterization of HDAC11, a novel member of the human histone deacetylase family. J Biol Chem. 2002 Jul 12;277(28):25748–55.

70. Vannini A, Volpari C, Filocamo G, Casavola EC, Brunetti M, Renzoni D, et al. Crystal structure of a eukaryotic zinc-dependent histone deacetylase, human HDAC8, complexed with a hydroxamic acid inhibitor. PNAS. 2004 Oct 19;101(42):15064–9.

71. Finnin MS, Donigian JR, Cohen A, Richon VM, Rifkind RA, Marks PA, et al. Structures of a histone deacetylase homologue bound to the TSA and SAHA inhibitors. Nature. 1999 Sep 9;401(6749):188–93.

72. Fersht AR, Sperling J. The charge relay system in chymotrypsin and chymotrypsinogen. J Mol Biol. 1973 Feb 25;74(2):137–49.

73. Bressi JC, Jennings AJ, Skene R, Wu Y, Melkus R, De Jong R, et al. Exploration of the HDAC2 foot pocket: Synthesis and SAR of substituted N-(2-aminophenyl)benzamides. Bioorg Med Chem Lett. 2010 May 15;20(10):3142–5.

74. Watson PJ, Fairall L, Santos GM, Schwabe JWR. Structure of HDAC3 bound to co-repressor and inositol tetraphosphate. Nature. 2012 Jan 19;481(7381):335–40.

75. Soriano FX, Hardingham GE. In cortical neurons HDAC3 activity suppresses RD4-dependent SMRT export. PLoS ONE. 2011;6(6):e21056.

76. Guenther MG, Lane WS, Fischle W, Verdin E, Lazar MA, Shiekhattar R. A core SMRT corepressor complex containing HDAC3 and TBL1, a WD40-repeat protein linked to deafness. Genes Dev. 2000 May 1;14(9):1048–57.

77. Yoon H-G, Chan DW, Huang Z-Q, Li J, Fondell JD, Qin J, et al. Purification and functional characterization of the human N-CoR complex: the roles of HDAC3, TBL1 and TBLR1. EMBO J. 2003 Mar 17;22(6):1336–46.

78. Oberoi J, Fairall L, Watson PJ, Yang J-C, Czimmerer Z, Kampmann T, et al. Structural basis for the assembly of the SMRT/NCoR core transcriptional repression machinery. Nat Struct Mol Biol. 2011 Feb;18(2):177–84.

79. You S-H, Liao X, Weiss RE, Lazar MA. The interaction between nuclear receptor corepressor and histone deacetylase 3 regulates both positive and negative thyroid hormone action in vivo. Mol Endocrinol. 2010 Jul;24(7):1359–67.

80. Ishizuka T, Lazar MA. The nuclear receptor corepressor deacetylase activating domain is essential for repression by thyroid hormone receptor. Mol Endocrinol. 2005 Jun;19(6):1443–51.

81. Yin L, Wu N, Curtin JC, Qatanani M, Szwergold NR, Reid RA, et al. Rev-erbalpha, a heme sensor that coordinates metabolic and circadian pathways. Science. 2007 Dec 14;318(5857):1786–9.

82. Guenther MG, Yu J, Kao GD, Yen TJ, Lazar MA. Assembly of the SMRT-histone deacetylase 3 repression complex requires the TCP-1 ring complex. Genes Dev. 2002 Dec 15;16(24):3130–5.

83. Somoza JR, Skene RJ, Katz BA, Mol C, Ho JD, Jennings AJ, et al. Structural snapshots of human HDAC8 provide insights into the class I histone deacetylases. Structure. 2004 Jul;12(7):1325–34.

84. Jung M, Brosch G, Kölle D, Scherf H, Gerhäuser C, Loidl P. Amide analogues of trichostatin A as inhibitors of histone deacetylase and inducers of terminal cell differentiation. J Med Chem. 1999 Nov 4;42(22):4669–79.

85. Almenara J, Rosato R, Grant S. Synergistic induction of mitochondrial damage and apoptosis in human leukemia cells by flavopiridol and the histone deacetylase inhibitor suberoylanilide hydroxamic acid (SAHA). Leukemia. 2002 Jul;16(7):1331–43.

86. Richon VM, Emiliani S, Verdin E, Webb Y, Breslow R, Rifkind RA, et al. A class of hybrid polar inducers of transformed cell differentiation inhibits histone deacetylases. Proc Natl Acad Sci USA. 1998 Mar 17;95(6):3003–7.

87. Yoshida M, Kijima M, Akita M, Beppu T. Potent and specific inhibition of mammalian histone deacetylase both in vivo and in vitro by trichostatin A. J Biol Chem. 1990 Oct 5;265(28):17174–9.

88. Yoshida M, Hoshikawa Y, Koseki K, Mori K, Beppu T. Structural specificity for biological activity of trichostatin A, a specific inhibitor of mammalian cell cycle with potent differentiation-inducing activity in Friend leukemia cells. J Antibiot. 1990 Sep;43(9):1101–6.

89. Kanyo ZF, Scolnick LR, Ash DE, Christianson DW. Structure of a unique binuclear manganese cluster in arginase. Nature. 1996 Oct 10;383(6600):554–7.

90. Whitehead L, Dobler MR, Radetich B, Zhu Y, Atadja PW, Claiborne T, et al. Human HDAC isoform selectivity achieved via exploitation of the acetate release channel with structurally unique small molecule inhibitors. Bioorg Med Chem. 2011 Aug 1;19(15):4626–34.

91. Lee H, Rezai-Zadeh N, Seto E. Negative regulation of histone deacetylase 8 activity by cyclic AMP-dependent protein kinase A. Mol Cell Biol. 2004 Jan;24(2):765–73.

92. Lechner T, Carrozza MJ, Yu Y, Grant PA, Eberharter A, Vannier D, et al. Sds3 (suppressor of defective silencing 3) is an integral component of the yeast Sin3[middle dot]Rpd3 histone deacetylase complex and is required for histone deacetylase activity. J Biol Chem. 2000 Dec 29;275(52):40961–6.

93. Guenther MG, Barak O, Lazar MA. The SMRT and N-CoR corepressors are activating cofactors for histone deacetylase 3. Mol Cell Biol. 2001 Sep;21(18):6091–101.

94. Wen YD, Perissi V, Staszewski LM, Yang WM, Krones A, Glass CK, et al. The histone deacetylase-3 complex contains nuclear receptor corepressors. Proc Natl Acad Sci USA. 2000 Jun 20;97(13):7202–7.

95. Zhang Y, LeRoy G, Seelig HP, Lane WS, Reinberg D. The dermatomyositis-specific autoantigen Mi2 is a component of a complex containing histone deacetylase and nucleosome remodeling activities. Cell. 1998 Oct 16;95(2):279–89.

96. Hakimi M-A, Bochar DA, Chenoweth J, Lane WS, Mandel G, Shiekhattar R. A core-BRAF35 complex containing histone deacetylase mediates repression of neuronal-specific genes. Proc Natl Acad Sci USA. 2002 May 28;99(11):7420–5.

97. Humphrey GW, Wang Y, Russanova VR, Hirai T, Qin J, Nakatani Y, et al. Stable histone deacetylase complexes distinguished by the presence of SANT domain proteins CoREST/kiaa0071 and Mta-L1. J Biol Chem. 2001 Mar 2;276(9):6817–24.

98. Laherty CD, Yang WM, Sun JM, Davie JR, Seto E, Eisenman RN. Histone deacetylases associated with the mSin3 corepressor mediate mad transcriptional repression. Cell. 1997 May 2;89(3):349–56.

99. Heinzel T, Lavinsky RM, Mullen TM, Söderstrom M, Laherty CD, Torchia J, et al. A complex containing N-CoR, mSin3 and histone deacetylase mediates transcriptional repression. Nature. 1997 May 1;387(6628):43–8.

100. Nare B, Allocco JJ, Kuningas R, Galuska S, Myers RW, Bednarek MA, et al. Development of a scintillation proximity assay for histone deacetylase using a biotinylated peptide derived from histone-H4. Anal Biochem. 1999 Feb 15;267(2):390–6.

101. Hoffmann K, Brosch G, Loidl P, Jung M. A non-isotopic assay for histone deacetylase activity. Nucleic Acids Res. 1999 May 1;27(9):2057–8.

102. Hoffmann K, Brosch G, Loidl P, Jung M. First non-radioactive assay for in vitro screening of histone deacetylase inhibitors. Pharmazie. 2000 Aug;55(8):601–6.

103. Hoffmann K, Söll RM, Beck-Sickinger AG, Jung M. Fluorescence-labeled octapeptides as substrates for histone deacetylase. Bioconjug Chem. 2001 Feb;12(1):51–5.

104. Heltweg B, Jung M. A homogeneous nonisotopic histone deacetylase activity assay. J Biomol Screen. 2003 Feb;8(1):89–95.

105. Wegener D, Wirsching F, Riester D, Schwienhorst A. A fluorogenic histone deacetylase assay well suited for high-throughput activity screening. Chem Biol. 2003 Jan;10(1):61–8.

106. Halley F, Reinshagen J, Ellinger B, Wolf M, Niles AL, Evans NJ, et al. A bioluminogenic HDAC activity assay: validation and screening. J Biomol Screen. 2011 Dec;16(10):1227–35.

107. Riester D, Hildmann C, Schwienhorst A, Meyer-Almes F-J. Histone deacetylase inhibitor assay based on fluorescence resonance energy transfer. Anal Biochem. 2007 Mar 1;362(1):136–41.

108. Riester D, Hildmann C, Haus P, Galetovic A, Schober A, Schwienhorst A, et al. Non-isotopic dual parameter competition assay suitable for high-throughput screening of histone deacetylases. Bioorg Med Chem Lett. 2009 Jul 1;19(13):3651–6.

109. Marks BD, Fakhoury SA, Frazee WJ, Eliason HC, Riddle SM. A substrate-independent TR-FRET histone deacetylase inhibitor assay. J Biomol Screen. 2011 Dec;16(10):1247–53.

110. Gantt SL, Gattis SG, Fierke CA. Catalytic activity and inhibition of human histone deacetylase 8 is dependent on the identity of the active site metal ion. Biochemistry. 2006 May 16;45(19):6170–8.

111. Vannini A, Volpari C, Gallinari P, Jones P, Mattu M, Carfí A, et al. Substrate binding to histone deacetylases as shown by the crystal structure of the HDAC8-substrate complex. EMBO Rep. 2007 Sep;8(9):879–84.

112. Vanommeslaeghe K, De Proft F, Loverix S, Tourwé D, Geerlings P. Theoretical study revealing the functioning of a novel combination of catalytic motifs in histone deacetylase. Bioorg Med Chem. 2005 Jun 2;13(12):3987–92.

113. Liu L, Scolnick DM, Trievel RC, Zhang HB, Marmorstein R, Halazonetis TD, et al. p53 sites acetylated in vitro by PCAF and p300 are acetylated in vivo in response to DNA damage. Mol Cell Biol. 1999 Feb;19(2):1202–9.

114. Vaghefi H, Neet KE. Deacetylation of p53 after nerve growth factor treatment in PC12 cells as a post-translational modification mechanism of neurotrophin-induced tumor suppressor activation. Oncogene. 2004 Oct 21;23(49):8078–87.

115. Dowling DP, Gantt SL, Gattis SG, Fierke CA, Christianson DW. Structural studies of human histone deacetylase 8 and its site-specific variants complexed with substrate and inhibitors. Biochemistry. 2008 Dec 23;47(51):13554–63.

116. Haider S, Joseph CG, Neidle S, Fierke CA, Fuchter MJ. On the function of the internal cavity of histone deacetylase protein 8: R37 is a crucial residue for catalysis. Bioorg Med Chem Lett. 2011 Apr 1;21(7):2129–32.

117. Wang D-F, Wiest O, Helquist P, Lan-Hargest H-Y, Wiech NL. On the function of the 14 A long internal cavity of histone deacetylase-like protein: implications for the design of histone deacetylase inhibitors. J Med Chem. 2004 Jun 17;47(13):3409–17.

118. Wang D-F, Helquist P, Wiech NL, Wiest O. Toward selective histone deacetylase inhibitor design: homology modeling, docking studies, and molecular dynamics simulations of human class I histone deacetylases. J Med Chem. 2005 Nov 3;48(22):6936–47.

119. Delcuve GP, Khan DH, Davie JR. Targeting class I histone deacetylases in cancer therapy. Expert Opinion on Therapeutic Targets. 2013 Jan;17(1):29–41.

120. Boffa LC, Vidali G, Mann RS, Allfrey VG. Suppression of histone deacetylation in vivo and in vitro by sodium butyrate. J Biol Chem. 1978 May 25;253(10):3364–6.

121. Warrell RP Jr, He LZ, Richon V, Calleja E, Pandolfi PP. Therapeutic targeting of transcription in acute promyelocytic leukemia by use of an inhibitor of histone deacetylase. J Natl Cancer Inst. 1998 Nov 4;90(21):1621–5.

122. Archer SY, Hodin RA. Histone acetylation and cancer. Curr Opin Genet Dev. 1999 Apr;9(2):171–4.

123. Newmark HL, Young CW. Butyrate and phenylacetate as differentiating agents: practical problems and opportunities. J Cell Biochem Suppl. 1995;22:247–53.

124. Pouillart PR. Role of butyric acid and its derivatives in the treatment of colorectal cancer and hemoglobinopathies. Life Sci. 1998;63(20):1739–60.

125. Pili R, Kruszewski MP, Hager BW, Lantz J, Carducci MA. Combination of phenylbutyrate and 13-cis retinoic acid inhibits prostate tumor growth and angiogenesis. Cancer Res. 2001 Feb 15;61(4):1477–85.

126. Qiu L, Kelso MJ, Hansen C, West ML, Fairlie DP, Parsons PG. Anti-tumour activity in vitro and in vivo of selective differentiating agents containing hydroxamate. Br J Cancer. 1999 Jun;80(8):1252–8.

127. Kijima M, Yoshida M, Sugita K, Horinouchi S, Beppu T. Trapoxin, an antitumor cyclic tetrapeptide, is an irreversible inhibitor of mammalian histone deacetylase. J Biol Chem. 1993 Oct 25;268(30):22429–35.

128. Kwon HJ, Owa T, Hassig CA, Shimada J, Schreiber SL. Depudecin induces morphological reversion of transformed fibroblasts via the inhibition of histone deacetylase. Proc Natl Acad Sci USA. 1998 Mar 31;95(7):3356–61.

129. Furumai R, Komatsu Y, Nishino N, Khochbin S, Yoshida M, Horinouchi S. Potent histone deacetylase inhibitors built from trichostatin A and cyclic tetrapeptide antibiotics including trapoxin. Proc Natl Acad Sci USA. 2001 Jan 2;98(1):87–92.

130. Chakrabarty S, Jasmine, Bhadaliya C, Sinha BN, Mahesh A, Bai H, et al. Inhibitors of human histone deacetylase: synthesis and enzyme assay of hydroxamates with piperazine linker. Arch Pharm (Weinheim). 2010 Mar;343(3):167–72.

131. Kim YB, Lee KH, Sugita K, Yoshida M, Horinouchi S. Oxamflatin is a novel antitumor compound that inhibits mammalian histone deacetylase. Oncogene. 1999 Apr 15;18(15):2461–70.

132. Krämer OH, Göttlicher M, Heinzel T. Histone deacetylase as a therapeutic target. Trends in Endocrinology & Metabolism. 2001 Sep;12(7):294–300.

133. Van Lint C, Emiliani S, Verdin E. The expression of a small fraction of cellular genes is changed in response to histone hyperacetylation. Gene Expr. 1996;5(4-5):245–53.

134. Mitsiades CS, Mitsiades NS, McMullan CJ, Poulaki V, Shringarpure R, Hideshima T, et al. Transcriptional signature of histone deacetylase inhibition in multiple myeloma: biological and clinical implications. Proc Natl Acad Sci USA. 2004 Jan 13;101(2):540–5.

135. Lee J-H, Park J-H, Jung Y, Kim J-H, Jong H-S, Kim T-Y, et al. Histone deacetylase inhibitor enhances 5-fluorouracil cytotoxicity by down-regulating thymidylate synthase in human cancer cells. Mol Cancer Ther. 2006 Dec;5(12):3085–95.

136. Gray SG, Qian C-N, Furge K, Guo X, Teh BT. Microarray profiling of the effects of histone deacetylase inhibitors on gene expression in cancer cell lines. Int J Oncol. 2004 Apr;24(4):773–95.

137. Peart MJ, Smyth GK, van Laar RK, Bowtell DD, Richon VM, Marks PA, et al. Identification and functional significance of genes regulated by structurally different histone deacetylase inhibitors. Proc Natl Acad Sci USA. 2005 Mar 8;102(10):3697–702.

138. Hong J, Luesch H. Largazole: From discovery to broad-spectrum therapy. Natural Product Reports. 2012;29(4):449.

139. Zhang Y, Feng J, Jia Y, Xu Y, Liu C, Fang H, et al. Design, synthesis and primary activity assay of tripeptidomimetics as histone deacetylase inhibitors with linear linker and branched cap group. European Journal of Medicinal Chemistry. 2011 Nov;46(11):5387–97.

140. Dokmanovic M, Marks PA. Prospects: histone deacetylase inhibitors. J Cell Biochem. 2005 Oct 1;96(2):293–304.

141. Xu WS, Parmigiani RB, Marks PA. Histone deacetylase inhibitors: molecular mechanisms of action. Oncogene. 2007 Aug 13;26(37):5541–52.

142. Rasheed WK, Johnstone RW, Prince HM. Histone deacetylase inhibitors in cancer therapy. Expert Opin Investig Drugs. 2007 May;16(5):659–78.

143. Boumber Y, Younes A, Garcia-Manero G. Mocetinostat (MGCD0103): a review of an isotype-specific histone deacetylase inhibitor. Expert Opin Investig Drugs. 2011 Jun;20(6):823–9.

144. Haggarty SJ, Koeller KM, Wong JC, Grozinger CM, Schreiber SL. Domain-selective small-molecule inhibitor of histone deacetylase 6 (HDAC6)-mediated tubulin deacetylation. Proc Natl Acad Sci USA. 2003 Apr 15;100(8):4389–94.

145. Jose B, Oniki Y, Kato T, Nishino N, Sumida Y, Yoshida M. Novel histone deacetylase inhibitors: cyclic tetrapeptide with trifluoromethyl and pentafluoroethyl ketones. Bioorg Med Chem Lett. 2004 Nov 1;14(21):5343–6.

146. Belvedere S, Witter DJ, Yan J, Secrist JP, Richon V, Miller TA. Aminosuberoyl hydroxamic acids (ASHAs): a potent new class of HDAC inhibitors. Bioorg Med Chem Lett. 2007 Jul 15;17(14):3969–71.

147. He J, Liu H, Chen Y. Effects of trichostatin A on HDAC8 expression, proliferation and cell cycle of molt-4 cells. J Huazhong Univ Sci Technol Med Sci. 2006;26(5):531–3.

148. Mann BS, Johnson JR, Cohen MH, Justice R, Pazdur R. FDA approval summary: vorinostat for treatment of advanced primary cutaneous T-cell lymphoma. Oncologist. 2007 Oct;12(10):1247–52.

149. Ito K, Ito M, Elliott WM, Cosio B, Caramori G, Kon OM, et al. Decreased histone deacetylase activity in chronic obstructive pulmonary disease. N Engl J Med. 2005 May 12;352(19):1967–76.

150. Ito K, Lim S, Caramori G, Cosio B, Chung KF, Adcock IM, et al. A molecular mechanism of action of theophylline: Induction of histone deacetylase activity to decrease inflammatory gene expression. Proc Natl Acad Sci USA. 2002 Jun 25;99(13):8921–6.

151. Singh RK, Mandal T, Balsubramanian N, Viaene T, Leedahl T, Sule N, et al. Histone deacetylase activators: N-acetylthioureas serve as highly potent and isozyme selective activators for human histone deacetylase-8 on a fluorescent substrate. Bioorg Med Chem Lett. 2011 Oct 1;21(19):5920–3.

152. Alcaín FJ, Villalba JM. Sirtuin activators. Expert Opinion on Therapeutic Patents. 2009 Apr;19(4):403–14.

153. Deardorff MA, Bando M, Nakato R, Watrin E, Itoh T, Minamino M, et al. HDAC8 mutations in Cornelia de Lange syndrome affect the cohesin acetylation cycle. Nature. 2012 Sep 13;489(7415):313–7.

154. Thangapandian S, John S, Lee Y, Arulalapperumal V, Lee KW. Molecular modeling study on tunnel behavior in different histone deacetylase isoforms. PLoS ONE. 2012;7(11):e49327.

155. Greenfield NJ. Using circular dichroism spectra to estimate protein secondary structure. Nat Protoc. 2006;1(6):2876–90.

156. Greenfield NJ. Using circular dichroism collected as a function of temperature to determine the thermodynamics of protein unfolding and binding interactions. Nat Protoc. 2006;1(6):2527–35.

157. Kelly SM, Jess TJ, Price NC. How to study proteins by circular dichroism. Biochim Biophys Acta. 2005 Aug 10;1751(2):119–39.

158. Bradford MM. A rapid and sensitive method for the quantitation of microgram quantities of protein utilizing the principle of protein-dye binding. Anal Biochem. 1976 May 7;72:248–54.

159. Wiseman T, Williston S, Brandts JF, Lin LN. Rapid measurement of binding constants and heats of binding using a new titration calorimeter. Anal Biochem. 1989 May 15;179(1):131–7.

160. Santoro MM, Bolen DW. Unfolding free energy changes determined by the linear extrapolation method. 1. Unfolding of phenylmethanesulfonyl alpha-chymotrypsin using different denaturants. Biochemistry. 1988 Oct 18;27(21):8063–8.

161. Cabrita LD, Dai W, Bottomley SP. A family of E. coli expression vectors for laboratory scale and high throughput soluble protein production. BMC Biotechnol. 2006;6:12.

162. Hassig CA, Tong JK, Fleischer TC, Owa T, Grable PG, Ayer DE, et al. A role for histone deacetylase activity in HDAC1-mediated transcriptional repression. Proc Natl Acad Sci USA. 1998 Mar 31;95(7):3519–24.

163. Johnson CA, Barlow AL, Turner BM. Molecular cloning of Drosophila melanogaster cDNAs that encode a novel histone deacetylase dHDAC3. Gene. 1998 Oct 9;221(1):127–34.

164. Dowling DP, Gattis SG, Fierke CA, Christianson DW. Structures of metal-substituted human histone deacetylase 8 provide mechanistic inferences on biological function. Biochemistry. 2010 Jun 22;49(24):5048–56.

165. Dietz KC, Casaccia P. HDAC inhibitors and neurodegeneration: At the edge between protection and damage. Pharmacological Research. 2010 Jul;62(1):11–7.

166. Grishin NV, Phillips MA, Goldsmith EJ. Modeling of the spatial structure of eukaryotic ornithine decarboxylases. Protein Sci. 1995 Jul;4(7):1291–304.

167. Davie JR. Inhibition of histone deacetylase activity by butyrate. J Nutr. 2003 Jul;133(7 Suppl):2485S–2493S.

168. Lee HJ, Chun M, Kandror KV. Tip60 and HDAC7 interact with the endothelin receptor a and may be involved in downstream signaling. J Biol Chem. 2001 May 18;276(20):16597–600.

169. Vinolo MAR, Rodrigues HG, Nachbar RT, Curi R. Regulation of inflammation by short chain fatty acids. Nutrients. 2011 Oct;3(10):858–76.

170. Schultz BE, Misialek S, Wu J, Tang J, Conn MT, Tahilramani R, et al. Kinetics and comparative reactivity of human class I and class IIb histone deacetylases. Biochemistry. 2004 Aug 31;43(34):11083–91.

171. Morrison JF. Kinetics of the reversible inhibition of enzyme-catalysed reactions by tight-binding inhibitors. Biochim Biophys Acta. 1969;185(2):269–86.

172. Singh RK, Mandal T, Balasubramanian N, Cook G, Srivastava DK. Coumarin-suberoylanilide hydroxamic acid as a fluorescent probe for determining binding affinities and off-rates of histone deacetylase inhibitors. Anal Biochem. 2011 Jan 15;408(2):309–15.

173. Scruggs AW, Flores CL, Wachter R, Woodbury NW. Development and characterization of green fluorescent protein mutants with altered lifetimes. Biochemistry. 2005 Oct 11;44(40):13377–84.

174. Pollak E, Talkner P. Reaction rate theory: what it was, where is it today, and where is it going? Chaos. 2005 Jun;15(2):26116.

175. Haberland M, Montgomery RL, Olson EN. The many roles of histone deacetylases in development and physiology: implications for disease and therapy. Nat Rev Genet. 2009 Jan;10(1):32–42.

176. Kazantsev AG, Thompson LM. Therapeutic application of histone deacetylase inhibitors for central nervous system disorders. Nat Rev Drug Discov. 2008 Oct;7(10):854–68.

177. Drummond DC, Noble CO, Kirpotin DB, Guo Z, Scott GK, Benz CC. Clinical development of histone deacetylase inhibitors as anticancer agents. Annu Rev Pharmacol Toxicol. 2005;45:495–528.

178. Gregoretti IV, Lee Y-M, Goodson HV. Molecular evolution of the histone deacetylase family: functional implications of phylogenetic analysis. J Mol Biol. 2004 Apr 16;338(1):17–31.

179. Hernick M, Fierke CA. Zinc hydrolases: the mechanisms of zinc-dependent deacetylases. Arch Biochem Biophys. 2005 Jan 1;433(1):71–84.

180. Frye RA. Phylogenetic classification of prokaryotic and eukaryotic Sir2-like proteins. Biochem Biophys Res Commun. 2000 Jul 5;273(2):793–8.

181. Milne JC, Denu JM. The Sirtuin family: therapeutic targets to treat diseases of aging. Curr Opin Chem Biol. 2008 Feb;12(1):11–7.

182. Balasubramanian S, Ramos J, Luo W, Sirisawad M, Verner E, Buggy JJ. A novel histone deacetylase 8 (HDAC8)-specific inhibitor PCI-34051 induces apoptosis in T-cell lymphomas. Leukemia. 2008 May;22(5):1026–34.

183. Durst KL, Lutterbach B, Kummalue T, Friedman AD, Hiebert SW. The inv(16) fusion protein associates with corepressors via a smooth muscle myosin heavy-chain domain. Mol Cell Biol. 2003 Jan;23(2):607–19.

184. Wilson BJ, Tremblay AM, Deblois G, Sylvain-Drolet G, Giguère V. An acetylation switch modulates the transcriptional activity of estrogen-related receptor alpha. Mol Endocrinol. 2010 Jul;24(7):1349–58.

185. Gurard-Levin ZA, Kilian KA, Kim J, Bähr K, Mrksich M. Peptide arrays identify isoform-selective substrates for profiling endogenous lysine deacetylase activity. ACS Chem Biol. 2010 Sep 17;5(9):863–73.

186. Gurard-Levin ZA, Mrksich M. The activity of HDAC8 depends on local and distal sequences of its peptide substrates. Biochemistry. 2008 Jun 10;47(23):6242–50.

187. Gurard-Levin ZA, Kim J, Mrksich M. Combining mass spectrometry and peptide arrays to profile the specificities of histone deacetylases. Chembiochem. 2009 Sep 4;10(13):2159–61.

188. Smith BC, Denu JM. Acetyl-lysine analog peptides as mechanistic probes of protein deacetylases. J Biol Chem. 2007 Dec 21;282(51):37256–65.

189. Alarcón R, Orellana MS, Neira B, Uribe E, García JR, Carvajal N. Mutational analysis of substrate recognition by human arginase type I--agmatinase activity of the N130D variant. FEBS J. 2006 Dec;273(24):5625–31.

190. Gantt SL, Joseph CG, Fierke CA. Activation and Inhibition of Histone Deacetylase 8 by Monovalent Cations. J Biol Chem. 2010 Feb 26;285(9):6036–43.

191. Riester D, Wegener D, Hildmann C, Schwienhorst A. Members of the histone deacetylase superfamily differ in substrate specificity towards small synthetic substrates. Biochem Biophys Res Commun. 2004 Nov 19;324(3):1116–23.

192. Fersht A. Structure and Mechanism in Protein Science : A Guide to Enzyme Catalysis and Protein Folding / A. Fersht.

193. Bar-Even A, Noor E, Savir Y, Liebermeister W, Davidi D, Tawfik DS, et al. The moderately efficient enzyme: evolutionary and physicochemical trends shaping enzyme parameters. Biochemistry. 2011 May 31;50(21):4402–10.

194. Kim H, Buongiorno J. Detection of liquid–vapor–solid triple contact line in two-phase heat transfer phenomena using high-speed infrared thermometry. International Journal of Multiphase Flow. 2011 Mar;37(2):166–72.

195. Lemoine M, Younes A. Histone deacetylase inhibitors in the treatment of lymphoma. Discov Med. 2010 Nov;10(54):462–70.

196. Dai Y, Chen S, Kramer LB, Funk VL, Dent P, Grant S. Interactions between bortezomib and romidepsin and belinostat in chronic lymphocytic leukemia cells. Clin Cancer Res. 2008 Jan 15;14(2):549–58.

197. Estiu G, West N, Mazitschek R, Greenberg E, Bradner JE, Wiest O. On the Inhibition of Histone Deacetylase 8. Bioorg Med Chem. 2010 Jun 1;18(11):4103–10.

198. Nobeli I, Favia AD, Thornton JM. Protein promiscuity and its implications for biotechnology. Nat Biotechnol. 2009 Feb;27(2):157–67.

199. Hedstrom L. Serine protease mechanism and specificity. Chem Rev. 2002 Dec;102(12):4501–24.

200. Ollis DL, Cheah E, Cygler M, Dijkstra B, Frolow F, Franken SM, et al. The alpha/beta hydrolase fold. Protein Eng. 1992 Apr;5(3):197–211.

201. Weikl TR, von Deuster C. Selected-fit versus induced-fit protein binding: kinetic differences and mutational analysis. Proteins. 2009 Apr;75(1):104–10.

202. Fluorescence-Based Biosensors: From Concepts to Applications. Academic Press; 2012.

203. Matthews BW, Nicholson H, Becktel WJ. Enhanced protein thermostability from site-directed mutations that decrease the entropy of unfolding. Proc Natl Acad Sci U S A. 1987 Oct;84(19):6663–7.

204. Random coil [Internet]. Wikipedia, the free encyclopedia. 2013 [cited 2013 May 9]. Available from: http://en.wikipedia.org/w/index.php?title=Random_coil&oldid=541209257

205. Truong K, Su Y, Song J, Chen Y. Entropy-driven mechanism of an E3 ligase. Biochemistry. 2011 Jun 28;50(25):5757–66.

206. Dunitz JD. The entropic cost of bound water in crystals and biomolecules. Science. 1994 Apr 29;264(5159):670.

207. Dunker AK, Lawson JD, Brown CJ, Williams RM, Romero P, Oh JS, et al. Intrinsically disordered protein. Journal of Molecular Graphics and Modelling. 2001 Feb;19(1):26–59.

208. Uversky VN, Dunker AK. Understanding protein non-folding. Biochimica et Biophysica Acta (BBA) - Proteins and Proteomics. 2010 Jun;1804(6):1231–64.

209. Fersht AR. Denaturation (Proteins). In: Editors-in-Chief: Stanley Maloy, Kelly Hughes, editors. Brenner's Encyclopedia of Genetics (Second Edition) [Internet]. San Diego: Academic Press; 2013 [cited 2013 May 14]. p. 302–3. Available from: http://www.sciencedirect.com/science/article/pii/B9780123749840003934

210. Vaidya AS, Neelarapu R, Madriaga A, Bai H, Mendonca E, Abdelkarim H, et al. Novel histone deacetylase 8 ligands without a zinc chelating group: Exploring an "upside-down" binding pose. Bioorg Med Chem Lett [Internet]. 2012 Sep 7 [cited 2012 Oct 9]; Available from: http://www.ncbi.nlm.nih.gov/pubmed/23010266

211. Suzuki T, Ota Y, Ri M, Bando M, Gotoh A, Itoh Y, et al. Rapid discovery of highly potent and selective inhibitors of histone deacetylase 8 using click chemistry to generate candidate libraries. J Med Chem. 2012 Nov 26;55(22):9562–75.

212. Bermúdez-Lugo JA, Perez-Gonzalez O, Rosales-Hernández MC, Ilizaliturri-Flores I, Trujillo-Ferrara J, Correa-Basurto J. Exploration of the valproic acid binding site on histone deacetylase 8 using docking and molecular dynamic simulations. J Mol Model. 2012 Jun;18(6):2301–10.